2013-09

Assessment of tropical cyclone structure variability

Stenger, Robert A.

Monterey, California: Naval Postgraduate School

NAVAL POSTGRADUATE SCHOOL

MONTEREY, CALIFORNIA

DISSERTATION

ASSESSMENT OF TROPICAL CYCLONE STRUCTURE VARIABILITY

by

Robert A. Stenger

September 2013

Dissertation Supervisor: Russell L. Elsberry

THIS PAGE INTENTIONALLY LEFT BLANK

REPORT DOCUMENTATION PAGE

Form Approved OMB No. 0704-0188

1. AGENCY USE ONLY (*Leave blank*)	2. REPORT DATE	3. REPORT TYPE AND DATES COVERED
	September 2013	Dissertation

4. TITLE AND SUBTITLE:

ASSESSMENT OF TROPICAL CYCLONE STRUCTURE VARIABILITY

5. FUNDING NUMBERS

6. AUTHOR(S)

Robert A. Stenger

7. PERFORMING ORGANIZATION NAME(S) AND ADDRESS(ES)

Naval Postgraduate School
Monterey, CA 93943-5000

8. PERFORMING ORGANIZATION REPORT NUMBER

9. SPONSORING/MONITORING AGENCY NAME(S) AND ADDRESS(ES)

N/A

10. SPONSORING/MONITORING AGENCY REPORT NUMBER

11. SUPPLEMENTARY NOTES

The views expressed in this dissertation are those of the author and do not reflect the official policy or position of the Department of Defense or the U.S. Government.

12a. DISTRIBUTION/AVAILABILITY STATEMENT

Approved for public release; distribution unlimited

12b. DISTRIBUTION CODE

A

13. ABSTRACT (*maximum 200 words*)

The landfall of large hurricanes in densely populated areas has increased the awareness that tropical cyclone structure plays an important role in the destructive potential of a storm. A unique set of H*Wind analyses of Atlantic tropical cyclones during the 2003-2005 seasons is studied to better understand the internal and external mechanisms that lead to significant variability in surface wind structure. Secondary eyewall formation, asymmetric convection, land interaction, and environmental vertical wind shear were generally found to be mechanisms for radius of maximum wind increases, intensity decreases, and size of the radius of 34-kt wind increases. Two modes of size changes were documented that may lead to 100 km increases in 12-24 h, or near-zero size changes when a sharper than average outer wind structure profiles are generated. The statistical relationships among the radius of maximum wind, intensity, and outer-core wind structure from this sample may provide perturbed vortex initial conditions for an ensemble model to predict structure changes.

14. SUBJECT TERMS

Tropical Meteorology; Tropical Cyclone Structure; Tropical Cyclone Prediction; Western North Pacific Typhoons; Atlantic Hurricanes; H*Wind Analysis; H*Wind Analysis Tool; Ensemble Modelling; Secondary Eyewall Formation; Asymmetric Convection; Land Interaction; Vertical Wind Shear

15. NUMBER OF PAGES

311

16. PRICE CODE

17. SECURITY CLASSIFICATION OF REPORT	18. SECURITY CLASSIFICATION OF THIS PAGE	19. SECURITY CLASSIFICATION OF ABSTRACT	20. LIMITATION OF ABSTRACT
Unclassified	Unclassified	Unclassified	UL

NSN 7540-01-280-5500

Standard Form 298 (Rev. 2-89)
Prescribed by ANSI Std. 239-18

THIS PAGE INTENTIONALLY LEFT BLANK

Approved for public release; distribution is unlimited

ASSESSMENT OF TROPICAL CYCLONE STRUCTURE VARIABILITY

Robert A. Stenger
Lieutenant Colonel, United States Air Force
B.S., Texas A&M University, 1994
M.S., Air Force Institute of Technology, 2000

Submitted in partial fulfillment of the
requirements of the degree of

DOCTOR OF PHILOSOPHY IN METEOROLOGY

from the

NAVAL POSTGRADUATE SCHOOL
September 2013

Author: _____
Robert A. Stenger

Approved by:

_____
Russell L. Elsberry
Distinguished Research Professor of Meteorology
Dissertation Supervisor

_____
Wendell A. Nuss
Professor of Meteorology
Assistant Dissertation Supervisor

_____
Patrick A. Harr
Professor of Meteorology
Assistant Dissertation Supervisor

_____
Michael T. Montgomery
Professor of Meteorology

_____
Robert A. Koyak
Associate Professor of Operations Research

Approved by: _____
Wendell A. Nuss, Chair, Department of Meteorology

Approved by: _____
O. Douglas Moses, Associate Provost for Academic Affairs

THIS PAGE INTENTIONALLY LEFT BLANK

ABSTRACT

The landfall of large hurricanes in densely populated areas has increased the awareness that tropical cyclone structure plays an important role in the destructive potential of a storm. A unique set of H*Wind analyses of Atlantic tropical cyclones during the 2003–2005 seasons is studied to better understand the internal and external mechanisms that lead to significant variability in surface wind structure. Secondary eyewall formation, asymmetric convection, land interaction, and environmental vertical wind shear were generally found to be mechanisms for radius of maximum wind increases, intensity decreases, and size of the radius of 34-kt wind increases. Two modes of size changes were documented that may lead to 100 km increases in 12–24 h, or near-zero size changes when a sharper than average outer wind structure profiles are generated. The statistical relationships among the radius of maximum wind, intensity, and outer-core wind structure from this sample may provide perturbed vortex initial conditions for an ensemble model to predict structure changes.

THIS PAGE INTENTIONALLY LEFT BLANK

TABLE OF CONTENTS

THIS PAGE INTENTIONALLY LEFT BLANK

LIST OF FIGURES

LIST OF TABLES

THIS PAGE INTENTIONALLY LEFT BLANK

ACKNOWLEDGMENTS

The sheer magnitude and complexity in bringing this research project to completion has required me to seek advice and assistance from a handful of individuals to whom I owe a great deal of thanks. First, I would like to offer my sincere gratitude to my dissertation supervisor, Distinguished Research Professor Russ Elsberry, for his unwavering patience and support in bringing this eight year project to completion. His skilled guidance and our numerous meaningful discussions were invaluable in perfecting this research and the resulting manuscript. I would also be remiss if I failed to thank my committee members Professor Wendell Nuss, Professor Pat Harr, Professor Mike Montgomery, and Associate Professor Bob Koyak for their insightful comments in reviewing the final draft of this dissertation manuscript. Their contributions have undoubtedly resulted in an improved final synopsis of this research project.

Additionally, I appreciate the time of Dr. Craig Bishop of the Naval Research Laboratory Monterey during several meetings which helped shape the final direction of this research. I would also like to thank Mr. Mike Clancy of Fleet Numerical Meteorology and Oceanography Center for providing the sponsorship that allowed this research project to move forward. Dr. Mark Powell of the Hurricane Research Division is also acknowledged for making his H*Wind analyses available.

Finally, I owe my utmost appreciate to my wife Christy and my children for the sacrifices they endured while I spent lengthy hours in bringing this research to completion. My wife has always been a steadfast source of optimism in raising my spirits even when I had doubts in my own abilities to bring this enormous project to fruition.

THIS PAGE INTENTIONALLY LEFT BLANK

I. INTRODUCTION

A. MOTIVATION

Hurricanes are among the most costly natural disasters in the United States as a result of strong winds (Pielke and Landsea 1998) and flooding (Elsberry 2002). In recent years, the landfall of large hurricanes in densely populated areas along the Gulf Coast of the United States has increased the awareness that tropical cyclone structure plays an important role in the destructive potential of a storm (Powell and Reinhold 2007). The tropical cyclone structure change can be quite large over relatively short periods of time. Without a complete understanding of these structure variations, accurate wind and surge forecasting for tropical cyclone damage potential will remain elusive.

In the United States, the emergency management community requires warnings of when sustained (one-minute average) surface winds exceeding gale-force ($\geq$34 kt) winds will arrive at a location in advance of a tropical cyclone. That is, the objective is to give the public sufficient time to complete all disaster preparedness activities prior to the onset of gale-force winds and the often coincident heavy precipitation, so that these activities (including evacuation or moving to a secure shelter) are completed safely.

While an accurate understanding of structure change for landfalling cyclones is a concern to populated coastal regions, they are equally important to commercial shipping vessels, and the airplanes and warships of the United States Air Force and Navy and those of its allies. When a threat of damaging 50-kt winds exists from a tropical cyclone within 48 hours, the Air Force will evacuate airborne assets and personnel to inland locations. Airborne assets that are not flight-ready and are not repairable within a reasonable amount of time must be placed inside a hangar and tied down. Total evacuation of a military installation is very costly, but the direct impact of damaging tropical cyclone winds can be absolutely devastating. Unfortunately, our inability to forecast tropical cyclone track, intensity, and structure with great accuracy leads decision makers to error on the side of safety and results in unnecessary expenditure of limited funds for false alarms.

As for the Navy, surface vessels that are under way must remain outside the radius of gale-force winds. Since there is little certainty in our ability to forecast

tropical cyclone structure, ships must remain well beyond the perimeter of danger. This leads to increased fuel costs and lost time to missions within the assigned area of operations. In addition, a naval surface fleet that is in port must be sortied when a tropical cyclone is a threat to the port. Once again, uncertainty can lead to the unnecessary expenditure of tax dollars (as much as 15 million dollars) when the forecast results in a false alarm.

1. Definition of Inner and Outer Core

While prediction of tropical cyclone motion has steadily improved over the past two decades, comparatively lesser progress has been made toward the understanding of intensity or structure change until recent work such as Montgomery and Smith (2013). The structure of a tropical cyclone is often divided into two regions: the inner core and the outer core. The inner-core region includes the eye of the storm, the eyewall clouds, and convective asymmetries (e.g., spiral rainbands). However, the definition of the inner-core region varies with author. For example, Weatherford and Gray (1988a) defined the inner core as the portion of the storm contained within a 1° radius (∼111 km) of the storm center and Wang and Wu (2004) define it as the structure contained within twice the radius of maximum winds.

The outer-core region can be defined as the tropical cyclone structure outside of the inner-core region to the radius of gale-force winds, or the last closed isobar. Holland and Merrill (1984) define strength as the magnitude of cyclonic circulation in the outer-core region of the tropical cyclone. While structure changes in the inner-core region have been shown to be correlated with tropical cyclone intensity change, the correlation between intensity change and changes in the tropical cyclone outer-core structure appear to be weak (Weatherford and Gray 1988b; Wang and Wu 2004).

2. Surface Wind Profiles

Fiorino and Elsberry (1989) emphasized the importance of the tropical cyclone outer wind structure on the beta-effect propagation (BEP) component of storm motion. Employing a non-divergent barotropic model, they demonstrated that even when the BEP remained unchanged the inner (within 300 km in their vortex simulation) wind profiles had intensity variations from 20 m s^{-1} to 50 m s^{-1}. Conversely, BEP changed significantly with corresponding intensity changes in the outer (beyond 300 km) wind

profiles. For example, larger storms with stronger winds in outer region have a larger poleward and westward BEP component of motion.

Carr and Elsberry (1997) derived a simple wind structure relationship based on partial conservation of angular momentum concepts

$$v(r) = \frac{M}{r^x} - \frac{1}{2} f_o r, \tag{1}$$

where v is the tangential wind as a function of radius r, the exponent x is given as 0.4, and f_o is the Coriolis parameter at the latitude of the storm center. The constant $M = 0.5 f_o R_o^{1+x}$ is specified at a radius R_o where the cyclonic tangential wind goes to zero, which could also be considered as another "size" measure of the tropical cyclone. Examples of the resulting tangential wind profiles for a storm centered at 15° latitude and radii of different values of R_o are given in Fig. 1.

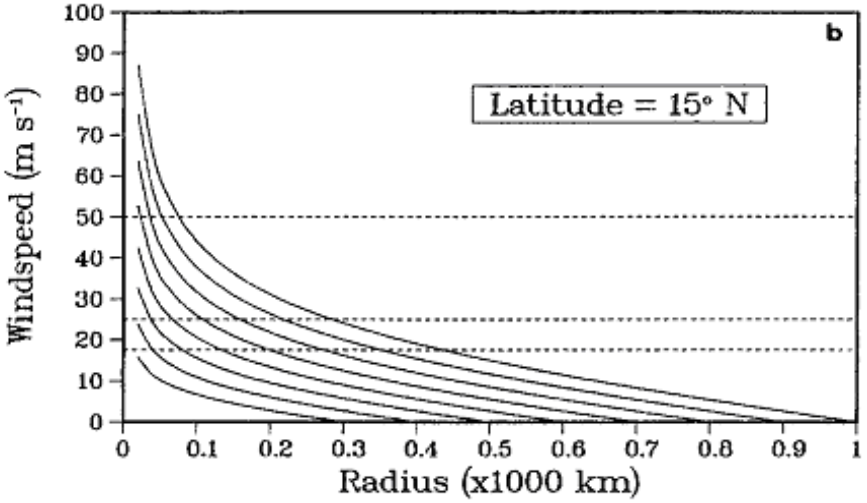

Figure 1 Tangential wind profiles with x = 0.4 in Eq. (1) for various radial extents R_o (the radius where tangential wind speed is zero) at 15° latitude. Threshold wind speeds of 17, 25, and 50 m s^{-1} are highlighted by horizontal dashed lines (From Carr and Elsberry 1997).

At large radii where the winds are small and the resulting frictional effects are small, the wind profile is primarily determined by conservation of earth angular momentum for the air parcel at the radius R_o (where the relative angular momentum is equal to zero). Therefore, the outer tangential wind increases nearly linearly with radius toward the storm center given the last term in Eq. (1) depends on the first power of radius. In the inner-core region, frictional influences are larger and angular momentum

is not conserved. Because the first term in Eq. (1) then becomes the dominant effect, the wind speed increases more rapidly toward the storm center. Following Fiorino and Elsberry (1989), Carr and Elsberry (1997) demonstrated that much larger BEP values resulted when outer wind profiles began at large values of R_o.

Due to the lack of adequate spatial coverage of observations, several numerical weather prediction (NWP) centers (e.g., Japan Meteorological Agency and U.S. Fleet Numerical Meteorology and Oceanography Center) use empirical relationships to specify the outer wind structure in tropical cyclones. As a result, two NWP models with different specifications of the outer wind structure in the tropical cyclone would predict different tracks even if the observations, data assimilation, and model physics and configuration were identical. So improved observations, understanding, and prediction of outer wind structure is expected to lead to improved track forecasts and thus better wind warnings for the public.

The implication from an empirical wind profile such as in Fig. 1 is that the outer- and inner-core wind structure vary together. That is, physical processes that increase (decrease) the intensity would have a corresponding increase (decrease) in the entire wind structure. In this simple model, the outer winds would increase during the intensification stage and would decrease during the weakening stage of the tropical cyclone life cycle.

In the idealized axisymmetric models of the intensification stage, a similar scenario occurs with outer wind speed increases following the spin-up of the inner core. In the Emanuel (1986, 1995a, b) model, it is assumed that the flow above a well-mixed surface boundary layer is thermodynamically reversible, and that gradient wind and hydrostatic balance apply. The temperature profile is assumed to be moist-neutral at each radius, so that the entire vertical temperature profile is known given the temperature and moisture near the surface, and from the hydrostatic equation the surface pressure is known. Emanuel's (1995a, b) model is formulated using axisymmetric balance dynamics and employs potential radius coordinates. Given an initial cyclonic vortex with near saturation of the tropospheric column, downdrafts that normally accompany deep convection are suppressed which allows surface fluxes to increase the subcloud layer entropy as the tangential force associated with surface friction leads to inflow of air parcels. As these air parcels approach the storm center, conservation of absolute angular momentum results in greater tangential wind speeds until the air parcels ascend in the eyewall cloud. Given potential radius coordinates can be derived,

the azimuthal velocity at any radius can be diagnosed. Smith et al. (2011) caution that this model focuses "largely on thermodynamic processes, making drastic simplifications to the dynamics through the assumption of gradient balance and hydrostatic balance."

Montgomery and Smith (2013) have proposed a new tropical cyclone intensification paradigm that recognizes the presence of localized, rotating deep convection that grows in a rotation-rich environment of a developing tropical cyclone. As such, this new paradigm is distinguished from the previous paradigms of CISK (conditional instability of the second kind; Charney and Eliassen 1964), cooperative intensification (Ooyama 1969), and WISHE (wind-induced surface heat exchange; Emanuel 1986), paradigms that model tropical cyclone intensification as an axisymmetric phenomenon. This new paradigm identifies two mechanisms of the mean tangential circulation spin-up: (i) convergence of absolute angular momentum above the boundary layer which is approximately materially conserved; and (ii) convergence of absolute angular momentum within the boundary layer which is not materially conserved (Bao et al. 2012; Montgomery and Smith 2013). Montgomery and Smith (2013) suggest that the convergence of absolute angular momentum within the boundary layer is responsible for producing the maximum tangential winds in the boundary layer, whereas convergence of absolute angular momentum above the boundary layer acts to broaden the outer circulation.

If the tropical wind structure changes are driven by the inner-core processes, the implication from empirical wind profile reasoning or the idealized, axisymmetric models would be that the outer winds would increase during the intensification stage and decrease during the decaying stage. Whereas the forecaster rules of thumb are compatible with the idea of increasing outer winds during the intensification stage, the general expectation (e.g., Merrill 1984) is that the tropical cyclone size expands (i.e., outer winds at a radius would be increasing) during the decay or extratropical transition stage. Especially in the case of extratropical transition in which the tropical cyclone is moving into the midlatitude westerlies, the apparent expansion may be due to the circulation being superposed on an environment with stronger winds.

Kimball and Mulekar (2004) produced a 15-year climatology of the six size parameters from the extended best track dataset of North Atlantic tropical cyclones. Kimball and Mulekar calculated the means, medians, and standard deviations of the radii of the eye, maximum winds, hurricane-force winds, damaging-force winds (defined at 25.7 m s^{-1}), gale-force winds, and the outer-most closed isobar. The advantage

of the Atlantic dataset is that aircraft reconnaissance observations are available in most of the tropical cyclones west of 55°W, which allows the calculation of these wind radii that are not directly observed in other basins where aircraft reconnaissance is not available. A possible disadvantage is the practice of including extratropical cyclones in the Atlantic dataset that may bias the statistics compared to other basins in which the tropical cyclones are only considered to exist in much lower latitudes.

Kimball and Mulekar (2004) construct a climatological evolution of the Saffir-Simpson categories based on the median values of the various radii (Fig. 2).

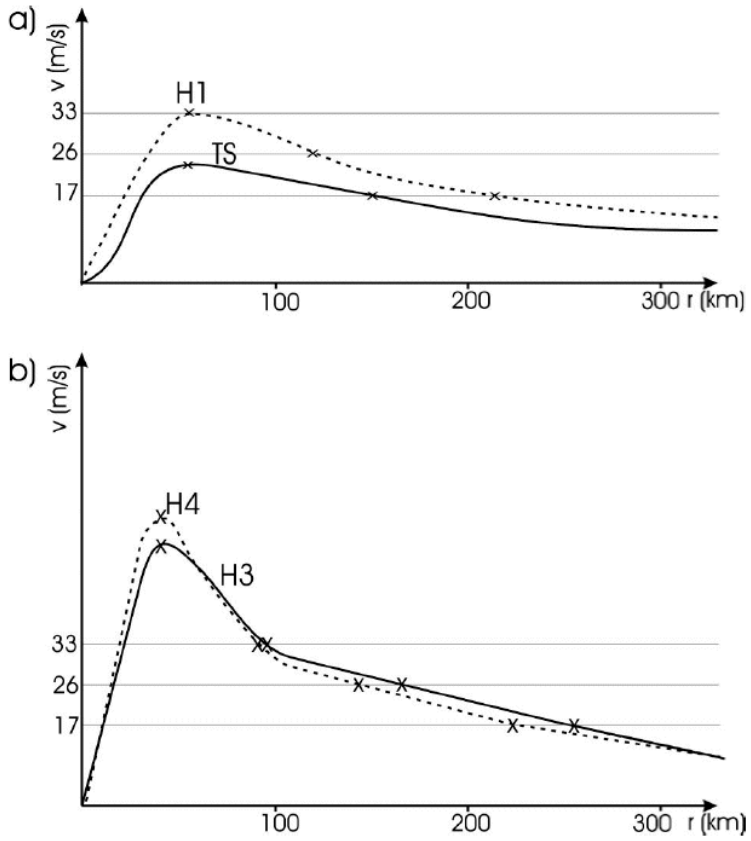

Figure 2 Median tangential wind profiles for Atlantic (a) tropical storms (TS) versus Saffir-Simpson Category 1 (H1) hurricanes and (b) Category 3 (H3) and Category 4 (H4) hurricanes (From Kimball and Mulekar 2004).

Note that the outer winds also increase as the intensity increases from Tropical Storm (TS) stage to Category 1 hurricanes (H1) in Fig. 2a. However, the 34-kt wind radius (R_{34}) value did not increase from Category 1 to Category 2 (not shown), but then did increase from Category 2 to Category 3. As shown in Fig. 2b, the median R_{34}

value for the Category 4 hurricanes actually decreases relative to the Category 3 value, which is different from the simple model of an increase in outer wind structure during intensification. The caution is that this climatological model of hurricane evolution is based on median values in each category in the sample rather than the evolution of individual cyclones.

Knaff et al. (2008) have developed a climatological and persistence technique for predicting the wind radii evolution in 12 h increments to 120 h. The key step in their technique is the fitting of the wind profile to the operational estimates of the 34, 50, and 64 kt radii. Their climatological wind profile has a symmetric component with a modified Rankine vortex profile that varies with latitude, storm translation speed, and maximum wind with statistical relationships derived from a 1998–2004 dataset in the Atlantic basin and 2001–2004 in the North Pacific basin. The modified Rankine vortex, $Vr^x = constant$ (where V is the tangential wind, r is the radius, and x is the dissipation rate) was proposed by Depperman (1947) to account for the loss of cyclonic relative angular momentum due to frictional dissipation at the surface which was not previously accounted for by the Rankine vortex (Holland 1980). The exponent x has been empirically determined using hurricane wind observations to be between 0.4 and 0.6 (Hughes 1952; Riehl 1954, 1963; Gray and Shea 1973). Knaff et al. (2008) found that the increase in tangential winds toward the center in the modified Rankine profile is more (less) rapid for all larger intensity tropical cyclones located below (above) 25°N latitude. In practice, the departures of operational estimates from this climatological wind profile are calculated and the deviations from climatology are assumed to decay over the 120-h forecast period based on a statistical persistence relationship. Because the persistence decay function decreases rapidly from 0.45–0.68 at 12 h to a value of 0.10 by 30–60 h (Fig. 1; Knaff et al. 2008), the "forecasts" after these times are essentially a reversion to the climatological profile, since the climatological profile is a modified Rankine profile tied to the maximum wind and a radius of maximum wind speeds for tropical cyclones at latitudes less than 25°N. For latitudes north of 25°N, the contribution of the increasing latitudinal effect due to the Coriolis, especially with a decreasing maximum wind speed, will then broaden the vortex (smaller value of exponent x in the modified Rankine vortex).

3. Secondary Eyewall Scenario

Willoughby et al. (1982) described secondary eyewalls in which a concentric ring of convection develops at an outer radii, and these convective regions have an associated wind maximum not accounted for by the simple profiles as in Fig. 1. Instead, a profile as in Fig. 1 would extend outward from the radius of maximum wind associated with the secondary eyewall, thus forming a decreasing wind profile farther outward from the original eyewall maximum closer to the tropical cyclone center. Because the secondary eyewalls in the cases described by Willoughby et al. (1982) tended to contract inward, progressively larger wind speeds evolved at smaller radii as in the modified Rankine vortex (vr^x = constant). Meanwhile, the maximum wind speed (i.e., the intensity) associated with the inner eyewall decreased such that it became smaller than the wind speed coincident with the secondary eyewall. This evolution has been termed an *eyewall replacement cycle*, although it is not always clear that the inner eyewall cloud band disappears. Elsberry et al. (2007) provide a more general characterization of the life cycle intensity changes: a decay and re-intensification cycle (Stage IIa, as used below).

Based on microwave imagery during 1997–2005, Hawkins et al. (2006) observed that 80 percent (70 percent, 50 percent, 40 percent) of the tropical cyclones with maximum winds exceeding 120 kt in the western North Pacific (Atlantic, eastern North Pacific, Southern Hemisphere) had one or more secondary eyewall formations. If an external environmental physical mechanism led to the secondary eyewall formation and assuming the profiles in Fig. 1 with the same exponent $x = 0.4$ are applicable, one may expect the outer wind speeds would increase, and the radius of 34-kt winds would increase. Alternately, an internal mechanism might create the secondary eyewall wind maximum and subsequently "spin-up" the wind speeds at outer radii along a profile as in Fig. 1.

A high-resolution numerical simulation by Terwey and Montgomery (2008) simulated secondary eyewall formation following the formation of an intense vortex (87 m s^{-1}) at a relatively small radius (30 km). Following secondary eyewall formation, the inner wind maximum decreased until about Hour 180 and the outer wind maximum at 80 km was stronger (65 m s^{-1}), thus defining a eyewall replacement cycle (see Fig. 3). Terwey and Montgomery do not display the outer wind profiles before and after the secondary eyewall formation and eyewall replacement cycle. To demonstrate the potential magnitude of the outer wind structure changes, a modified Rankine vortex with

an exponent $x = 0.5$ was assumed. Given the two wind maxima and corresponding radii in Fig. 3, the 50-kt wind radius would increase from 363 km to 541 km, and the 34-kt wind radius would increase from 785 km to 1170 km. While these outer wind radii are likely excessive, increases from before to after a secondary eyewall formation and eyewall replacement cycle suggest large outer wind structure modifications during such events. The possible implication of such an event occurring as the tropical cyclone was approaching the coast would be a decrease in the disaster preparation time needed before gale-force winds would reach the coast and an increase in the coastal regions affected by the tropical cyclone.

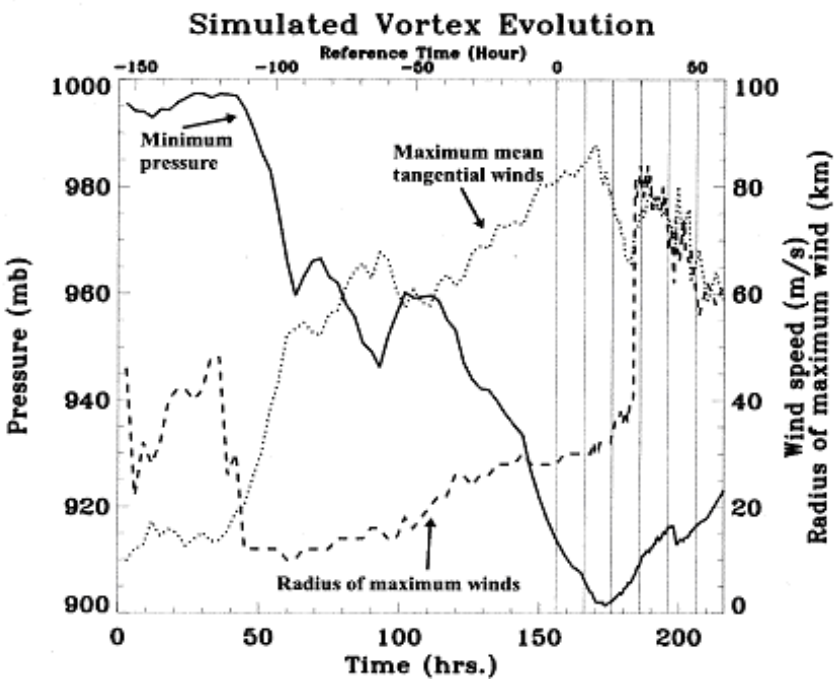

Figure 3 Modeled storm evolution through the simulation time for the control experiment. The solid line is the minimum pressure at 150 m above the surface. The dashed line is the radius of maximum mean tangential winds at 150 m above the surface. The dotted line is the radius of maximum azimuthally-averaged tangential winds through the domain (From Terwey and Montgomery 2008).

Kuo et al. (2009) studied intensity change of 55 western North Pacific typhoons with concentric eyewalls between 1997 and 2006. The authors found that the intensity of the typhoons tend to peak at the time of secondary eyewall formation, but only half

of those storms fit the standard model of intensification that would predict weakening following the formation of a secondary eyewall. They also found that the major difference between the concentric eyewall cases and nonconcentric eyewall cases is that the concentric eyewall cases are marked by relatively high intensity that has a longer duration prior to secondary eyewall formation. By contrast, the nonconcentric eyewall cases tended to experience rapid intensification and reach higher peak intensities.

Yang et al. (2013) developed an objective method to identify concentric eyewalls for western North Pacific typhoons using passive microwave imagery. Using 70 typhoon cases between 1997 and 2011, they identified three concentric eyewall types: (i) concentric eyewalls with an eyewall replacement cycle; (ii) concentric eyewalls with no eyewall replacement cycle; and (iii) concentric eyewalls that are maintained for an extended period of time. The typhoons that developed concentric eyewalls that are maintained for an extended period had relatively high intensity, and 50 percent larger moats and outer eyewall widths than those of the other two types of concentric eyewalls. The authors suggest that both internal dynamics and environmental conditions are important in determining the type of concentric eyewalls that form.

4. Annular Storm Structure

Under favorable environmental conditions, a tropical cyclone can form a stable, persistent axisymmetric wind structure coined as "annular" by Knaff et al. (2003). The formation of this special structure has been shown to be systematic through asymmetric mixing of entropy and vertical vorticity between the eye and eyewall of a storm involving one or two mesovortices. Annular tropical cyclones present a significant challenge to forecasters since their behavior does not follow the climatological norms of storm evolution or intensity. The intensity forecast errors for annular hurricanes in the Atlantic and eastern North Pacific during 1995–2001 are reported to be 10–40 percent larger than for typical hurricanes in these basins (Knaff et al. 2003). Intensity tendencies of annular systems indicate that these storms maintain their intensity longer than the average tropical cyclone with a mean intensity of greater than 100 kt.

Knaff et al. (2003) examined the characteristics of six annular hurricanes that occurred in the Atlantic and eastern North Pacific basins from 1995–1999. The following characteristics were found to separate annular hurricanes from the general population of hurricanes: (i) a nearly circular eye size with a larger than average radius; (ii) a symmetric annulus of deep convection with small asymmetries in cloud-top brightness

temperatures; and (iii) a general lack of deep convective features, such as spiral rainbands, beyond the annulus of deep convection surrounding the eye. Furthermore, Knaff et al. (2003) found environmental conditions to be favorable for annular hurricane development when: (i) there was relatively weak vertical wind shear that was easterly in the deep layer (850–200 hPa) and east-southeasterly in the shallow layer (850–500 hPa); (ii) easterly flow and colder than average temperatures at 200 hPa; (iii) nearly constant sea-surface temperatures (SST) in the range of 25.4–28.5°C; and (iv) the absence of interaction with an adjacent trough that would cause upper-level eddy momentum flux convergence.

Since Knaff et al. (2003) found that the formation of annular hurricanes occurred after an asymmetric mixing of the eye and eyewall components as a result of mesovortices, it can be assumed that the storm was quite intense prior to becoming an annular hurricane. Indeed, the discriminant analysis technique proposed by Knaff et al. (2003) for objectively identifying an annular hurricane in the Atlantic and eastern North Pacific performs best if all hurricanes with intensities $\leq$84 kt are first eliminated. For the six (eight) Atlantic (eastern North Pacific) annular hurricanes that they identified during 1995–2006, the minimum intensity was 100 kt (90 kt). While annular typhoons have also been observed, it is unknown if the same SST, minimum intensity, and other thresholds apply.

Given that annular tropical cyclones form a secondary eyewall during an intense stage, it can be assumed that a similarity exists with the secondary eyewall formations discussed in the previous subsection. For the 14 annular hurricanes during 1995–2006, the mean radius of the lowest azimuthally-averaged cloud-top temperatures (i.e., eyewall radius) was 81 km, with a minimum of 62 km, and a maximum of 128 km. With a minimum intensity of 90 kt at such large radii, the outer wind speeds would likely be larger than for an average tropical cyclone. The differences are assumed to be: (i) annular tropical cyclones form from an internal mechanism following an eyewall mixing event in which the intense inner wind maximum is diminished; and (ii) the secondary (outer) eyewall is stable to radial deflection in the mid- to lower-troposphere (as opposed to contraction) as a result of the special environmental conditions listed above.

Wang (2008b) simulated the formation of an annular tropical cyclone with a high-resolution fully compressible, nonhydrostatic numerical model. Because the storm transitioned from a non-annular to an annular structure after several secondary eyewall

formation cycles, the triggering mechanism is attributed to the internal dynamics of the storm. A comparison of the non-annular to annular phases of the simulation revealed several distinct differences in the annular structure: (i) the simulated 20 dBZ radar reflectivity contour has more uniformity and extends to a greater radius from the storm's center; (ii) the eyewall updrafts have a much greater radial extent and have a greater tilt outward with height; and (iii) the subsidence in the eye and outside the eyewall are greater due in part to the stronger updrafts in the eyewall convection. According to Wang (2008b), the dynamic response to the greater outward tilt of the eyewall is an increase (decrease) in low-level tangential winds outside (inside) of the radius of maximum winds, and thus prohibited contraction of the eyewall as occurs during a typical eyewall replacement cycle. The increased mass flux in the eyewall and corresponding strong overturning subsidence suppresses the development of major rainbands outside of the eyewall.

The significance for outer wind structure changes is similar to that for secondary eyewall formation, i.e., forming an intense outer wind maximum in an annular tropical cyclone is likely to increase the observed 34-kt wind radius.

5. Importance of Wind Structure

The five categories of the Saffir-Simpson scale (SS1-5; Simpson 1974; Saffir 1975) are currently used to communicate damage potential to vulnerable populations in coastal regions of the Western Hemisphere. The SS categories are tied to intensity via the maximum sustained surface winds (V_{max}). However, V_{max} is a poor measure of tropical cyclone destructive potential since intensity alone does include potential impacts of storm size (Powell and Reinhold 2007). While V_{max} is a measure of the destructive potential by the wind, the storm surge potential is more closely associated with the tropical cyclone outer-core structure. For example, Hurricane Katrina (2005) caused more property damage and loss of life as a SS3 storm with its larger structural size at landfall than Hurricane Camille (1969) produced as a SS5 at landfall.

Powell and Reinhold (2007) have proposed the use of integrated kinetic energy (IKE) as a measure of tropical cyclone destructive potential. Calculations of IKE are generated for an objectively analyzed, gridded wind field using the following equation:

$$IKE = \int_V \frac{1}{2}\rho U^2 dV, \tag{2}$$

where ρ is the density of the air, U is the tangential component of the wind field, and dV is a 1 km high circular annulus at some arbitrary distance from the tropical cyclone center. The growth in tropical cyclone outer-core structure that often accompanies secondary eyewall formation or as a result of the transition to an annular storm structure leads to a marked increase in tangential winds at greater distances from the storm center. Stronger tangential winds across a greater cylindrical volume increases IKE and thus the destructive potential of a tropical cyclone.

Sawada and Iwasaki (2010a, b) evaluated the impacts of evaporative cooling on tropical cyclone evolution and asymmetric structure. They found that evaporative cooling in the vicinity of the eyewall during the early stages of tropical cyclone development suppressed organization, and thus limited the structural size and IKE in the outer-core structure of the storm. On the other hand, the author found that evaporative cooling was an essential ingredient for structural growth during the mature stages of tropical cyclone development. In their numerical simulation, Sawada and Iwasaki (2010a, b) showed that evaporative cooling was responsible for forming cold pools in the outer-core region that became the triggering mechanism in the formation of outer spiral rainbands and inhibiting radial inflow of warm, moist air to the eyewall.

The lifting of high equivalent potential temperature air slantwise inward with rain falling over the cold pools led to convective downdrafts and associated evaporative cooling over the cold pools, which thus reinforced the cold air (Sawada and Iwasaki 2010b). While the convective cells were found to circle the eyewall at a relative fixed distance from the tropical cyclone center, new convective cells formed along the radial upwind edge of the cold pools, which gave the appearance of outward propagation of convective cells as the outer spiral rainbands expanded radially outward. Thus, Sawada and Iwasaki (2010a) suggest the increase in spiral rainband convection drives a stronger secondary circulation that transports absolute angular momentum inward and increases the tropical cyclone structural size and IKE in the outer-core structure of the storm.

The presence of strong outer spiral rainbands also leads to potential vorticity (PV) asymmetries on the eyewall of a tropical cyclone (Bister 2001; Wang 2002c, 2009; discussed in greater detail in section on Asymmetric Convection). When the PV asymmetries become large in the eyewall, a breakdown of the eyewall may occur that may trigger a secondary eyewall formation event. As discussed earlier, a second eyewall may form near the stagnation zone for the outward-propagating Vortex Rossby Waves

(VRWs) at some greater radial distance from the original eyewall. Thus, calculation of the modified Rankine vortex based on the new radius of maximum winds and assuming an insignificant change in storm intensity suggests an increase in the outer-core winds of the tropical cyclone. Therefore, a secondary eyewall formation would be expected to increase IKE and the destructive potential of a tropical cyclone as it approaches a coastal region.

B. RELATED RESEARCH AND BACKGROUND

The mechanisms leading to structure change in a tropical cyclone can be categorized as internal, external, or both. One example of an internal mechanism is the VRWs (see Chapter I.B.1 below) since their horizontal propagation is limited by the stagnation radius where the radial group velocity goes to zero (Wang 2002a). Through the use of a numerical simulation, Wang (2002b) found the existence of the stagnation radius at 70–90 km from the tropical cyclone center. Environmental flow, vertical wind shear, upper-tropospheric troughs, sea-surface temperature, ocean heat content, sea spray, and frictional drag (e.g., land) are all examples of external mechanisms that can affect tropical cyclone structure. Some external mechanisms directly impact tropical cyclone structure (e.g., vertical wind shear) while others affect the structure indirectly through intensity change (e.g., sea-surface temperature).

Changes to tropical cyclone structure by spiral rainbands and asymmetric convection can be categorized as both internal and external mechanisms. Although it has been suggested that outer spiral rainbands form as outward-propagating internal inertia-gravity waves that are intensified by radial shear in the inner core (Diercks and Anthes 1976; Kurihara 1976; Willoughby 1978), recent numerical studies (Wang 2002c; 2009) suggest that outer spiral bands are determined by the outflow radial wind speed and terminal velocity of ice species, such as snow and graupel. Regardless of the mechanisms that lead to spiral bands, the effects on tropical cyclone structure by inner and outer spiral rainbands can be quite distinct. Asymmetric convection can be found in the inner core of a tropical cyclone (e.g., eyewall and inner spiral rainbands) or in the outer-core region (e.g., outer spiral rainbands and disorganized convection). As with spiral rainbands, the location of convection can have a varied affect on tropical cyclone structure and intensity.

1. Vortex Rossby Waves

Vortex Rossby Waves may be considered to be a restoring mechanism to radial perturbations that occur in the elevated cyclonic PV concentrated in the inner-core region near the radius of maximum winds (R_{max}) of a tropical cyclone (Montgomery and Kallenbach 1997; Wang and Wu 2004). These VRWs are often forced by and coupled with asymmetric convection in the eyewall. These convective asymmetries can result from barotropic or three-dimensional instabilities of the tropical cyclone vortex (Schubert et al. 1999; Nolan and Montgomery 2000), beta effect (Wang and Holland 1996a, b), or environmental flow and vertical shear (Shapiro 1983; Wang and Holland 1996c; Bender 1997; Frank and Ritchie 1999). MacDonald (1968) originally proposed the concept of Rossby-type waves to explain the formation of spiral rainbands in tropical cyclones. It was later recognized that VRWs could exist in the inner-core region of the tropical cyclone and play a significant role in structure and intensity changes (Guinn and Schubert 1993; Montgomery and Kallenbach 1997; Montgomery and Lu 1997; Kuo et al. 1999; Reasor et al. 2000).

The eddy potential energy created by the asymmetric diabatic heating associated with moist convection in the eyewall is the main source for the eddy kinetic energy that drives VRWs (Wang 2002a). Eddies associated with inward-propagating VRWs transport angular momentum from the eyewall to the eye of the tropical cyclone (Kuo et al. 1999; Wang 2002a, b). This inward mixing of PV spins up the tangential winds in the eye at the expense of the eyewall leading to an asymmetric pathway for eyewall contraction and intensification of the tropical cyclone (Möller and Montgomery 1999; 2000). The deposition of kinetic energy from the VRWs to the mean tropical cyclone vortex represent an upscale energy cascade (Montgomery and Kallenbach 1997; Wang 2002a). To conserve angular momentum during this redistribution process, the inward mixing of PV has to be balanced by outward mixing of PV (Montgomery and Kallenbach 1997). The PV wave (or VRW) is able to propagate outward along the PV gradient to the stagnation zone, the zone where the PV gradient goes to zero. The result of outward PV mixing is the formation of inner spiral rainbands.

In a numerical modeling study, Wang (2002a) found that azimuthal wavenumber-1 and wavenumber-2 VRWs dominated the waves generated by asymmetries in the inner core of the tropical cyclone. Carr and Williams (1989) noted that wavenumber-2 perturbations were damped four times faster than wavenumber-1 perturbations, which suggests a damping rate equal to the square of the wavenumber. Thus, higher

wavenumbers tend to have their kinetic energy dampen quickly as they propagate away from the eyewall. Given conservation of PV, a VRW that propagates outward against the radial inflow will also move to the left of the PV gradient or upstream against the tangential winds (Montgomery and Kallenbach 1997; Kuo et al. 1999; Chen and Yau 2001). Wang (2002a) found that both wavenumber-1 and wavenumber-2 VRWs retrogressed against the tangential winds at a speed of about 36 m s^{-1}. As a result, the inner spiral rainbands associated with outward propagating VRWs are transported downwind at a slower rate than the tangential wind speed at a given radius from the tropical cyclone center (Willoughby 1978). Thus, the strong tangential wind gradient of a tropical cyclone vortex causes inner-core rainbands to spiral cyclonically inward toward the radius of maximum winds. The outward radial propagation of wavenumber-2 VRWs was found to be much faster (10–20 m s^{-1}) when compared to wavenumber-1 VRWs (4–5 m s^{-1}) (Wang 2002a).

2. Spiral Rainbands

Wang (2002b) showed that inner spiral rainbands could be initiated by outward propagating VRWs. However, spiral rainbands in the outer-core region may not be explained by the outward propagation of VRWs since the radial PV gradient becomes too weak beyond the inner-core region. The numerical simulations by Wang (2001, 2002b) suggest that outer spiral rainbands may form and develop in the region 80–150 km from the center of the storm. Willoughby et al. (1984) proposed that the outer spiral rainbands were a result of downdrafts from the anvil clouds in the tropical cyclone outflow layer. A second explanation proposed by Montgomery and Kallenbach (1997) is that outer spiral rainbands could form near the VRW stagnation radius where the group velocity of the waves vanishes.

An annular region of strain-dominated flow exists between the eyewall of a strong tropical cyclone and the stagnation zone for VRW propagation (Rozoff et al. 2006; Wang 2008a). Rozoff et al. (2006) hypothesized that this region of rapid filamentation in conjunction with subsidence from the eyewall creates an unfavorable environment to sustain deep convection, and thus supported the formation of a moat (a weak-echo region outside the primary eyewall). Rapid filamentation is defined as conditions that lead to atmospheric overturning time scales typically shorter than for moist convective (30 min). Based on a numerical simulation, Wang (2008a) suggested that rapid filamentation plays a crucial role in the formation and organization of inner spiral

rainbands. The inner core of a strong tropical cyclone is dominated by shear deformation. Thus, PV carried radially outward during the process of axisymmetrization is stretched into filaments that form the inner spiral rainbands (Chen and Yau 2001; Wang 2008a). Wang (2008a) argued that the rapid filamentation zone provided a favorable environment for deep, moist convection in the form of inner spiral rainbands and that subsidence from the eyewall and stratiform precipitation plays the primary role in the formation of a moat.

Sawada and Iwasaki (2010b) suggest that inertia gravity waves do not organize outer spiral rainbands, but may act as a trigger for deep, moist convection in the outer core of a tropical cyclone. In their high resolution numerical study, Sawada and Iwasaki (2010a, b) found that the evaporative cooling of precipitation associated with deep convection created cold pools on the inner side of the convective updraft. These cold pools provide a feedback mechanism to sustain deep convection in the spiral rainband as the convection propagates downstream along a rainband at a given radius. The interaction of these cold pools with the radial planetary boundary layer inflow lifts this high equivalent potential temperature air to form new convective cells on the upstream side of the cold pool, which allows the spiral rainbands to effectively grow outward. Wang (2002b) showed that strong perturbations from spiral rainbands in the outer-core region could amplify VRWs and cause a partial breakdown of the eyewall and subsequent weakening of the tropical cyclone. The eyewall could later recover from this breakdown through the process of axisymmetrization, which was discussed above as a mechanism for inner spiral rainband development.

3. Asymmetric Convection

The effects of asymmetric convection on a tropical cyclone can be considered a function of location within the storm: eyewall, inner core, or outer core. The presence of asymmetric eyewall convection tends to increase the asymmetry of PV (Guinn and Schubert 1993; Kuo et al. 1999; Wang 2002a, b) and becomes a generation mechanism for VRWs that may act as restoring mechanism during the axisymmetrization process (Carr and Williams 1989; Montgomery and Kallenbach 1997). Asymmetric convection in the eyewall also leads to the development of cyclonically rotating polygonal eyewalls (Kuo et al. 1999; Wang 2002b). Through a combination of one or more wavenumbers, VRWs have been observed to produce a variety eyewall shapes, such as ellipses, triangles, squares, pentagons, and hexagons (Lewis and Hawkins 1982).

Asymmetric convection in the inner core of a tropical cyclone is most often found in the form of inner spiral rainbands. The intersection of the wave forming the inner spiral rainbands with the eyewall provides a positive feedback mechanism that reinforces both features (Wang 2002b). The wave enhances low-level convergence and associated upward motion, thus reinforcing PV asymmetries in the eyewall. In turn, the PV asymmetries in the eyewall provide the energy source to maintain the wave. Wang (2008b) showed in a high-resolution numerical modeling study that the interaction between the eyewall and inner spiral rainbands can lead to two possible responses. The first type of response is the contraction of the eyewall followed by the formation of a secondary eyewall. The second type of response is expansion of the eyewall, which is often associated with the formation of an annular tropical cyclone.

Outer spiral rainbands are an organized form of asymmetric convection that often develops in the outer-core region of a tropical cyclone. Wang (2001, 2002a, b) showed with his tropical cyclone simulations that outer spiral rainbands most frequently form in the region 80–150 km from storm center or outside the VRW stagnation zone. Outer spiral rainbands are viewed as predominately owing their existence to the outward propagation of inertia-gravity waves (Diercks and Anthes 1976; Kurihara 1976; Willoughby 1978). In a more recent numerical study, Wang (2002c) showed that the absence of melting from ice species and evaporation of rain suppressed the development of spiral rainbands. In addition to outer spiral rainbands, disorganized asymmetric convection is occasionally observed in the outer-core region of a tropical cyclone when there is peripheral interaction with a land mass. Regardless of the source of outer-core convection, the result is most often to weaken and expand the tropical cyclone (Bister 2001; Wang 2002c, 2009), which is accomplished through "hydrostatic adjustment". According to Wang (2009), the net diabatic heating in the spiral rainbands causes a drop in surface pressure, and thus reduces the pressure gradient across the radius of maximum winds that leads to a decrease in tangential wind speed and a corresponding expansion of the eyewall radius.

4. Environmental Influences

In addition to the internal dynamics discussed above, external forcing on larger scales can also lead to tropical cyclone structure change (Wu and Cheng 1999). A uniform environmental background flow can induce asymmetries in surface heat and moisture fluxes, and friction, and thus cause asymmetries to occur in the inner-core

region of the tropical cyclone (Shapiro 1983; Kepert 2001; Kepert and Wang 2001). Peng et al. (1999) showed that tropical cyclones that move slowly will generally weaken in intensity as a result of ocean cooling caused by tropical cyclone-induced mixing of the upper ocean layer. On the other hand, the authors concluded that a tropical cyclone that moves rapidly may have intensification inhibited by the asymmetries that result in the tropical cyclone inner-core region. Peng et al. found the speeds of motion most favorable for tropical cyclone development and intensification are 3–6 m s^{-1}.

The relative humidity of the environment in which a tropical cyclone develops has been found to play a key role in storm intensification (Bister 2001), structure (Wang 2009), and size (Hill and Lackmann 2009; Lee et al. 2010). The intensification of a warm-core vortex can be delayed by insufficient mid-tropospheric relative humidity in the inner-core region of a tropical cyclone (Emanuel 1989; Bister 2001). According to Bister (2001), increased moisture in the outer-core region of a storm leads to the development of more convection and outer spiral rainbands that can slow the intensification of a tropical cyclone. An increase of convection and outer spiral rainbands may trigger structure change as a result of VRW generation (Wang 2009). Hill and Lackman (2009) found that large tropical cyclones are more likely to form and persist in an environment with high relative humidity. By contrast, the lack of a sufficiently moist environment favors the development of small, compact tropical cyclones.

5. Vertical Wind Shear

The vertical shear of the horizontal wind field has been found to have a negative impact on the intensity of the storm (Gray 1968; Merrill 1988). The common explanation for this effect is that the latent heat released in upper portions of the tropical cyclone is advected downshear of the low-level cyclonic circulation, which thus "ventilates" the heat away from the storm center (Gray 1968). In addition to ventilation, DeMaria (1996) found that a tilt in the upper- and low-level PV resulted in a mid-level temperature increase near the tropical cyclone vortex, which is hypothesized to reduce convective activity and inhibit storm development. Vertical shear-induced convective asymmetries in the tropical cyclone eyewall are believed to have negative effects on storm development (Elsberry et al. 1992).

As mentioned earlier, weak easterly or southeasterly vertical wind shear was found to be a factor in the formation of an annular tropical cyclone (Knaff et al. 2003). In a numerical simulation, Wang (2008b) attributed the formation of an annu-

lar structure to internal dynamics of the storm in which the interaction of inner spiral rainbands with the eyewall convection creates asymmetries. These asymmetries are axisymmetrized by the restoring mechanism of VRW that can lead to an expanded, quasi-symmetric annular convective structure under favorable environmental conditions. While it is not clear that the environmental vertical shear is a trigger for the formation of an annular tropical cyclone, Knaff et al. (2003) speculated that weak easterly or southeasterly shear suppresses convective asymmetries in the eyewall by offsetting the vertical shear due to the β effect. This process leads to a quasi-steady storm structure in which the resultant eyewall is stable to contraction or expansion for long periods of time.

6. Upper-tropospheric Trough Interaction

Upper-tropospheric trough interaction can have both positive and negative effects on tropical cyclone development and intensification. The influence of upper-level environmental forcing can be more easily felt in upper portions of the tropical cyclone outflow layer where the inertial stability is smaller (Wang and Wu 2004). Holland and Merrill (1984) found that cooperative interaction between an upper-level trough and a tropical cyclone could enhance the outflow jet of the tropical cyclone, and thus invigorate eyewall convection and increase the intensity. On the other hand, an upper-level trough with a strong PV anomaly can induce greater vertical shear over the tropical cyclone, and thus have a negative impact on structure and intensity (Hanley et al. 2001).

7. Other Effects on Wind Structure Change

While the internal and external forcing mechanisms addressed above are not an inclusive list of mechanisms that can affect tropical cyclone intensity and structure, they are the primary mechanisms to be considered in the current research. Sea-surface temperature, ocean heat content, sea spray, and land effects are additional mechanisms that can influence tropical cyclone intensity and structure. However, the effects of these mechanisms are much harder to measure or quantify in an observational study.

C. RESEARCH OBJECTIVE

The objective of this research is to better understand the internal and external mechanisms that lead to significant variability in tropical cyclone wind structure,

especially in the outer-core region. Secondary eyewall formation and enhanced asymmetric near-core convection are believed to be two internal mechanisms that may lead to large structure changes (note: for the purposes of this research, "structure" refers to the surface wind field and it derived components). It is hypothesized that the primary external mechanisms of interest in structure change are upper-tropospheric trough interaction and its associated vertical wind shear, and peripheral land interaction with the outer structure of the storm. While it may not be possible to fully isolate the impact each of these mechanisms has on structure change without the addition of idealized modeling studies, this research will be a first step using special observations to gain a better understanding of which mechanism contributed to cases with significant tropical cyclone structure variations.

A second goal of this research is to characterize the observed variability in the R_{max}, V_{max}, and R_{34} that will provide bounds to perturb tropical cyclone vortex initial conditions in an ensemble model. Few research projects have attempted to quantitatively assess the observed variability of these three instrumental parameters in order to synthetically represent a tropical cyclone in the initial conditions of a numerical weather prediction model. Understanding the variability of these three parameters is essential to building an ensemble capability that will improve tropical cyclone structure forecasting.

Better understanding of the internal and external mechanisms will aid operational forecasters in improving their prediction capabilities of rapidly changing storm structure in the outer-core regions of tropical cyclones. The research dataset and analysis tool used to evaluate tropical cyclone structure change will be discussed in Chapter II. In Chapter III, the dataset will be validated and characterized, and the implications for ensemble modeling will be addressed. Analysis of tropical cyclone structure changes and the likely mechanisms associated with the observed variability will be discussed in Chapter IV. Chapter V presents a summary of the results of observed tropical cyclone structure change and addresses areas in need of future emphasis.

THIS PAGE INTENTIONALLY LEFT BLANK

II. METHODOLOGY

A. DATA SET

The unique dataset used to study outer wind structure change was from the National Oceanic and Atmospheric Administration (NOAA)-Atlantic Oceanographic and Meteorological Laboratory (AOML) Hurricane Wind Analysis System (H*Wind; Powell and Houston 1996, Powell et al. 1996, 1998). The H*Wind grid is centered on the storm and has a horizontal grid spacing of approximately 6 km in a domain of 920 km by 920 km. The H*Wind analyses incorporate all available surface observations, such as ships, buoys, coastal platforms, surface aviation reports, and reconnaissance aircraft data adjusted to the surface (NOAA 2007). Observations that are fit to the analysis framework include data transmitted from NOAA P-3 research aircraft equipped with the Stepped Frequency Microwave Radiometer (SFMR) flown by the Hurricane Research Division (HRD), and the United States Air Force Reserve (AFRES) C-130 reconnaissance aircraft flight-level winds. Additional sources of data include remotely sensed winds from the polar-orbiting satellite platforms of Special Sensor Microwave/Imager (SSM/I) and European Remote Sensing (ERS), the microwave imagers of QuikScat and Tropical Rainfall Measuring Mission (TRMM), and Geostationary Operational Environmental Satellites (GOES) drift winds from the geostationary satellites. All data are processed to conform to the common height of 10 m and an averaging period of 1-minute maximum sustained wind speed.

Data available for H*Wind analyses varies with tropical cyclone location, storm intensity, time of day, threat to populated areas, and resource availability. Observation availability within 8 degrees latitude and longitude for Katrina (2005) are shown in Fig. 4. During the early stages of Katrina's development (Fig. 4a), the density of available observations was limited to one AFRES aircraft reconnaissance flight in which the storm center was not intercepted, and a few buoy and coastal platform (CMAN) observations in the outer-core region of the storm. At 0730 UTC 24 August 2005, Katrina was a weak tropical storm (37 kt observed maximum winds) with a small, asymmetric wind structure that presented a minimal threat to populated areas. When the tropical cyclone was in the formation stage (i.e., weak maximum winds) or when the tropical cyclone was moving away from populated areas (e.g., back over the North Atlantic), few H*Wind analyses could be generated for this research due to sparse observations.

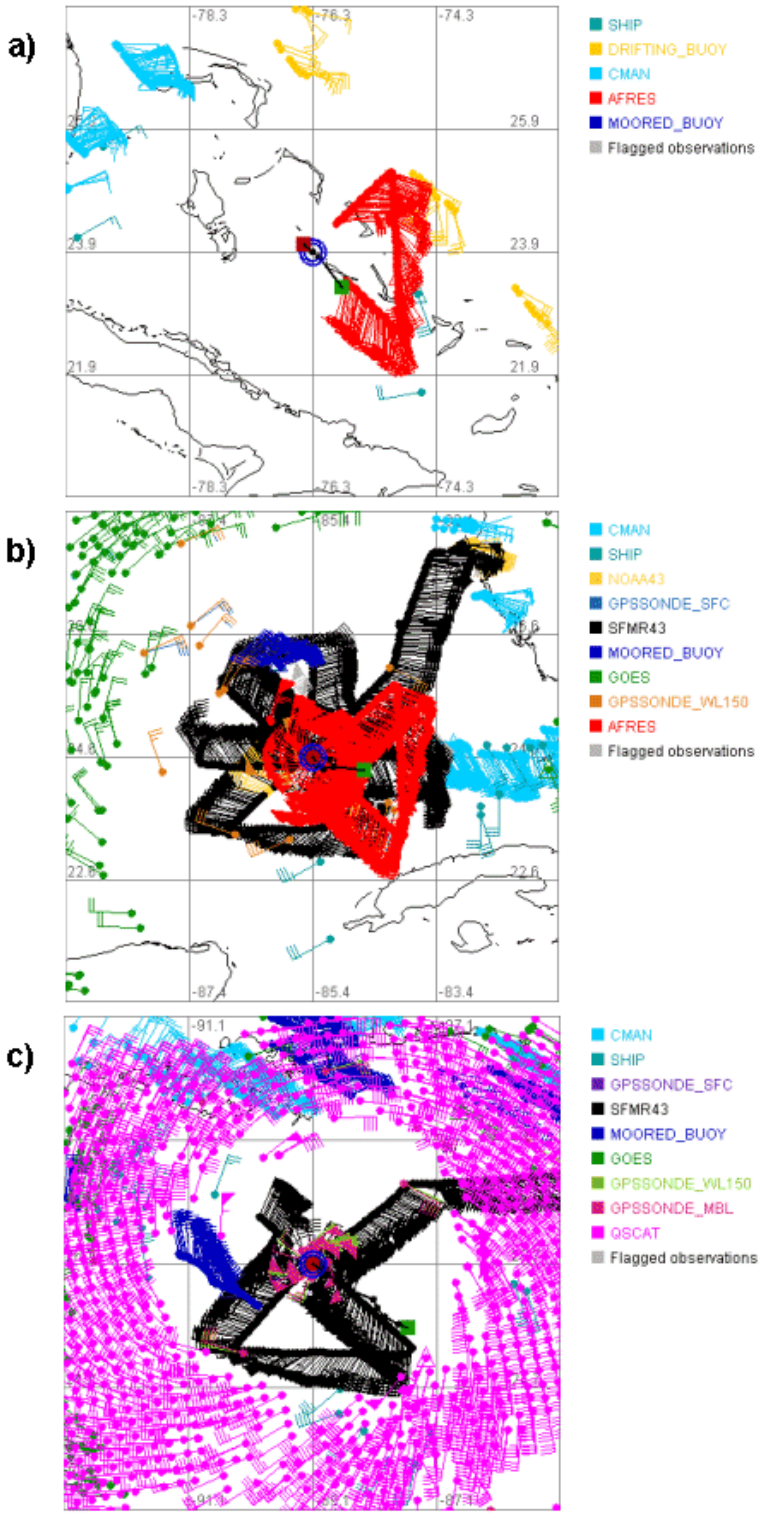

Figure 4 Observations available to H*Wind analyses on (a) 24 August at 0730 UTC, (b) 27 August at 2130 UTC, and (c) 28 August at 2030 UTC for Katrina (2005; from NOAA 2007).

As Katrina intensified into a strong Category 3 hurricane (maximum observed winds of 112 kt) over the Gulf of Mexico at 2130 UTC 27 August 2005 at (Fig. 4b), there was a plethora of SFMR observations from NOAA aircraft, AFRES aircraft, dropsondes, GOES drift winds, ships, buoys, and coastal platforms for assimilation using H*Wind. Near Katrina's peak intensity of 133 kt at 2030 UTC 28 August 2005 (Fig. 4c), once again there was dense observations to include QuickSat data to help define the outer-core wind structure of this intense Category 4 hurricane.

B. H*WIND ANALYSIS ROUTINE

The surface wind analyses are an objective assimilation of quality-controlled observations that are fitted to a Cartesian grid to allow for easier use in research, and for compatibility with wave modeling. The underlying numerical method is based upon the Spectral Application of Finite Element Representation (SAFER) system developed by Ooyama (1984, 1987) to enable the representation of multiple horizontal scales in numerical models. The use of spectral elements provides greater accuracy than finite-difference methods and allows for flexible lateral boundary conditions not afforded by other spectral methods (DeMaria et al. 1992). The SAFER system uses a two-dimensional, least-squares fitting algorithm in combination with a derivative constraint term that acts as a low-pass filter on the analysis field (Franklin et al. 1993). Thus, a unique filter wavelength can be chosen for each nested domain based on desired resolution and availability of observations with sufficient density to support the desired resolution. Analyzed fields are represented by a bilinear combination of local basis function (cubic B splines) centered on a two-dimensional array of nodal points (Franklin et al. 1993). Thus, the analyzed fields are defined continuously throughout the domain, not just at a finite number of grid points. Additional information on the formulation of numerical techniques for SAFER is in Ooyama (1987), Lord and Franklin (1987), and DeMaria et al. (1992).

1. History of SFMR

A key data source of the analysis routine is the SFMR. The concept for the first experimental SFMR was proposed by C. T. Swift at the University of Massachusetts Microwave Remote Sensing Laboratory and built by the National Aeronautics and Space Administration in 1978 (Uhlhorn and Black 2003). A single nadir-viewing antenna and receiver were employed to measure sea-surface emissions at four selectable

frequencies between 4.5 and 7.2 GHz. The stepping of frequencies allowed for the estimation of surface wind speed in tropical cyclones by correcting for the rain-induced effects in the measurement, which enabled the recovery of the rain rate. The new SFMR was first flown into Hurricane Allen in 1980.

In 1982, a second generation SFMR was designed and built under the supervision of C. T. Swift (Uhlhorn and Black 2003). The number of frequencies was increased to six with a range of 4.6 to 7.2 GHz and the instrument integration time was reduced to 1 s, which improved the spatial sampling rate. This instrument was first flown aboard a NOAA WP-3D aircraft in 1984 and on 12 flights during the 1985 hurricane season. After further modifications in 1986, the SFMR was used to study sea ice structure. Using the data retrieved from Hurricanes Earl (1985), Gilbert (1988), and Hugo (1989), a refinement was made to the empirical emissivity-wind speed relationships to include winds in excess of 60 m s^{-1}.

In 1993, the existing feed horn antenna was replaced by a dipole array antenna that allowed for the retrieval of higher quality wind estimates (Uhlhorn and Black 2003). Additionally, the SFMR receiver was upgraded to allow for improved calibration stability. The reconfigured SFMR was first flown into Hurricane Jerry (1995). Minor modifications were made to reduce instrument background noise following the 1995 hurricane season and the SFMR was flown in that same configuration through the completion of the 2003 hurricane season. A total of 95 flights into 30 hurricanes were conducted between 1980 and 2002.

Beginning in 2004, an upgraded SFMR was flown on one of the two NOAA WP-3D aircraft (Uhlhorn et al. 2007). The second aircraft was equipped with the newer SFMR prior to the start of the 2005 hurricane season. While the design was similar to the previous SFMR, the quality of retrievals was improved. Thus, the current research, which spans the 2003–2005 hurricane seasons, is expected to have only minor differences in data quality across the time period.

2. Data-processing Methodology

The SFMR measures radiative emissions from the ocean and atmosphere in the form of brightness temperatures (T_B) for each of six frequencies from 4.55 to 7.22 GHz (Uhlhorn and Black 2003). Barrick and Swift (1980) found a monotonic increase in the amount of sea foam on the surface of the ocean with increasing wind speed. Given

that sea foam can be treated as a blackbody at microwave frequencies and assuming a constant sea-surface temperature, an increase in sea foam results in greater microwave emissions and a T_B increase (Webster et al. 1976). Given an accurate physical model relating surface wind speed to T_B at several frequencies, one can theoretically invert a set of simultaneous equations to calculate the surface wind speed under nearly all weather conditions (Uhlhorn and Black 2003).

Since the SFMR is fairly insensitive to small changes in T_B at lower wind speeds because of minimal sea foam generation, surface winds $<$10 m s^{-1} are excluded since the inversion algorithm will often fail to converge to a unique solution (Uhlhorn and Black 2003). The algorithm is able to recognize measurements entirely over land (typically $T_B \geq 280$ K), but false wind speed retrievals may occur when land partially fills the sidelobes of the radiometer footprint. Thus, measurements within 10 km of land are not considered in these analyses. Observations of T_B are limited to near-nadir by removing those associated with aircraft roll or pitch greater than 2 degrees. Observations containing radio frequency interference from ground-based sources (e.g., communications and weather radar) are eliminated by passing the data through a median filter. A minimum of two SFMR channels is necessary to solve the system of equations, but a minimum of three channels is required to achieve error reduction.

3. SFMR Algorithm

The SFMR infers surface wind speed by using the blackbody radiance emitted by the ocean surface, as governed by Planck's law (Uhlhorn and Black 2003). Using the Rayleigh-Jeans approximation to Planck's law (applicable at microwave frequencies), a linear relationship between T_B and physical temperature, T, is implied. The portion of energy emitted by the atmosphere and the sea surface is expressed as emissivity (ε)

$$\varepsilon = \frac{T_B}{T}. \tag{3}$$

Utilizing Kirchoff's energy conservation law, the absorption and emission of a material in local thermodynamic equilibrium must be equal. Thus, radiation not emitted by the material (where scattering is neglected) must be transmitted,

$$\varepsilon = 1 - \tau, \tag{4}$$

where τ is the transmissivity.

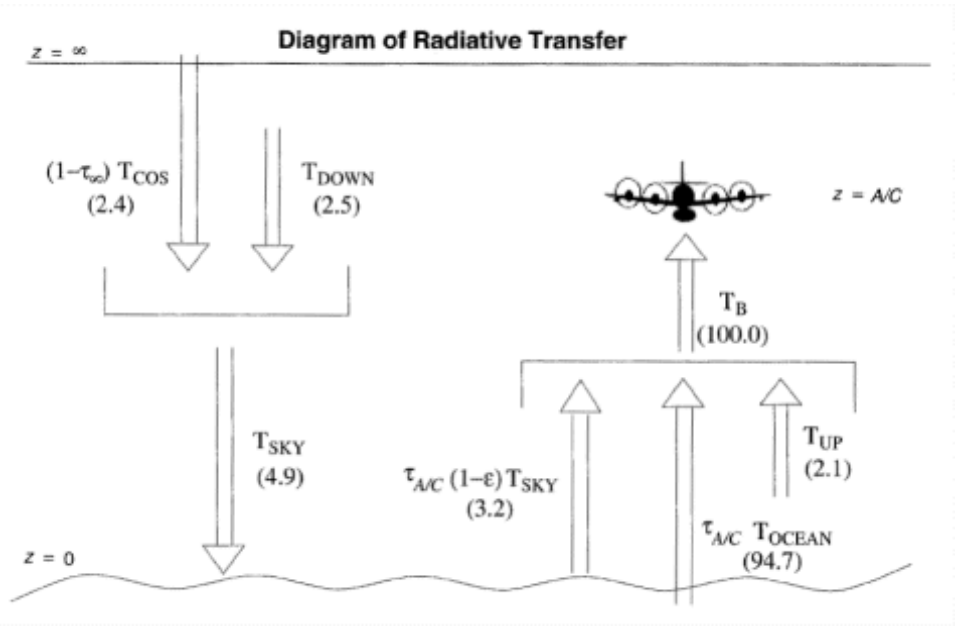

Figure 5 Radiative contributions to total T_B as measured from a nadir-looking radiometer. The values in parentheses are percentages of contributions to the total T_B. All values are computed using the assumed atmospheric profile found in the SFMR algorithm with zero wind and rain rate at a frequency of 5 GHz (Diagram from Appendix A of Uhlhorn and Black 2003).

As shown by Fig. 5, the apparent T_B observed by the nadir-looking SFMR is the sum of the following radiative sources: (i) cosmic radiation that has not been attenuated by the atmosphere and is reflected by the sea surface (T_{COS}); (ii) downward atmospheric emissions that are reflected by the sea surface (T_{DOWN}); (iii) emissions from the sea surface that are not attenuated by the intervening atmosphere (T_{OCEAN}); and (iv) upward emissions from the intervening atmosphere (T_{UP}). The absorption, emission, and transmission of the atmosphere is predominantly due to absorption by oxygen and water vapor molecules, and absorption and scattering by liquid water constituents.

The atmospheric contribution T_{DOWN} to the apparent T_B can be considered to be the sum of the contributions from gaseous and hydrometeor constituents

$$T_{DOWN} = (1 - \tau_{r,\infty}) \langle T_{r,\infty} \rangle + (1 - \tau_{a,\infty}) \langle T_{a,\infty} \rangle , \tag{5}$$

where T is measured in Kelvin; the subscripts a and r indicate transmission by the atmosphere and rain, respectively; ∞ represents the contribution by the entire at-

mospheric column; and angle brackets denote a mass-weighted layer average. The total sky T_B (T_{SKY}) thus becomes the sum of T_{DOWN} and the extraterrestrial source (T_{COS})

$$T_{SKY} = T_{DOWN} + (1 - \tau_{r,\infty}\tau_{a,\infty})\, T_{COS}. \tag{6}$$

The ocean T_B is directly related to SST and is given by $T_{OCEAN} = \varepsilon\,(SST)$, where ε is the variable to be solved in the SFMR algorithm. The ocean and reflected sky contributions that are not attenuated by the intervening atmosphere can be represented as $(1 - \epsilon)\, T_{SKY}$. The upward emission of radiation from the atmospheric below the aircraft flight level is represented by

$$T_{UP} = \left(1 - \tau_{r,A/C}\tau_{a,A/C}\right) \left\langle T_{a,A/C} \right\rangle, \tag{7}$$

where A/C denotes the emission from atmospheric layers below the aircraft. The total T_B observed by the nadir-looking SFMR aboard the aircraft is the sum of the upwelling components

$$T_B = \left(\tau_{r,A/C}\right) \left(\tau_{a,A/C}\right) \left[T_{OCEAN} + (1 - \varepsilon)\, T_{SKY}\right] + T_{UP}. \tag{8}$$

Under calm winds and the typical rain-free tropical atmosphere with a nominal flight level, T_{OCEAN} represents approximately 95 percent of the total apparent T_B from the ocean surface.

Since the ocean absorbs only a portion of the incident radiation, the remainder is reflected and is represented as $\varepsilon = 1 - \Gamma$. The reflectivity of a smooth (specular) ocean surface can be expressed in functional form as

$$\Gamma_p = \Gamma_p\,(\theta,\ f,\ SST,\ S), \tag{9}$$

where p is the polarized state (horizontal or vertical), θ is the incident angle, f is the electromagnetic frequency, and S represents the ocean salinity. Since SFMR measurements are taken at nadir, the incident angle is zero and reflection is independent of polarization. Assuming the SST and salinity are known, the reflectivity can be calculated at each SFMR frequency.

As energy is transferred to the ocean surface by the wind, the scattering and emission properties become much more complicated. The ocean surface becomes roughened by capillary and short gravity waves as the wind stress increases. When a critical steepness is reached, the waves break and produce foam patches and streaks on the ocean surface. Foam emits microwave energy more readily than a specular ocean surface, and thus a fractional foam model must be incorporated. The SFMR algorithm assumes that wind speed-dependent and specular components make up the total emissivity of the ocean surface.

Black and Swift (1984) established the relationship between emissivity and hurricane-force winds through dual aircraft missions in which one aircraft was flown 0.5- to 1.5-km altitude and a second aircraft was flown at approximately 3 km in altitude to take in situ wind speed measurements. These measurements were reduced to near-surface wind speed values using the Powell (1980) boundary layer model. The emissivity of the wind-driven sea is determined by removing the emissivity of a specular sea surface from the total apparent emissivity. The specular Fresnel power reflection coefficient (Γ) is calculated using an algorithm developed by Klein and Swift (1977). The specular Fresnel power reflection coefficient is added to the wind-driven excess to obtain the total emissivity.

The emissivity of the rain column is left to be determined. As in Appendix A of Uhlhorn and Black (2003), solving Eq. (8) for emissivity (ϵ) gives

$$\epsilon = \frac{a\tau_{r,\infty} - b}{a\tau_{r,\infty} - c\tau_{r,A/C}}, \tag{10}$$

where

$$a = \frac{\left(\langle T_{a,\infty}\rangle - T_{COS}\right)\tau_{a,\infty}}{\langle T_{a,\infty}\rangle},\ b = \frac{\langle T_{r,\infty}\rangle - T_B}{\langle T_{a,\infty}\rangle},\ c = \frac{\left\langle T_{r,A/C}\right\rangle - SST}{\langle T_{a,\infty}\rangle}.$$

Since $\left(\left\langle T_{r,A/C}\right\rangle - SST\right)$ and T_{COS} can be neglected compared to $\langle T_{a,\infty}\rangle$, $a = \tau_{a,\infty}$ and $c = 0$. Thus the approximate expression for emissivity from the ocean surface in the presence of rain becomes

$$\varepsilon \approx \left[\frac{T_B - \langle T_{r,\infty}\rangle}{\langle T_{a,\infty}\rangle}\right]\frac{1}{\tau_{a,\infty}\tau_{r,\infty}^2} + 1. \tag{11}$$

Given the small ratio of rain droplet size to SFMR electromagnetic wavelength, scattering can also be neglected at even the high rain rates present in tropical cyclones. Thus, rain rate can be estimated solely as a result of absorption processes. Transmissivity of a rain column is a function of hydrometeor content that is proportional to electromagnetic frequency and rain rate. The relationship between transmissivity and absorption, κ_r, is given by

$$\tau_r = \exp\left(-\kappa_r h\right), \tag{12}$$

where h is rain column depth. Rainfall absorption coefficient is derived using

$$\kappa_r = aR^b, \tag{13}$$

where R denotes rain rate in mm h^{-1}, and a and b have been empirically determined. Olsen et al. (1978) have shown a to be a function or frequency and rain rate with the following relationship:

$$a = gf^{n(R)}, \tag{14}$$

where $n \approx 2.6R^{0.0736}$ according to Atlas and Ulbrich (1977) and $g = 1.87x10^{-6}$ Np km^{-1} based on a calibration by Black and Swift (1984). The exponent $b = 1.35$ in Eq. (13) was determined by the C-band radar reflectivity measurements in hurricanes made by Jorgensen and Willis (1982). According to Uhlhorn and Black (2003), the SFMR is capable of measuring rain rates >5 mm h^{-1}. As shown in Fig. 12b of Uhlhorn and Black (2003), the spread of apparent T_B increases between microwave frequencies with increased rain rate, such as in the eyewall of a tropical cyclone.

The retrieval of surface wind speed and rain rate from a set of SFMR T_B measurements constitutes an inverse problem that requires the number of measurements to be greater than or equal to the number of parameters to be solved. Since the SFMR uses six frequencies, the solution is over-determined and a least squares inversion method is applied (Uhlhorn and Black 2003). Using a physical model designed by Pedersen (1990), an n-length vector of T_B measurements ($\mathbf{H}$) to an m-length vector of retrieved parameters ($\mathbf{y}$) is

$$\mathbf{H}_n = \mathbf{W}_{nm} \cdot \mathbf{y}_m, \tag{15}$$

where the matrix $\mathbf{W}$ consists of the partial derivatives of $\mathbf{H}$ with respect to $\mathbf{y}$

$$\mathbf{W}_{nm} = \frac{\partial \mathbf{H}_n}{\partial \mathbf{y}_m}. \tag{16}$$

A set of radiometer observations is given by

$$\hat{\mathbf{H}}_n = \mathbf{W}_{nm} \cdot \mathbf{y}_m + \boldsymbol{\epsilon}_n = \mathbf{H}_n + \boldsymbol{\epsilon}_n, \tag{17}$$

where $\boldsymbol{\epsilon}_n$ is an error vector and the top hat denotes an estimate of the true vector. The solution vector for the parameter estimates is given by

$$\hat{\mathbf{y}} = \left(\mathbf{W}^T\mathbf{W}\right)^{-1}\mathbf{W}^T\hat{\mathbf{H}}, \tag{18}$$

and is obtained from the condition that the sum of squared differences between the observed and model-predicted T_B is minimized as follows:

$$\sum_{i=1}^{n}\left[\hat{\mathbf{H}}_i - \sum_{j-1}^{m}\mathbf{W}_{ij}\hat{\mathbf{y}}_j\right]^2 = \text{minimum}. \tag{19}$$

Solutions are possible when the derivative matrix elements $\mathbf{W}_{ij}$ are significantly different so that errors $\boldsymbol{\epsilon}_i$ are not spuriously amplified by the elements of $\left(\mathbf{W}^T\mathbf{W}\right)^{-1}$. When wind speeds are <10 m s^{-1} or rain rate <5 mm h^{-1}, the sensitivity of changes in T_B observed by SFMR frequencies at nadir incident angle is typically too weak for the SFMR algorithm to converge to a solution.

4. Verification of SFMR Winds

Uhlhorn and Black (2003) verified the SFMR retrieval algorithm using GPS dropwindsondes. Since the sondes often fail to measure winds all the way down to the sea surface, the 10-m wind was approximated by using the lowest 500-m mean (or mean boundary layer) wind speed and a least-squares best fit $G_{10} = 0.798(G_{MBL})$, where G_{10} and G_{MBL} are the 10-m and lowest 500-m mean winds, respectively. However, it should be noted that using the mean boundary layer GPS dropwindsonde winds underestimates the 10-m wind speed when <15-20 m s^{-1} and >60 m s^{-1} (Dunion et al. 2003; Uhlhorn and Black 2003). Uhlhorn and Black (2003) collected a total of 249 paired samples of SFMR and surface-adjusted GPS mean boundary layer winds from

the 1998, 1999, and 2001 seasons. Paired observations were required to be within 15 km of each other and within 10 km radially with respect to the storm center. The least-squares best fit to the data (Fig. 6) is $S_{10} = 2.68 + 0.98(G_{10})$, where S_{10} is the surface wind speed (m s^{-1}) measured by the SFMR. The least-squares best fit to the paired surface wind speed estimates has a root-mean square error of 3.31 m s^{-1} and a high bias of 1.4 m s^{-1}. Uhlhorn and Black (2003) postulate that the high bias in the SFMR-GPS dropwindsonde comparison may be due to the differences in the time scales implicit to the measurements.

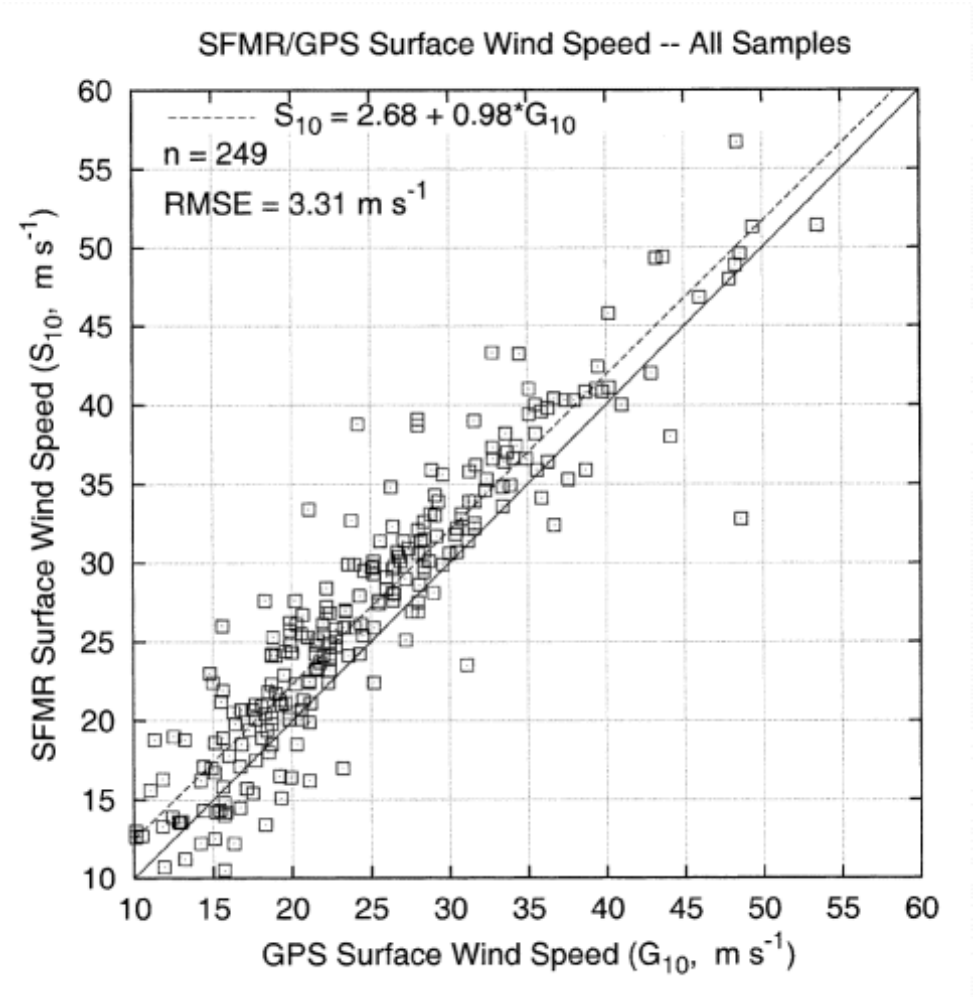

Figure 6 SFMR-GPS dropwindsonde comparison of surface wind speeds. The solid line represents the perfect correlation of the paired samples. The dashed line represents the actual best fit to the data (From Uhlhorn and Black 2003).

Uhlhorn and Black (2003) found the over-estimate of surface wind speed decreases with increased distance from the tropical cyclone center. However, little error dependence was found based on wind speed. When Uhlhorn and Black (2003) compared SFMR measurements to GPS dropwindsonde data in storm-relative coordinates, the greatest over-estimation of wind speeds occurred in the right-front and left-rear quadrants. By contrast, there was a slight under-estimation of wind speeds in the right-rear quadrant. Uhlhorn and Black (2003) hypothesized that the under-estimation of surface wind speed in the right-rear quadrant may be related to limited fetch length that would result in decreased foam coverage and lead to an under-estimate of the local surface wind speed.

Uhlhorn et al. (2007) found that the geophysical model function (GMF) used to relate surface emissivity to wind speed had a low bias at wind speeds in excess of 50 m s^{-1}. This under-estimate likely resulted from the lack of in situ data in excess of 55 m s^{-1} in deriving the GMF. During the 2005 season, a large dataset of SFMR and GPS dropwindsonde observations were obtained from a number of particularly strong tropical cyclones, such as Hurricanes Katrina and Rita. Using these new observations, significant improvements where made to the SFMR emissivity-wind speed GMF, especially at extreme winds speeds. The root-mean square error of the new GMF is similar to the previous GMF. However, the overall bias of -0.5 m s^{-1} for the new GMF is an improvement. The new GMF was only implemented in 2006, thus was not included in the dataset for this research.

5. H*Wind Algorithm Limitations

The introduction of global positioning system (GPS) dropwindsondes in 1997 greatly improved the ability to retrieve in situ atmospheric winds and thermodynamic profiles, especially within the tropical cyclone inner core (Uhlhorn and Black 2003; Uhlhorn et al. 2007). However, obtaining accurate measurements of the 10-m wind speed is complicated by the horizontal displacement of the dropwindsonde as it falls and by the tilt of the tropical cyclone eyewall. A dropwindsonde measures atmospheric variables in a Lagrangian framework as it falls, and has increased horizontal displacements with increasing wind speeds near and within the eyewall. Thus, a dropwindsonde is unable to provide measurements at a vertically fixed spatial location because it may be horizontally advected 10 km or more (Uhlhorn et al. 2007). Because of variable tropical cyclone eyewall tilt, a sonde dropped in the elevated eyewall at flight

level may be outside the eyewall when it reaches the surface. Therefore, dropwindsondes are often released just inside the radius of maximum winds at flight level in order to measure the near-surface maximum wind speed (Franklin et al. 2003).

The H*Wind analyses are not without limitations. It is possible that V_{max} in a given tropical cyclone might not be sampled during the typical reconnaissance pattern along four radial flight legs during the 4–6 h period required for an analysis (Powell and Reinhold 2007). Uncertainty of the analyzed V_{max} depends on data coverage and the quality of the data from the individual platforms contributing to the final analysis. Powell and Reinhold (2007) estimate that uncertainty is 10 percent when the peak wind is measured within the eyewall by the SFMR-equipped aircraft, or if measured outside the eyewall where in situ observations are more plentiful. They also estimate that uncertainty is approximately 20 percent when the peak wind within the eyewall is measured using a simple reduction of flight-level wind data to the surface. Thus, H*Wind analyses are generally not available east of 50°W longitude in the Atlantic basin due to the fuel load limits imposed by available basing locations and flight duration of airborne assets.

6. Sensitivity Analysis

Uhlhorn and Black (2003) conducted a sensitivity analysis on atmospheric and ocean quantities that contribute to the apparent ocean T_B, such as sea-surface temperature (SST) and salinity, and atmospheric temperature, pressure and moisture. The sensitivity analysis was conducted using a radiative transfer model in which all variables were held constant while each variable was individually perturbed. The resulting differences in estimated surface wind speeds for each perturbation gave the range of variability inherent to each variable. Uhlhorn and Black (2003) found that a lower (higher) SST leads to a lower (higher) apparent T_B, and thus leads to weaker (stronger) surface wind speed estimates. At wind speeds >20 m s^{-1}, the wind speed error is $\pm$ 2 m s^{-1} for SST errors of $\pm$ 3 K. In the case of ocean salinity, Uhlhorn and Black (2003) found that T_B increased (decreased) with decreased (increased) salinity, which results in an over-estimate (under-estimate) of surface wind speed. Since the ocean is generally well mixed in a tropical cyclone environment, wind speed errors associated with salinity are typically <0.5 m s^{-1}. Uhlhorn and Black (2003) concluded that the errors due to SST and salinity were tolerable compared to the magnitudes of the errors found in the SFMR–GPS dropwindsonde comparison.

Knowledge of the intervening atmospheric column between the ocean surface and the airborne sensor is a difficult challenge to remote sensing since it can account for approximately 5 percent of the apparent T_B in a rain-free column (Uhlhorn and Black 2003). Since the columnar structure of the atmosphere cannot currently be sampled adequately in real-time, a climatological temperature profile is specified in the radiative transfer model. Uhlhorn and Black (2003) documented an increased spread in atmospheric transmissivity at the higher frequencies of the SFMR due to the known water vapor absorption band at 22 GHz. Thus, a drier intervening atmosphere is more transparent at the frequencies used by the SFMR. In the eyewall of a tropical cyclone, the increased water vapor content decreases atmospheric transparency (more absorptive), which leads to a higher calculated T_B from the radiative transfer model and an over-estimation of the surface wind speed. Uhlhorn and Black (2003) reported the largest errors associated with atmospheric temperature, pressure, and moisture to be less than $\pm$ 1.5 m s^{-1}, which is relatively small compared to the error magnitudes found in the SFMR–GPS dropwindsonde comparison.

C. ANALYSIS TOOL

An original software program, hereafter referred to as the Tropical Cyclone Structure Analysis Tool or TC-SAT, was written to analyze tropical cyclone structure using a Windows general user interface (GUI) and more than 13,000 lines of Visual Basic code. The software was designed to utilize the raw H*Wind analyses to produce the types of analyses required for this research and future work on tropical cyclone structure. The software GUI was designed to allow the user maximum flexibility in extracting available H*Wind analyses and producing analyses of choice. The user interface is shown in Fig. 7.

This analysis software package allows the user to select up to five significant wind thresholds ranging from 25–200 kt. The standard critical wind thresholds of 34, 50, and 64 kt were chosen in the current research. The software GUI also allows the user to extract the H*Wind analyses in time, by available data type (SFMR, aircraft, and dropsonde), and by Cartesian quadrant. The user provides the list of available analysis times, which is also used to identify regions where the tropical cyclone interacts with land within the 34-kt wind radius. The software currently limits the number of H*Wind analyses that can be run simultaneously to 5,000 input files. At the current

rate of H*Wind analyses produced during each storm season, it is estimated that 25–30 years of data could be run with one input file.

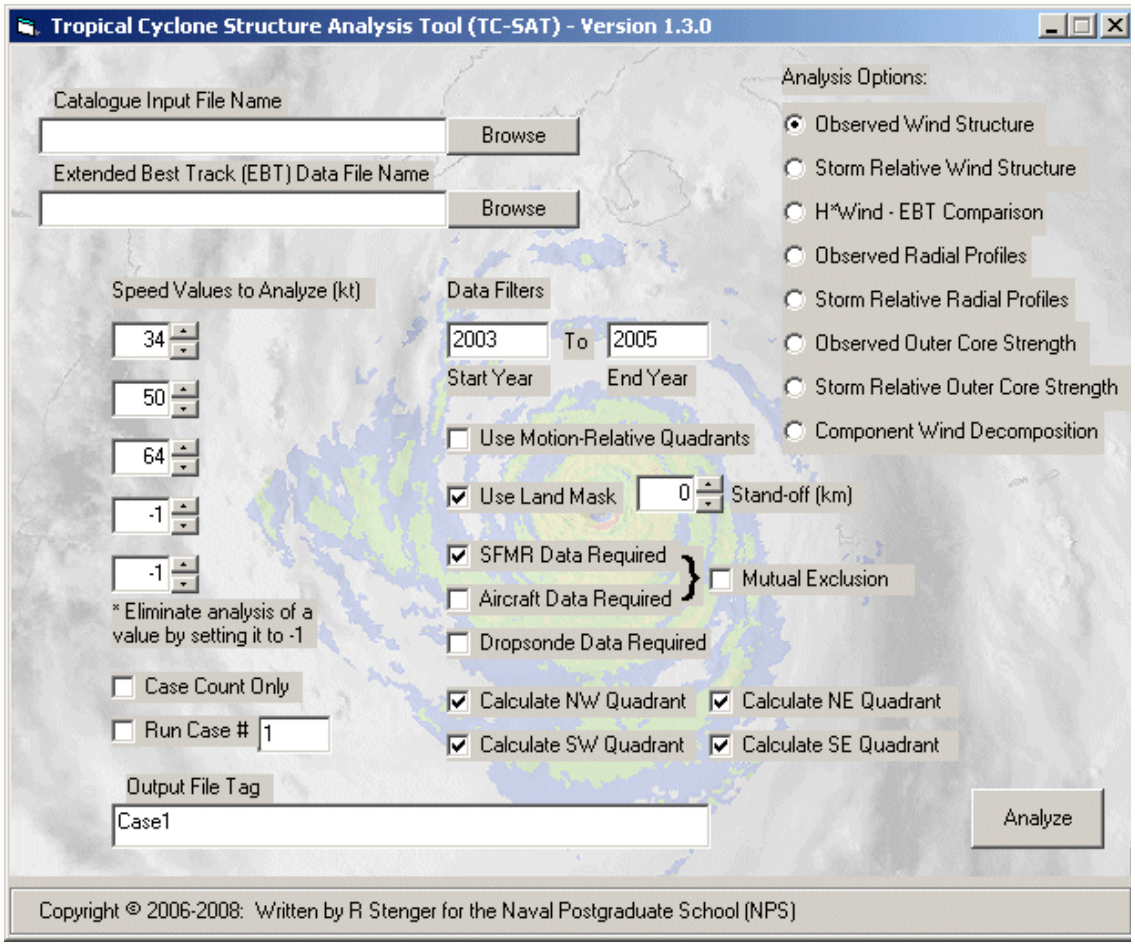

Figure 7 Interface of the tool designed to support research on tropical cyclone structure change using H*Wind analyses.

The analysis options currently available in the software include the evaluation of inner- and outer-core radii in either a geographical or storm-relative framework, geographical or storm-relative profiles of tangential and radial winds, geographical and storm-relative outer-core strength calculations, wind field decomposition on a Cartesian grid, and the comparison of H*Wind and extended best track (EBT) data (Demuth et al. 2006) at critical wind radii. Any storm-relative output requires the availability of storm motion information from the EBT file, which presently eliminates evaluations of eastern North Pacific tropical cyclones. All of the above analysis outputs may be evaluated for the four Cartesian quadrants (NW, NE, SE, and SW) independently.

The analysis software can also locate critical wind radii and generate wind profiles in the motion-relative framework. In this framework, the standard Cartesian quadrants are replaced by the motion-relative quadrants: left front (LF), right front (RF), right rear (RR), and left rear (LR). This type of analysis is particularly useful in comparing data from various storms or one storm during its life cycle, since the tropical cyclone data have one common framework in which the storm motion has been removed. If desired, the axisymmetric vortex can be removed from the observed wind field to yield an estimate of the background surface wind field. This background wind field may then be used to evaluate environmental spin (or vorticity) in three influence regions (e.g., one in which the storm core is removed).

Other fields of interest that are generated by the TC-SAT software (not specifically listed above) include divergence, relative and absolute vorticity, relative and absolute vorticity radial gradients, rate of intensity change, rate of structure change over various time intervals (3–24 h), and stage of storm development. The specific details of how each of the fields above are calculated or analyzed will be specifically addressed in the section in which the results are presented.

III. VALIDATION AND CHARACTERIZATION

A. VALIDATION

Previous descriptions of structure have mainly been along radial legs. Here the primary observation input has been along radial legs but a two-dimensional analysis has been produced. Thus, some comparisons with previous structure studies is necessary to validate the H*Wind analyses. Moyer et al. (2007) analyzed 691 H*Wind analyses generated for 69 Atlantic basin tropical cyclones during the 2000–2005 hurricane seasons. Through the use of multiple statistical analyses of the outer wind radii, they demonstrated that the H*Wind dataset presents a physically realistic representation of the outer wind radii. However, a comparison of the H*Wind dataset with the National Hurricane Center (NHC) Best Track re-analyses during the 2004 and 2005 hurricane seasons showed some inconsistencies. In their comparison, statistically significant differences were noted, with the H*Wind R_{34} wind radii being consistently larger than the NHC Best Track wind radii for all Saffir-Simpson categories of hurricanes (i.e., Category 1 through Category 5).

In the current study, an objective analysis was performed using a subgrid analysis technique (see Appendix B for details) on each of the 6 km^2 H*Wind gridded analyses provided by HRD (NOAA 2007) during the 2003–2005 Atlantic hurricane seasons to determine the average R_{34} wind radii (Fig. 8) in each Cartesian quadrant (i.e., NW, NE, SE, and SW). All data (by quadrant) were screened and eliminated if the R_{34} wind radii intersected any landmass (except very small islands). The extended best track (EBT, Demuth et al. 2006) dataset was used to compare with the R_{34} wind radii from the gridded H*Wind analyses. A time-weighted linear interpolation (see Appendix C for details) of the EBT dataset was calculated to match the H*Wind analysis times.

As in Moyer et al. (2007, their Fig. 7), significant R_{34} variability exists in all of the quadrants (Fig. 8a). Considering all Saffir-Simpson categories, no significant R_{34} biases are noted between the datasets with the exception of a small positive H*Wind radii bias in the SW quadrant (i.e., the H*Wind R_{34} wind radii are larger than the EBT wind radii). The R_{50} (Fig. 8b) and R_{64} wind radii (Fig. 8c) both have a negative H*Wind radii bias in the NW, NE, and SE quadrants (i.e., the H*Wind R_{50} and R_{64} wind radii are smaller than the EBT wind radii).

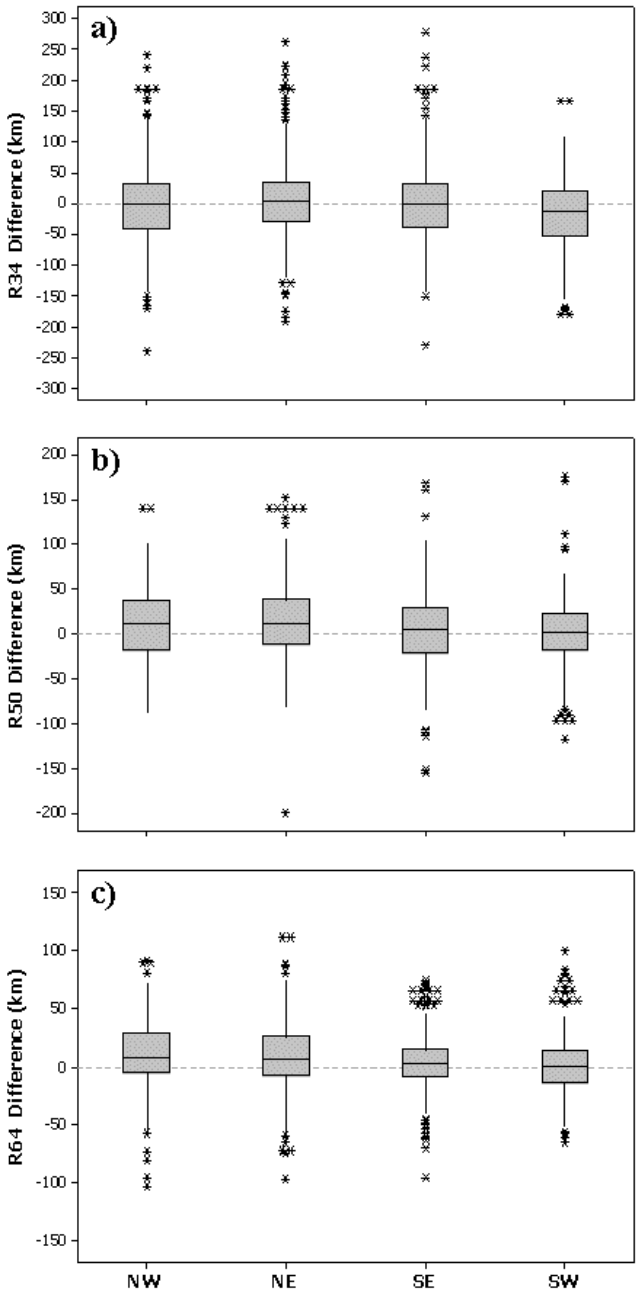

Figure 8 Comparison of the EBT wind radii to H*Wind analyzed wind radii for the Atlantic tropical cyclone radii at (a) R_{34}, (b) R_{50}, and (c) R_{64} for each Cartesian quadrant: northwest (NW), northeast (NE), southeast (SE), and southwest (SW).

Individual case studies (not shown) indicate varying results – one storm may compare well while another storm has large deviations. Time sequential plots of individual cases seem to indicate subjectivity in the definition of the wind radii in the EBT dataset by various forecasters.

B. CHARACTERIZATION

1. Definition of Life Cycle

Elsberry and Stenger (2008) tested these simple conceptual ideas of outer wind structure changes (discussed in Chapter I) through application of the tropical cyclone life cycle intensity change definitions of Elsberry et al. (2007) displayed in Fig. 9. The Elsberry et al. (2007) formation Stage I is limited to V_{max} less than 34 kt.

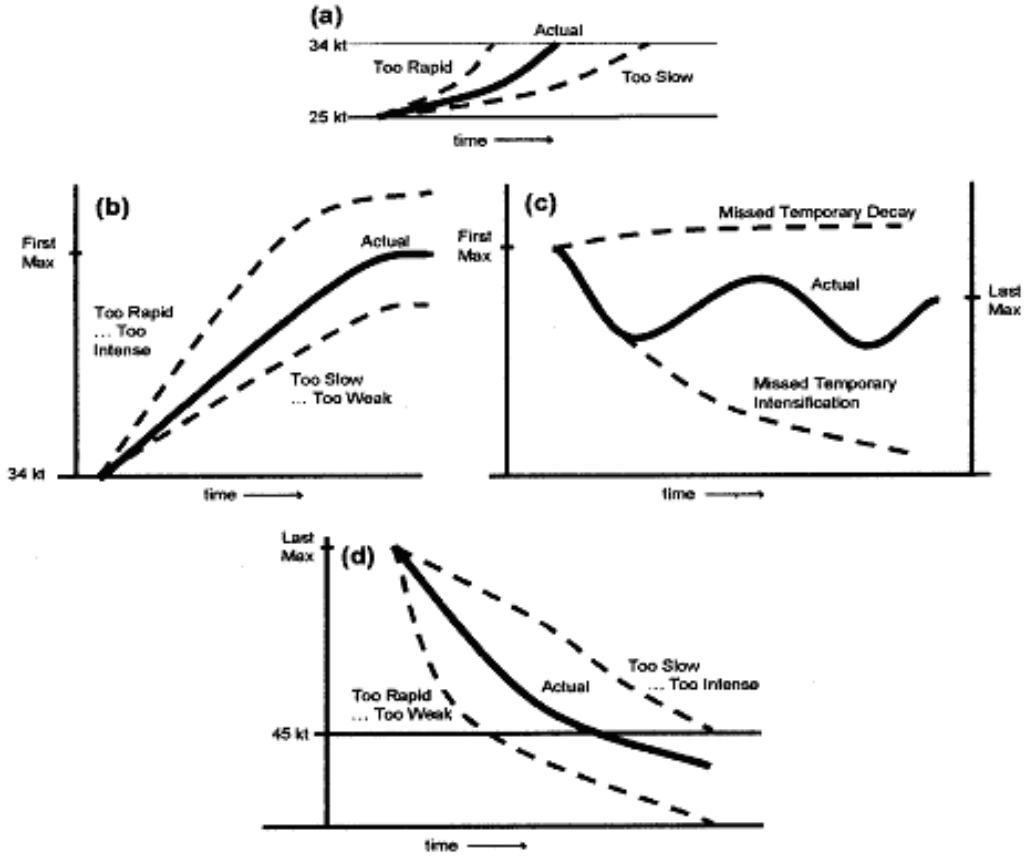

Figure 9 Intensity change phases during the life cycle of a tropical cyclone: (a) phase I, formation; (b) phase II, intensification; (c) phase IIa, decay and re-intensification cycle; and (d) phase III, decay. See text for specific definitions (Definitions from Elsberry et al. 2007).

Storm intensification from 34 kt to the first intensity peak (or end of this stage) is defined as Stage II. After the first intensity peak, if the storm intensity decays by at least 10 kt and then re-intensifies by at least 10 kt, it is defined as a decay and re-intensification cycle that is labeled as Stage IIa. If the re-intensification criterion of Stage IIa is not met, the storm is decaying and classified as Stage III. In addition, Stage II is subdivided into rapid or non-rapid intensification, and Stage IIa is subdivided into a decay followed by either a rapid or a non-rapid intensification. Rapid intensification is defined here as an increase equal to or greater than 15 kt in 12 h. A 12-h interval was selected to better capture rapid intensification events during storm intensity cycles and exclude intensity fluctuations that occur over shorter periods of time.

2. Variability in Time

In the current research, the TC-SAT software has been used to analyze 35 tropical cyclones that occurred in the Atlantic and three tropical cyclones that occurred in the eastern North Pacific basins from 2003 through 2005 (see Appendix A for a list of storms). During this period, 571 H*Wind analyses were produced. However, the raw fields for six analysis times were unavailable, and one field was eliminated due to suspect wind values. The remaining 564 H*Wind analyses contain dropsonde data in 508 analyses, aircraft flight-level reduced data in 470 analyses (hereafter referred to as "aircraft FLR data"), and 135 analyses with SFMR data. Dropsonde data were generally absent from eastern North Pacific tropical cyclones and for weak storms. Dropsonde, aircraft FLR, and SFMR data were simultaneously available in 55 of the H*Wind analyses. However, most analyses contain a combination of dropsondes and aircraft FLR data, or dropsondes and SFMR data.

Those H*Wind analyses that include the SFMR observations are considered to have the most reliable representation of the surface wind fields because of the continuous profiles along the radial flight paths of the aircraft. Due to the limited number of analyses with SFMR data, it was necessary to include surface wind analyses that were primarily based on the reduction of aircraft flight-level winds (usually flown at 700 mb). A comparison of the time evolution of R_{34} and R_{50} for Hurricane Ivan (2004) using mutually exclusive analyses that contain SFMR data versus aircraft FLR data is given in Fig. 10 for different quadrants of the storm. The differences between these wind radii derived from H*Wind analyses based primarily on these two data sources

are within the range of variability depicted by the aircraft FLR data. Other storm cases have a similar agreement as in Fig. 10.

Figure 10 Time series of structure change for Hurricane Ivan (2004) comparing values for H*Wind analyses that include only aircraft FLR or SFMR estimates in each Cartesian quadrant.

3. Observed Structure Change

Histograms of 12-h axisymmetric outer wind structure changes in terms of R_{34} values are shown in Figs. 11–13. These calculations of axisymmetric wind structure are computed along 24 equally-spaced radial legs at consecutive rings spaced every 6 km from the center of the tropical cyclone. It is important to note that all quadrants in which land intersects the 34-kt wind radii are eliminated from the calculations, but no fewer than two quadrants or 13 radial legs are used in the calculation at any analysis time. After eliminating all cases that involve landfall, or where insufficient analyses are available to compute the 12-h structure change, 400 cases remained to evaluate R_{34} structure variability during the 2003–2005 Atlantic tropical cyclone seasons.

Without consideration of the life cycle stage, the histogram for the all-sample of 12-h changes in R_{34} approximates a Gaussian distribution (Fig. 11a, dashed line).

A bias toward positive 12-h R_{34} changes is evident in this sample that includes all stages. Outer wind structure changes in terms of 12-h R_{34} values between ±10 km were deemed as steady state, and the clustering of values in this range appears to be justified by the distribution, if not a little conservative. Note that the changes in the axisymmetric radial structure in the entire sample can be quite large over a 12-h period, with values as large as ±135 km. For a hurricane approaching a coastline at 5 m s^{-1}, an undetected 12-h expansion of the gale-force wind radius by 135 km would decrease the preparation time by about 8 hours.

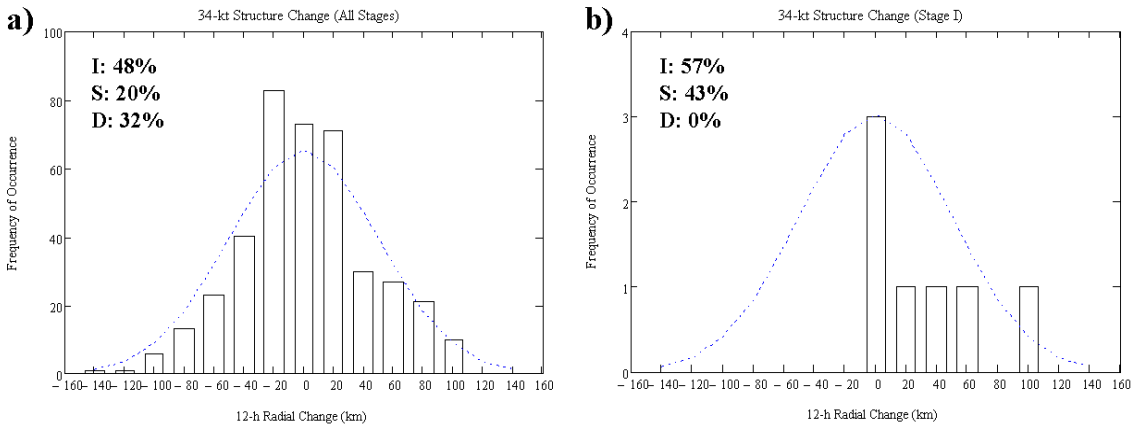

Figure 11 Histograms of 12-h axisymmetric outer wind structure changes in terms of R_{34} values for (a) all H*Wind analyses and (b) Stage I of the life cycle as in Fig. 9. The percentage of storms exhibiting an increase (I), steady (S), or decrease (D) in structure size are listed in the upper left corner of each histogram. The short dashed line is a normal Gaussian distribution.

Only a very small sample of H*Wind analyses are available for the Formation Stage I as defined in Fig. 9. Thus, the histogram of 12-h R_{34} changes for Stage I in Fig. 11b should be viewed as tentative. This limited sample of R_{34} change values does seem to indicate a general tendency toward an expansion in size during the formation stage. It is noteworthy that one expansion of 120 km in 12 h was documented. Given the limitations of this sample, it seems unlikely that a larger sample will make the distribution more Gaussian. The tendency for positive increases in R_{34} in the formation stage is consistent with the expectation of the empirical profiles as in Fig. 1 and the axisymmetric models discussed in Chapter I.

The histograms for 12-h R_{34} changes during rapid (Fig. 12a) and non-rapid (Fig. 12b) intensification during Stage II suggest "a tendency for more" increases (54 per-

cent and 56 percent, respectively) than decreases (32 percent and 28 percent) in outer wind speeds. The non-rapid intensification following a decay in Stage IIa has similar percentages (Fig. 12d) of positive (54 percent) and negative (26 percent) 12-h R_{34} changes. For the rapid intensifications following a decay in Stage IIa (Fig. 12c), the percentages of positive (44 percent) and negative (33 percent) 12-h R_{34} changes are more nearly balanced, and with a large percentage of steady-state ($\pm$10 km) conditions (23 percent). The relatively large number of decreases in the R_{34} values for the intensification Stages II and IIa does not agree with the expectations from the empirical wind distribution in Fig. 1 or the axisymmetric models that would suggest an increase in outer winds (R_{34}) during intensification. Thus, further study is required to understand the physical processes that lead to a decrease in R_{34} during intensification.

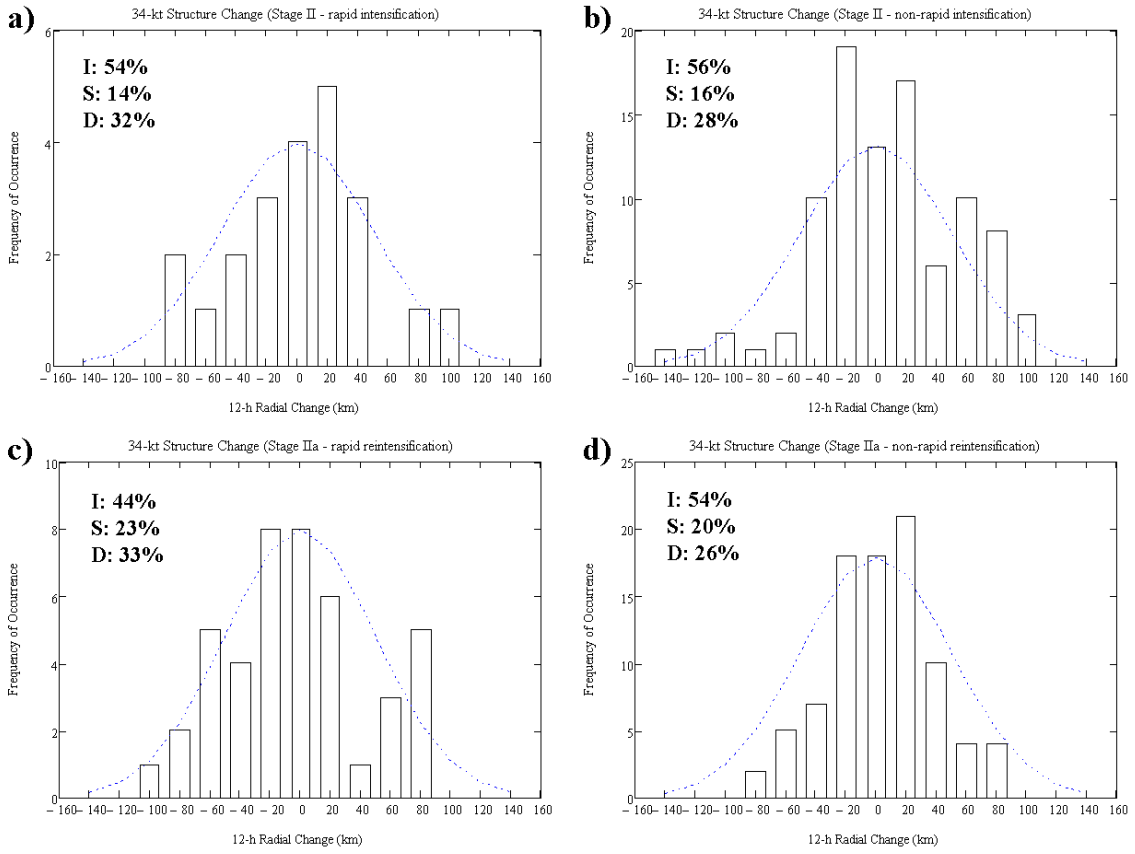

Figure 12 Histograms of 12-h axisymmetric outer wind structure changes in terms of R_{34} values as in Fig. 11, except for (a) Stage II rapid intensification, (b) Stage II non-rapid intensification, (c) Stage IIa rapid intensification, and (d) Stage IIa non-rapid intensification.

The histogram for 12-h R_{34} changes during the Decay Stage III (Fig. 13b) indicates a tendency for more negative (49 percent) than positive (26 percent) values, with a considerable fraction of steady-state conditions ($\pm$10 km). Approach to land may account for some shift toward negative R_{34} changes in the distribution during the Decay Stage III, whereas storms such as Hurricane Ophelia during 2005 shrunk in size while at higher latitudes with little or no intensity change, no significant land interaction, and under weak vertical wind shear conditions. By contrast, the 12-h R_{34} changes during the decay stage of the Stage IIa decay and re-intensification cycle (Fig. 13a) has proportionally more increases (51 percent) than decreases (37 percent), and has a distribution that approaches Gaussian centered on +20 km increase in R_{34} over 12 h. Recall that a decrease in R_{34} values during the decay stage might be expected from the empirical wind profile in Fig. 1, and from subsequent solutions of the axisymmetric model to fit a decreasing intensity. By contrast, the forecaster rule-of-thumb is to expect an increase in the size during the decay of tropical cyclones (Merrill 1988). Again, further study is required to understand the physical processes that lead to both decreases and increases in the outer winds when the tropical cyclone intensity is decreasing either in the Stage IIa decay or the final decay in Stage III.

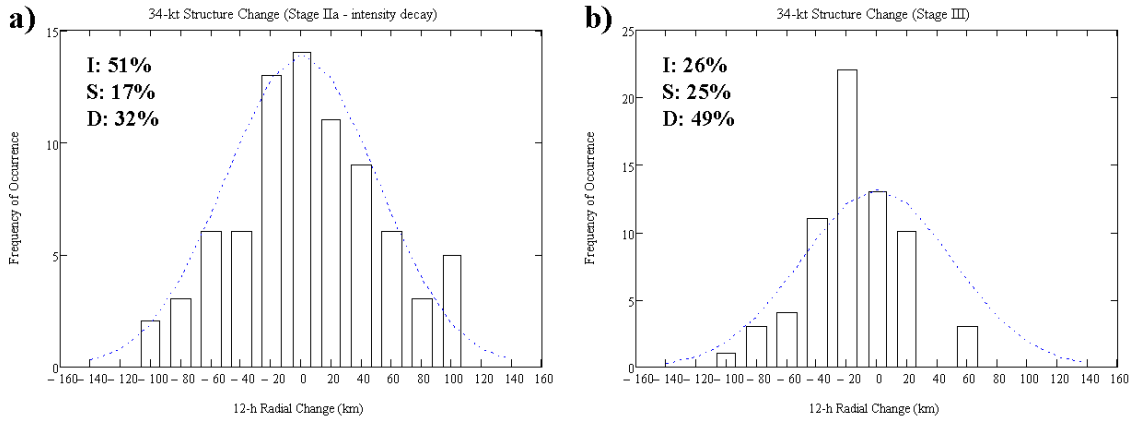

Figure 13 Histograms of 12-h axisymmetric outer wind structure changes in terms of R_{34} values as in Fig. 11, except for (a) Stage IIa decay and (b) Stage III decay.

The histograms for R_{50} and R_{64} changes (Figs. 14–16 and Figs. 17–19, respectively) have similar distributions for the different life cycle stages in Figs. 11–13. Steady states for R_{50} and R_{64} changes over 12 h have been defined as $\pm$7 km and $\pm$3 km, respectively. These definitions were based on examination of the histograms of all

analyses compared to a Gaussian distribution. Structure changes reflected by these radii can also be quite large over a 12-h period. For example, the 12-h R_{50} and R_{64} changes can be as large as ±99 km and ±85 km, respectively. Whereas the distribution for R_{34}, R_{50}, and R_{64} have similarities, there are also notable differences. A comparison of 12-h R_{64} changes for all stages (Fig. 17a) with 12-h R_{34} and R_{50} changes (Figs. 11a and 14a, respectively) suggests the R_{64} distribution has a positive shift on the order of 6 km. This positive shift is readily apparent by comparing a Gaussian distribution with a 6 km shift toward the positive direction with the observed distribution (long-dashed line in Fig. 17). During Stage II rapid intensification, there is a greater percentage of increases in 12-h R_{50} and R_{64} wind structure changes than seen in the R_{34} wind field (increased percentage of 8 percent and 27 percent, respectively). Similar increases are seen for Stage II non-rapid intensification with increased percentages of 5 percent and 18 percent, respectively. Conversely, a 10 percent decrease is noted in 12-h R_{50} structure changes for Stage IIa rapid intensification. For Stage IIa non-rapid intensification, a 13 percent increase in 12-h R_{64} changes is observed. During Stage IIa decay, both 12-h R_{50} and R_{64} structure changes are observed to increase by 8 percent over the observed R_{34} changes. Lastly, the 12-h R_{50} and R_{64} changes for Stage III have similar distributions to R_{34}; however, both distributions appear to be less likely to exhibit steady state conditions (i.e., more increases and decreases are observed at the expense of the steady state category).

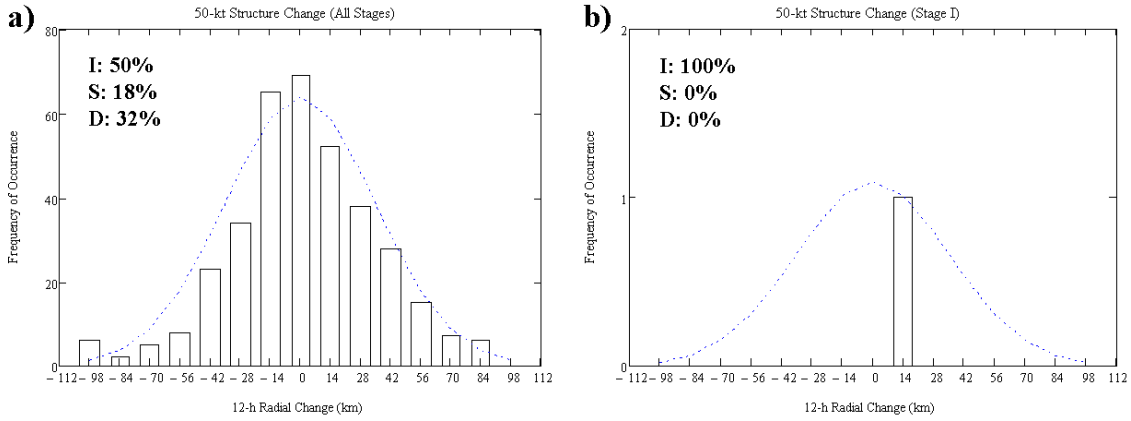

Figure 14 Histograms of 12-h axisymmetric wind structure changes in terms of R_{50} values as in Fig. 11.

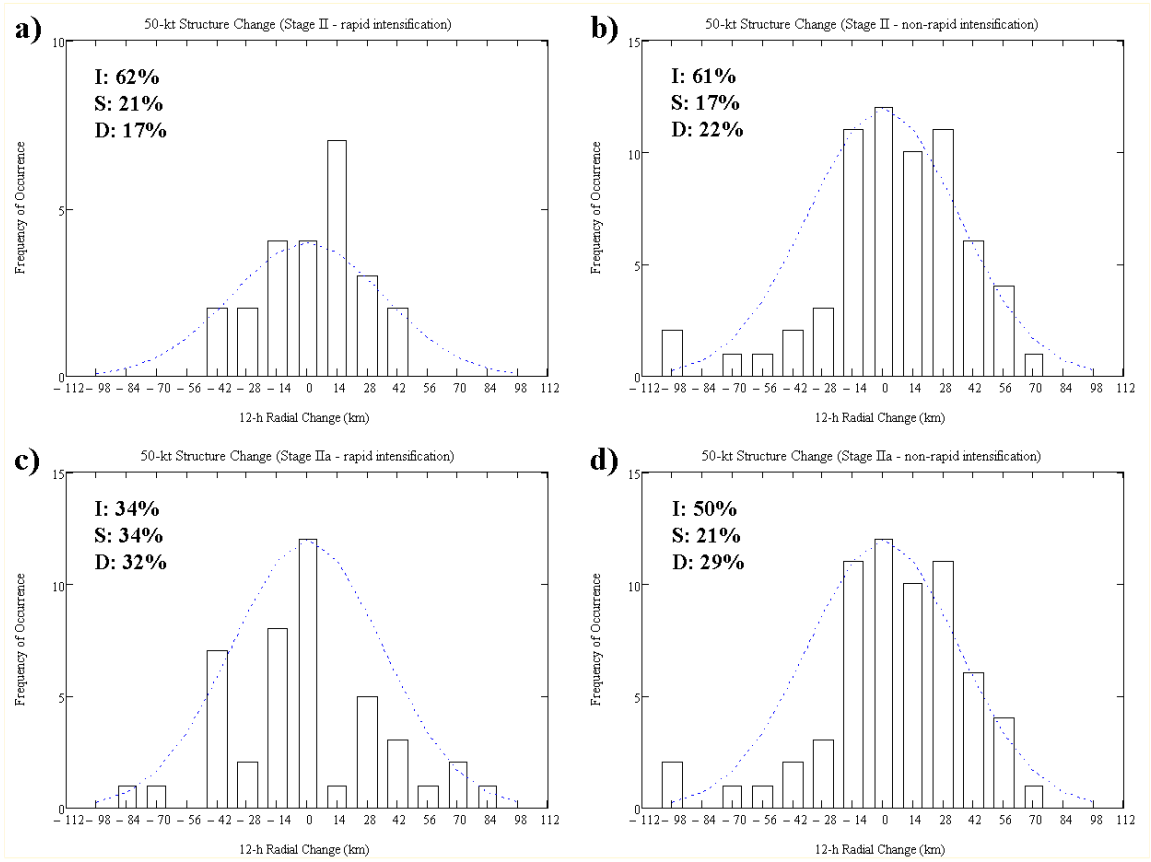

Figure 15 Histograms of 12-h axisymmetric wind structure changes in terms of R_{50} values as in Fig. 12.

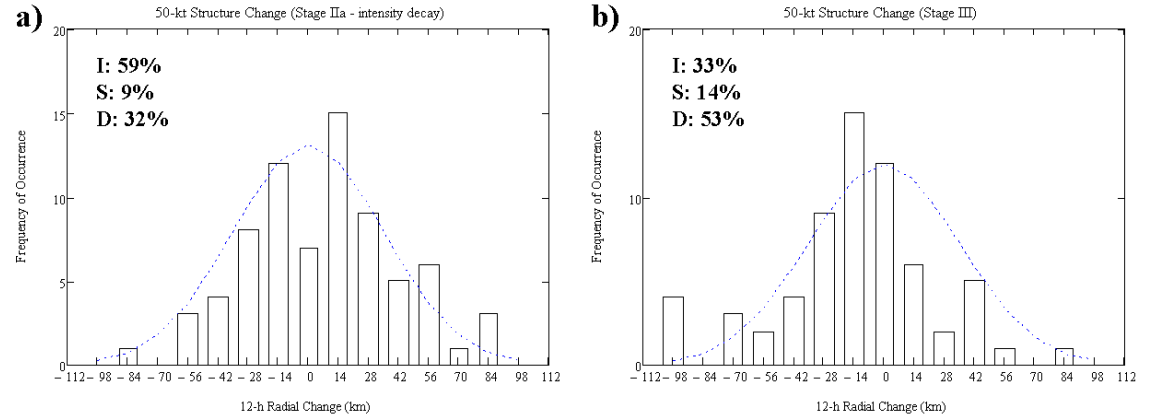

Figure 16 Histograms of 12-h axisymmetric wind structure changes in terms of R_{50} values as in Fig. 13.

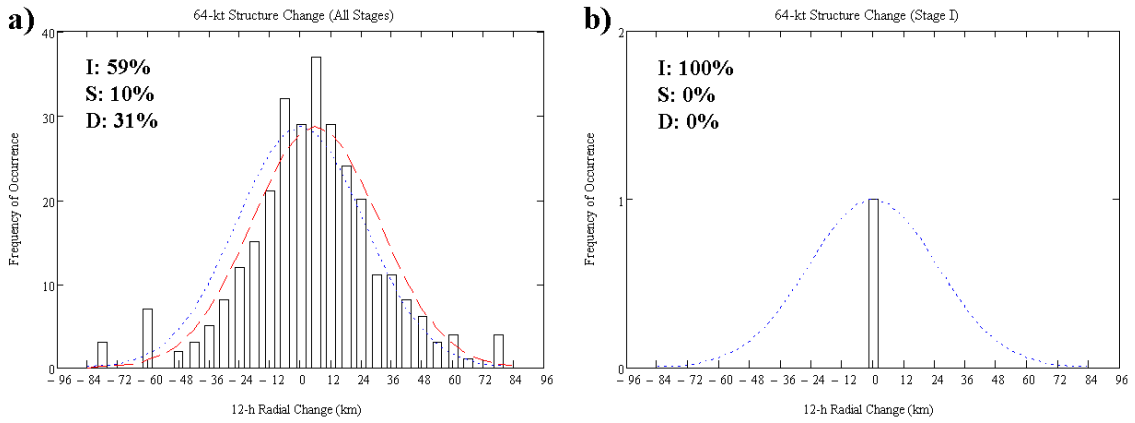

Figure 17 Histograms of 12-h axisymmetric wind structure changes in terms of R_{64} values as in Fig. 11, except the long dashed line is a Gaussian distribution that has been shifted along the positive axis.

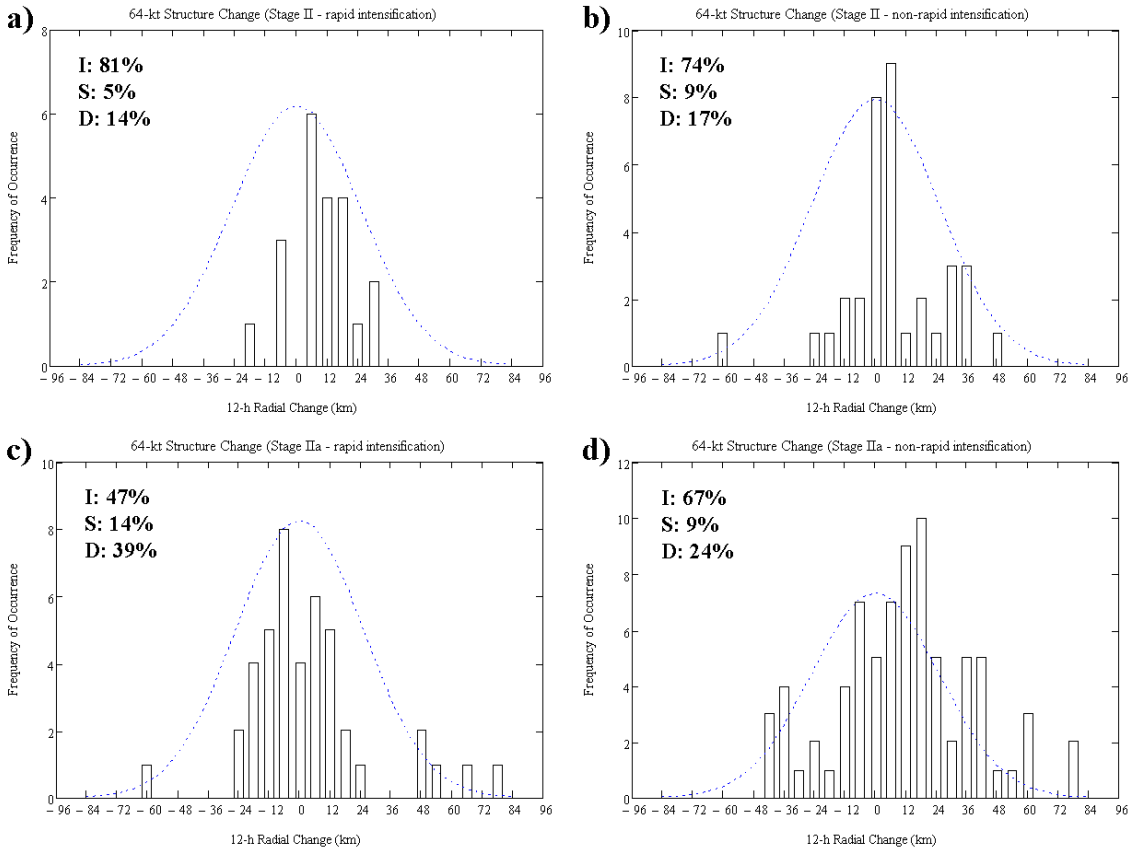

Figure 18 Histograms of 12-h axisymmetric wind structure changes in terms of R_{64} values as in Fig. 12.

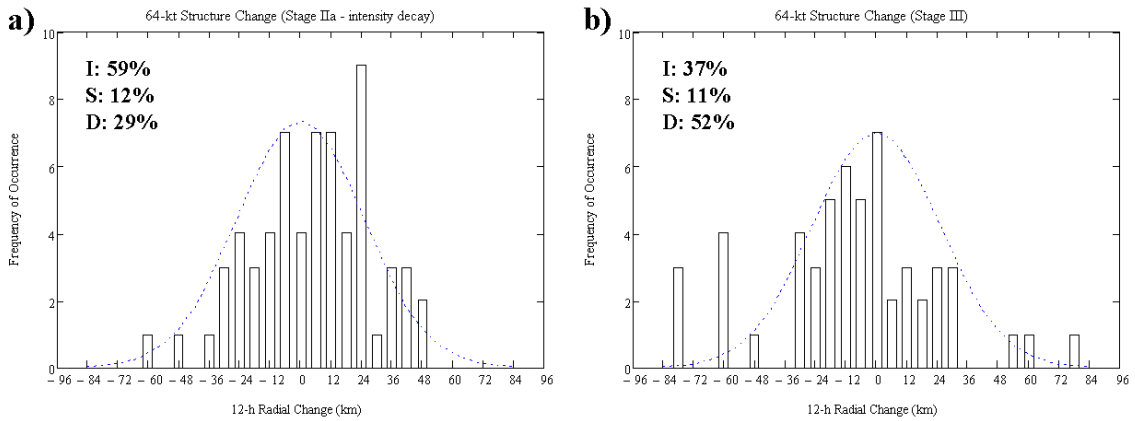

Figure 19 Histograms of 12-h axisymmetric wind structure changes in terms of R_{64} values as in Fig. 13.

Scatterplots of the 24-h axisymmetric wind structure change were compared to 24-h intensity change for all Stages of development to further illustrate differences in R_{34}, R_{50}, and R_{64} wind radii distributions (Fig. 20). The scatterplot comparing 24-h R_{34} structure change to 24-h intensity change in Fig. 20a indicated the correlation (0.341) of observed R_{34} wind radii is only weakly correlated to intensity change. Thus, the simple conceptual model of structure change discussed in Chapter I can only explain a portion of the wind structure changes observed in the Atlantic and eastern North Pacific basins during the 2003 to 2005 hurricane seasons. The observed correlation values for R_{50} and R_{64} (0.400 and 0.523, respectively; see Figs. 20b–c) are similar to the R_{34} distribution in the fact that the correlation between 24-h structure change and 24-h intensity change is not particularly strong. However, one difference of note is the correlation value increases as from R_{34} to R_{64}. In other words, the scatterplots in Fig. 20 indicate that inner-core tropical cyclone structure changes are more closely tied to intensity changes than structure changes in the outer-core region.

In summary, a considerable fraction of R_{34} changes over 12 h during the intensification or re-intensification phases are decreases rather than the increases that would be expected from the simple conceptual models discussed in Chapter I. Similarly, a considerable fraction of R_{34} increases over 12 h are found during the decay phases when decreases might have been expected from the simple conceptual model.

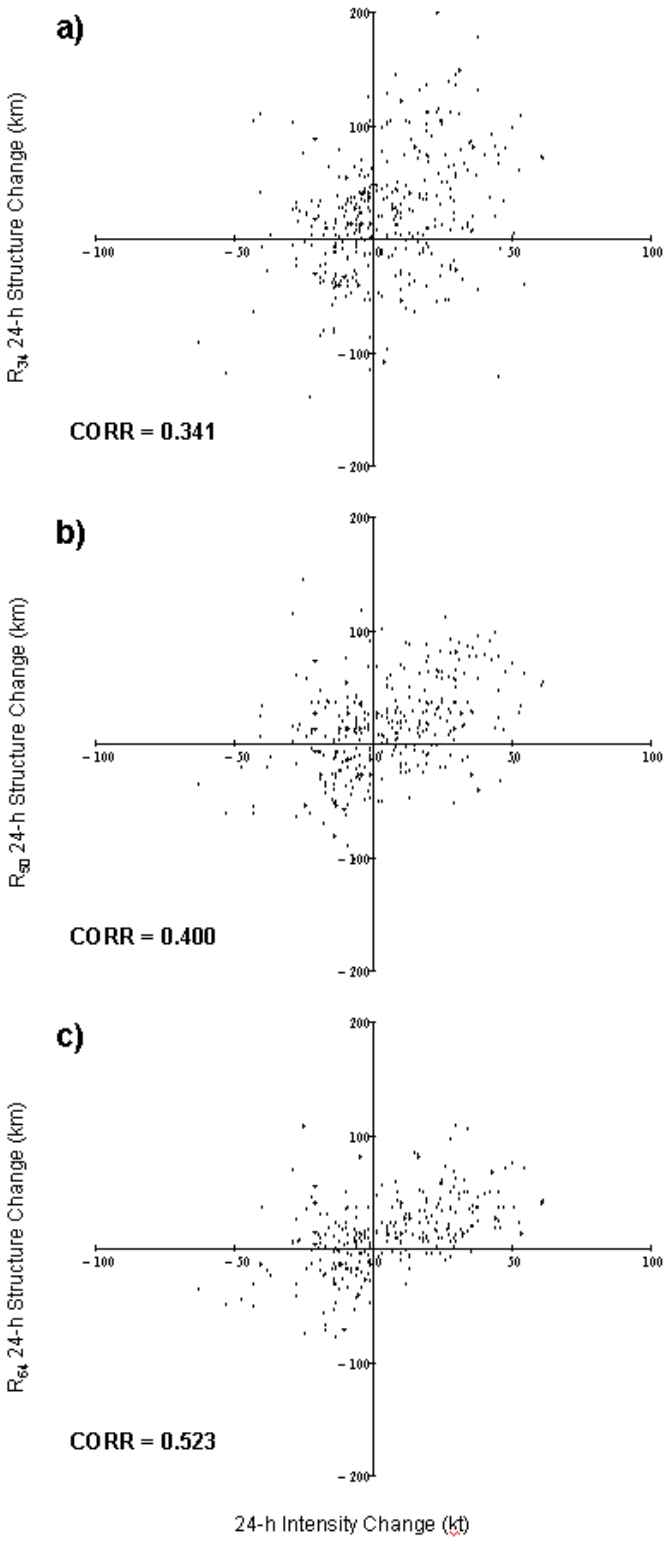

Figure 20 Scatterplots of 24-h axisymmetric wind structure changes in terms of (a) R_{34}, (b) R_{50}, and (c) R_{64} values compared to 24-h intensity change.

However, Merrill (1984, 1988) had suggested that the radii of the surface closed isobars increase during the decay phase and the Knaff et al. (2008) model has a latitudinal dependence that may predict R_{34} increases at latitudes greater the 25°N where decay is expected. Thus, these axisymmetric (and quadrant-by-quadrant, not shown) R_{34} changes are more complicated than the simple conceptual model that directly correlates R_{34} changes to intensity changes.

These life cycle histograms may indicate two possibilities: (i) structure change is random and unpredictable; or (ii) identifiable internal and external mechanisms exist that lead to the observed structure changes. Through analysis of individual storm cases as in Fig. 3, structure change mechanisms are being studied to demonstrate the second possibility applies in the majority of the cases with large changes. Through examination of tropical cyclones that undergo similar structure changes, it may be possible to isolate the most probable mechanism(s) that lead to the changes observed. In Chapter IV, individual storm analysis is applied by examining cases of large R_{34} changes that may be explainable in terms of the internal or external mechanisms that have been proposed for structure changes (see Chapter I).

C. IMPLICATION FOR ENSEMBLE INITIAL CONDITIONS

1. Overview

The predictability of a numerical weather model is primarily limited by: (i) uncertainty in the physical laws that govern atmospheric motions resulting from numerical approximations and sub-grid parameterizations; (ii) uncertainty in the specification of initial conditions arising from systematic and random errors in the observations, inhomogeneity in coverage and lack of sufficient density to represent spatial and temporal scales being resolved in the model, and errors in the approximations of the data assimilation system; (iii) uncertainty in the specification of lateral boundary condition updates for a limited-area model that result from the coarser mesh model having poorer horizontal and vertical resolution, significantly different physical parameterizations, or inadequate handling of the interface between the two grids; and (iv) uncertainty caused by the ability of the model to resolve topography within the domain, or the interaction of topography with the model lateral boundaries (Thompson 1957; Warner et al. 1997; Zhu and Thorpe 2006). Lorenz (1963) identified the chaotic nature of weather prediction that causes a numerical modeling system to be sensitive to the initial conditions.

As such, Lorenz (1963) theorized that there is a near-total loss in model predictive skill after a period of 7 to 14 days. In their numerical study of an East Coast snowstorm from 23–26 January 2000, Langland et al. (2002) showed that small, nearly indiscernible errors in the temperature and wind fields of the initial conditions led to very large 72-h forecast errors, including a cyclone track error of 1860 km. Using an adjoint sensitivity-based correction to the original initial condition specification, they were able to reduce forecast errors by 75 percent and the cyclone track error was limited to 105 km. Mullen and Baumhefner (1989) conducted a numerical simulation of oceanic cyclogenesis and suggest that initial condition error growth is much greater in an explosive cyclogenetic environment than for "normal" midlatitude flow patterns.

The error growth in limited area numerical model simulations is quite different from what has been observed in global model simulations (Anthes et al. 1985; Errico and Baumhefner 1987; Warner et al. 1989). The introduction of lateral boundaries to a model domain allows initial condition errors to propagate out of the domain or to be replaced by errors introduced at the lateral boundaries that sweep into the domain over time. Using a mesoscale simulation of lee cyclogenesis, Alpert et al. (1996) found that nonlinear interaction between the lateral boundaries and the initial conditions contributed the most to the observed error growth, followed by the interaction between topography and the initial conditions. They also showed that the initial conditions dominated the first 9–15 h of model integration, followed by significant influence from the lateral boundary conditions. Using a regional prediction system, Hsiao et al. (2009) demonstrated that the use of initial and lateral boundary conditions from a global model system with superior forecast skill can significantly improve the regional model's ability to accurately specify the track of a tropical cyclone. In their study, synthetic data were introduced to better represent the initial structure of the tropical cyclone given the lack of observational data over the open ocean areas. They also state that lateral boundary conditions have a greater impact on the tropical cyclone track since specifying the strength and extent of the subtropical ridge plays a major role in track prediction. In general, lateral boundary condition errors can be more damaging to forecast accuracy than initial condition errors, especially during longer model simulations (Vukicevic and Errico 1990; Errico et al. 1993). Fortunately, lateral boundary error advection speeds are generally slower at lower latitudes since conditions are more barotropic and cross-boundary flow is weaker (Baumhefner and Perkey 1982). However, as a tropical cyclone migrates northward and is influenced by

a greater amount of synoptic vertical wind shear, the error introduced at the lateral boundaries is likely to increase.

As in the approach of Hsiao et al. (2009), the data-sparse regions of the vast oceanic areas suggest the need to synthetically represent the structure of a tropical cyclone in the initial conditions of a numerical prediction model. While many past numerical simulation studies have attempted to accurately represent the initial tropical cyclone vortex with approximations such as the modified Rankine profile, these methods are limited by their deterministic nature. In reality (as will be shown in this section), tropical cyclone vortex structure has a significant amount of variability that can not be adequately described by a simple deterministic approach. Instead, capturing the uncertainty of a tropical cyclone structure, intensity, and track requires an ensemble approach.

2. Variability of Outer Wind Structure

Stenger and Elsberry (2008) documented the observed variability of the R_{34} outer-core radius of tropical cyclones in the western North Atlantic from 2003 through 2005 using Saffir-Simpson categories of hurricanes and the tropical cyclone life cycle intensity change definitions of Elsberry et al. (2007) displayed in Fig. 9. The use of box plots to display the tropical cyclone wind radii can be quite instructional. In Fig. 21, the H*Wind R_{34} wind radii are plotted for each Saffir-Simpson storm category and for each Cartesian quadrant. The box plot widths are proportional to the sample size used to compute the statistics. All land interaction cases within the R_{34} wind radii have been identified and eliminated from the plots. In addition, all trivial "zeros" have been eliminated from the plots, i.e., cases with a maximum wind speed less than tropical storm strength (<34 kt).

A broad overview of Fig. 21 reveals a general asymmetry in the R_{34} structure for most of the Saffir-Simpson categories. With the exception of Category 5 (H5) hurricanes, the NE quadrant has the largest size (R_{34} values), the NW and SE quadrants are nearly equal in size, and the SW quadrant has the smallest size. The asymmetric distribution of R_{34} wind radii is partially explained by the addition or subtraction of the average tropical cyclone motion vector (i.e., in the Atlantic basin storm motion generally adds to the winds in the NE quadrant and subtracts from the winds in the SW quadrant).

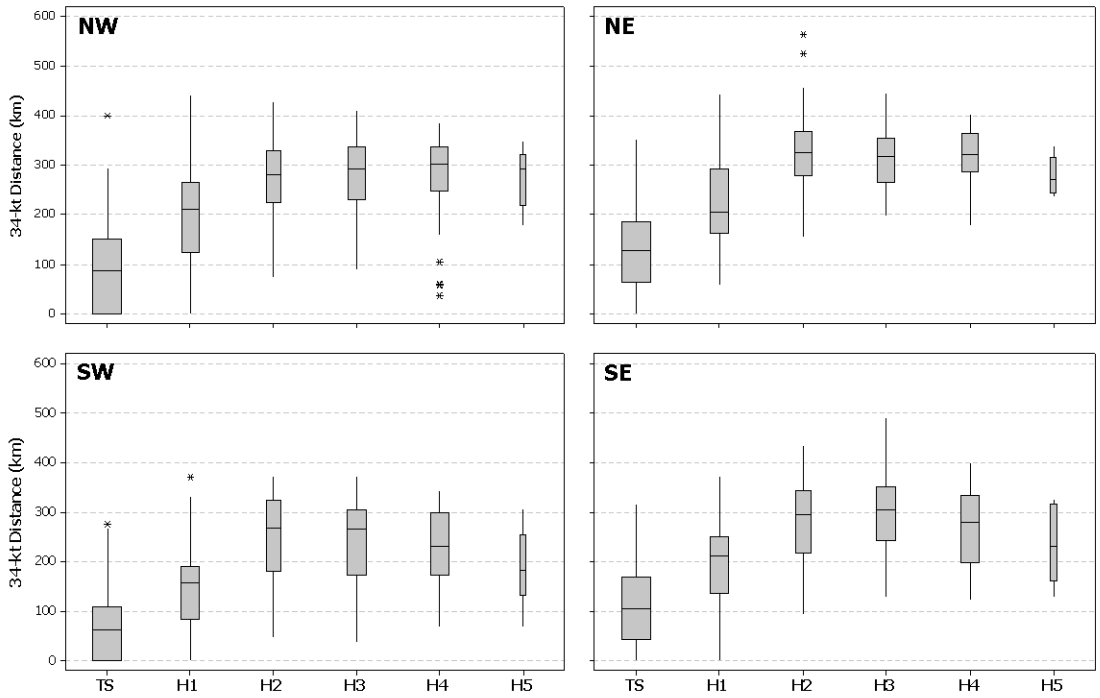

Figure 21 Box plots of H*Wind R_{34} wind radii for Saffir-Simpson tropical storms (TS), Category 1 (H1) hurricanes, Category 2 (H2) hurricanes, Category 3 (H3) hurricanes, Category 4 (H4) hurricanes, and Category 5 (H5) hurricanes for each Cartesian quadrant as in Fig. 8. The box plot widths are proportional to the sample size used to compute the statistics.

Increasing size (R_{34} wind radii) from tropical storms (TS) through Category 2 (H2) hurricanes is readily apparent in Fig. 21 for all storm quadrants. The R_{34} wind radii then level off for development between Category 2 (H2) and Category 4 (H4) hurricanes, except in the southern quadrants where some size decrease is noted from Category 3 (H3) to Category 4 (H4) hurricanes. Category 5 (H5) hurricanes appear to decrease in size for all quadrants. However, caution is advised in making any size interpretations of the Category 5 (H5) hurricane data from the R_{34} wind radii, since the sample size (n = 8) is too small to be considered statistically valid.

In Fig. 22, similar box plots of the H*Wind R_{34} wind radii are plotted for each stage of tropical cyclone development (as previously defined in Fig. 9) for each Cartesian quadrant. Tropical cyclone formation (i.e., Stage I) is not displayed since by definition these cases have no wind speeds above 34 kt. A similar asymmetric R_{34} size distribution as in Fig. 21 is apparent through each stage of tropical cyclone

development for the same reasons as noted earlier. Sample sizes are likely large enough (n >30) to ensure confident results for all stages of development. Ideally, the sample size of Stage II (S-II) rapid (R) intensification should be larger. However, the sample sizes of S-II (R) in all four quadrants are very close to 30 cases and therefore are likely reliable.

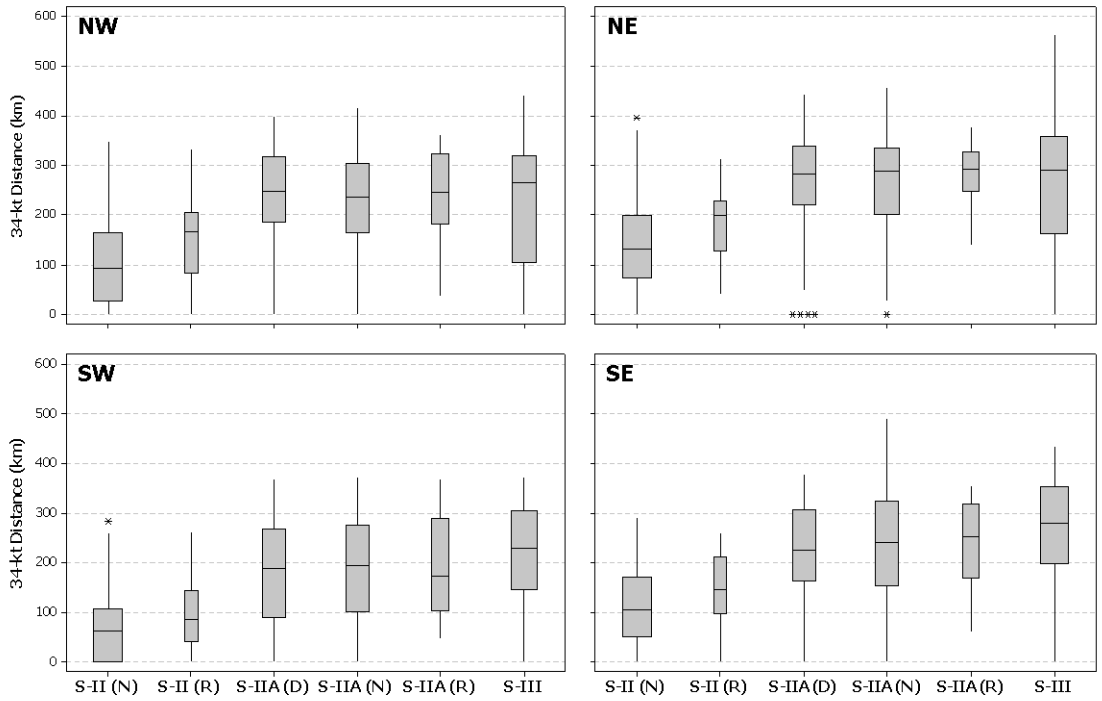

Figure 22 Box plots of H*Wind R_{34} wind radii for Stage II (S-II) non-rapid (N) and rapid (R) intensification; Stage IIa (S-IIA) intensity decay (D), non-rapid (N) and rapid (R) intensification; and Stage III (S-III) for each Cartesian quadrant as in Fig. 8. The box plot widths are proportional to the sample size used to compute the statistics.

Stage II (S-II) rapid (R) intensification consistently has larger R_{34} values than for the non-rapid intensification S-II (N) in all four quadrants (Fig. 22). From this result, one might hypothesize that the outer wind structure either plays a role in rapid intensification or is indicative of a favorable environment for rapid intensification. This will be further studied in Chapter IV.

The most rapid R_{34} size increase relative to a prior life cycle stage in Fig. 22 is noted during the Stage IIa (S-IIA) intensity decay (D) phase, which occurs when the intensity temporarily decreases before again increasing in a secondary eyewall forma-

tion (Fig. 9c). This result is consistent with the findings of Terwey and Montgomery (2008) in their idealized high-resolution numerical simulation of secondary eyewall replacement. Their numerical study appeared to predict an outer wind radii increase during the S-II (D) phase of storm development. Some case studies will be presented in Chapter IV.

Whether the re-intensification is non-rapid (N) or rapid (R) during Stage IIa (S-IIA) does not affect the R_{34} size, although the R_{34} value is slightly smaller in the SW quadrant (Fig. 22). During the decay Stage III (S-III), most of the Atlantic tropical cyclones will be moving toward the northeast. Therefore, the most relevant R_{34} comparison is between the SE and NW quadrants where the background southwesterly steering flow is expected to be adding to or opposing the vortex flow, respectively. Indeed, the median R_{34} value in the SE quadrant is slightly larger than in the NW quadrant, but the more reliable difference may be the larger fraction of small (<200 km) R_{34} values in the NW quadrant. In the SE quadrant, this is inconsistent with the size decrease during the decay stage that would be implied by the simple model that a decrease in intensity will be accompanied by a decrease in size, but is consistent with the forecaster rule-of-thumb that an expansion of the tropical cyclone R_{34} wind radii will occur during the decay phase of the tropical cyclone.

3. Assessment of Key Vortex Parameters

In this section, the observed variability of V_t (maximum tangential velocity), R_{max}, and R_{34} of tropical cyclones in the western North Atlantic from 2003 through 2005 will be assessed in a motion-relative coordinate system. In motion-relative coordinates, the vortex structure in LF, RF, RR, and LR quadrants can be directly compared without the added contribution from the storm motion. Observed profiles of tangential and radial winds in motion-relative coordinates for Stage II non-rapid intensification of Atlantic tropical cyclones are shown in Fig. 23. Two distinct distributions seem to exist: cases during storm development from tropical storm strength (17 m s^{-1}) to hurricane strength (33 m s^{-1}); and cases with winds in excess of 50 m s^{-1} that have not yet entered Stage IIa of development. The four tropical cyclones that intensified to greater than 50 m s^{-1} prior to entering Stage IIa were Fabian (2003), Isabel (2003), Frances (2004), and Ivan (2004). All four tropical cyclones were over the open waters of the western North Atlantic east of the Lesser Antilles and had intense eyewall convection.

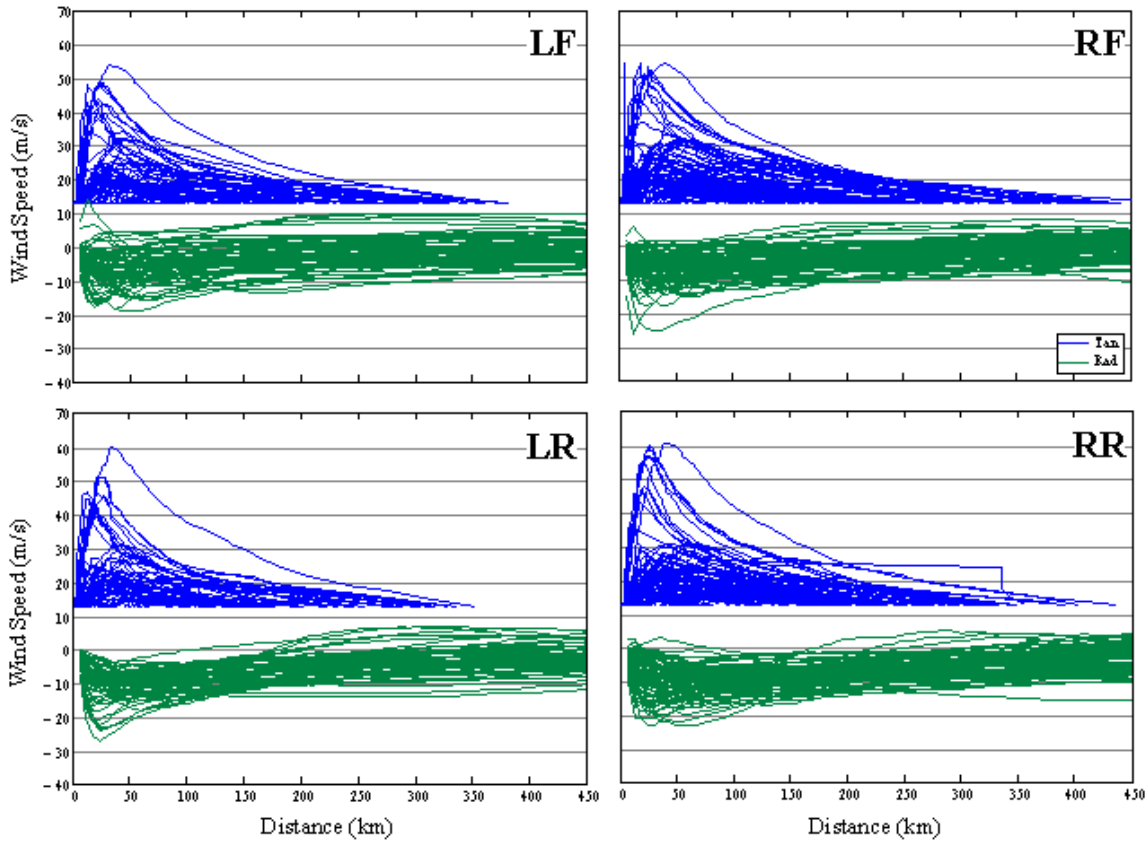

Figure 23 Observed tangential and radial (negative values represent inward motion) wind profiles in motion-relative coordinates for Stage II non-rapid intensification.

The multivariate regressions in this section are displayed in two dimensions, but are three-dimensional surfaces fitted to each set of observed V_t, R_{max}, and R_{34} using a second-order polynomial. The surface mesh is colorized to represent the variation of V_t in the third dimension, such that smaller values of V_t are dark blue and larger values of V_t are orange to red. A multivariate regression of V_t, R_{max}, and R_{34} (Fig. 24) in motion-relative coordinates for Stage II non-rapid intensification of tropical cyclone development demonstrates the nonlinear association of these three parameters. This multivariate regression also suggests that two surface wind profile distributions exist. In the first distribution, the radii of R_{max} and R_{34} are positively correlated, i.e., large (small) values of R_{max} are paired with large (small) values R_{34}, whereas there is minimal spread in the observed tropical cyclone intensity (V_t). In the second distribution, the

R_{34} radii varies from 180 km to >300 km (values clustered in upper right portion of each plot in Fig. 24) while the variations in R_{max} and V_t are small.

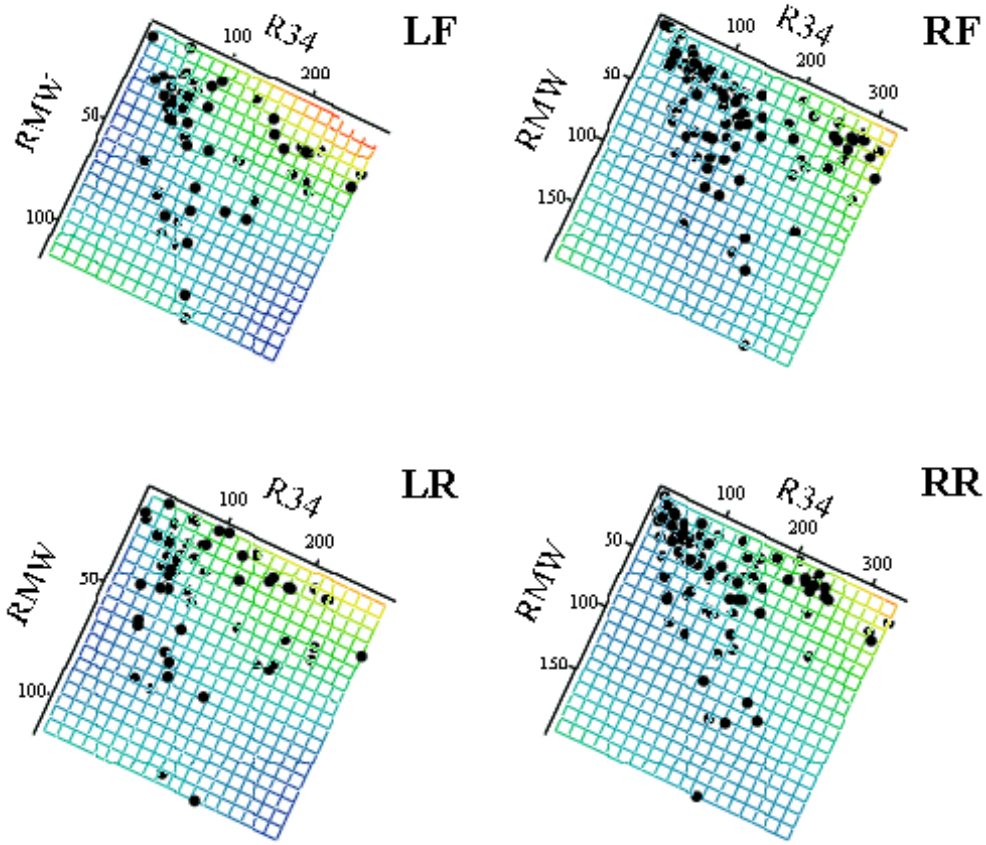

Figure 24 Multivariate regression of V_t (m s^{-1}), R_{max} (km, denoted as RMW in graphic), and R_{34} (km) in motion-relative coordinates for Stage II non-rapid intensification. The mesh is the second-order polynomial surface fit to the data where smaller values of V_t are dark blue and larger values are orange to red.

The analysis of paired-parameters in motion-relative coordinates for Stage II non-rapid intensification of tropical cyclone development is shown in Fig. 25. The comparison of V_t and R_{max} (Figs. 25a, d, g, and j) generally reveals the expected outcome that a decrease in R_{max} is accompanied by in an increase in V_t as predicted by conservation of angular momentum.

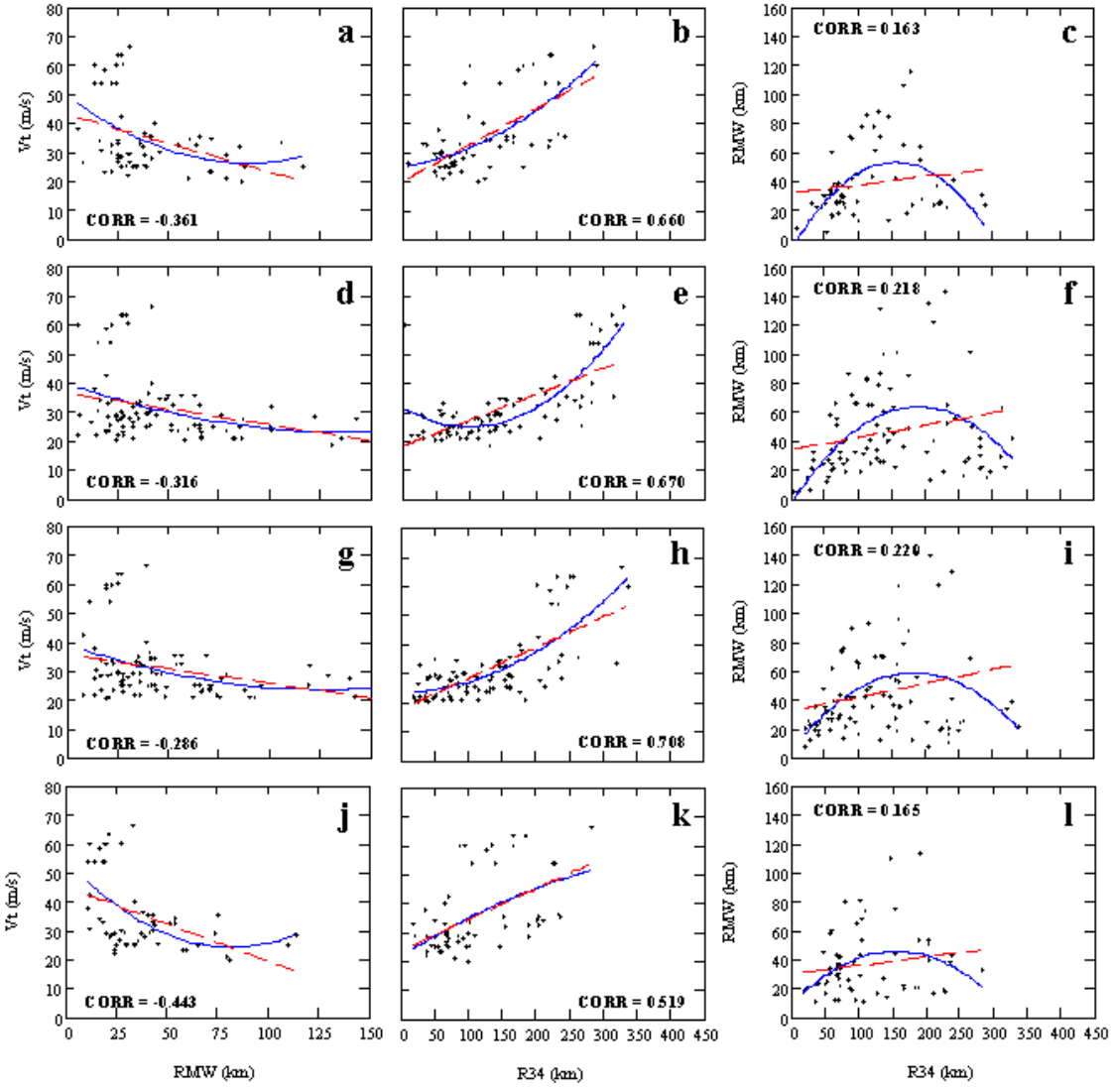

Figure 25 Pair-parameter regressions of V_t, R_{max} (denoted as RMW in graphic), and R_{34} in motion-relative coordinates for Stage II non-rapid intensification. A second-order curve (blue line) is assumed to best fit to the data for the LF (a–c), RF (d–f), RR (g–i), and LR (j–l) quadrants. A linear fit (red dashed line) and correlation coefficient are also provided for each panel.

However, the grouping of observed V_t values greater than 50 m s^{-1} suggests that smaller values of R_{max} can result in a range of observed V_t values. Thus, the correlation coefficients for the LF, RF, RR, and LR quadrants (-0.361, -0.316, -0.286, and -0.443, respectively) would be larger by limiting the comparison to V_t values of less than 40 m s^{-1}. The comparison of V_t and R_{34} (Figs. 25b, e, h, and k) suggests that increases in R_{34} generally occur with corresponding increases in V_t, which again is in general agreement with the expectations from the empirical wind distribution in Fig. 1 or the axisymmetric models that have an increase in outer winds (R_{34}) during the intensification stage. Whereas this tendency is best illustrated in the RF quadrant (Fig. 25e), the LR quadrant (Fig. 25k) has a weaker tendency with some intense storms with small R_{34} values. The correlation coefficients for the LF, RF, RR, and LR quadrants (0.660, 0.670, 0.708, and 0.519, respectively) indicate a linear relationship between V_t and R_{34}, although with some scatter about the curves. The variability is largest at larger values of R_{34} for the right quadrants (180 km or more). Greater asymmetry generally exists during early stages of tropical cyclone development, and generally with smaller R_{34} values in the left quadrants.

The comparison of R_{max} and R_{34} radial distances (Figs. 25c, f, i, and l) reveals the existence of a bimodal distribution. In the first mode, larger (smaller) R_{34} radii are almost linearly associated with larger (smaller) R_{max} values. In the second mode, the large outer-core structure (R_{34}) values are associated with small R_{max} values. Specifically, the second distribution mode in the outer-core structure is most readily apparent for R_{34} radii greater than 180 km in the right quadrants and 150 km in the left quadrants. The small (0.163 to 0.220) correlation coefficients suggest that changes in the outer-core structure of a tropical cyclone do not have strong ties to inner-core structure changes. More details on the means and standard deviations for the R_{max} and R_{34} radial distances of Atlantic tropical cyclones in Stage II non-rapid intensification are provided in Tables 10–11 of Appendix E, where the observed maximum tangential velocities in each motion-relative quadrant are binned in 5 m s^{-1} increments.

The probability density plot of azimuthal-average values for exponent x in the modified Rankine vortex

$$V_t R_{max}^x = V_{34} R_{34}^x \tag{20}$$

for Stage II non-rapid intensification (Fig. 26a) has a mean of 0.56 and a standard deviation of 0.21 for sample size n = 274.

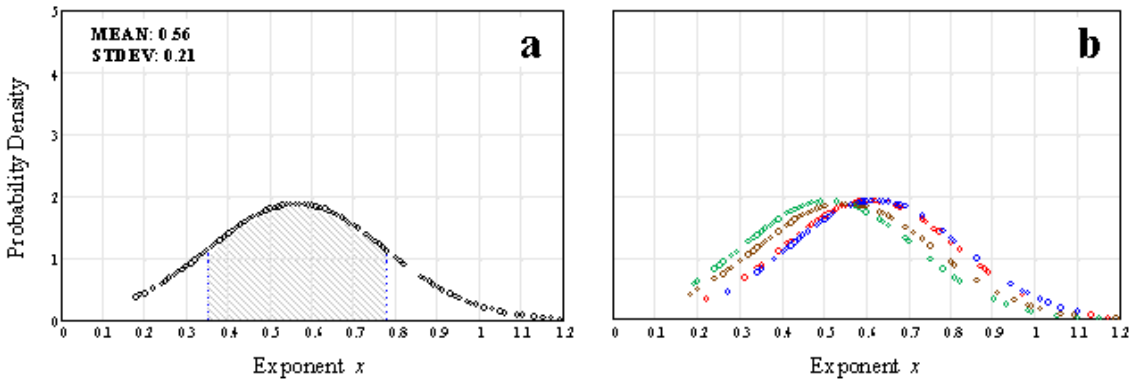

Figure 26 Probability density plots of (a) azimuthal-average and (b) motion-relative quadrants exponent x values in the modified Rankine vortex of Eq. (20) for Stage II non-rapid intensification. The hashed region (panel a) is a standard deviation about the mean. The LF (red), RF (green), RR (brown) and LR (blue) quadrants are displayed in panel (b).

The range of expected values of exponent x within a standard deviation of the mean (hashed region in Fig. 26a) is 0.35–0.78. In Fig. 26b, the probability density plots of the motion-relative quadrant values for exponent x in the modified Rankine vortex indicate a greater probability of larger (smaller) R_{34} radii in the right (left) quadrants of the tropical cyclone. Using Eq. (20) and assuming a typical storm motion of 15 kt, a variation of ± 0.035 in exponent x from the azimuthal-average mean (0.56) can be explained by the addition or subtraction of the average tropical cyclone motion vector. Details on the sample size (n), mean, median, standard deviation, and range within a standard deviation of the mean for each motion-relative quadrant are presented in Table 1. A comparison of the mean and median values indicates a slightly right-skewed distribution of values for exponent x during Stage II non-rapid intensification. Using Eq. (20), the smaller values of exponent x in the RF and RR quadrants (0.51 and 0.55, respectively) yield larger R_{34} sizes than for the left quadrants.

Table 1 Modified Rankine vortex exponents for Stage II non-rapid intensification.

QUADRANT	n	MEAN	MEDIAN	STDEV	MEAN $\pm$ STDEV
LF	57	0.61	0.59	0.21	0.40–0.82
RF	81	0.51	0.45	0.21	0.30–0.72
RR	82	0.55	0.54	0.21	0.34–0.76
LR	51	0.62	0.59	0.21	0.41–0.83

However, approximately 80 percent of the outer-core structure asymmetries can be explained by the addition or subtraction of the average tropical cyclone motion vector.

Observed profiles of tangential and radial winds in motion-relative coordinates for Stage II rapid intensification of Atlantic tropical cyclones are shown in Fig. 27.

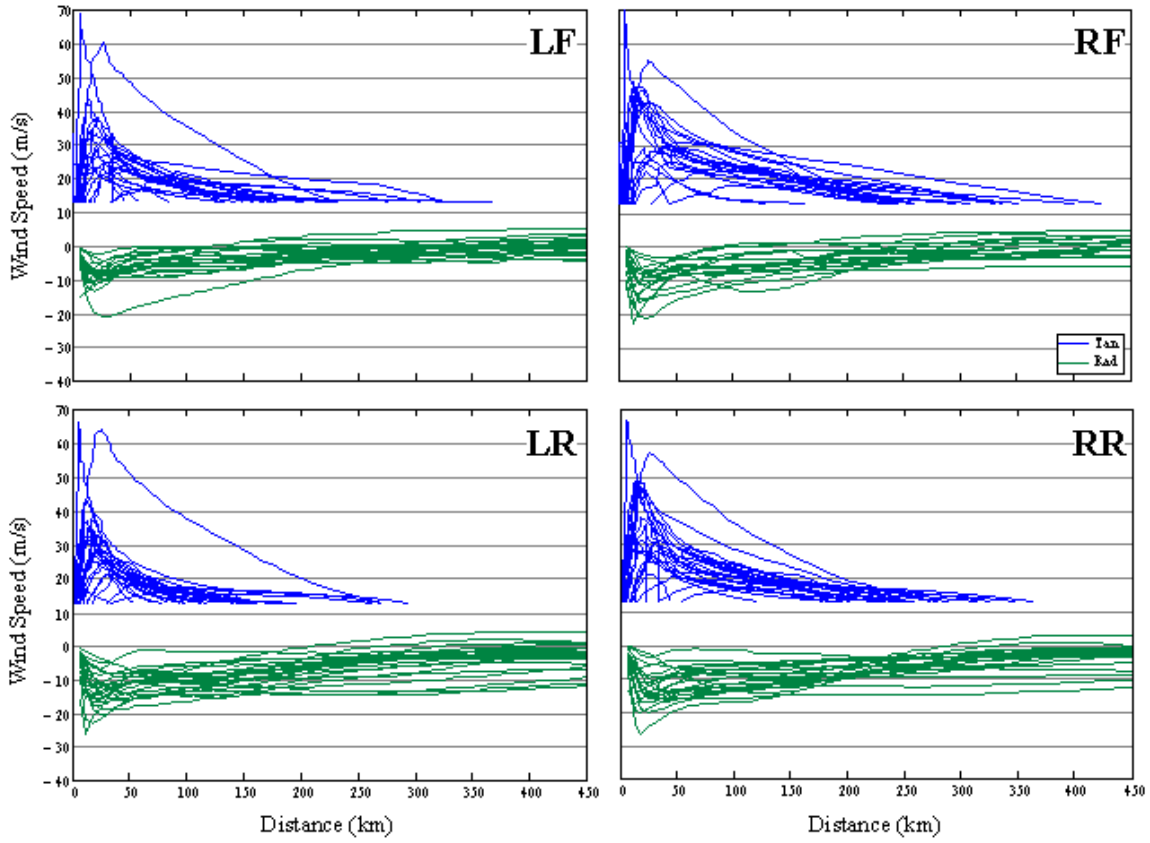

Figure 27 Observed tangential and radial wind profiles as in Fig. 23, except for Stage II rapid intensification.

The profiles indicate a greater asymmetry in the tropical cyclone structure with the largest R_{34} radii found in the RF quadrant. Additionally, the inner- and outer-core storm structures are more compact than for Stage II non-rapid intensification (where V_t is less than 50 m s^{-1}) with smaller R_{max} and R_{34} values. Most of the profiles with V_t values greater than 45 m s^{-1} are represented by Dennis (2005) prior to landfall over western Cuba, and Ivan (2004) and Emily (2005) prior to entering Stage IIa of development over the southern Caribbean Sea. The profile with a V_t of more than 72 m s^{-1} and a 5 km R_{max} is associated with the unusually rapid intensification of Wilma

(2005) over the northwestern Caribbean Sea. The broad profile with R_{max} equal to 25 km and V_t equal to 66 m s^{-1} is associated with Isabel (2003) as it became an annular hurricane over the central North Atlantic. It is also noteworthy that the asymmetric tangential velocities in Isabel with maxima in the left quadrants is contrary to what is observed with other Atlantic tropical cyclones.

A multivariate regression of V_t, R_{max}, and R_{34} (Fig. 28) in motion-relative coordinates for Stage II rapid intensification of tropical cyclone development is markedly different from the Stage II non-rapid intensification (Fig. 24). When weak systems with large R_{max} radii are removed from the sample, the dominant surface wind profile distribution has large (small) R_{34} radii and large (small) storm intensity (V_t) with smaller values of R_{max}.

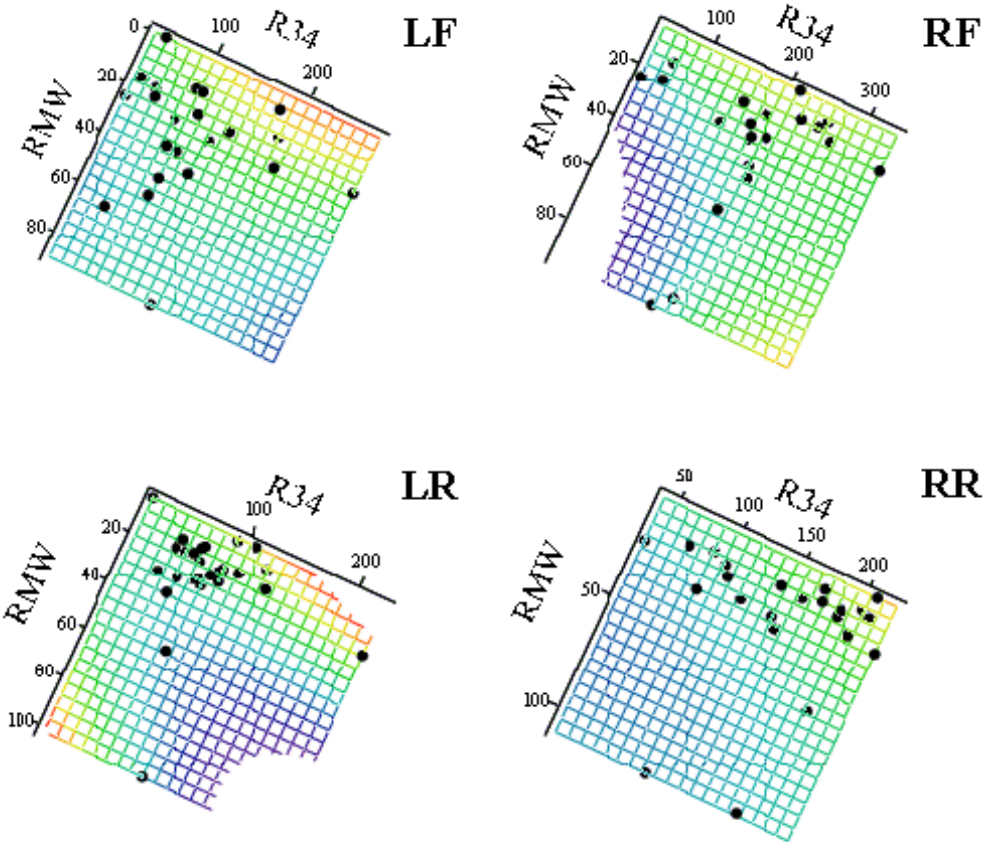

Figure 28 Multivariate regression of V_t , R_{max}, and R_{34} as in Fig. 24, except for Stage II rapid intensification.

The analysis of paired-parameters in motion-relative coordinates for Stage II rapid intensification of tropical cyclone development is shown in Fig. 29. The comparison of V_t and R_{max} (Figs. 29a, d, g, and j) generally reveals the expected outcome in which smaller R_{max} radii are associated with larger V_t as predicted by conservation of angular momentum. Correlation coefficients for the LF, RF, RR, and LR quadrants (-0.560, -0.585, -0.530, and -0.478, respectively) are larger than for Stage II non-rapid intensification (see Fig. 25).

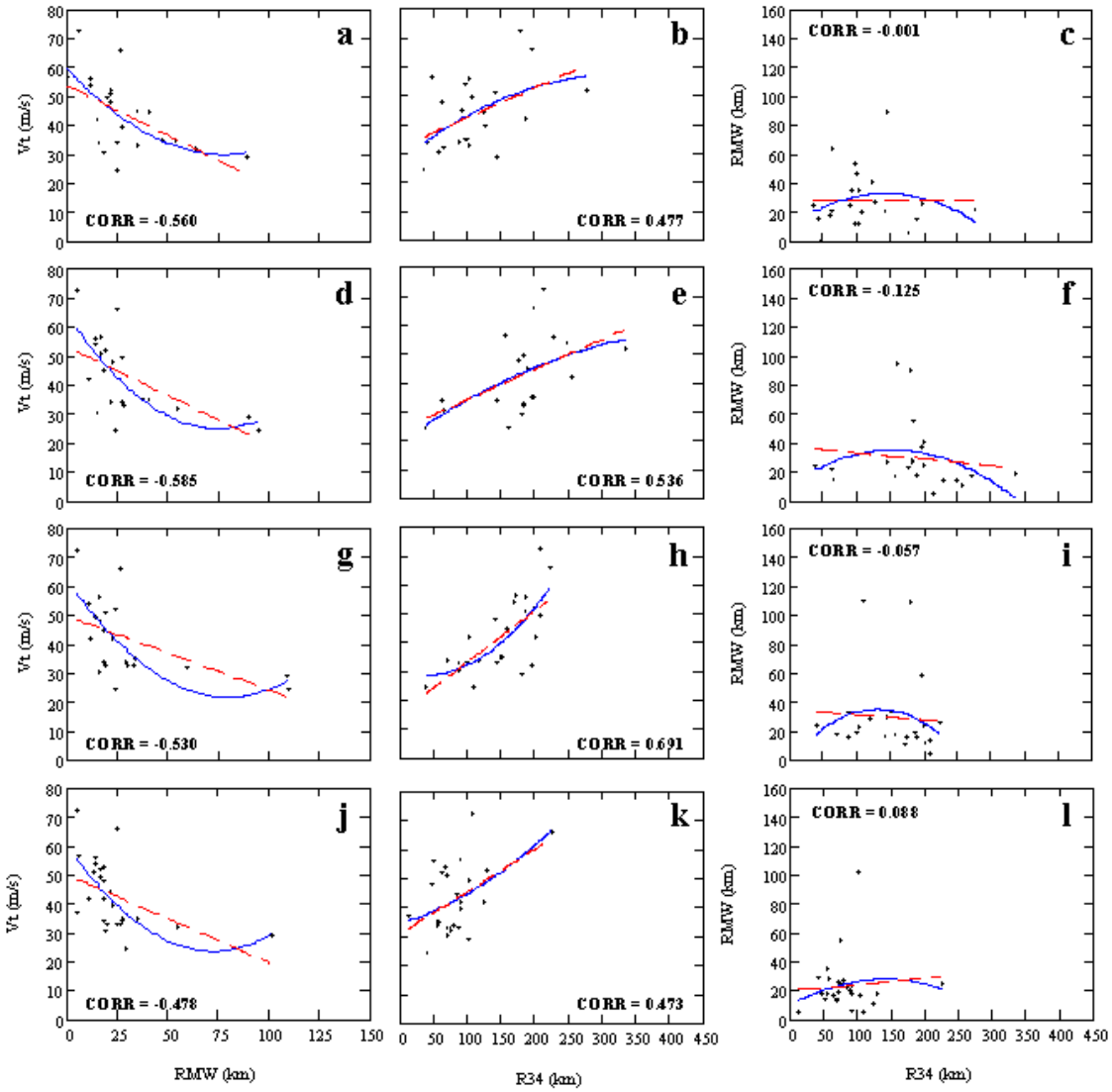

Figure 29 Pair-parameter regressions of V_t, R_{max}, and R_{34} as in Fig. 25, except for Stage II rapid intensification.

The comparison of V_t and R_{34} (Figs. 29b, e, h, and k) suggests that larger R_{34} radii are also associated with larger V_t values, which is in general agreement with the expectations from the empirical wind distribution in Fig. 1 or the axisymmetric models that suggest an increase in outer winds (R_{34}) during intensification. The correlation coefficients for the LF, RF, RR, and LR quadrants (0.477, 0.536, 0.691, and 0.473, respectively) are smaller than for Stage II non-rapid intensification with the greatest variability in the left quadrants (Figs. 29b and k). The small (-0.001 to 0.126) correlation coefficients between the R_{max} and R_{34} radial distances (Figs. 29c, f, i, and l) indicates the aspect that the inner-core structure has very little effect on the outer-core structure during rapid intensification. More details on the means and standard deviations for the R_{max} and R_{34} radial distances of Atlantic tropical cyclones in Stage II rapid intensification are provided in Tables 12–13 of Appendix E.

The probability density plot of azimuthal-average values for exponent x in the modified Rankine vortex for Stage II rapid intensification (Fig. 30a) has a mean of 0.58 and a standard deviation of 0.20 for a sample size n = 85.

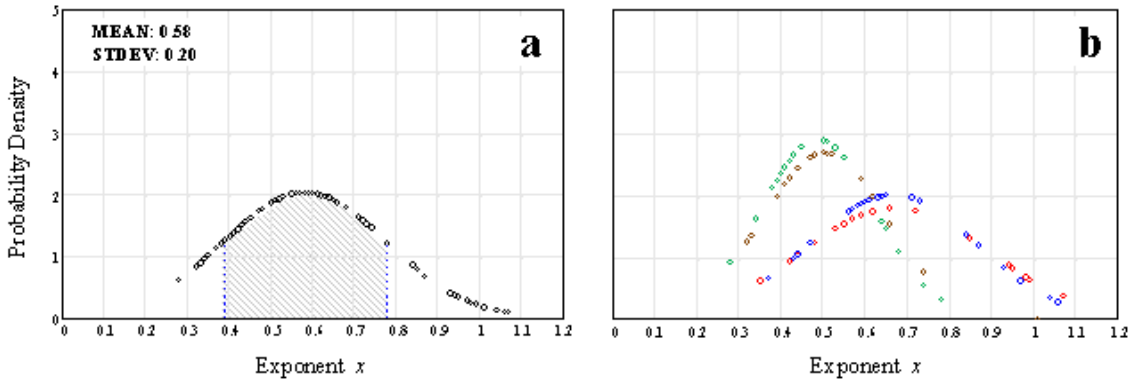

Figure 30 Probability density plots as in Fig. 26, except for Stage II rapid intensification.

The range of expected values of exponent x within a standard deviation of the mean (hashed region in Fig. 30a) is 0.39–0.78. In Fig. 30b, the probability density plots of the motion-relative quadrant values for exponent x in the modified Rankine vortex again indicate a greater probability of larger (smaller) R_{34} radii in the right (left) quadrants of the tropical cyclone. For the Stage II rapid intensification, there appears to be a larger difference in the mean values of exponent x between the left and right quadrants, and a reduction in the expected range of values for exponent x in the right quadrants than observed during Stage II non-rapid intensification. Indeed, the

difference in mean values for exponent x in the RF and RR quadrants (0.49 and 0.50, respectively, Table 2) compared to the left quadrants (0.67 for each) are nearly twice as large as for Stage II non-rapid intensification. For this stage, only about 40 percent of the outer-core structure asymmetries can be explained by the addition or subtraction of the average tropical cyclone motion vector. This suggests that an asymmetric R_{34} structure with larger (smaller) R_{34} values in the right (left) quadrants may be associated with rapid intensification of a tropical cyclone. In Table 2, the decreases in the standard deviations for the right quadrants represent an approximate 31 percent reduction in the range of the expected values for exponent x within a standard deviation of the mean compared to the left quadrants (depicted by the increase in probability density in Fig. 30b). As before, a comparison of the mean and median values indicates a slightly right-skewed distribution of values for exponent x during Stage II rapid intensification. It should be noted that while the sample sizes in Table 2 are smaller than desired to represent the population distribution, the values for exponent x are consistent with those for the other stages of the tropical cyclone life cycle.

Table 2 Modified Rankine vortex exponents for Stage II rapid intensification.

QUADRANT	n	MEAN	MEDIAN	STDEV	MEAN $\pm$ STDEV
LF	18	0.67	0.59	0.22	0.45–0.89
RF	20	0.49	0.43	0.14	0.35–0.63
RR	22	0.50	0.48	0.15	0.35–0.65
LR	22	0.67	0.61	0.20	0.47–0.87

Observed profiles of tangential and radial winds in motion-relative coordinates during the Stage IIa decay phase of the secondary eyewall formation are shown in Fig. 31. These profiles indicate that two distinct distributions exist: those cyclones with smaller R_{max} radii that have asymmetries with maximum winds in the right quadrants; and those cyclones with larger R_{max} radii that have asymmetries with maximum winds in the left quadrants. Those profiles with smaller R_{max} values and V_t values larger than 45 m s^{-1} are associated with Ivan (2004), Emily (2005), Katrina (2005), and Wilma (2005). The profiles with larger R_{max} radial distances are associated with Isabel (2003) and Frances (2004). It is interesting to note that the tropical cyclones with smaller R_{max} radii occurred over the higher sea-surface temperatures in the Caribbean Sea and Gulf of Mexico. By contrast, the tropical cyclones with larger R_{max} radii, but similar V_t values, occurred in the northwestern Atlantic. Once again, it is apparent that storms

with larger R_{max} radii tend to have larger V_t in the left quadrants. The Stage IIa decay of Isabel is exceptional in that it was associated with intensity fluctuations during its annular phase, but then a transition from an annular to more typical structure was a result of vertical wind shear (discussed further in Chapter IV).

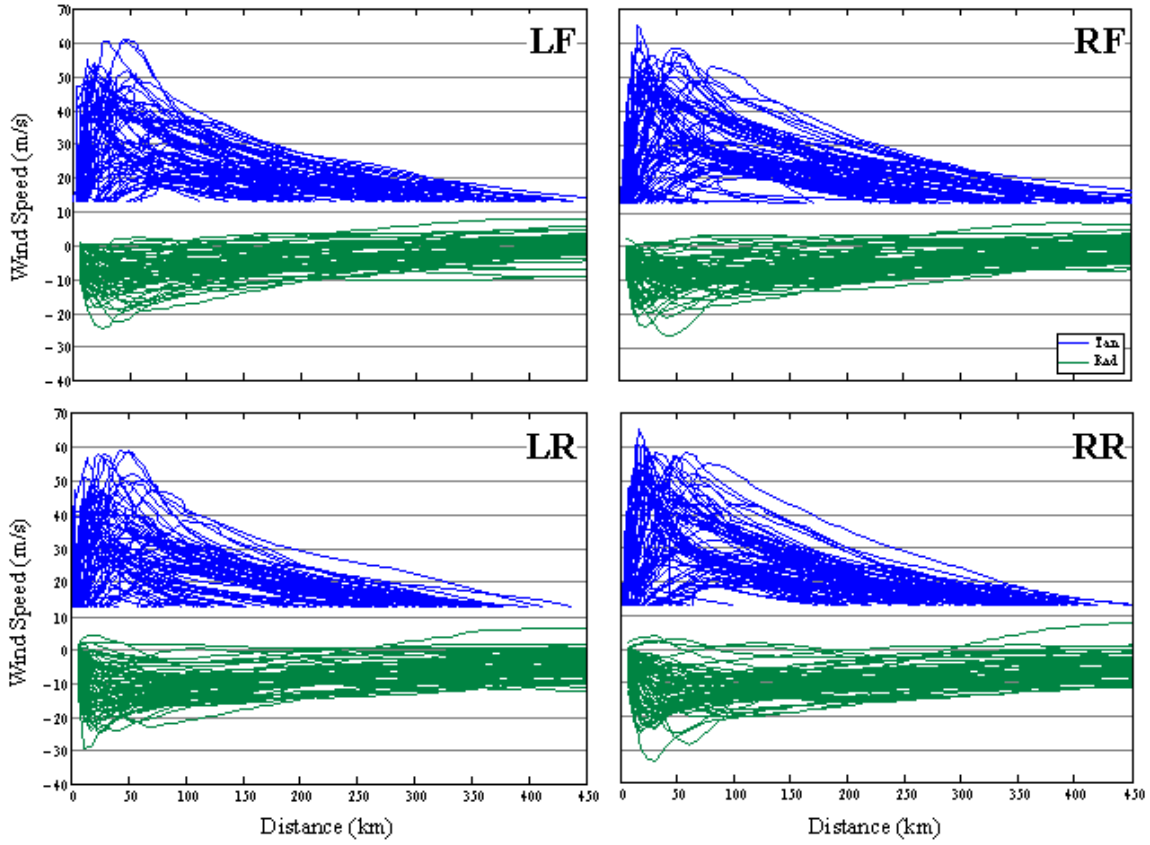

Figure 31 Observed tangential and radial wind profiles as in Fig. 23, except for Stage IIa decay.

A multivariate regression of V_t, R_{max}, and R_{34} (Fig. 32) in motion-relative coordinates during the Stage IIa decay phase of the secondary eyewall formation has a significantly different relationship from either the Stage II rapid or non-rapid intensification. That is, the most frequent distribution of outer-core radii (R_{34}) occurs with small variations in V_t. Recall from the definition of Stage IIa in Chapter III.B.1 that the decrease in V_t only has to be at least 10 kt. More importantly, the larger values of R_{max} during the Stage IIa decay are often paired with larger R_{34} values, i.e., a larger size cyclone. The R_{max} and R_{34} values have considerable variability during this stage, whereas the tropical cyclone intensity is only fluctuating by small amounts.

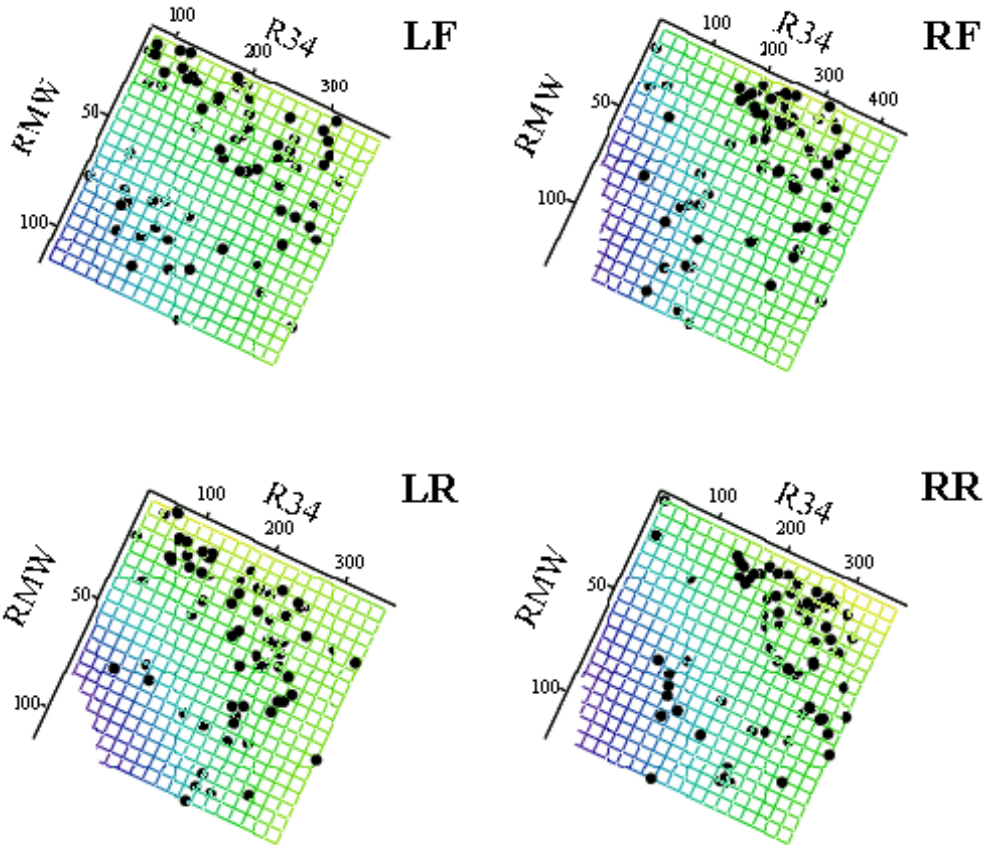

Figure 32 Multivariate regression of V_t , R_{max}, and R_{34} as in Fig. 24, except for Stage IIa decay.

The analysis of paired-parameters in motion-relative coordinates during the Stage IIa decay phase of the secondary eyewall formation is shown in Fig. 33. The comparison of V_t and R_{max} (Figs. 33a, d, g, and j) again have the expected association between smaller R_{max} radii and larger V_t values as predicted by conservation of angular momentum. Even though considerable scatter exists about the fitted curves, correlation coefficients for the LF, RF, RR, and LR quadrants (-0.615, -0.598, -0.578, and -0.585, respectively) are larger than for Stage II rapid or non-rapid intensification. Small correlations between V_t and R_{34} (Figs. 33b, e, h, and k) exist because the R_{34} radii variations occur with minimal changes of V_t, which is depicted by almost horizontal curve fits. Indeed, the correlation coefficients of 0.413 and 0.389 for the RF and RR quadrants are spurious as they are influenced by some very small R_{34} values

that do not represent secondary eyewall formations of a mature cyclone. This result is contrary to the expectations from the empirical wind distribution in Fig. 1. The displays of R_{max} versus R_{34} radial distances (Figs. 33c, f, i, and l) indicate two sets of R_{max} – a set of smaller (<45 km) values that are the pre-condition and a second set of larger (∼80 km) values that are the result of secondary eyewall formation. This results in a small correlation between the two variables.

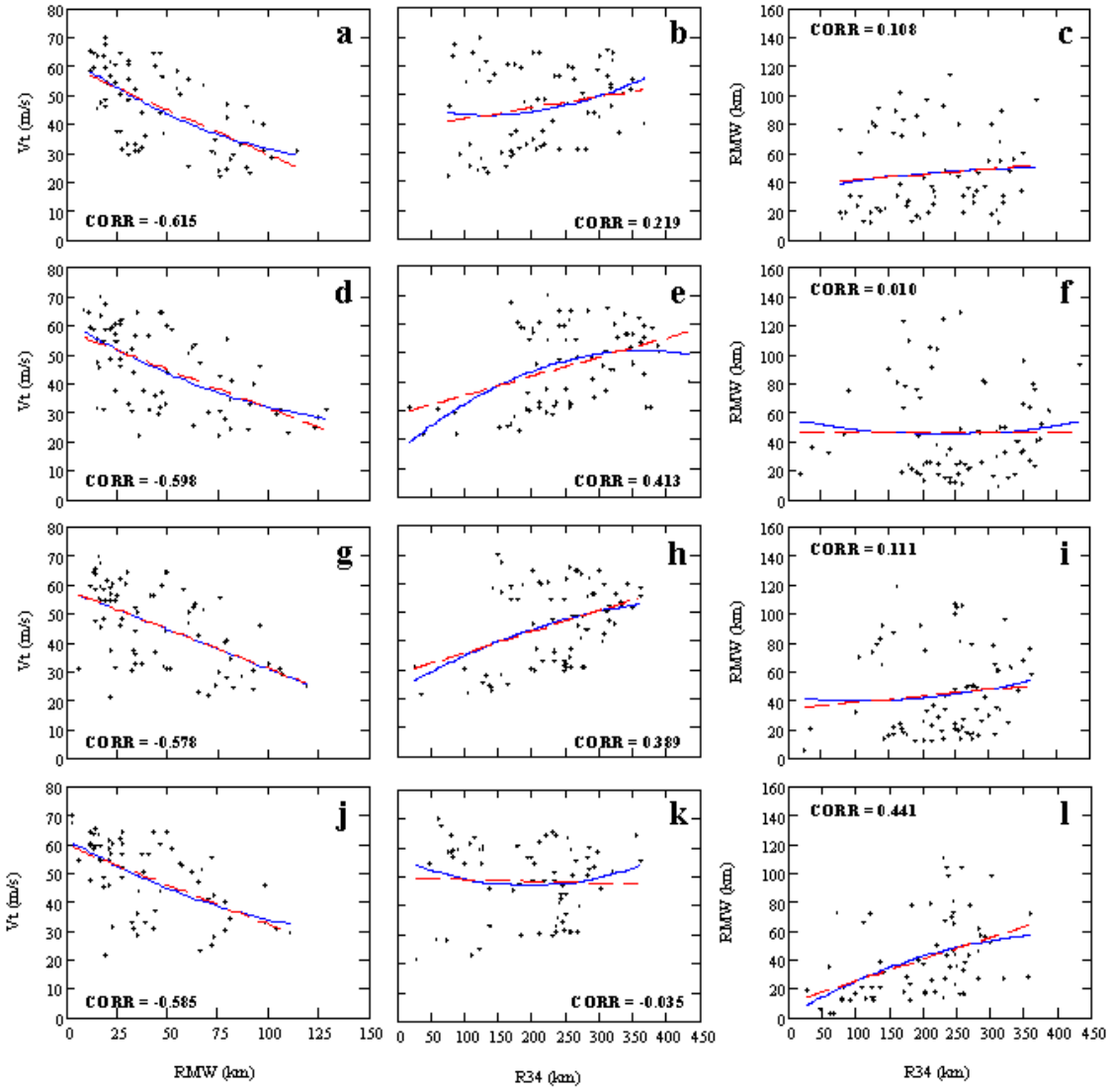

Figure 33 Pair-parameter regressions of V_t, R_{max}, and R_{34} as in Fig. 25, except for Stage IIa decay.

The exception is the 0.441 correlation for the LR quadrant. More details on the means and standard deviations for the R_{max} and R_{34} radial distances of Atlantic tropical cyclones in Stage IIa decay are provided in Tables 14–15 of Appendix E. While displays as in Figs. 33c, f, i, and l illustrate distinct groupings of R_{max} during the Stage IIa decay phase, the linkages to the corresponding R_{34} changes in individual cases are not revealed. Thus, case studies of the Stage IIa decay events will be presented in Chapter IV.

The probability density plot of azimuthal-average values for exponent x in the modified Rankine vortex for Stage IIa decay (Fig. 34a) has a mean of 0.58 and a standard deviation of 0.17 for a sample size n = 289.

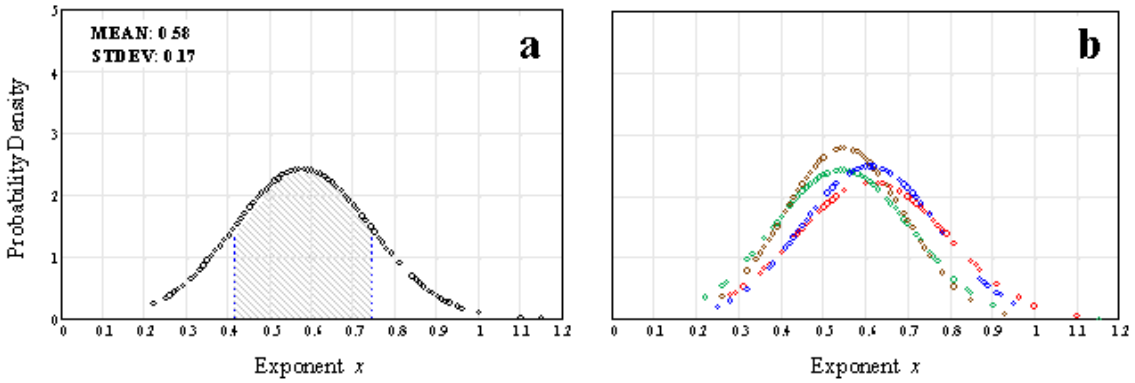

Figure 34 Probability density plots as in Fig. 26, except for Stage IIa decay.

The range of expected values of exponent x within a standard deviation of the mean (hashed region in Fig. 34a) is 0.41–0.74, which is about 17 percent smaller than for Stage II. In Fig. 34b, the probability density plots of the motion-relative quadrant values for exponent x in the modified Rankine vortex once again indicate a greater probability of larger (smaller) R_{34} radii in the right (left) quadrants of the tropical cyclone. The differences in the mean values of exponent x between the left and right quadrants for Stage IIa decay are similar to those for Stage II non-rapid intensification. However, there is a decrease in the expected range of values for exponent x for all quadrants compared to the Stage II non-rapid intensification. Indeed, the standard deviations are smaller (0.14–0.18, Table 3) compared to the 0.21 standard deviations for all quadrants during Stage II non-rapid intensification. For this stage, nearly 100 percent of the outer-core structure asymmetries can be explained by the addition or subtraction of the average tropical cyclone motion vector, and thus suggests an

axisymmetric outer-core structure prevails during Stage IIa decay. Contrary to Stage II non-rapid and rapid intensification, a comparison of the mean and median values in Table 3 indicates a normal (symmetric) distribution of values for exponent x.

Table 3 Modified Rankine vortex exponents for Stage IIa decay.

QUADRANT	n	MEAN	MEDIAN	STDEV	MEAN $\pm$ STDEV
LF	69	0.62	0.64	0.18	0.44–0.80
RF	73	0.54	0.53	0.17	0.37–0.71
RR	75	0.55	0.54	0.14	0.41–0.69
LR	69	0.61	0.62	0.16	0.45–0.77

Observed profiles of tangential and radial winds in motion-relative coordinates for Stage IIa non-rapid intensification that follows the decay phase (see Fig. 9c) are shown in Fig. 35. The profiles indicate that two distinct distributions exist: tropical cyclones with smaller R_{max} radii (but broader than previous stages of development) with larger values of V_t that are fairly axisymmetric; and tropical cyclones with large R_{max} radii with smaller V_t values that are more asymmetric with the maximum wind speeds in the right quadrants. Those profiles with smaller R_{max} radial distances and V_t values greater than 45 m s^{-1} are associated with Isabel (2003), Charley (2004), Frances (2004), Ivan (2004), Jeanne (2004), Emily (2005), Katrina (2005), and Wilma (2005). The broad profiles with very large R_{max} radial distances are associated with Isabel (2003) along the eastern seaboard of the United States following a transition in its structure (discussed further in Chapter IV) and Wilma (2005) following landfall over the Yucatan Peninsula. It is noteworthy that while asymmetries were present during Stage IIa decay, it is hypothesized that the process of axisymmetrization following secondary eyewall formation will balance the structure between the left and right storm quadrants.

A multivariate regression of V_t, R_{max}, and R_{34} (Fig. 36) in motion-relative coordinates for Stage IIa non-rapid intensification that follows the decay phase displays a significant amount of variability that has some similarity to the variability during Stage II non-rapid intensification (Fig. 24). This regression suggests that three surface wind profile distributions exist.

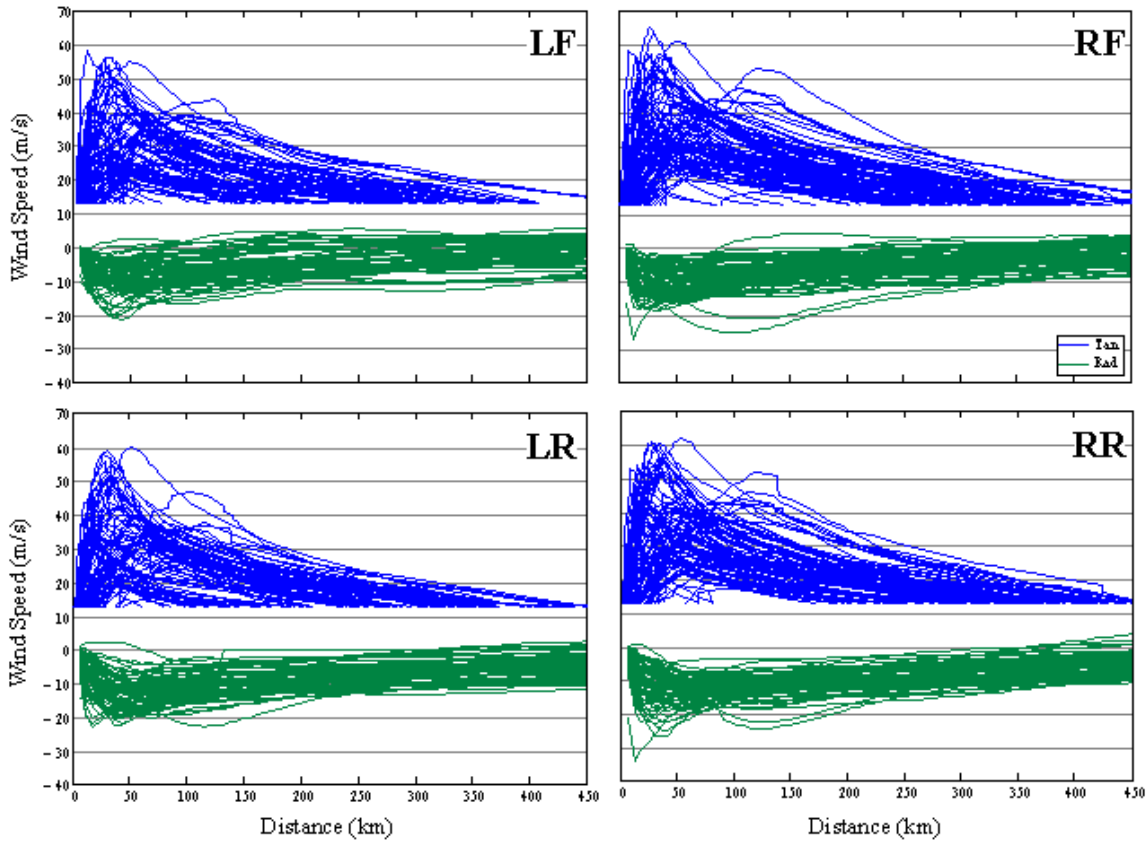

Figure 35 Observed tangential and radial wind profiles as in Fig. 23, except for Stage IIa non-rapid intensification.

In the first distribution, the R_{34} radii (from 180 km to <400 km along axis in upper right portion of each plot in Fig. 36) are positively correlated with larger magnitudes of intensity (V_t), i.e., large (small) values of R_{34} are paired with large (small) values V_t, while the variation in R_{max} is small. In the second distribution, the values of R_{max} and R_{34} are positively correlated, whereas there is minimal spread in the observed tropical cyclone intensity (V_t). The final distribution includes very large R_{max} (>50 km) cases where larger R_{max} values are coupled with larger R_{34} and V_t values.

The analysis of paired-parameters in motion-relative coordinates for Stage IIa non-rapid intensification of tropical cyclone development is shown in Fig. 37. The comparison of V_t and R_{max} (Figs. 37a, d, g, and j) appears to have two trends. For R_{max} <50 km, decreases in R_{max} values are associated with increases of V_t as predicted by conservation of angular momentum.

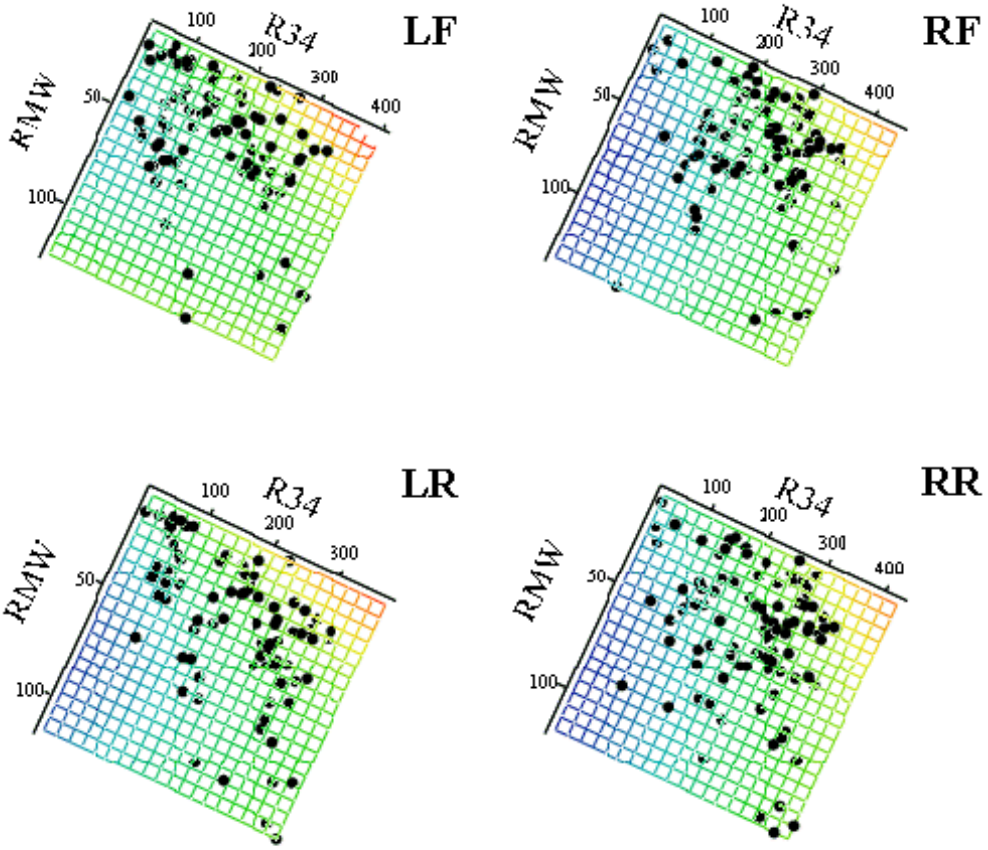

Figure 36 Multivariate regression of V_t , R_{max}, and R_{34} as in Fig. 24, except for Stage IIa non-rapid intensification.

For R_{max} >50 km, the intensities may be nearly the same or even larger at larger R_{max} (Figs. 37a and j), which may be associated with annular-type cyclones. Thus, the correlation coefficients for the LF, RF, RR, and LR quadrants (-0.204, -0.226, -0.188, and -0.227, respectively) are not large due to these larger R_{max} values. However, the comparison of V_t and R_{34} (Figs. 37b, e, h, and k) indicates that increases in R_{34} radii are associated with increases in V_t, which is in general agreement with the expectations from the empirical wind distribution in Fig. 1 or the axisymmetric models that would suggest an increase in outer winds (R_{34}) during the intensification following the Stage IIa decay phase. The correlation coefficients for the LF, RF, RR, and LR quadrants (0.548, 0.687, 0.640, and 0.479, respectively) represent a linear relationship between V_t and R_{34} and are similar to those observed in Stage II non-rapid

intensification. This is evidence that the spin-up of the outer-core vortex following a secondary eyewall formation leads to a larger size vortex.

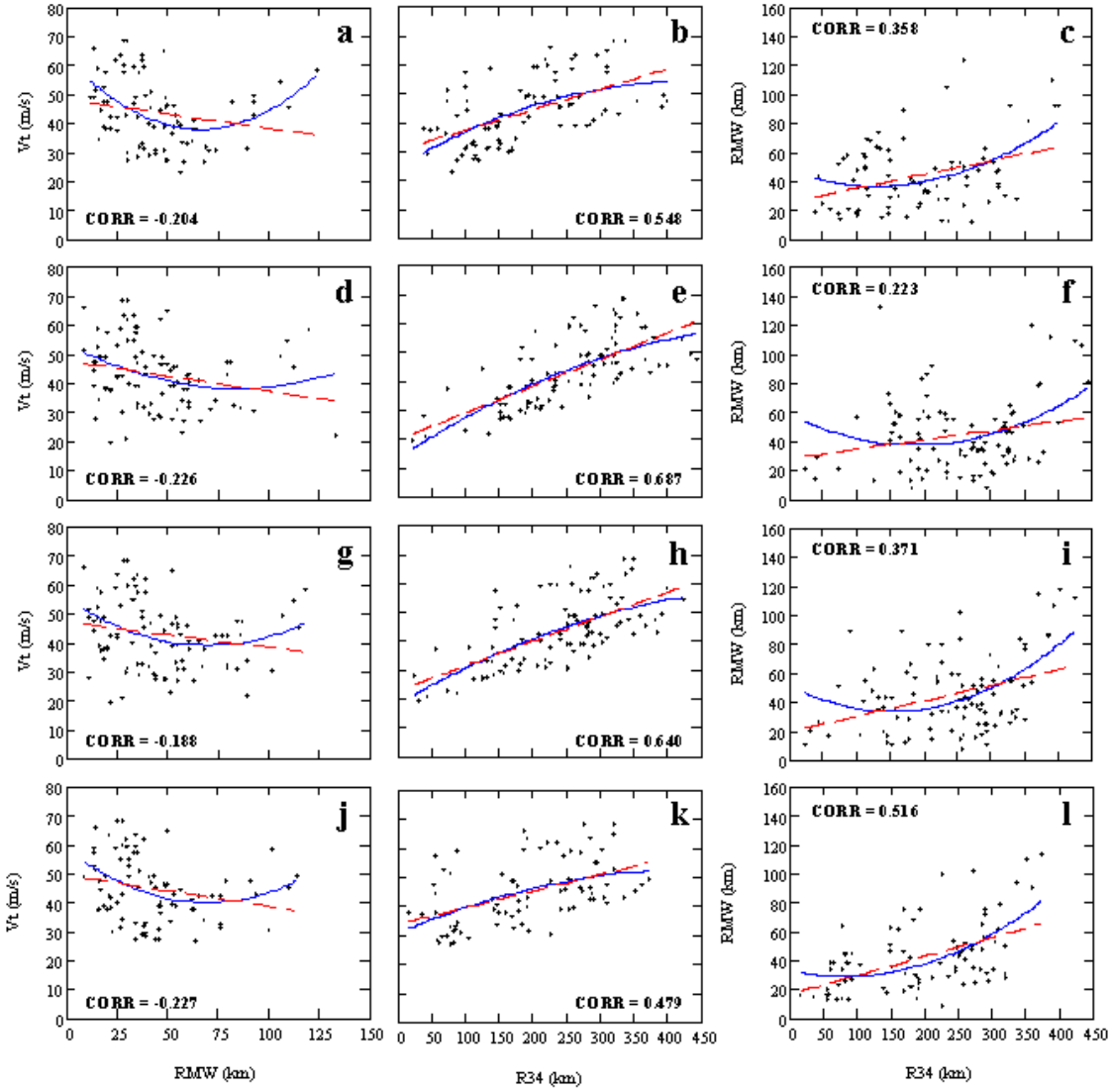

Figure 37 Pair-parameter regressions of V_t, R_{max}, and R_{34} as in Fig. 25, except for Stage IIa non-rapid intensification.

The comparison of R_{max} and R_{34} radial distances (Figs. 37c, f, i, and l) reveals two trends. Within R_{max} <50 km, little correlation exists. For larger R_{max} values that are associated with secondary eyewalls, the larger R_{34} values are more evident. Since a majority of the points are in the second category, a higher correlation exists between the two parameters (0.358, 0.223, 0.371, and 0.516 for the LF, RF, RR, and LR

quadrants, respectively) than in the earlier stages discussed above. This association between expansions in the outer-core structure (R_{34}) with expansion of the inner-core structure (R_{max}) during Stage IIa non-rapid intensification will be further explored with case studies in Chapter IV. More details on the means and standard deviations for the R_{max} and R_{34} radial distances of Atlantic tropical cyclones in Stage IIa non-rapid intensification are provided in Tables 16–17 of Appendix E.

The probability density plot of azimuthal-average values for exponent x in the modified Rankine vortex for Stage IIa non-rapid intensification (Fig. 38a) has a mean of 0.58 and a standard deviation of 0.17 for a sample size n = 353.

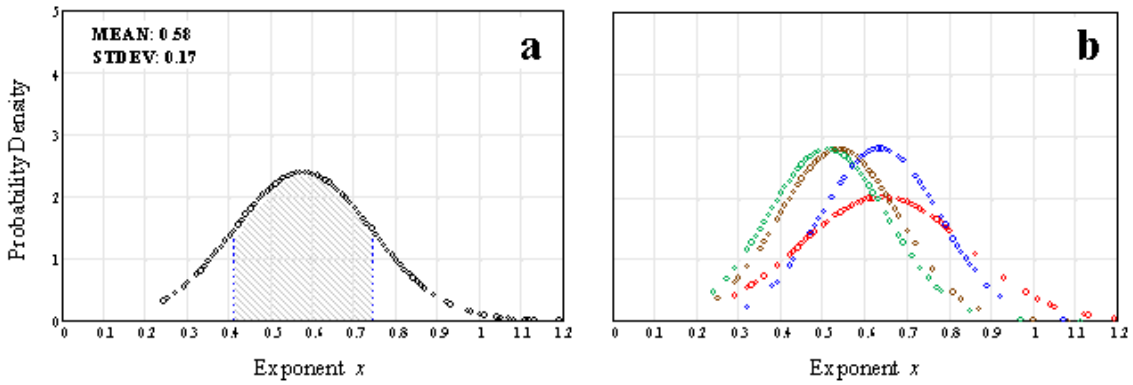

Figure 38 Probability density plots as in Fig. 26, except for Stage IIa non-rapid intensification.

The range of expected values of exponent x within a standard deviation of the mean (hashed region in Fig. 38a) is 0.41–0.74, which is the same as for Stage IIa decay. In Fig. 38b, the probability density plots of the motion-relative quadrant values for exponent x in the modified Rankine vortex indicate a greater probability of larger (smaller) R_{34} radii in the right (left) quadrants of the tropical cyclone. The difference in the mean values of exponent x between the left and right quadrants appear to be a little larger for this stage of the storm life cycle than for Stage II non-rapid intensification. Indeed, only about 60 percent of the outer-core structure asymmetries can be explained by the addition or subtraction of the average tropical cyclone motion vector. In Table 4, the decrease in the standard deviations for all quadrants (except the LF) represents an approximate 33 percent reduction in the range of the expected values for exponent x within a standard deviation of the mean compared to the Stage II non-rapid intensification (depicted by the increase in probability density in Fig. 38b). Increased variability in the value of exponent x (standard deviation of 0.20

compared to 0.14 for other quadrants, see Table 4) is apparent for the LF quadrant in Fig. 38b. As with Stage II, a comparison of the mean and median values indicates a slightly right-skewed distribution of values for exponent x during Stage IIa non-rapid intensification.

Table 4 Modified Rankine vortex exponents for Stage IIa non-rapid intensification.

QUADRANT	n	MEAN	MEDIAN	STDEV	MEAN $\pm$ STDEV
LF	78	0.64	0.60	0.20	0.44–0.84
RF	94	0.51	0.49	0.14	0.37–0.65
RR	98	0.54	0.54	0.14	0.40–0.68
LR	80	0.64	0.61	0.14	0.50–0.78

Observed profiles of tangential and radial winds in motion-relative coordinates for Stage IIa rapid intensification that follows the decay phase (see Fig. 9c) are shown in Fig. 39. Compared to the non-rapid intensification cases in Fig. 35, these cases tend to have smaller R_{max} radii of 50 km or less and more axisymmetric R_{34} radii. These profiles have similar V_t, larger R_{max} and R_{34} radii, and greater symmetry of the inner- and outer-core structures as in the Stage II rapid intensification (Fig. 27). It is also interesting to note that the radial inflow in this stage is 5–10 m s^{-1} greater than for Stage II rapid intensification. The profiles with V_t values greater than 45 m s^{-1} are associated with Charley (2004), Frances (2004), Ivan (2004), Dennis (2005), Emily (2005), Katrina (2005), Rita (2005), and Wilma (2005). Rapid intensification during this stage generally occurred following landfall or near-core interaction with land. In two cases (Frances over the northwestern Atlantic and Ivan over the north Caribbean Sea), the rapid intensification occurred following secondary eyewall formation.

A multivariate regression of V_t, R_{max}, and R_{34} (Fig. 40) in motion-relative coordinates for Stage IIa rapid intensification that follows the decay phase reveals two surface wind distributions. In the first distribution, the R_{34} radii (from 150 km to >350 km along axis in upper right portion of each plot in Fig. 40) are positively correlated with larger magnitudes of intensity (V_t) while the variation in R_{max} is small. In the second distribution, the values of R_{max} and R_{34} are positively correlated, whereas there is minimal spread in the observed tropical cyclone intensity (V_t).

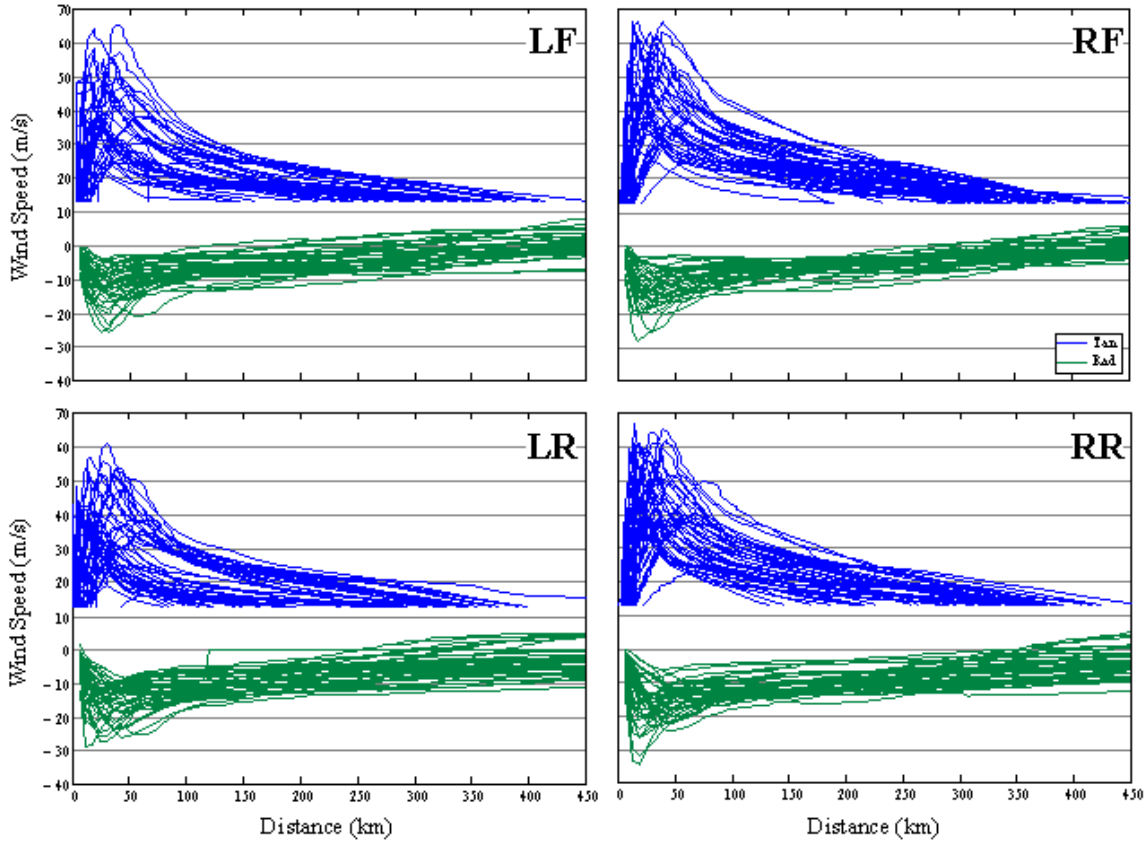

Figure 39 Observed tangential and radial wind profiles as in Fig. 23, except for Stage IIa rapid intensification.

The wind profiles in the RR and LR quadrants (Fig. 40) appear to be predominately from the second distribution, which is markedly different from the earlier stages discussed.

The analysis of paired-parameters in motion-relative coordinates for Stage IIa rapid intensification that follows the decay phase is shown in Fig. 41. The comparison of V_t and R_{max} (Figs. 41a, d, g, and j) indicates the small range of R_{max} values over which these rapid intensification events are observed to occur. Within this small range, smaller R_{max} radii are associated with larger V_t values, but with a more linear relationship rather than as predicted by conservation of angular momentum. Nevertheless, correlation coefficients for the LF, RF, RR, and LR quadrants (-0.441, -0.460, -0.356, and -0.418, respectively) are about twice as large as for the Stage IIa non-rapid intensification sample in Fig. 37.

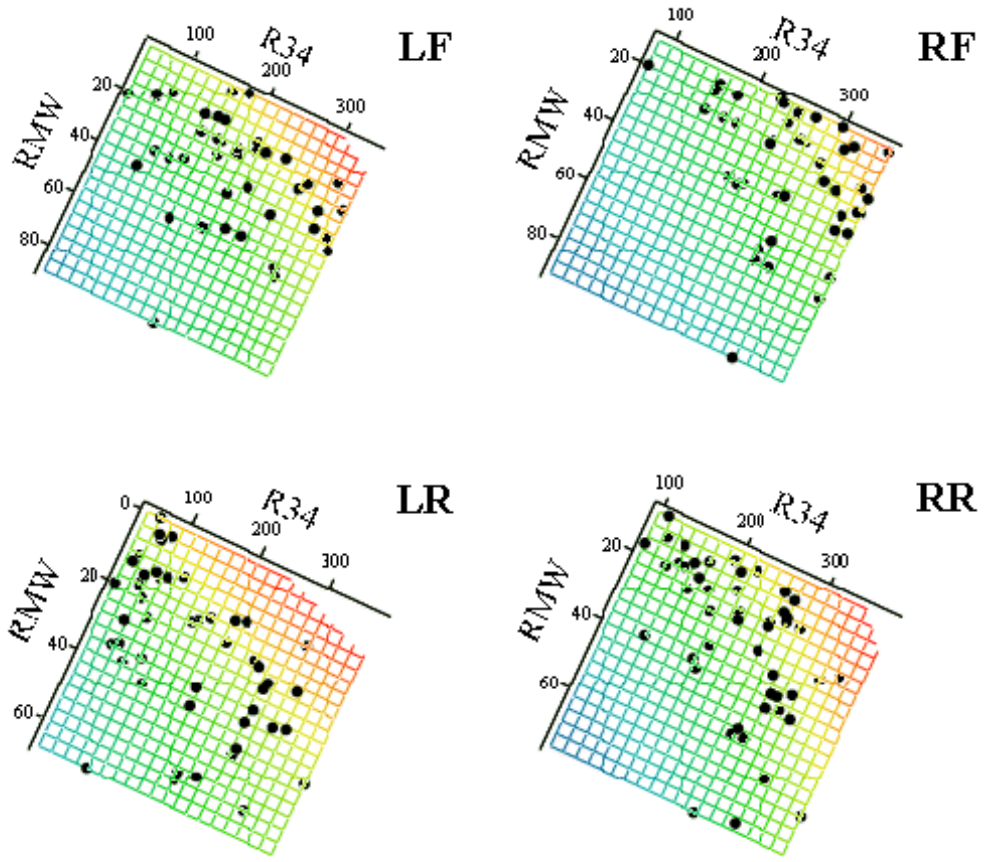

Figure 40 Multivariate regression of V_t , R_{max}, and R_{34} as in Fig. 24, except for Stage IIa rapid intensification.

The comparison of V_t and R_{34} (Figs. 41b, e, h, and k) indicates that increases in R_{34} radii are associated with increases in V_t for the front quadrants (Figs. 41b and e), and thus are generally in agreement with the expectations from the empirical wind distribution in Fig. 1 or the axisymmetric models that would suggest an increase in outer winds (R_{34}) during intensification. However, the association of the large R_{34} radii in the rear quadrants (Figs. 41h and k) with the V_t values is somewhat weaker. This difference in relationships is evident in the correlation coefficients for the LF, RF, RR, and LR quadrants (0.512, 0.502, 0.203, and 0.291, respectively).

The comparison of R_{max} and R_{34} radial distances (Figs. 41c, f, i, and l) is limited by the small range of R_{max} values. Nevertheless, there is a weak association in the rear quadrants (Figs. 41i and l) where the correlation coefficients for the RR and

LR quadrants are 0.588 and 0.496, respectively. Thus, expansions in the outer-core structure (R_{34}) in the rear storm quadrants have some association with expansion of the inner-core structure (R_{max}) during Stage IIa rapid intensification following the decay phase. More details on the means and standard deviations for the R_{max} and R_{34} radial distances of Atlantic tropical cyclones in Stage IIa rapid intensification are provided in Tables 18–19 of Appendix E.

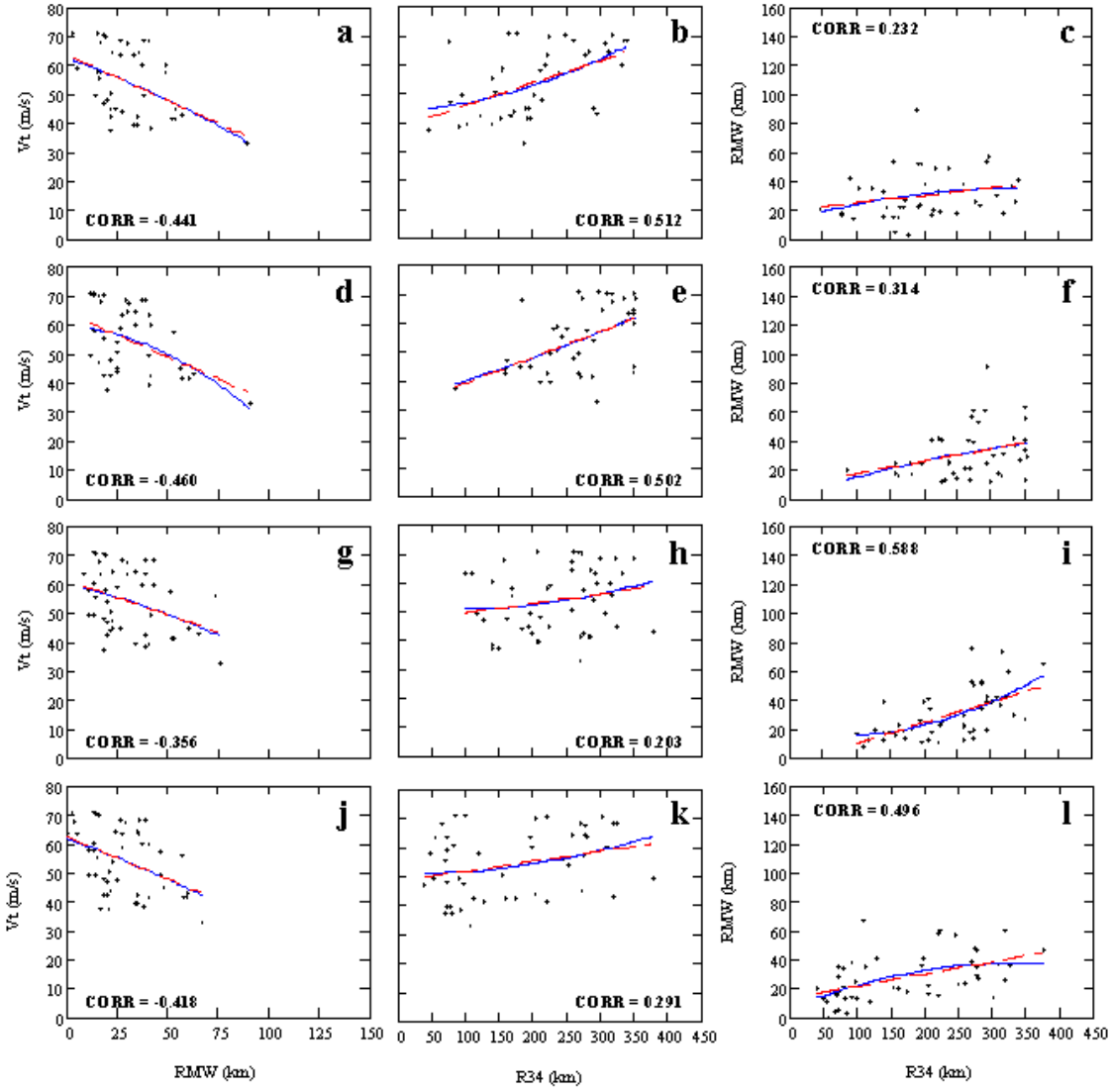

Figure 41 Pair-parameter regressions of V_t, R_{max}, and R_{34} as in Fig. 25, except for Stage IIa rapid intensification.

The probability density plot of azimuthal-average values for exponent x in the modified Rankine vortex for Stage IIa rapid intensification (Fig. 42a) has a mean of 0.57 and a standard deviation of 0.13 for a sample size n = 175.

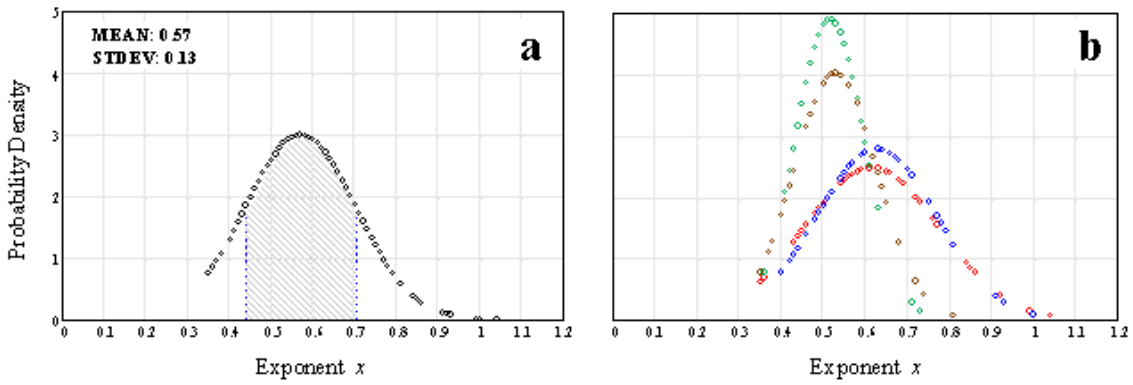

Figure 42 Probability density plots as in Fig. 26, except for Stage IIa rapid intensification.

The range of expected values of exponent x within a standard deviation of the mean (hashed region in Fig. 42a) is 0.44–0.70, which is about 37 percent smaller than for Stage II. In Fig. 42b, the probability density plots of the motion-relative quadrant values for exponent x in the modified Rankine vortex again indicate a greater probability of larger (smaller) R_{34} radii in the right (left) quadrants of the tropical cyclone. Stage IIa rapid intensification appears to have a similar difference in the mean values of exponent x between the left and right quadrants as for Stage IIa non-rapid intensification, but the expected range of values for exponent x in the right quadrants appear to be substantially smaller than for the left quadrants. Indeed, the range of values for exponent x in the RF and RR quadrants (0.44–0.60 and 0.43–0.63, respectively, Table 5) are only about half of the range values for the left quadrants. This suggests that the structures of the left and right quadrants are significantly different, and thus structure asymmetries may be associated with rapid intensification of a tropical cyclone. For this stage, about 70 percent of the outer-core structure asymmetries can be explained by the addition or subtraction of the average tropical cyclone motion vector. In Table 5, the decrease in the standard deviation for the right quadrants represent an approximate 40 percent reduction in the range of the expected values for exponent x within a standard deviation of the mean compared to the left quadrants (depicted by the increase in probability density in Fig. 42b). Contrary to Stage IIa non-rapid intensification, a comparison of the mean and median values indicates a slightly right-

skewed distribution of values for exponent x in the left quadrants only during Stage IIa rapid intensification.

Table 5 Modified Rankine vortex exponents for Stage IIa rapid intensification.

QUADRANT	n	MEAN	MEDIAN	STDEV	MEAN $\pm$ STDEV
LF	41	0.62	0.57	0.16	0.46–0.78
RF	41	0.52	0.52	0.08	0.44–0.60
RR	48	0.53	0.52	0.10	0.43–0.63
LR	42	0.63	0.59	0.14	0.49–0.77

Observed profiles of tangential and radial winds in motion-relative coordinates for the Stage III decay of Atlantic tropical cyclones are shown in Fig. 43. Although somewhat obscured by the large number of profiles for this stage, two types of profiles with similar R_{34} values, but vastly different R_{max} radii, may be discerned. In the more frequent profile set with R_{max} values around 25–30 km and large values of V_t, wind speeds decrease slowly with radius. The profiles in this first set are comprised of most of the tropical cyclones listed in Tables 7–9 of Appendix A. The somewhat obscured profiles in Fig. 43 have similar R_{34} values as with the first set, but the V_t values range from 20–45 m s^{-1} with R_{max} radii of 65–80 km. These profiles for the second set are related to tropical cyclones along the east coast of the United States that have experienced vertical wind shear (discussed further in Chapter IV). The storms in this category for part of their life cycle during the 2003–2005 Atlantic hurricane seasons were Fabian (2003), Isabel (2003), Franklin (2005), and Ophelia (2005). These profiles also have some inner- and outer-core asymmetries with larger wind speeds in the RF quadrant. The asymmetries may result from increasing vertical wind shear that is often present during the later portion of the life cycle.

A multivariate regression of V_t, R_{max}, and R_{34} (Fig. 44) in motion-relative coordinates for the Stage III decay of Atlantic tropical cyclones suggests that there are two surface wind distributions. In the first distribution, larger values of R_{max} are coupled with smaller R_{34} and V_t values. In the second distribution, the R_{max} and R_{34} radii are positively correlated, i.e., smaller R_{max} values are coupled with smaller values of R_{34}, with minimal variation in the storm intensity (V_t).

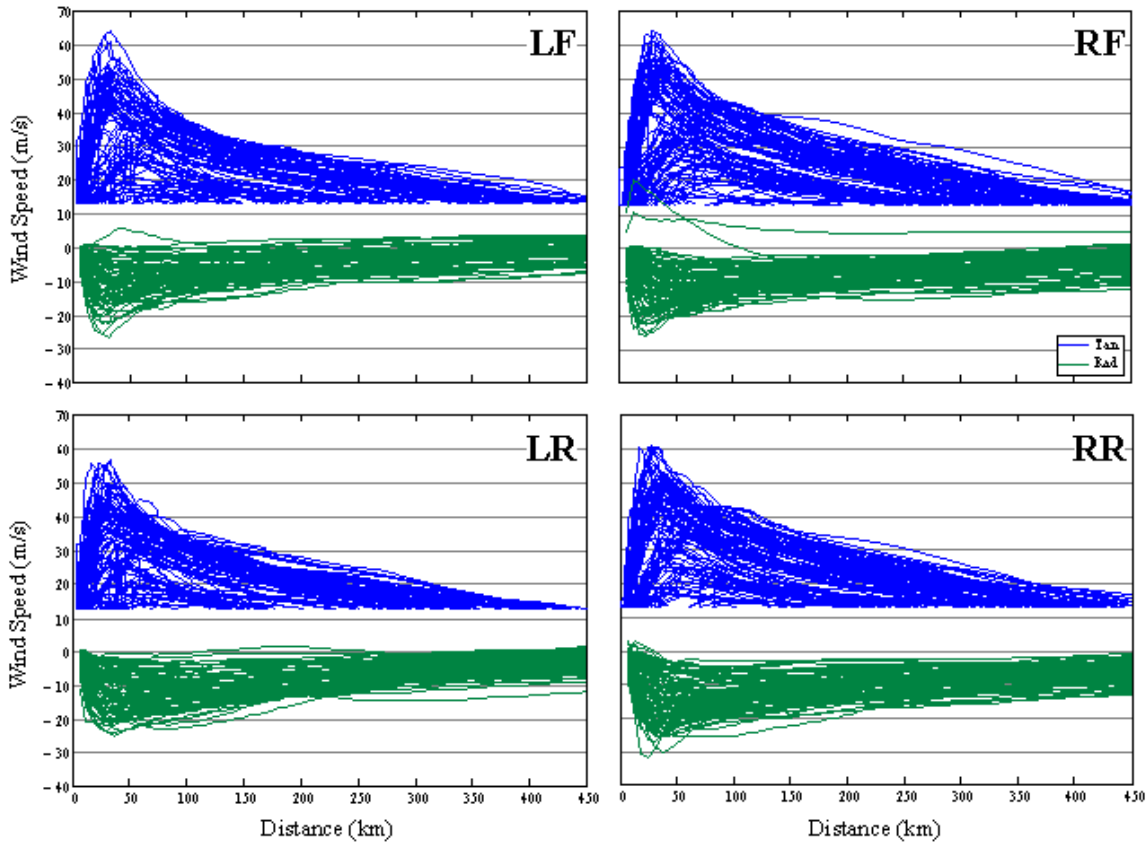

Figure 43 Observed tangential and radial wind profiles as in Fig. 23, except for Stage III decay.

The analysis of paired-parameters in motion-relative coordinates for the Stage III decay of Atlantic tropical cyclones is shown in Fig. 45. The comparison of V_t and R_{max} (Figs. 45a, d, g, and j) depicts the expected relationship in which smaller values of R_{max} are associated with larger values of V_t as predicted by conservation of angular momentum. The correlation coefficients for the LF, RF, RR, and LR quadrants (-0.389, -0.430, -0.493, and -0.462, respectively) are indicative of a large amount of spread about the fitted curves. Note in particular some quite small V_t values for R_{max} $<$50 km. The fitted curves in the comparison of V_t and R_{34} (Figs. 45b, e, h, and k) seem to indicate that smaller R_{34} radii are associated with smaller V_t values, and thus are in general agreement with the expectations from the empirical wind distribution in Fig. 1 or the axisymmetric models that would suggest an decrease in outer winds (R_{34}) during weakening of storm intensity. Indeed, the correlation coefficients for the LF, RF, RR, and LR quadrants (0.738, 0.758, 0.734, and 0.706, respectively) indicate a

linear relationship between V_t and R_{34}, in fact the best for all stages of tropical cyclone development. An alternate interpretation is that two categories of cyclones exist with large (>200 km) R_{34} values in conjunction with V_t >45 m s^{-1} or with small (<200 km) R_{34} values in conjunction with V_t <40 m s^{-1}. If these two categories are examined independently, only a relatively small dependence on V_t exists.

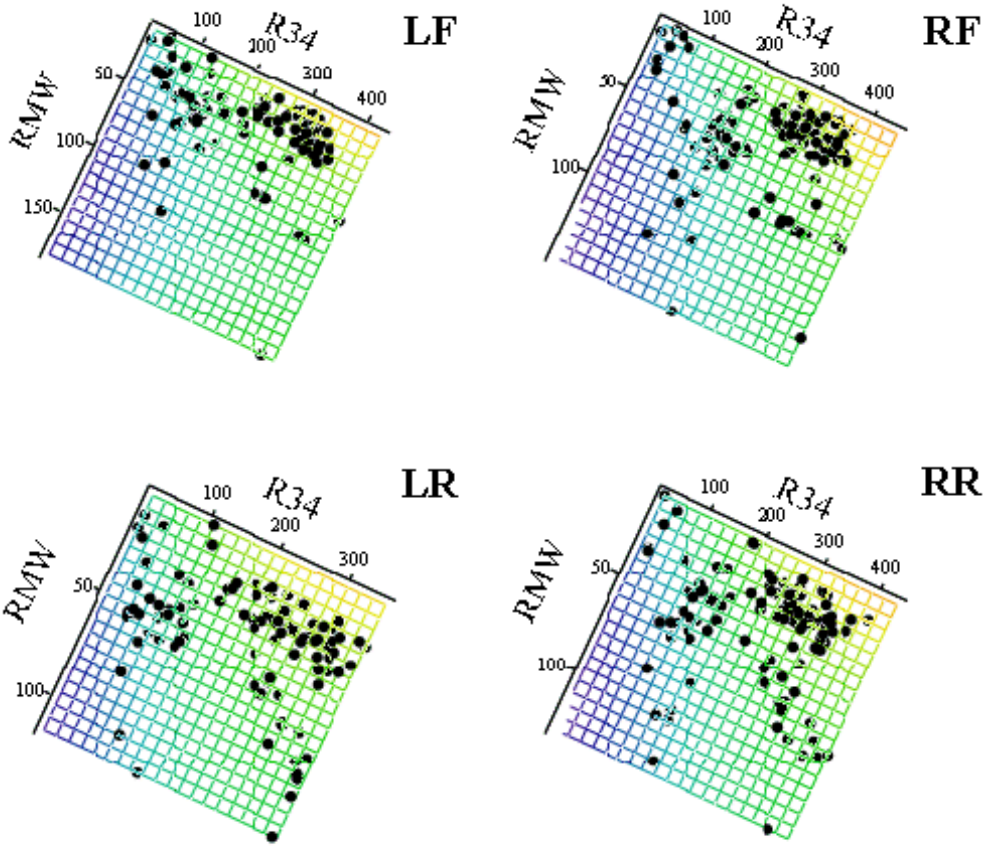

Figure 44 Multivariate regression of V_t , R_{max}, and R_{34} as in Fig. 24, except for Stage III decay.

The comparison of R_{max} and R_{34} radial distances (Figs. 45c, f, i, and l) reveals a lack of correlation between these two variables. Thus, changes to the outer-core structure (R_{34}) appear to be unrelated to inner-core structure changes (R_{max}) during Stage III decay. This lack of connection between the outer-core and inner-core winds during the decay stage certainly invalidates the use of the empirical wind profiles. Case studies in Chapter IV will explore this aspect. More details on the means and

standard deviations for the R_{max} and R_{34} radial distances of Atlantic tropical cyclones in Stage III decay are provided in Tables 20–21 of Appendix E.

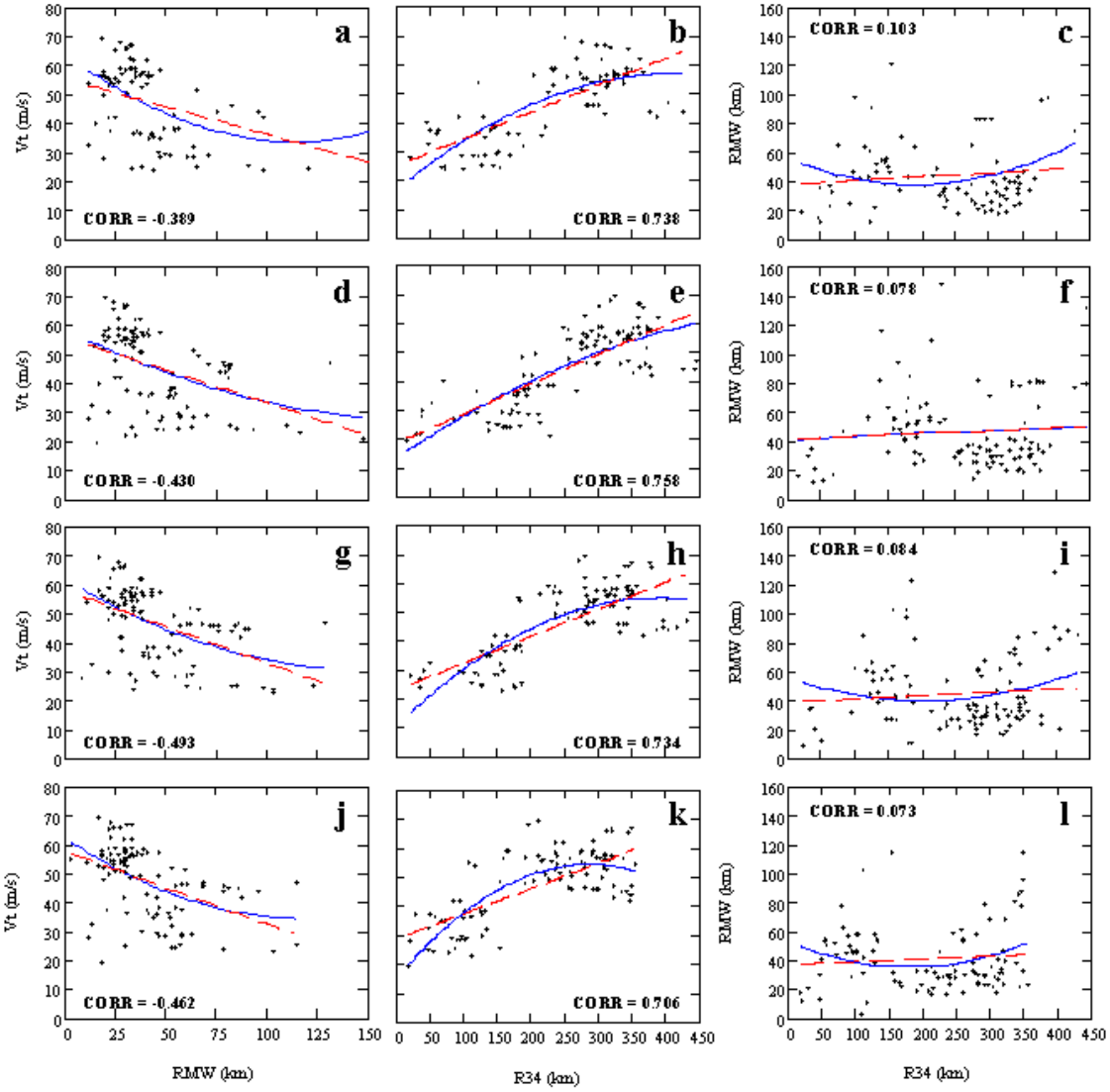

Figure 45 Pair-parameter regressions of V_t, R_{max}, and R_{34} as in Fig. 25, except for Stage III decay.

The probability density plot of azimuthal-average values for exponent x in the modified Rankine vortex for Stage III decay (Fig. 46a) has a mean of 0.58 and a standard deviation of 0.13 for a sample size n = 379. The range of expected values of exponent x within a standard deviation of the mean (hashed region in Fig. 46a) is 0.45–0.71, which is similar to Stage IIa rapid intensification.

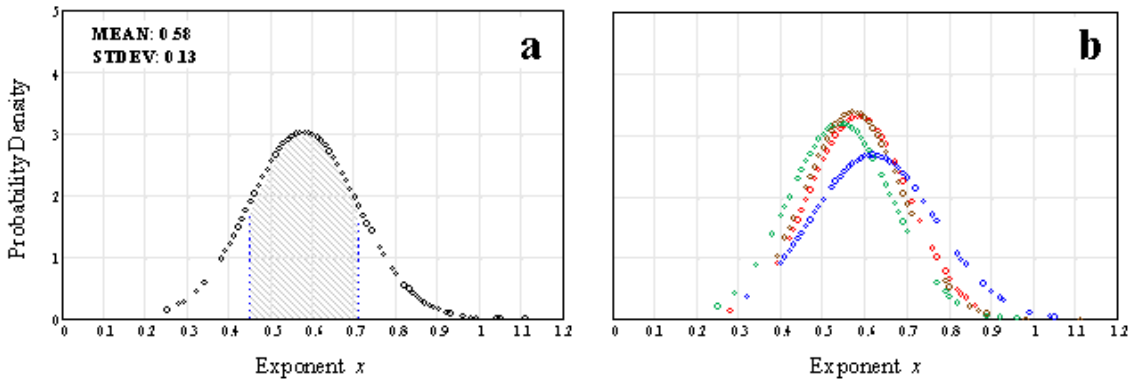

Figure 46 Probability density plots as in Fig. 26, except for Stage III decay.

In Fig. 46b, the probability density plots of the motion-relative quadrant values for exponent x in the modified Rankine vortex suggests greater symmetry between all quadrants of the tropical cyclone. For Stage III decay, the mean values of exponent x in the LF and RR quadrants appear to be similar. Indeed, the mean values for exponent x in the LF and RR quadrants are 0.58 and 0.57, respectively, whereas the mean values for exponent x in the RF and LR quadrants are 0.54 and 0.60, respectively (Table 6). Thus the outer-core structure asymmetries for this stage can not explained by the addition or subtraction of the average tropical cyclone motion vector alone. In fact, the addition (subtraction) of the storm motion vector to (from) the right (left) quadrant means in Table 6 suggests that the LF (RR) quadrant has the largest (smallest) R_{34} size, and thus is contrary to what has been observed for all other stages of the life cycle. The changes in outer-core structure asymmetries for Stage III decay may result from the vertical wind shear that often present during the later portion of the storm life cycle. As for Stage IIa decay, a comparison of the mean and median values indicates a normal (symmetric) distribution of values for exponent x.

Table 6 Modified Rankine vortex exponents for Stage III decay.

QUADRANT	n	MEAN	MEDIAN	STDEV	MEAN $\pm$ STDEV
LF	77	0.58	0.57	0.12	0.46–0.70
RF	102	0.54	0.54	0.13	0.41–0.67
RR	105	0.57	0.55	0.12	0.45–0.69
LR	92	0.62	0.60	0.15	0.47–0.77

In summary, objective analyses of the 10 m surface wind speed based on the H*Wind program for the different stages of the life cycle (Fig. 9) of Atlantic tropical cyclones during the 2003–2005 hurricane season were conducted. The primary focus has been on the outer-core structure changes or size changes represented by the R_{34} radius. Contrary to the simple conceptual model that intensification is accompanied by increases in R_{34}, about 30 percent of intensifying cyclones had decreasing values of R_{34} (Fig. 12). During the decay stage (Fig. 13b), about one half of the cyclones had decreases in R_{34} and about one quarter had increases in R_{34}, which then differs from the forecaster rule of thumb that tropical cyclones expand in size during the decay. Box plots of the R_{34} radii document significantly larger R_{34} values progressing from the Tropical Storm stage to the Category 1 hurricanes and then to the Category 2 hurricanes (Fig. 21). Further intensification does not lead to significantly larger R_{34} values; indeed, a small sample of Category 5 hurricanes appears to have smaller R_{34} values.

Various assessments of the characterizations of the inner-core vortex in terms of R_{max} and V_t, and the outer-core vortex in terms of R_{34} have been made for different stages of the life cycle. Although with considerable scatter, the R_{max} and V_t have the expected relationship that smaller R_{max} values are associated with larger V_t near the center, and especially for rapid intensification cases. The relationship of the R_{34} to the V_t and R_{max} is more complex and varies with stage of development. For the Stage II intensification and for R_{34} <150 km, the R_{34} has little association with V_t, but has larger R_{34} values for larger R_{max}. For R_{34} >150 km, larger R_{34} values are associated with larger V_t, but not larger R_{max}. During the decay and re-intensification Stage IIa, the above relationship for R_{34} <150 km are generally valid. For R_{34} >150 km, larger R_{34} values were associated with larger R_{max} values, which may be associated with a secondary eyewall formation. Although the Stage III decay had the largest correlation between V_t and R_{34}, this sample had different characteristics for R_{34} <150 km and R_{34} >150 km.

An assessment of the azimuthal-average values for exponent x in the modified Rankine vortex of Eq. (20) for the different stages of the life cycle (Figs. 26, 30, 34, 38, 42, and 46) yield a mean value of 0.56–0.58, whereas the standard deviation decreases from 0.21 to 0.13 as the storm progresses from Stage II (∼0.21) to Stage IIa decay and non-rapid intensification (0.17), and then to Stage IIa rapid intensification and Stage III decay (0.13). For the Stage II and Stage IIa periods of the life cycle,

the right (left) quadrant outer-core structures (as measured using R_{34}) were generally larger (smaller), whereas the LF (RR) quadrant had the largest (smallest) R_{34} values for the Stage III decay. Nearly 100 percent of the outer-core structure asymmetries can be accounted for by the addition or subtraction of the average tropical cyclone motion vector during Stage IIa decay. For the Stage II non-rapid intensification, and Stage IIa non-rapid and rapid intensification, only a portion (80 percent, 60 percent, and 70 percent, respectively) of the outer-core structure asymmetries can be explained by the addition or subtraction of the storm motion vector. The greatest amount of outer-core structure asymmetries were observed for Stage II rapid intensification since only 40 percent of the asymmetries can be explained by the addition or subtraction of the storm motion vector. The smaller mean and the $\sim$30 percent reduction in the standard deviation for the right quadrants compared to the left quadrants for the rapid intensification phases of Stage II and Stage IIa indicate a greater probability of larger R_{34} sizes on the right side of the tropical cyclone for these stages of the life cycle and may be a contributing factor in rapid intensification.

The biggest take-away from this section is the large variability between the Atlantic tropical cyclone inner- and outer-core structure characteristics. Simple wind profile relationships will not be adequate to represent the overall structure in all stages of the life cycle. In order to make significant improvements in the forecasts of tropical cyclone intensity and track, future work will require investment in ensemble techniques to better capture the observed variability and uncertainty of the inner- and outer-core storm structures in the initial conditions of numerical weather prediction models.

IV. MECHANISMS FOR STRUCTURE CHANGE

A. SECONDARY EYEWALL FORMATION

1. Complete Replacement Cycle

For the purposes of this research, complete eyewall replacement is defined using microwave satellite imagery from the National Aeronautics and Space Administration (NASA) TRMM and Aqua research satellites, and the Defense Meteorological Satellite Program (DMSP) polar-orbiting platforms. In the sequence of events that defines complete eyewall replacement, concentric convective rings form, the inner-most convective ring weakens, and the inner-most convective ring eventually disappears. The analysis of complete eyewall replacement in this section and the analyses in other sections of this chapter will be conducted using excerpts of the life cycles from individual Atlantic tropical cyclones.

a. *Fabian (2003)*

Fabian became a named storm by 1800 UTC 28 August over the central North Atlantic in the vicinity of 15.1°N, 38.2°W. This tropical cyclone had a west-northward track for approximately 24 h before strengthening into a hurricane at 1800 UTC 29 August. After reaching hurricane intensity, Fabian continued on a west-northwestward track across the North Atlantic for 84 h before turning poleward east of the Lesser Antilles and passing just west of Bermuda on 5 September. H*Wind analyses for Fabian became available at 1330 UTC 1 September and at regular increments until 0130 UTC 6 September after the storm passed west of Bermuda.

At 0730 UTC 4 September (hereafter referred to as Hour 66 of the analysis; Hours 0–66 will be analyzed in the asymmetric convection section of Chapter IV), Fabian had a tangential wind speed (V_t) of 45 m s^{-1} with azimuthal-average R_{max} and R_{34} values of 30 km and 325 km, respectively. Microwave satellite imagery at 0901 UTC 4 September ($\sim$67.5 h of the analysis, 47a) indicates strong, asymmetric convection existed in the northern eyewall with very strong convection in one spiral rainband in close proximity ($\sim$1 degree) to the eyewall. A second spiral rainband with sporadic convection extended outward to 2 degrees in the west and north quadrants. From 66 h to 78 h, the V_t and R_{max} gradually decreased to 44 m s^{-1} and 29 km, respectively, while R_{34} decreased more rapidly to 241 km (a 84 km decrease, Fig. 48).

The contraction of R_{34} during the nearly constant V_t is inconsistent with expectations using Eq. (1). Note that the large decreases in the R_{34} at Hour 78 is associated with a H*Wind analysis that incorporated SFMR data, whereas the value at Hour 66 is based on reconnaissance aircraft data adjusted to the surface (Fig. 48a). However, an examination of Hour 81 reveals a large R_{34} increase associated with a H*Wind analysis that also incorporated SFMR data. Dropsonde, drifting buoy, and other sources of data were generally incorporated in most analyses, and thus are not deemed as a source of the differences. Therefore, it is not apparent that changes in the R_{34} are caused by issues with the analyses.

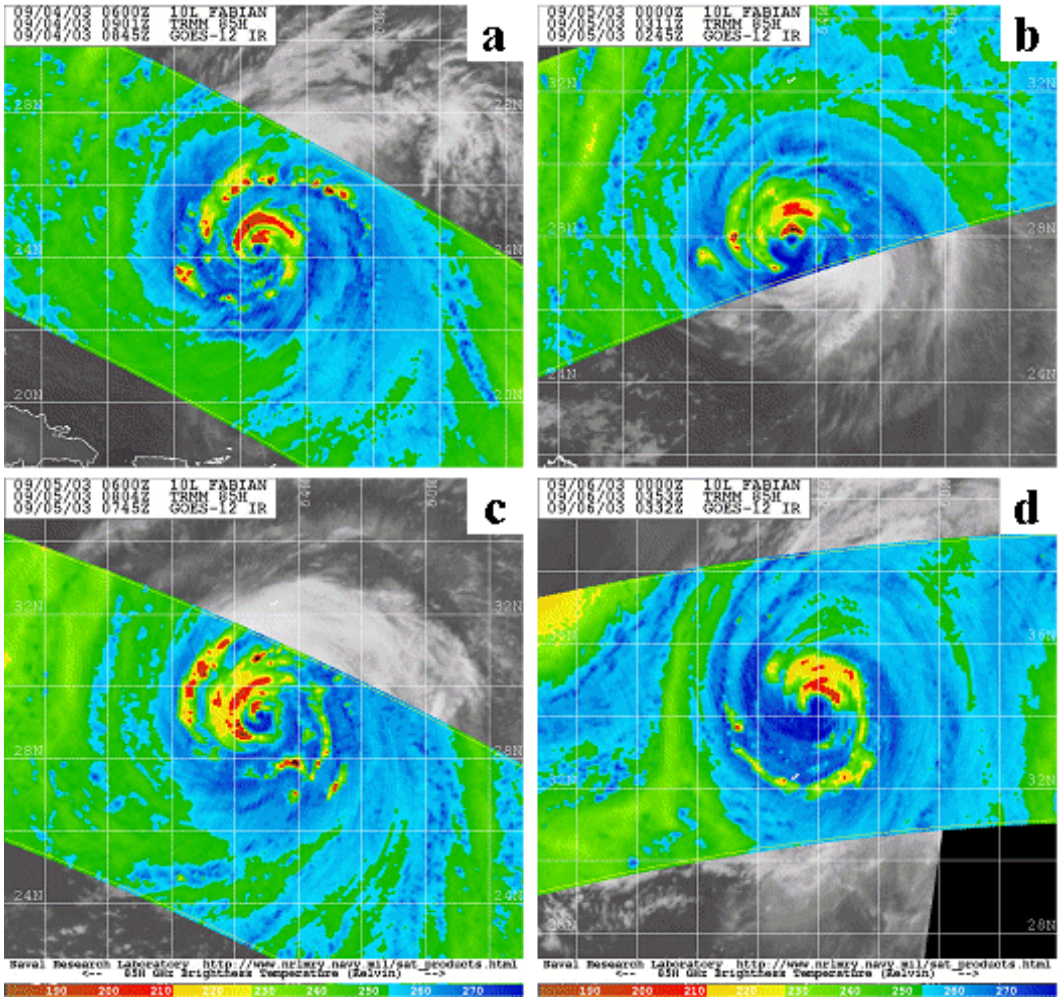

Figure 47 Microwave satellite imagery (85 GHz) for Hurricane Fabian from the TRMM polar orbiting platform on (a) 4 September at 0901 UTC, (b) 5 September at 0311 UTC, (c) 5 September at 0804 UTC, and (d) 6 September at 0353 UTC (2003; from NRL 2007).

In Fig. 48a (and the similar figures in this chapter), a radial wind variance is calculated as the variance along eight equidistant radial inflow directions compared to the azimuthal-average radial inflow values for the radial interval 25 km outside of the R_{max}. Based on the preliminary analysis of the dataset, this radial wind variance is hypothesized to be associated with asymmetric convection that occurs in the eyewall or in close proximity to the eyewall, and thus may also be a predictor of outer-core structure changes. That is, outward shifts in the heating distribution are expected to be correlated with increases in the R_{max} value, and subsequent increases in the R_{34} radii.

In Fig. 48b (blue dashed lines), the time and space differential of anomalous (i.e., the deviation from a standard modified Rankine vortex with an exponent $x = 0.5$) integrated kinetic energy per unit area (hereafter referred to as "ΔKE_{anom}") is displayed (see Appendix D for more details). The spatial difference is calculated using the annular rings of 1.0 to 1.5 degrees and 2.0 to 2.5 degrees where negative (positive) values in Fig. 48b represent an inward (outward) ΔKE_{anom} at the given analysis time. Again based on preliminary analysis of the dataset, the inward (outward) ΔKE_{anom} is hypothesized to be correlated with the decrease (increase) in the inner-core structure size (R_{max}). Two metrics of inner-core structure, the azimuthal-average inner-core size (R_{max}, green dotted line) and inner eyewall radius (black dotted line), are displayed using the right ordinate in Fig. 48b. The inner eyewall radius is normally calculated using the inner R_{50} value, except the R_{34} value is used for weak or highly asymmetric storms. The inner eyewall radius is calculated using a limited number of grid points and distance-weighted interpolation, and thus is used as a proxy to understand eyewall changes only. Since the diagnostic ΔKE_{anom} is calculated as a differential in time leading up to the current analysis time, the two inner-core structure metrics in Fig. 48b are expected to vary in unison with the ΔKE_{anom} (blue dashed line).

Microwave satellite imagery from 0311 UTC to 0804 UTC 5 September ($\sim$Hours 85.5 and 90.5 of the analysis, Figs. 47b–c) indicates the formation of a secondary eyewall with asymmetric strong convection in the west and north quadrants in close proximity to the asymmetric convection of the inner eyewall. By 0353 UTC 6 September ($\sim$Hour 110.5 of the analysis, Fig. 47d), it is evident from microwave satellite imagery that the asymmetric convective secondary eyewall had replaced the inner eyewall, thus completing the secondary eyewall replacement cycle.

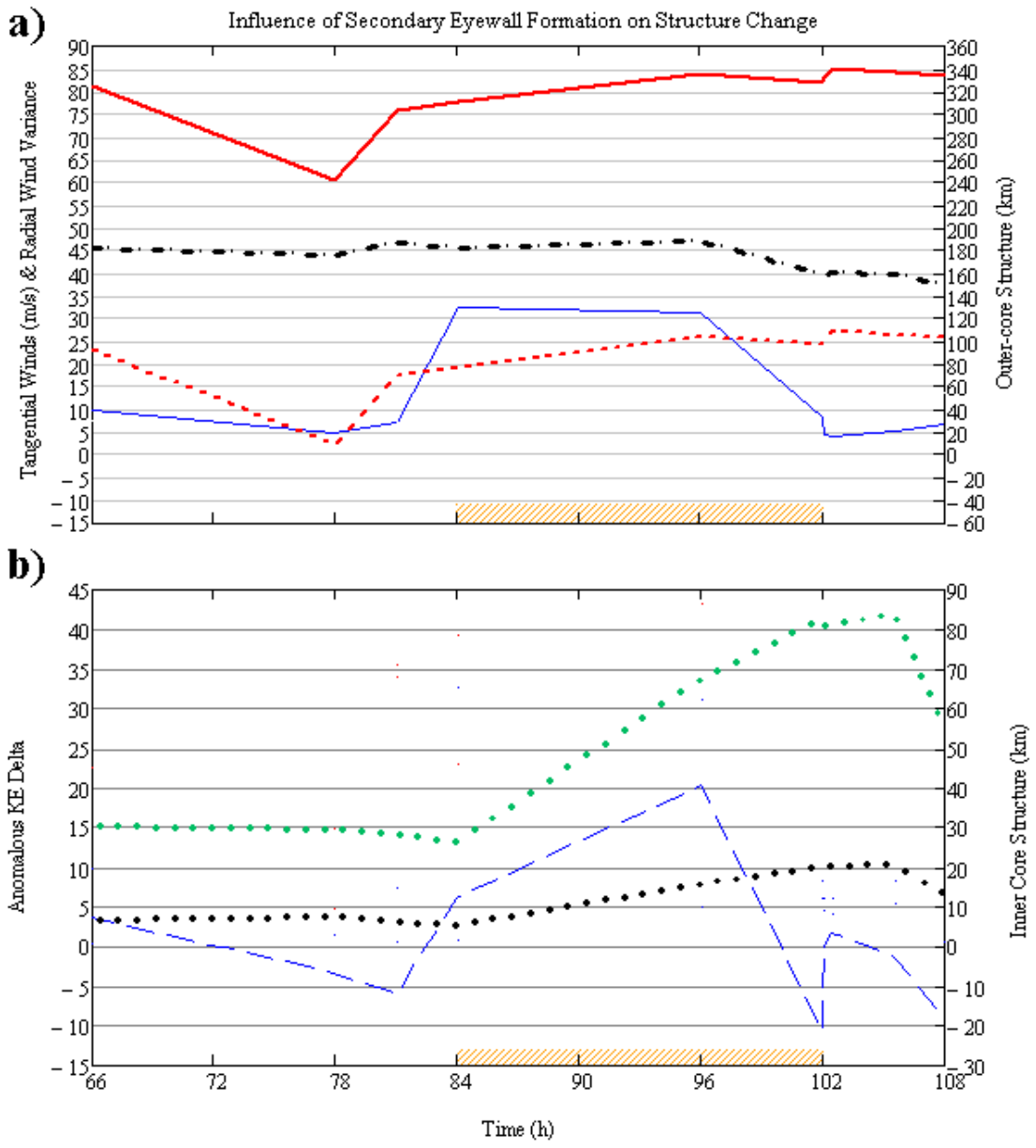

Figure 48 (a) Time series of structure changes for Hurricane Fabian (2003) from 4 September at 0730 UTC (Hour 66) to 6 September at 0130 UTC (Hour 108). The black dash-dot line is the azimuthal-average tangential winds (V_t). The red solid and dashed lines are the azimuthal-average R_{34} radius and the R_{34} changes relative to the initial hour (Hour 66 in this case), respectively, with the scale on the right ordinate. (b) The green and black dotted lines are the azimuthal-average R_{max} and inner eyewall radii, respectively. The blue solid (panel a) and dashed lines (panel b) are the radial wind variance and delta of anomalous kinetic energy per unit area (ΔKE_{anom}, in 10^{-3} kg s^{-2}), respectively. The orange-hashed rectangles are the nominal periods of secondary eyewall replacement.

An association exists between the asymmetric convection and an increase in the radial inflow variance between 84 h and 96 h (Fig. 48a).

During this eyewall replacement cycle (orange hashed rectangles from Hour 84 to Hour 102 in Fig. 48), R_{max} and the inner eyewall more than tripled (increased from 26 km to 82 km and from 5 km to 20 km, respectively) from 84 h to 102 h. This rapid expansion of the R_{max} coincided with an outward ΔKE_{anom} (Fig. 48b). As Fabian's inner-core structure changed in association with secondary eyewall replacement, the intensity (V_t) decreased from 45 m s^{-1} to 38 m s^{-1} between 84 h and 108 h (Fig. 48a).

The azimuthal-average wind profiles in Fig. 49a prior to, following, and 6 h after this eyewall replacement cycle (Hours 84, 102, and 108, respectively) suggest an initial increase in the outer-core structure (R_{34}), and then a continued increase during the 6 h after the cycle. Whereas R_{max} increased by 56 km in association with this eyewall replacement cycle and then decreased by 27 km 6 h after the cycle, R_{34} increased by 15 km during this eyewall replacement cycle (blue arrow in Fig. 49a) and continued to increase by an additional 5 km 6 h after the cycle (red arrow in Fig. 49a).

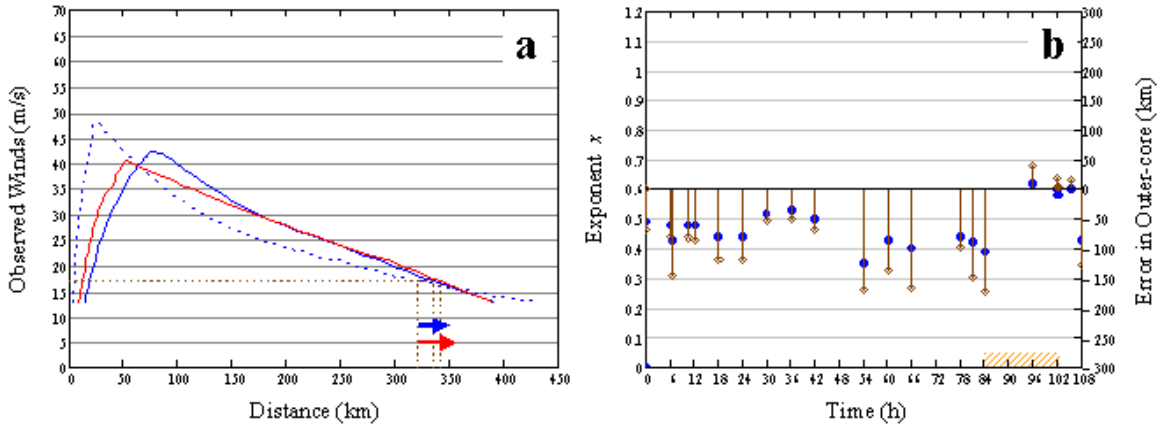

Figure 49 (a) Azimuthal-average wind profiles for Hurricane Fabian at Hour 84 (blue dashed line), Hour 102 (blue solid line) and Hour 108 (red solid line), and (b) observed values for exponent x in the modified Rankine vortex (blue circles) and the prediction error (stem plots) when the mean value for exponent $x = 0.58$ is applied in Eq. (20). The orange-hashed rectangle is the nominal third period of asymmetric convection associated inner-core structure changes.

The exponent x values assuming a modified Rankine vortex suggest that Fabian had a larger outer-core structure prior to and after, but not during, this eyewall replacement cycle than the overall population of Atlantic tropical cyclones during 2003–2005 (Fig. 49b). Indeed, applying the overall mean value for exponent $x = 0.58$ (see Chapter III.C.3) in the modified Rankine vortex in Eq. (20) results in an underprediction of R_{34} by 127–172 km prior to and after this eyewall replacement cycle, as depicted by the stem plots in Fig. 49b. The mean modified Rankine vortex exponent x during the life cycle of Fabian was 0.48 with individual values of $x = 0.39$, $x = 0.60$, and $x = 0.43$ at Hours 84, 102, and 108, respectively, for this eyewall replacement cycle.

In summary, one complete secondary eyewall replacement cycle occurred from 0730 UTC 4 September to 0130 UTC 6 September when Fabian was over the western North Atlantic. During the eyewall replacement cycle, Fabian had a V_t decrease of 7 m s^{-1} (Fig. 48a). The R_{max} tripled (56 km increase) during the beginning of the eyewall replacement cycle, but then a contraction occurred at the end of the cycle (Fig. 48b). Inward (outward) ΔKE_{anom} was generally associated with a decrease (increase) of the R_{max} radius. Indeed, the correlation coefficient of 0.709 indicates a linear relationship between ΔKE_{anom} and R_{max}. An increase in radial inflow variance was observed when convective asymmetries in or near the eyewall were present.

The azimuthal-average wind profiles prior to, following, and 6 h after the eyewall replacement cycle (Fig. 49) suggests that the R_{34} did have a small time-lagged increase following secondary eyewall replacement. The range of exponent x values was 0.35–0.62, where the smaller (larger) values occurred prior to (after) the secondary eyewall replacement cycle. Indeed, the exponent x increased from 0.39 to 0.60 during the eyewall replacement cycle.

b. *Frances (2004)*

Frances became a named storm by 1800 UTC 25 August over the central North Atlantic in the vicinity of 11.5°N, 39.8°W. This tropical cyclone strengthened into a hurricane by 1800 UTC 26 August and had a northwestward track (north of the Antilles) before making landfall on Florida's east coast around 0600 UTC 5 September. H*Wind analyses for Frances became available at 1930 UTC 29 August and at regular increments for the remainder of the storm life cycle.

At 1930 UTC 29 August (hereafter referred to as Hour 0 of the analysis), Frances had a tangential wind speed (V_t) of 46 m s^{-1} with azimuthal-average R_{max} and R_{34} values of 24 km and 244 km, respectively. Microwave satellite imagery at 1750 UTC 29 August (∼1.5 h prior to Hour 0 of the analysis, Fig. 50a) indicates Frances had a well-developed eyewall with one spiral rainband extending outward to approximately 2.5 degrees in the north and east quadrants. During the first 6 h of the analysis period, Frances weakened by 4 m s^{-1}, and the R_{max} and R_{34} values decreased by 10 km and 30 km, respectively (Fig. 51). The contraction of R_{34} during the decrease in V_t is consistent with expectations using Eq. (1), but the decrease in R_{max} is expected to be accompanied by a storm intensity increase.

Whereas tangential wind speed (V_t) continues to weaken until Hour 12 and decreases to 38 m s^{-1}, the R_{max} and R_{34} values increased by 5 km and 46 km, respectively (Fig. 51). By 1021 UTC 30 August (∼Hour 15 of the analysis, Fig. 50b), one spiral band almost completely encircles the eyewall and extends to 0.5–2.0 degrees from the storm center. Convection in the spiral rainband is very strong, but a lack of strong convection is observed in the northeast quadrant of the eyewall, which is the same quadrant that strong convection in the spiral band comes nearest to the eyewall. The satellite image at 1709 UTC 30 August (∼Hour 21.5 of the analysis, Fig. 50c) indicates the formation of a secondary eyewall that completely surrounds the weakening original eyewall with one strong convective spiral rainband that extends 2.0 degrees from the secondary eyewall in the north and east quadrants. Microwave satellite imagery depicts the breakdown (∼Hour 27.5 of the analysis, Fig. 50d) and eventual disappearance (∼Hour 40 of the analysis, Fig. 50e) of the original eyewall. The satellite imagery between 1021 UTC 30 August and 1121 UTC 31 August (Figs. 50b–e) depicts the first of two complete eyewall replacement cycles that Frances experienced between Hour 0 and Hour 84.

During the first eyewall replacement cycle (orange hashed rectangles from Hour 15 to Hour 36 in Fig. 51), the R_{max} doubled (increased from 20 km to 41 km) from 18 h to 24 h. This rapid expansion of the R_{max} coincided with an outward ΔKE_{anom} (Fig. 51b). As the secondary eyewall became the dominant eyewall (see Fig. 50d), there is an apparent lack of organized spiral rainband convection and the storm rapidly intensified (V_t increased from 40 m s^{-1} to 50 m s^{-1}, Fig. 51a) from 24 h to 36 h. Recall that rapid intensification is defined here (Chapter III.B.1) as an increase of 15 kt (∼7.5 m s^{-1}) in 12 h.

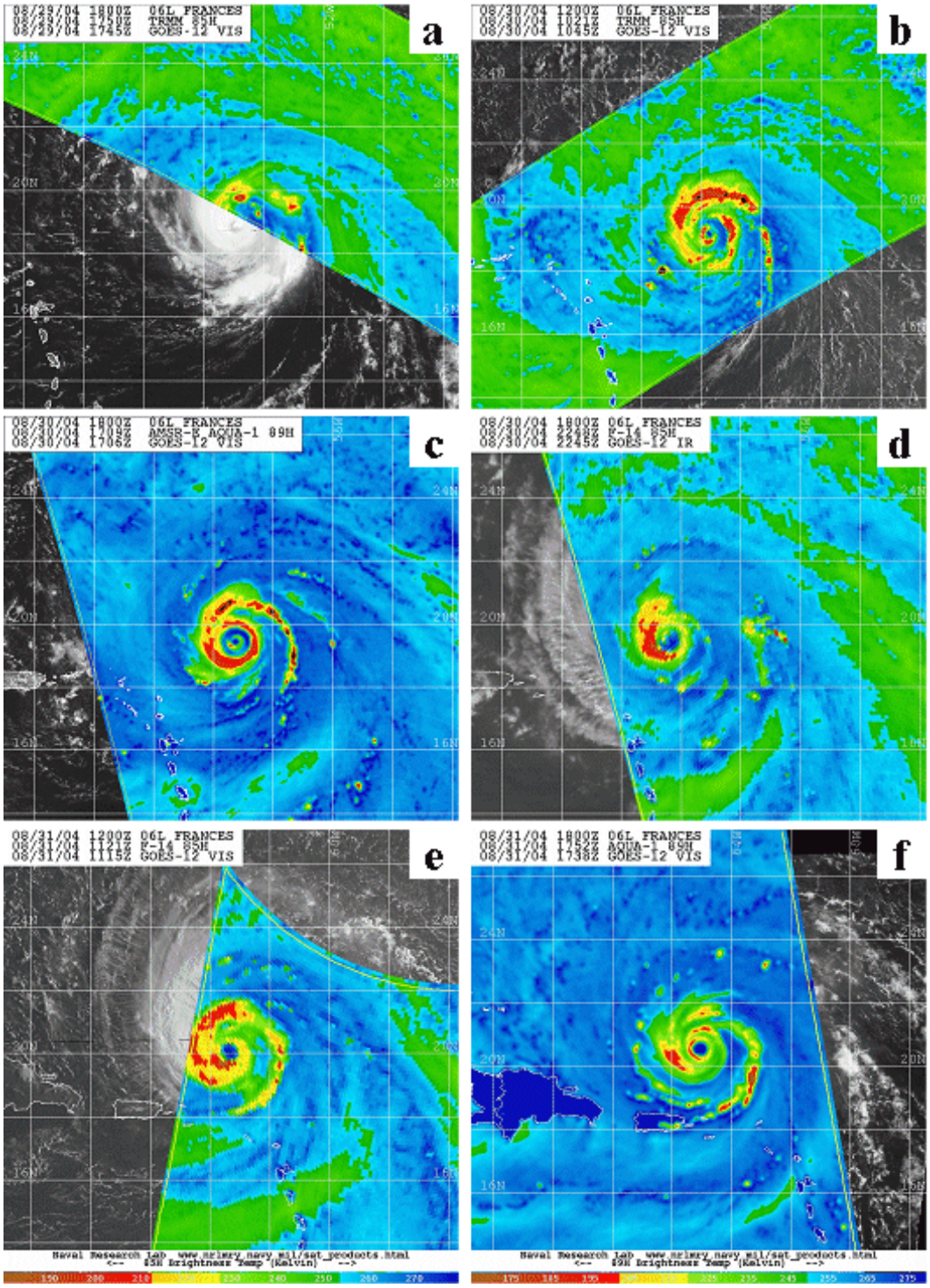

Figure 50 Microwave satellite imagery (85-89 GHz) for Hurricane Frances from Aqua, TRMM, and DMSP polar orbiting platforms on (a) 29 August at 1750 UTC, (b) 30 August at 1021 UTC, (c) 30 August at 1709 UTC, (d) 30 August at 2248 UTC, (e) 31 August at 1121 UTC, and (f) 31 August at 1752 UTC (2004; from NRL 2007).

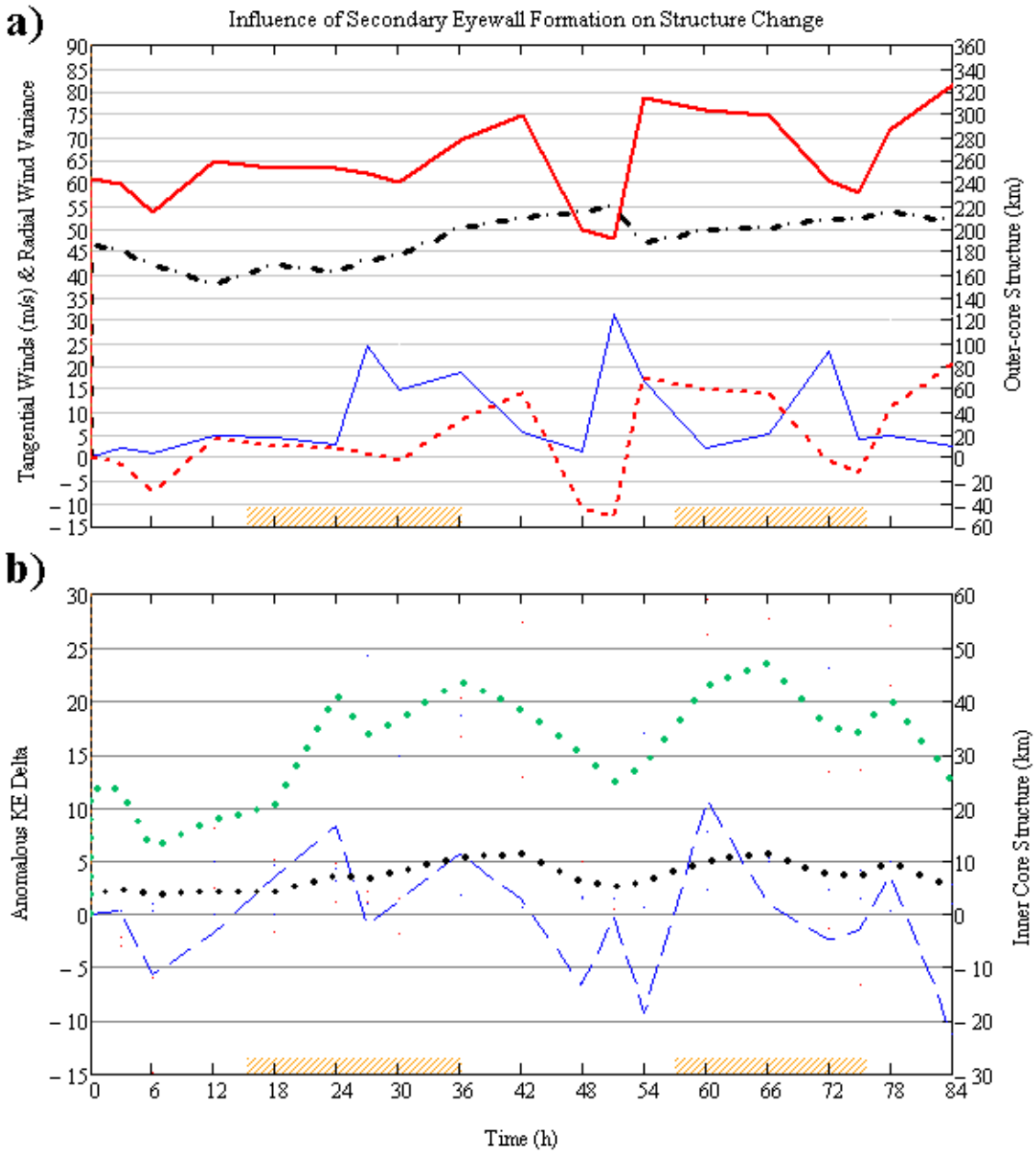

Figure 51 Time series of structure changes as in Fig. 48, except for Hurricane Frances from 29 August at 1930 UTC (Hour 0) to 2 September at 0730 UTC (Hour 84).

From 18 h to 42 h, the inner eyewall radius nearly tripled (4 km to 11 km, Fig. 51b) in association with the formation of a secondary eyewall.

From 12 h to 42 h during secondary eyewall replacement, the outer-core radius (R_{34}) first slowly decreased by 20 km through Hour 30 and then rapidly increased by 59 km (Fig. 51a). The azimuthal-average wind profiles in Fig. 52a prior to, following, and 6 h after the first eyewall replacement cycle (Hours 12, 36, and 42, respectively) suggest that there is a time lag between changes in the inner-core structure (R_{max}) and changes in the outer-core structure (R_{34}). Whereas the R_{max} increased by 26 km during this eyewall replacement cycle followed by a decrease of 6 km 6 h after the cycle, the R_{34} increased by 14 km during this eyewall replacement cycle (blue arrow in Fig. 52a) and continued to increase by an additional 24 km 6 h after the cycle (red arrow in Fig. 52a).

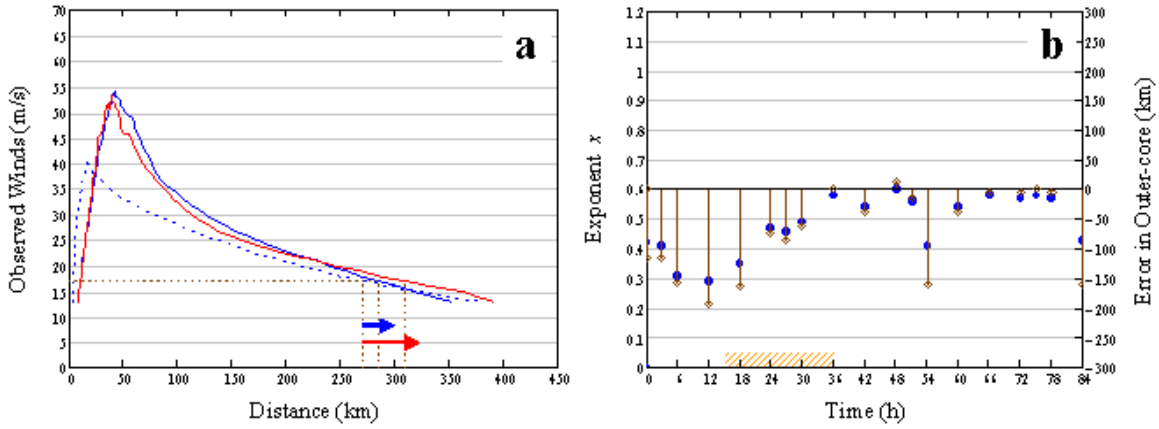

Figure 52 (a) Azimuthal-average wind profiles for Hurricane Frances at Hour 12 (blue dashed line), Hour 36 (blue solid line) and Hour 42 (red solid line), and (b) observed values for exponent x in the modified Rankine vortex (blue circles) and the prediction error (stem plots) when the mean value for exponent $x = 0.58$ is applied in Eq. (20). The orange-hashed rectangle is the nominal period of the first eyewall replacement cycle.

The exponent x values assuming a modified Rankine vortex suggest that Frances had a larger outer-core structure prior to the first eyewall replacement cycle than the overall population of Atlantic tropical cyclones during 2003–2005 (Fig. 52b). Indeed, applying the overall mean value for exponent $x = 0.58$ in the modified Rankine vortex in Eq. (20) results in an under-prediction of R_{34} by 60–192 km prior to and during the first eyewall replacement cycle, as depicted by the stem plots in Fig. 52b.

The mean modified Rankine vortex exponent x during the life cycle of Frances was 0.48 with individual values of $x = 0.29$, $x = 0.58$, and $x = 0.54$ at Hours 12, 36, and 42, respectively, for the first eyewall replacement cycle. A conceptual model might be that the tangential wind profile beyond the new eyewall following a secondary eyewall formation would have the same shape as the profile beyond the original eyewall, which would allow a simple prediction of the new R_{34} given the new V_{max} and R_{max}. This example demonstrates that Frances had a "flatter-than-average" profile prior to secondary eyewall formation that then became "sharper-than-average" following secondary eyewall formation. Thus, a simple prediction of the change in R_{34} with a fixed value for exponent x during secondary eyewall replacement does not apply in this case.

Microwave satellite imagery at 1752 UTC 31 August (∼Hour 46.5 of the analysis, Fig. 50f) depicts greater convective symmetry with a single spiral rainband that extends outward from the new eyewall up to 2 degrees from the storm center in all quadrants except the southwest quadrant. From 36 h to 51 h as the secondary eyewall becomes dominant, R_{max} and the inner eyewall decreased by 19 km and 6 km, respectively (Fig. 51b). Coincident with the contraction of the inner-core structure, there is an observed inward ΔKE_{anom}. Following this eyewall replacement cycle, the R_{34} value decreased by 106 km (Fig. 51a). Note that the large decreases in the R_{34} at Hours 48 and 51 are associated with H*Wind analyses that incorporate SFMR data, whereas the values at Hours 36 and 42 are based on reconnaissance aircraft data adjusted to the surface. Because the decrease in the R_{34} value associated with analyses incorporating SFMR data is again depicted at Hours 72 and 75 (Fig. 51a), one must examine whether these R_{34} differences are a result of differing observations in the H*Wind analyses. Dropsonde, QuikScat, and other sources of data were generally incorporated in most analyses, and thus are not deemed as a source of the differences. A review of the analyses from Frances reveals periods before and after Hours 48, 51, 72, and 75 that provide similar R_{34} radii; e.g., Hour 18 that incorporated reconnaissance aircraft data adjusted to the surface compared to Hour 24 that incorporated SFMR data. Therefore, it is not apparent that changes in the R_{34} are caused by issues with the analyses.

It is apparent that by Hour 58.5 of the analysis (0602 UTC 1 September, Fig. 53a) a new secondary eyewall has formed and completely surrounds the weakened primary eyewall.

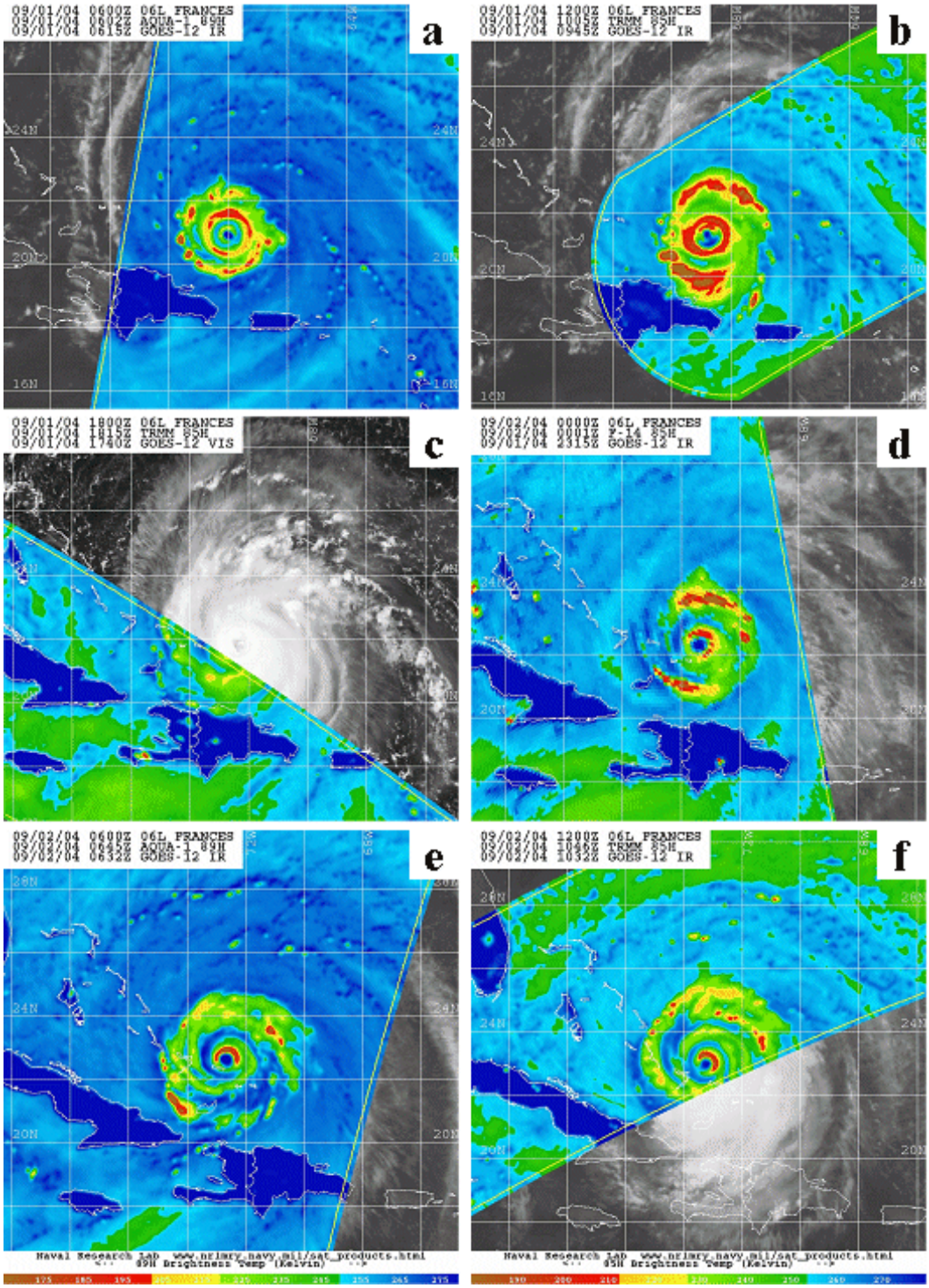

Figure 53 Microwave satellite imagery (85-89 GHz) for Hurricane Frances from Aqua, TRMM, and DMSP polar orbiting platforms on (a) 1 September at 0602 UTC, (b) 1 September at 1005 UTC, (c) 1 September at 1815 UTC, (d) 2 September at 0001 UTC, (e) 2 September at 0645 UTC, and (f) 2 September at 1046 UTC (2004; from NRL 2007).

The breakdown of the primary eyewall is evidenced by its displacement to the north of the center in microwave satellite imagery at 1005 UTC 1 September (∼Hour 62.5 of the analysis, Fig. 53b). The secondary eyewall has very strong convection with two spiral rainbands that extend 2 degrees outward in the north and south quadrants. The completion of the second eyewall replacement cycle is depicted by microwave and visible satellite imagery at 1815 UTC 1 September and 0001 UTC 2 September (∼Hours 71 and 76.5 of the analysis, Fig. 53c–d). The satellite imagery between 0602 UTC 1 September and 0001 UTC 2 September (Figs. 53a–d) depict the second of two complete eyewall replacement cycles for Frances. From 51 h to 54 h, prior to the nominal period of eyewall replacement, the tangential winds (V_t) decreased by 8 m s^{-1} and the R_{34} value increased 119 km (Fig. 51a).

During the second eyewall replacement cycle (orange hashed rectangles from Hour 57 to Hour 75 in Fig. 51), once again a doubling of the R_{max} value is observed (increased from 24 km to 47 km) from 51 h to 66 h. As with the first eyewall replacement cycle, this rapid expansion of the R_{max} is coincident with an outward ΔKE_{anom} (Fig. 51b). As the secondary eyewall becomes the dominant eyewall (see Fig. 53d), symmetrically-distributed strong convective spiral rainbands are present in the north and south quadrants 1–2 degrees from the storm center. As with the first eyewall replacement cycle, the storm intensified during this eyewall replacement cycle (V_t increased from 47 m s^{-1} to 54 m s^{-1}, Fig. 51a) from 54 h to 78 h. However, rapid intensification was not observed during this eyewall replacement cycle. One major structure difference in the microwave satellite imagery between the two eyewall replacement cycles is that the first cycle had greater convective asymmetry (Figs. 50d–e) compared to the second cycle (Fig. 53d). This may suggest that the process of axisymmetrization is a potential mechanism for rapid storm intensification during secondary eyewall replacement. From 51 h to 66 h, the inner eyewall radius also doubled (5 km to 11 km, Fig. 51b) in association with the formation of a secondary eyewall. After Hour 66, R_{max} and the inner eyewall radius generally decreased in the presence of inward ΔKE_{anom} (Fig. 51b).

From 54 h to 78 h during secondary eyewall replacement, the outer-core radius (R_{34}) first decreased by 24 km and then rapidly increased by 31 km between 78 h and 84 h (Fig. 51a) in the presence of weakened spiral rainband convection as observed by microwave satellite imagery at 0645 UTC and 1046 UTC 2 September (∼Hours 83.5 and 87.5 of the analysis, Figs. 53e–f). The azimuthal-average wind profiles in Fig.

54a prior to, following, and 6 h after the second eyewall replacement cycle (Hours 54, 78, and 84, respectively) again suggest that there is a time lag between changes in the inner-core structure (R_{max}) and changes in the outer-core structure (R_{34}). Contrary to the first eyewall replacement cycle, the R_{34} first decreased by 24 km (blue arrow in Fig. 54a) during this eyewall replacement cycle and then increased by 31 km (red arrow in Fig. 54a) following the cycle for a net increase of 7 km.

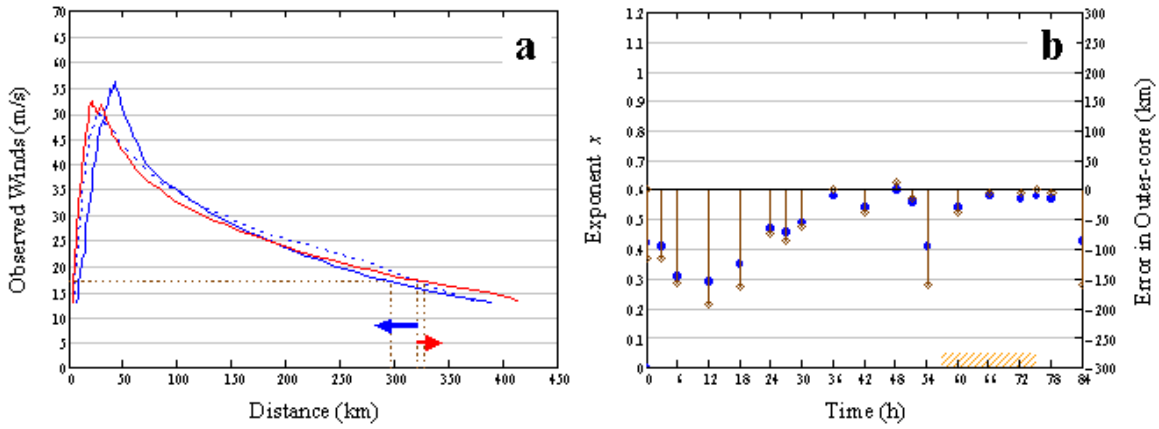

Figure 54 (a) Azimuthal-average wind profiles for Hurricane Frances at Hour 54 (blue dashed line), Hour 78 (blue solid line) and Hour 84 (red solid line), and (b) observed values for exponent x in the modified Rankine vortex (blue circles) and the prediction error (stem plots) when the mean value for exponent $x = 0.58$ is applied in Eq. (20). The orange-hashed rectangle is the nominal period of the second eyewall replacement cycle.

The exponent x values assuming a modified Rankine vortex suggest that the overall mean value for exponent $x = 0.58$ is a good predictor of the R_{34} values from Hour 36 to Hour 84, except at Hours 54 and 84 (Fig. 54b). Once again, applying the overall mean value for exponent x in Eq. (20) results in an under-prediction of the R_{34} at Hour 54 by 159 km prior to the second eyewall replacement cycle, as depicted by the stem plot in Fig. 54b. Individual values of $x = 0.41$, $x = 0.57$, and $x = 0.43$ for Hours 54, 78, and 84, respectively, were observed for the second eyewall replacement cycle. As previously noted, this suggests that accurately predicting the change in R_{34} with a fixed value for exponent x during secondary eyewall replacement may not be plausible.

Large increases of radial inflow variance are observed at Hours 27, 36, 51, and 72 (Fig. 51a). At Hours 27 and 36, convective asymmetries are observed in and

near Frances' eyewall (see Figs. 50d–e). While microwave satellite imagery is not available for the Hours 51 and 72, it might be inferred from Figs. 50f and 53b that convective asymmetries near the eyewall were likely present for these hours. Whereas a comparison of storm intensity to R_{34} for this Frances case results in a very small correlation coefficient of 0.058, comparing the 6-h change in R_{34} to the variance of radial inflow yields a correlation coefficient of 0.477. As hypothesized, the increase in observed radial inflow variance appears to be associated with convective asymmetries in or near the eyewall, which are followed by observed increases in the R_{34} radius.

In summary, two complete secondary eyewall replacement cycles occurred during Frances' life cycle from 1930 UTC 29 August to 0730 UTC 2 September. During each eyewall replacement cycle, this tropical cyclone intensified with V_t increases of 12 m s^{-1} and 5 m s^{-1}, respectively (Fig. 51a). Contrary to the expected R_{max} decrease with increased V_t as predicted by conservation of angular momentum, the R_{max} doubled(21 km and 23 km increases, respectively) during the beginning of both eyewall replacement cycles followed by contractions near the end of each cycle (Fig. 51b). Inward (outward) ΔKE_{anom} generally led to a decrease (increase) of the R_{max} radius. Indeed, the correlation coefficient of 0.743 indicates a linear relationship between ΔKE_{anom} and R_{max}. An increase in radial inflow variance was frequently observed when convective asymmetries in or near the eyewall were present and increases in the R_{34} value generally followed within 6 h of the increased variance (Fig. 51a). This suggests that radial inflow variance could possibly be used by forecasters as a predictor of outer-core expansion.

The azimuthal-average wind profiles prior to, following, and 6 h after the two eyewall replacement cycles (Figs. 52 and 54) suggest that the R_{34} experiences a time-lagged increase following secondary eyewall replacement. The range of exponent x values was 0.29–0.60, where the smaller (larger) values occurred prior to (after) a secondary eyewall replacement cycle. Indeed, the exponent x increased from 0.29 to 0.58 and from 0.41 to 0.57 during the first and second eyewall replacement cycles, respectively. The observed variability of exponent x for Frances demonstrates that accurate prediction of the R_{34} change using a fixed value for exponent x of the modified Rankine vortex during secondary eyewall replacement may not be plausible. A comparison of the analyses that included SFMR data (Hours 48, 51, 72, and 75) with non-SFMR analyses did not reveal a systemic issue with the H*Wind analyses. In fact, the similarity in the exponent x values assuming a modified Rankine vortex during the

applicable time periods (Figs. 52b and 54b) suggests that these decreases in outer-core structure (R_{34}) are likely associated with inner-core structure (R_{max}) decreases.

c. *Ivan (2004)*

Ivan became a named storm by 0000 UTC 3 September over the central North Atlantic in the vicinity of 9.6°N, 32.0°W. This tropical cyclone had a westward track before strengthening into a hurricane at 0600 UTC 5 September. Hurricane Ivan continued on a westward track for approximately 90 h and then had a west-northwestward track that passed south of Jamaica on 10 September and entered the Yucatan Gap on 13 September. As Ivan entered the Gulf of Mexico, the track became northwestward, and then northward until making landfall along the southern Alabama coast around 0600 UTC 16 September. H*Wind analyses for Ivan became available at 1930 UTC 6 September and at regular increments for the remainder of the storm life cycle.

At 2230 UTC 6 September (hereafter referred to as Hour 0 of the analysis), Ivan had a tangential wind speed (V_t) of 33 m s^{-1} with azimuthal-average R_{max} and R_{34} values of 12 km and 170 km, respectively. Microwave satellite imagery at 1712 UTC 6 September (∼5.5 h prior to Hour 0 of the analysis, Fig. 55a) indicates a lack of a convection in the southern eyewall with strong convection north of the storm center and a convective rainband to the west that extends outward to 3 degrees. During the first 3 h of the analysis period, Ivan weakened by 2.5 m s^{-1}, and the R_{max}, inner eyewall, and R_{34} expanded by 33 km, 18 km, and 47 km, respectively (Fig. 56). Note that an outward ΔKE_{anom} coincides with these inner- and outer-core structure expansions. While an increase of R_{max} with a decrease in V_t is consistent with expectations from Eq. (1), the increase in R_{34} might have been expected to be associated with an intensity increase. This example of a large inner-core structure expansion will be further discussed in the section on partial eyewall replacement later in this chapter. From 3 h to 9 h, Ivan rapidly intensified (an increase of 12 m s^{-1} in 6 h, Fig. 56a) as this tropical cyclone became better organized, which is indicated by an increase in eyewall convection at 0528 UTC 7 September (∼Hour 7 of the analysis, Fig. 55b). During this period, an inward ΔKE_{anom} was associated with R_{max} and inner eyewall decreases by 27 km and 17 km, respectively (Fig. 56b). The outer-core structure (R_{34}) continued to increase by an additional 15 km (Fig. 56a).

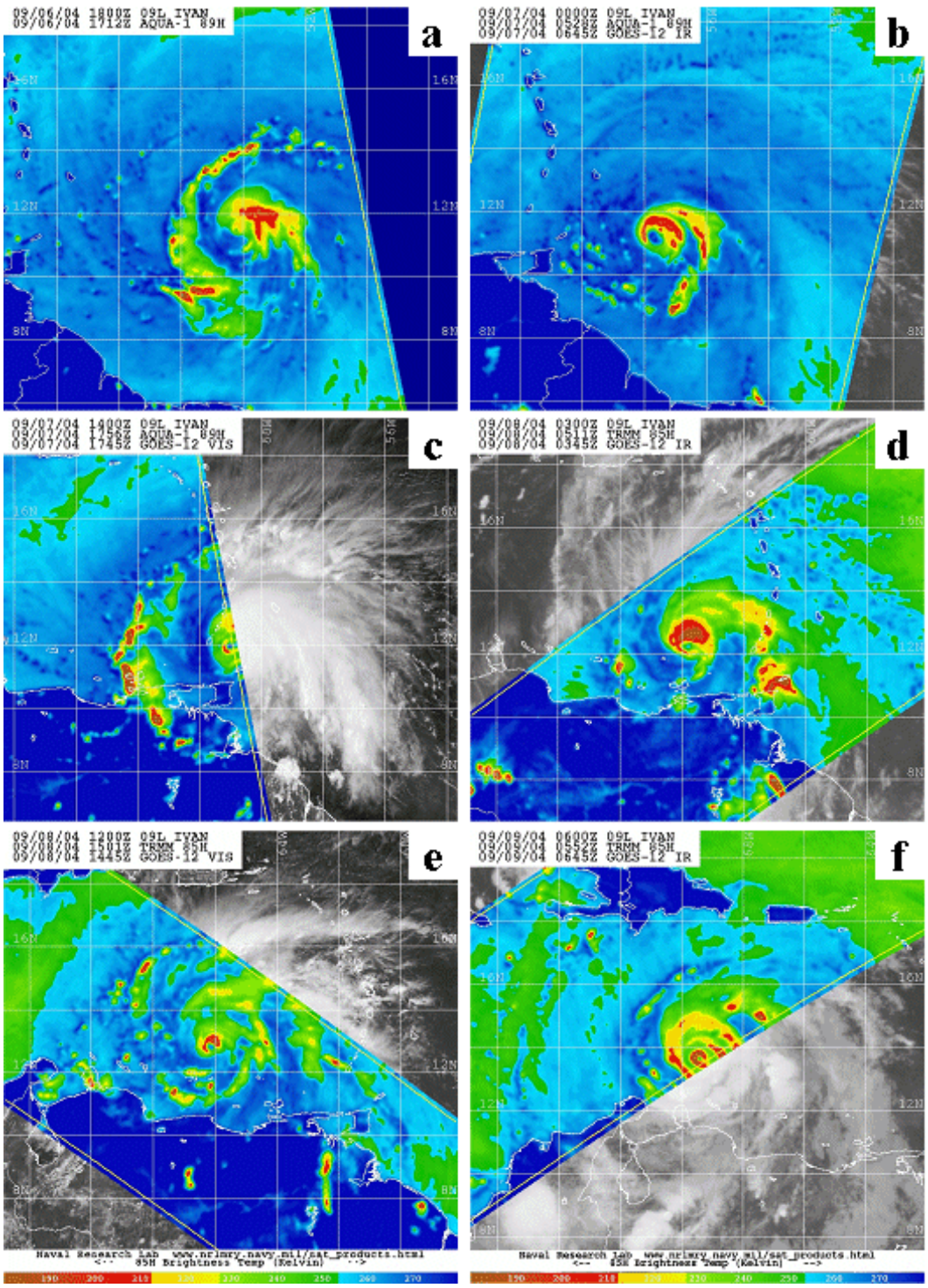

Figure 55 Microwave satellite imagery (85-89 GHz) for Hurricane Ivan from Aqua and TRMM polar orbiting platforms on (a) 6 September at 1712 UTC, (b) 7 September at 0528 UTC, (c) 7 September at 1756 UTC, (d) 8 September at 0511 UTC, (e) 8 September at 1501 UTC, and (f) 9 September at 0552 UTC (2004; from NRL 2007).

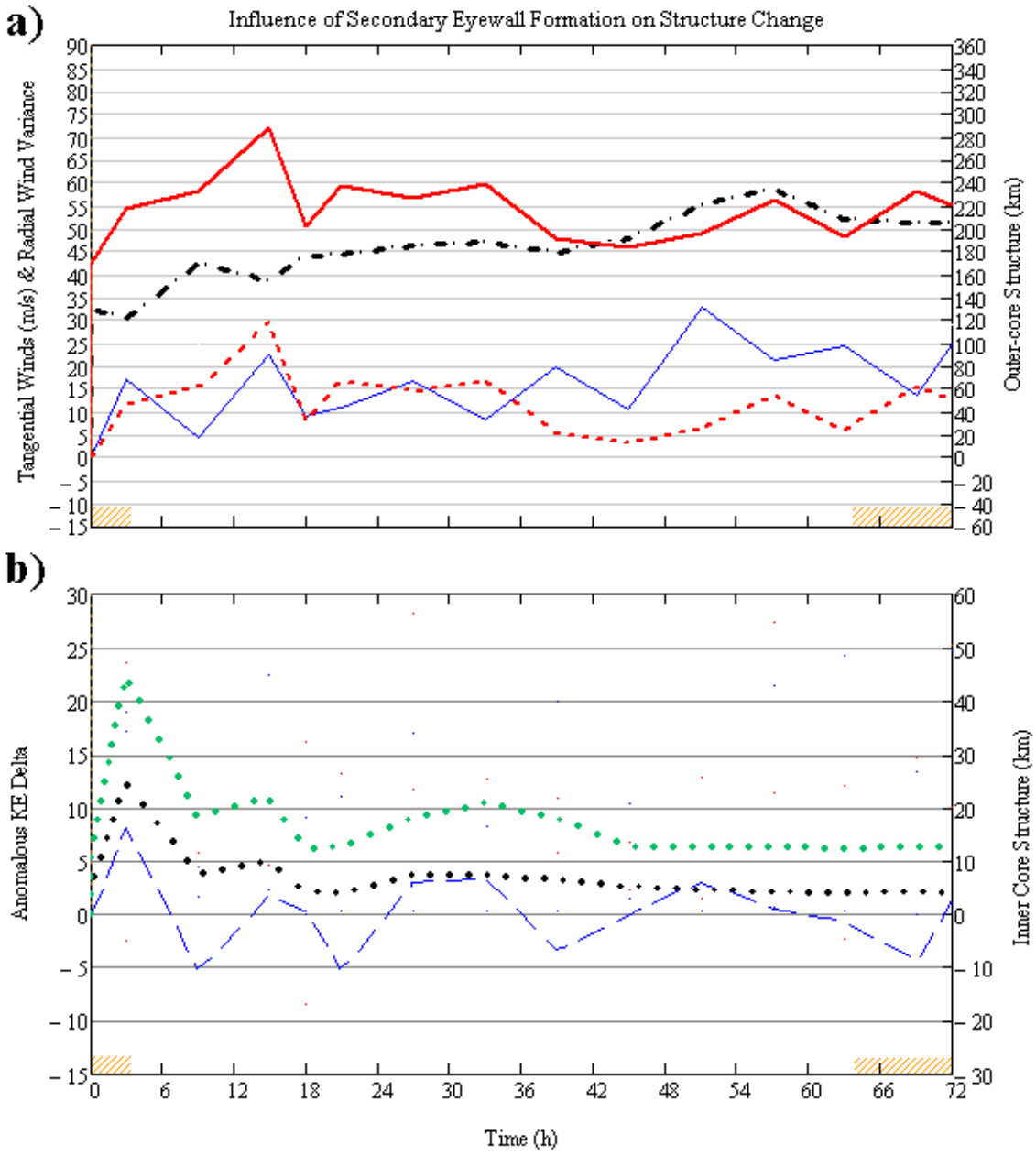

Figure 56 Time series of structure changes as in Fig. 48, except for Hurricane Ivan (2004) from 6 September at 2230 UTC (Hour 0) to 9 September at 2230 UTC (Hour 72).

From 9 h to 15 h, the tangential wind speed slowly decreased, and a small expansion of R_{max} and the inner eyewall was associated with outward ΔKE_{anom}. However, the R_{34} value continued to increase by an additional 56 km (Fig. 56). Ivan resumed intensification between 15 h and 21 h with a contraction of R_{max} and the inner eyewall by 9 km and 6 km, respectively, and with the hypothesized inward ΔKE_{anom} (Fig. 56). During this period, Ivan's outer-core structure (R_{34}) initially contracted by 86 km, and then increased by 35 km (Fig. 56a). From 18 h to 21 h, Ivan developed a small eyewall with two spiral rainbands that extended outward to 4 degrees as indicated by satellite imagery at 1756 UTC 7 September (∼Hour 19.5 of the analysis, Fig. 55c). While Ivan continued to intensify to 47 m s^{-1} during the period from 21 h to 33 h, the outer-core structure only experienced small fluctuations in size (Fig. 56a). An outward ΔKE_{anom} was observed along with an inner-core (R_{max}) expansion of 8 km (Fig. 56b) that coincided with broad, strong convection in the northern eyewall at 0511 UTC 8 September (∼Hour 30.5 of the analysis, Fig. 55d).

Microwave satellite imagery at 1501 UTC 8 September (∼Hour 40.5 of the analysis, Fig. 55e) indicates that strong convection was present in a small eyewall and several spiral rainbands with loosely organized convection surrounded the storm center and extended outward to 3.5 degrees. Following an intensity (V_t) decrease of 2 m s^{-1} between 33 h and 39 h, Ivan experienced rapid intensification through Hour 57 with a V_t increase from 45 m s^{-1} to 59 m s^{-1} in 18 h (Fig. 56a). During this same period, the inner-core structure (R_{max}) contracted by 8 km and remained at a radius of 12–13 km through Hour 75 (Figs. 56b and 57b). From 33 h to 45 h, the R_{34} decreased by 54 km, and then increased by 41 km during rapid intensification (Fig. 56a). During the first 72 h of Ivan's life cycle moderate radial inflow variance was frequently present and coincident with observed convective asymmetries in or near the storm eyewall (Figs. 55–58). Contrary to Hurricane Frances, the correlation between radial inflow variance and 6-h changes in R_{34} for Ivan was less obvious.

Two organized spiral rainbands became tightly wrapped around Ivan's eyewall by 0552 UTC 9 September (∼Hour 55.5 of the analysis, Fig. 55f), and then a secondary eyewall formed as indicated by microwave satellite imagery at 1404 UTC 9 September (∼Hour 63.5 of the analysis, Fig. 58a). Strong convection existed in both the original and secondary eyewalls, and two or three spiral rainbands extended outward from the secondary eyewall to 3.5 degrees.

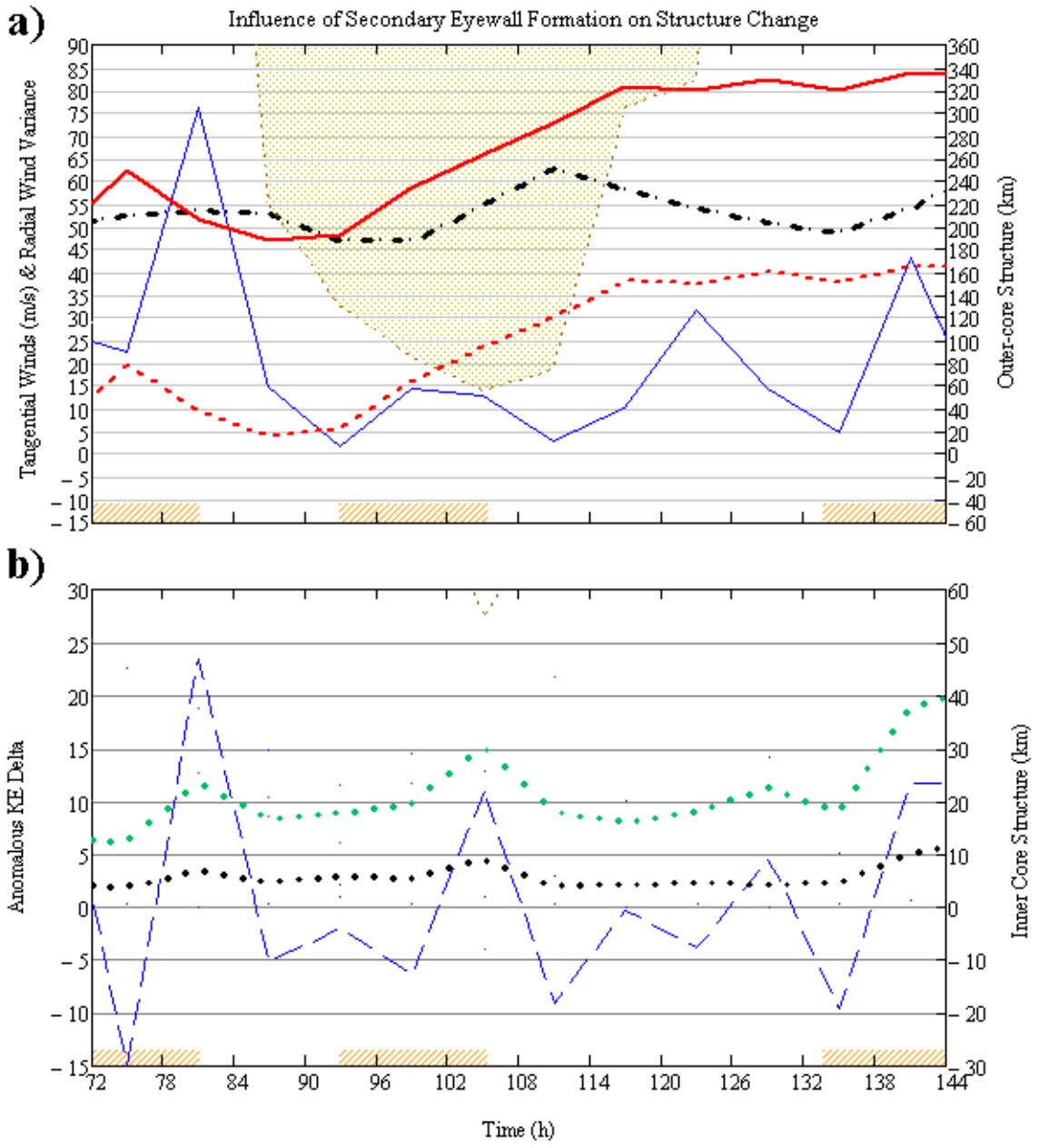

Figure 57 Time series of structure changes as in Fig. 48, except for Hurricane Ivan (2004) from 9 September at 2230 UTC (Hour 72) to 12 September at 2230 UTC (Hour 144), and the shaded region indicates land interaction within the R_{34} radius, where distance from storm center is on the right ordinate.

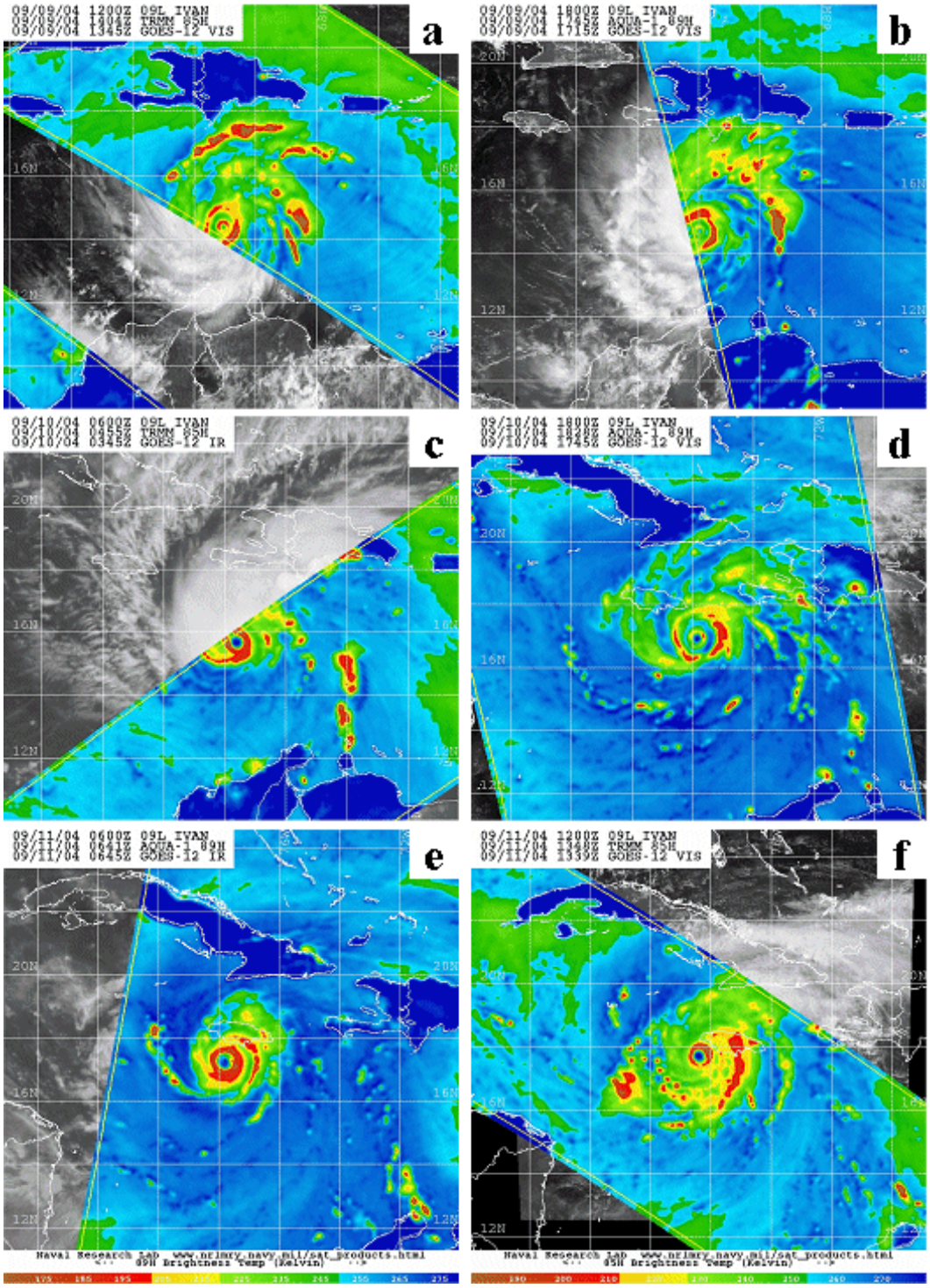

Figure 58 Microwave satellite imagery (85-89 GHz) for Hurricane Ivan from Aqua and TRMM polar orbiting platforms on (a) 9 September at 1404 UTC, (b) 9 September at 1745 UTC, (c) 10 September at 0455 UTC, (d) 10 September at 1828 UTC, (e) 11 September at 0641 UTC, and (f) 11 September at 1348 UTC (2004; from NRL 2007).

By 1745 UTC 9 September (∼Hour 67.5 of the analysis, Fig. 58b), it is evident that the convection in the original eyewall had weakened while the convection in the secondary eyewall remained strong, and then the original eyewall was replaced by the secondary eyewall as depicted by microwave satellite imagery at 0455 UTC 10 September (∼Hour 78.5 of the analysis, Fig. 58c).

During the first eyewall replacement cycle (orange hashed rectangles from Hour 64 to Hour 81 in Figs. 56 and 57), R_{max} and the inner eyewall both doubled (increased from 12 km to 24 km and from 4 km to 7 km, respectively) from 75 h to 81 h. This rapid expansion of the inner-core structure was associated with a strong outward ΔKE_{anom} (Fig. 57b). A large variance in radial inflow was also observed at Hour 81 during a period of time when a strong spiral rainband is interacting with the southern eyewall (Fig. 58c). During this first eyewall replacement cycle, only a modest increase in V_t from 52 m s^{-1} to 54 m s^{-1} occurred (Figs. 56a and 57a). Similar to Frances' second eyewall replacement cycle, microwave satellite imagery suggests more symmetry in the eyewall convection and surrounding spiral rainbands (Fig. 58c). Following secondary eyewall replacement, R_{max} and the inner eyewall radius contracted (Fig. 57b).

The azimuthal-average wind profiles in Fig. 59a prior to, following, and 6 h after the first eyewall replacement cycle (Hours 63, 81, and 87, respectively) suggest an initial increase in the outer-core structure (R_{34}), but only minimal changes during the 6 h after the replacement cycle. Whereas the R_{max} increased by 12 km during this eyewall replacement cycle followed by a decrease of 7 km 6 h after the cycle, the R_{34} increased by 14 km during this eyewall replacement cycle (blue arrow in Fig. 59a) and decreased by 4 km 6 h after the cycle (red arrow in Fig. 59a) for a net increase of 10 km.

The exponent x values assuming a modified Rankine vortex suggest that Ivan (as did Frances) had a larger outer-core structure prior to and during the first eyewall replacement cycle than the overall population of Atlantic tropical cyclones during 2003–2005 (Fig. 59b). Indeed, applying the overall mean value for exponent $x = 0.58$ in the modified Rankine vortex in Eq. (20) results in an under-prediction of R_{34} by 99–168 km prior to and during the first eyewall replacement cycle, as depicted by the stem plots in Fig. 59b. The mean modified Rankine vortex exponent x during the life cycle of Ivan was 0.44 with individual values of $x = 0.40$, $x = 0.52$, and $x = 0.46$ at Hours 63, 81, and 87, respectively. As with Frances, a sharper profile was

observed immediately after the secondary eyewall replacement. This time variability in the profile shapes suggests that accurately predicting the change in R_{34} with a fixed value for exponent x during secondary eyewall replacement may not be plausible.

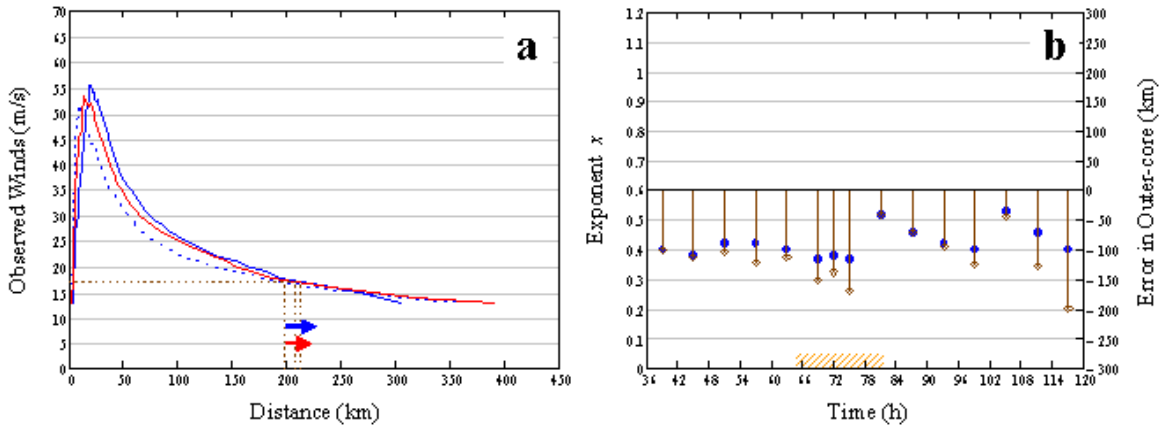

Figure 59 (a) Azimuthal-average wind profiles for Hurricane Ivan at Hour 63 (blue dashed line), Hour 81 (blue solid line) and Hour 87 (red solid line), and (b) observed values for exponent x in the modified Rankine vortex (blue circles) and the prediction error (stem plots) when the mean value for exponent $x = 0.58$ is applied in Eq. (20). The orange-hashed rectangle is the nominal period of the first eyewall replacement cycle.

The northwest quadrant of Ivan's outer-core structure (R_{34}) began to interact with the island of Jamaica at approximately Hour 86. From 87 h to 93 h, Ivan's intensity decreased by 6 m s^{-1} as the northwest quadrant of its outer-core structure approached Jamaica and moved from a distance 220 km to within 130 km (Fig. 57a). Microwave satellite imagery at 1828 UTC 10 September (~Hour 92 of the analysis, Fig. 58d) indicates that a new secondary eyewall had formed around the primary eyewall. Two spiral rainbands extended outward from the secondary eyewall to 3.5 degrees from the storm center. Ivan's intensity remained at 47 m s^{-1} between 93 h and 99 h as it approached Jamaica and moved within 85 km of the island (Fig. 57a). Microwave satellite imagery at 0641 UTC 11 September (~Hour 104 of the analysis, Fig. 58e) indicates that the secondary eyewall with broad convection had replaced the primary eyewall.

During this second eyewall replacement cycle (orange hashed rectangles from Hour 93 to Hour 105 in Fig. 57), R_{max} and the inner eyewall increased from 18 km to 30 km and 6 km to 9 km, respectively. This rapid expansion of the inner-core structure

was coincident with an outward ΔKE_{anom} (Fig. 57b). However, a rapid increase in V_t from 47 m s^{-1} to 63 m s^{-1} occurred from 99 h to 111 h as the storm center moved within 55 km of Jamaica's southern coast (Fig. 57a). Land interaction impacts will be further explored in a later section of this chapter. Similar to Frances' first eyewall replacement cycle, microwave satellite imagery suggests convective asymmetry in the spiral rainbands surrounding the eyewall (Fig. 58f). Following secondary eyewall replacement, R_{max} and the inner eyewall radius contracted to 18 km and 4 km, respectively (Fig. 57b).

The azimuthal-average wind profiles in Fig. 60a prior to, following, and 6 h after the second eyewall replacement cycle (Hours 87, 105, and 111, respectively) again suggest a time lag between changes in the inner-core structure (R_{max}) and changes in the outer-core structure (R_{34}). Whereas the R_{max} increase by 13 km during this eyewall replacement cycle was followed by a decrease of 12 km 6 h after the cycle, the R_{34} increased by 76 km during this eyewall replacement cycle (blue arrow in Fig. 60a) and continued to increase by an additional 23 km 6 h after the cycle (red arrow in Fig. 60a). Note that the profiles presented in Fig. 60a (as well as those in the remainder of this chapter) where land interaction is within the R_{34} are generated from the quadrants without land interaction.

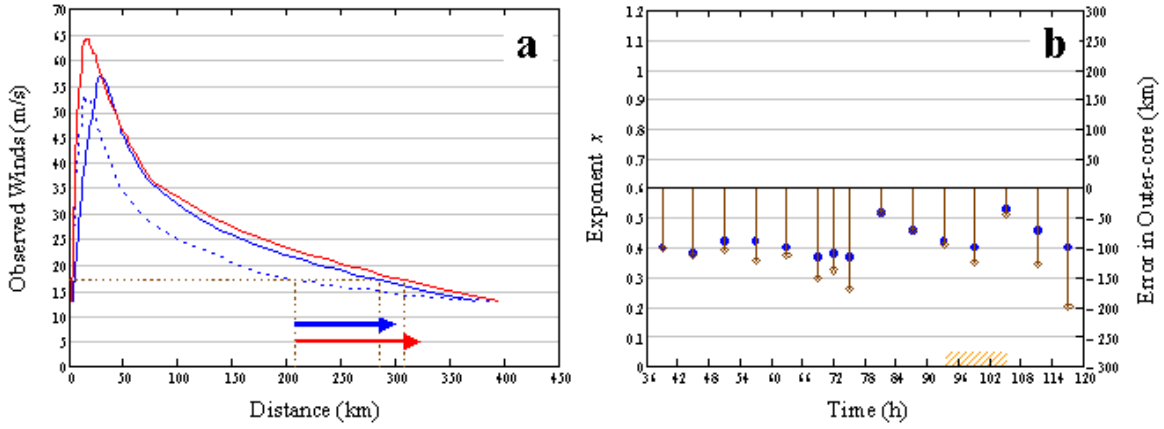

Figure 60 (a) Azimuthal-average wind profiles for Hurricane Ivan at Hour 87 (blue dashed line), Hour 105 (blue solid line) and Hour 111 (red solid line), and (b) observed values for exponent x in the modified Rankine vortex (blue circles) and the prediction error (stem plots) when the mean value for exponent $x = 0.58$ is applied in Eq. (20). The orange-hashed rectangle is the nominal period of the second eyewall replacement cycle.

Again, the exponent x values assuming a modified Rankine vortex suggest that Ivan had a larger outer-core structure prior to and during the second eyewall replacement cycle than the overall population of Atlantic tropical cyclones during 2003–2005 (Fig. 60b). Indeed, applying the overall mean value for exponent $x = 0.58$ in the modified Rankine vortex in Eq. (20) results in an under-prediction of R_{34} by 71–126 km prior to and during the second eyewall replacement cycle, as depicted by the stem plots in Fig. 60b. Individual exponent values for Hours 87, 105, and 111 were $x = 0.46$, $x = 0.53$, and $x = 0.46$, respectively. Again, a sharper profile was observed immediately after the secondary eyewall replacement. This time variability in the profile shapes suggests that accurately predicting the change in the R_{34} with a fixed value for exponent x during secondary eyewall replacement may not be plausible.

As Ivan moved away from Jamaica between 105 h and 117 h, the outer-core structure (R_{34}) continued to expand to an azimuthal-averaged value of 324 km (Fig. 57a). As hypothesized with an inward ΔKE_{anom}, R_{max} and the inner eyewall continued to contract to 11 km and 3 km, respectively (Fig. 57b). At 1348 UTC and 1911 UTC 11 September (∼Hours 111.5 and 116.5 of the analysis, Figs. 58f and 61a), very strong spiral rainbands surrounded the eyewall, except in the northwest quadrant. The enhanced convection in the spiral rainband approximately 1.5 degrees east of the storm center (Fig. 58f) may be the result of interaction with the island of Jamaica. Whereas the storm intensity (V_t) decreased to 54 m s^{-1} during the period from 117 h to 123 h, the inner- and outer-core structures of Ivan remain relatively unchanged (Fig. 57a).

Microwave satellite imagery at 0723 UTC 12 September (∼Hour 129 of the analysis, Fig. 61b) indicates that a new secondary eyewall had begun to form at a broad radius with two spiral rainbands that extended outward to 2.5 degrees. From 123 h to 135 h, the storm intensity continued to drop to 49 m s^{-1} (a 24-h decrease of 13 m s^{-1}), whereas the outer-core structure (R_{34}) remained relatively unchanged (Fig. 57a). Microwave satellite imagery at 1252 UTC 12 September (∼Hour 134.5 of the analysis, Fig. 61c) suggests the completion of secondary eyewall formation and the existence of well-defined spiral rainbands that extended outward to 3 degrees from the storm center. Visible satellite imagery at 1740 UTC 12 September (∼Hour 139.5 of the analysis, Fig. 61d), indicates the presence of a "moat" between the primary and secondary eyewalls.

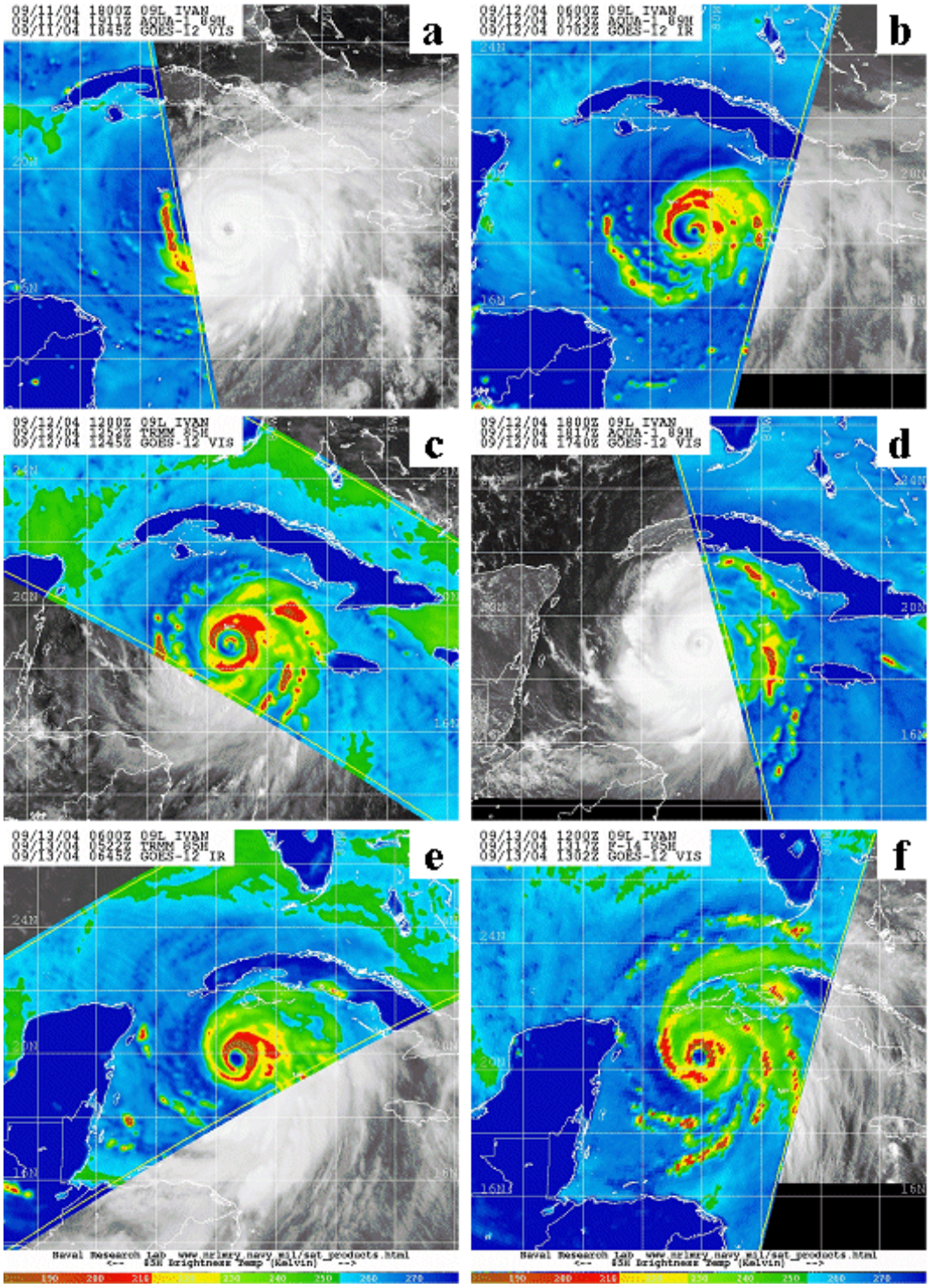

Figure 61 Microwave satellite imagery (85-89 GHz) for Hurricane Ivan from Aqua, TRMM, and DMSP polar orbiting platforms on (a) 11 September at 1911 UTC, (b) 12 September at 0723 UTC, (c) 12 September at 1252 UTC, (d) 12 September at 1817 UTC, (e) 13 September at 0522 UTC, and (f) 13 September at 1317 UTC (2004; from NRL 2007).

By 0522 UTC 13 September (∼Hour 151 of the analysis, Fig. 61e), the secondary eyewall had replaced the primary eyewall as evidenced by microwave satellite imagery.

During the third eyewall replacement cycle (orange hashed rectangles from Hour 134 to Hour 147 in Figs. 57 and 62), R_{max} and the inner eyewall increased by 23 km (from 18 km to 41 km) and 8 km (from 4 km to 12 km), respectively. As was the case in the previous case studies, an outward ΔKE_{anom} was present during rapid expansions of the inner-core structure (Figs. 57b and 62b). During this third eyewall replacement cycle, a rapid increase in V_t (13 m s^{-1} in 12 h) occurred and Ivan reached a second peak intensity of 62 m s^{-1} (Figs. 57a and 62a). Similar to Ivan's second eyewall replacement cycle, microwave satellite imagery suggests convective asymmetries were present in and near the eyewall (Fig. 61e). Contrary to above case studies of eyewall replacement cycles, R_{max} and the inner eyewall radius did not immediately contract following this eyewall replacement cycle (Fig. 62b).

The azimuthal-average wind profiles in Fig. 63a prior to, following, and 6 h after the third eyewall replacement cycle (Hours 135, 147, and 153, respectively) suggest an initial increase in the outer-core structure (R_{34}), but then minimal change during the 6 h after the replacement cycle. That is, the R_{34} initially increased by 17 km during this eyewall replacement cycle (blue arrow in Fig. 63a) and then decreased by 3 km 6 h after the cycle (red arrow in Fig. 63a), for a net increase of 14 km. Once again, the exponent x values assuming a modified Rankine vortex suggest that Ivan had a larger outer-core structure prior to and during the third eyewall replacement cycle than the overall population of Atlantic tropical cyclones during 2003–2005 (Fig. 63b). Indeed, applying the overall mean value for exponent $x = 0.58$ in the modified Rankine vortex in Eq. (20) results in an under-prediction of R_{34} by 67–213 km prior to and during the third eyewall replacement cycle, as depicted by the stem plots in Fig. 63b. Individual exponent values for Hours 135, 147, and 153 were $x = 0.36$, $x = 0.60$, and $x = 0.57$, respectively. As before, a sharper profile was observed immediately after the secondary eyewall replacement. This time variability in the profile shapes suggests that accurately predicting the change in the R_{34} with a fixed value for exponent x during secondary eyewall replacement may not be plausible.

Hurricane Ivan's outer-core structure (R_{34}) began to interact with western Cuba around Hour 147 and the storm center moved to within 110 km by Hour 171. However, minimal changes in the outer-core structure were observed until after 165 h when the storm center was within 150 km of western Cuba.

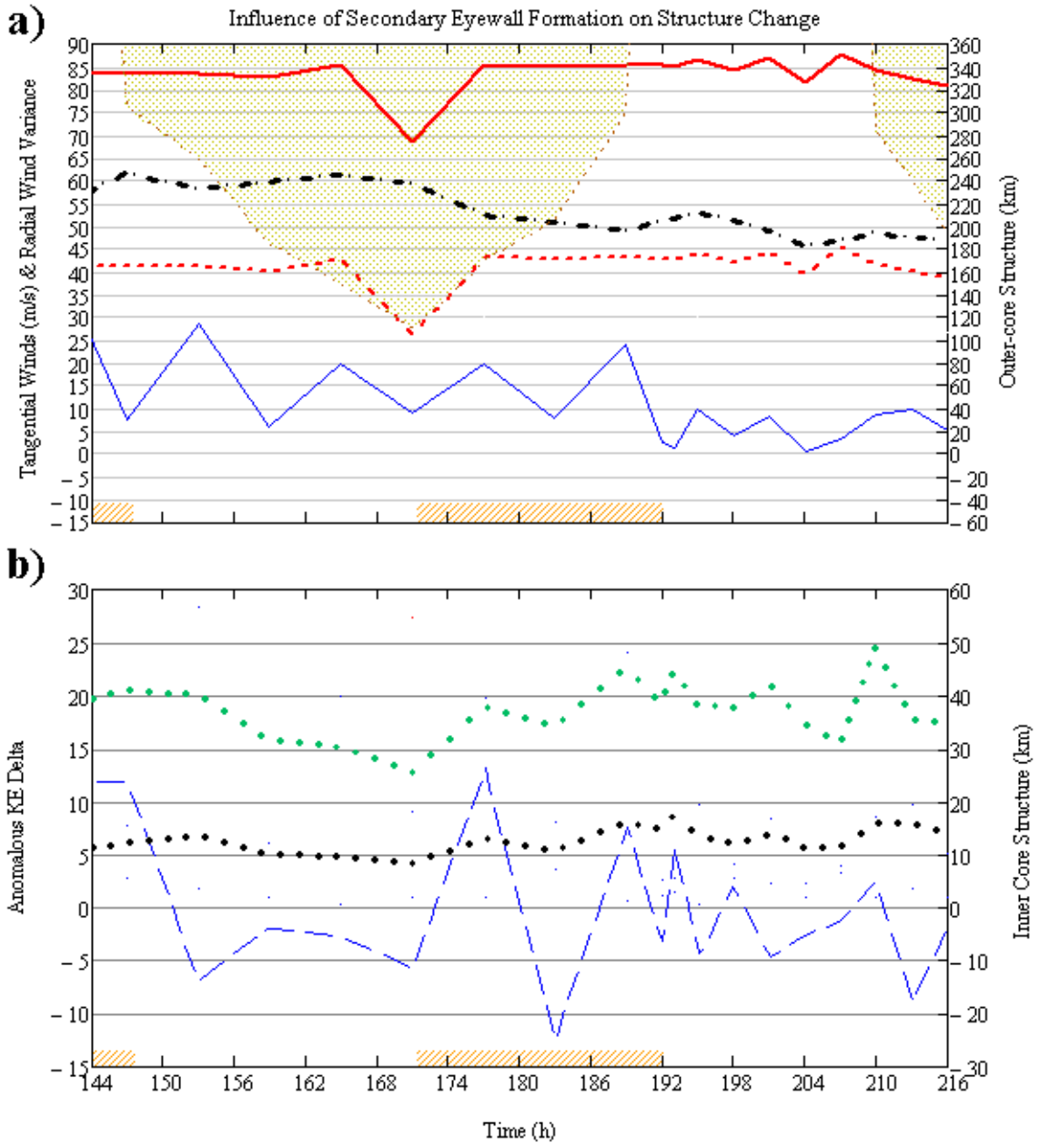

Figure 62 Time series of structure changes as in Fig. 48, except for Hurricane Ivan (2004) from 12 September at 2230 UTC (Hour 144) to 15 September at 2230 UTC (Hour 216), and the shaded region indicates land interaction within the R_{34} radius, where distance from storm center is on the right ordinate.

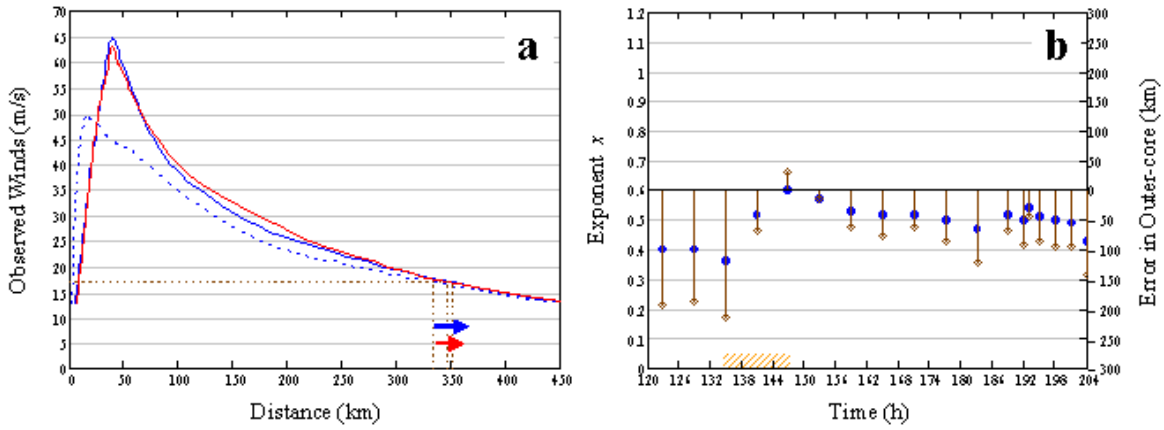

Figure 63 (a) Azimuthal-average wind profiles for Hurricane Ivan at Hour 135 (blue dashed line), Hour 147 (blue solid line) and Hour 153 (red solid line), and (b) observed values for exponent x in the modified Rankine vortex (blue circles) and the prediction error (stem plots) when the mean value for exponent $x = 0.58$ is applied in Eq. (20). The orange-hashed rectangle is the nominal period of the third eyewall replacement cycle.

From 165 h to 177 h, the R_{34} initially decreased by 67 km (from 342 km to 275 km), but quickly recovered to 343 km as the storm moved away for land (Fig. 62a). The effects of land interaction on storm structure will be further explored in a later section of this chapter. As the eyewall became more symmetric by 1317 UTC 13 September (∼Hour 159 of the analysis, Fig. 61f), R_{max} and the inner eyewall contracted by 15 km and 6 km, respectively, from 153 h to 171 h (Fig. 62b). During this inner-core contraction, an inward ΔKE_{anom} was observed (Fig. 62b). However, the intensity of Ivan remained nearly constant between 147 h and 171 h (Fig. 62a).

Microwave satellite imagery at 1900 UTC 13 September (∼Hour 164.5 of the analysis, Fig. 64a) indicates that one spiral rainband had wrapped fairly tightly around the eyewall at approximately 1.5 degrees from the storm center. Additionally, a second spiral rainband on the east side of the storm extended out to 2.5 degrees. Both spiral rainbands had enhanced convection where they interacted with western Cuba and along the band to the south. By 0427 UTC and 0710 UTC 14 September (∼Hours 174 and 176.5 of the analysis, Figs. 64b–c), a secondary eyewall appeared to have formed around the primary eyewall where the convection around this new eyewall was highly asymmetric with broad, strong convection toward the northeastern eyewall. The secondary eyewall became the dominant eyewall with a remnant of the primary

eyewall inward from the broad, strong convection in the northeast quadrant of the secondary eyewall by 1302 UTC 14 September (∼Hour 182.5 of the analysis, Fig. 64d). Microwave satellite imagery at 2344 UTC 14 September (∼Hour 193 of the analysis, Fig. 65a) indicates a large, broad secondary eyewall that has replaced the primary eyewall. During the fourth eyewall replacement cycle (orange hashed rectangles from Hour 171 to Hour 192 in Fig. 62), R_{max} and the inner eyewall approximately doubled with increases of 20 km (from 25 km to 45 km) and 8 km (from 8 km to 16 km), respectively. As in all of the previous eyewall case studies, an outward ΔKE_{anom} was present during this rapid expansion of the inner-core structure (Fig. 62b).

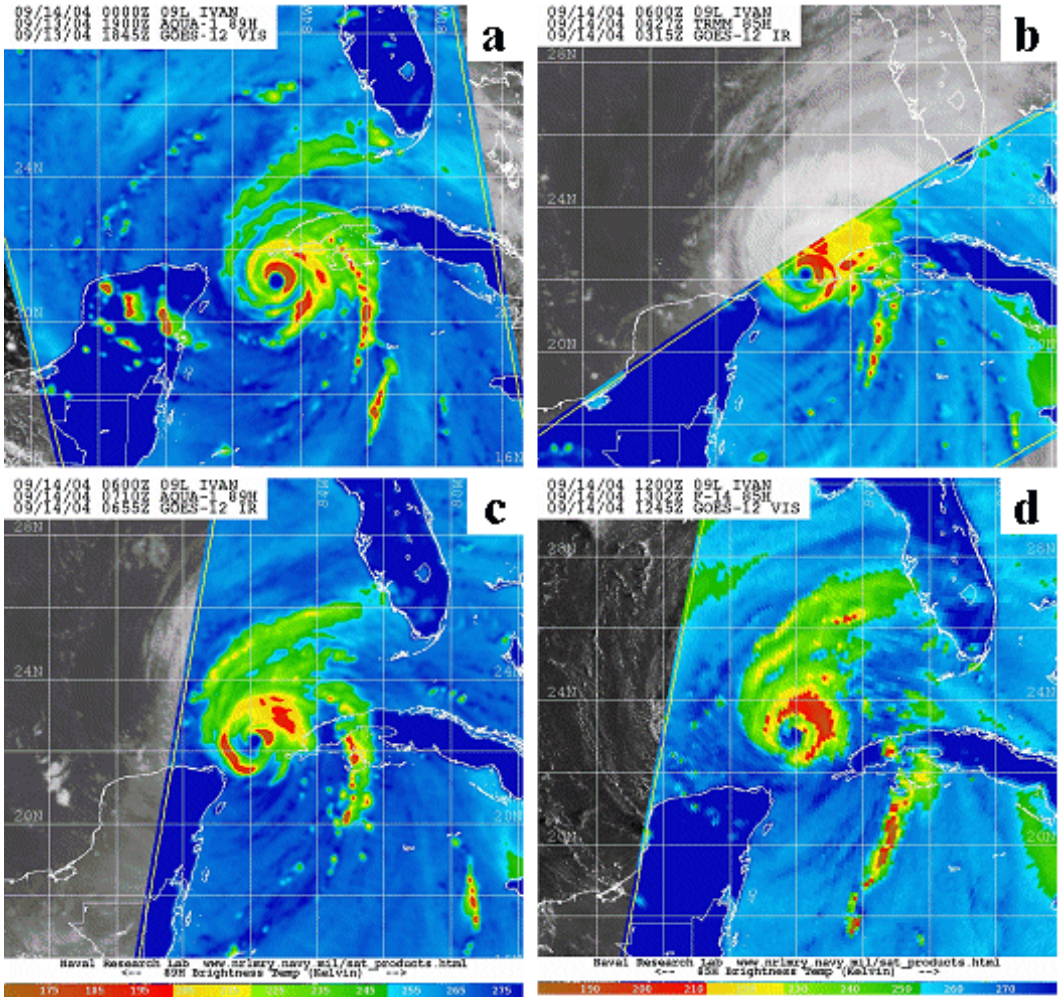

Figure 64 Microwave satellite imagery (85-89 GHz) for Hurricane Ivan from Aqua, TRMM, and DMSP polar orbiting platforms on (a) 13 September at 1900 UTC, (b) 14 September at 0427 UTC, (c) 14 September at 0710 UTC, and (d) 14 September at 1302 UTC (2004; from NRL 2007).

During this fourth eyewall replacement cycle, an initial decrease in storm intensity (V_t) by 10 m s^{-1} in 18 h was followed by an increase of 4 m s^{-1} in 6 h (Fig. 62a). As with Ivan's second and third eyewall replacement cycles, microwave satellite imagery suggests convective asymmetries were present in and near the eyewall (Figs. 64c–d). Following the completion of this eyewall replacement cycle, R_{max} and the inner eyewall radius contracted through Hour 207 (Fig. 62b).

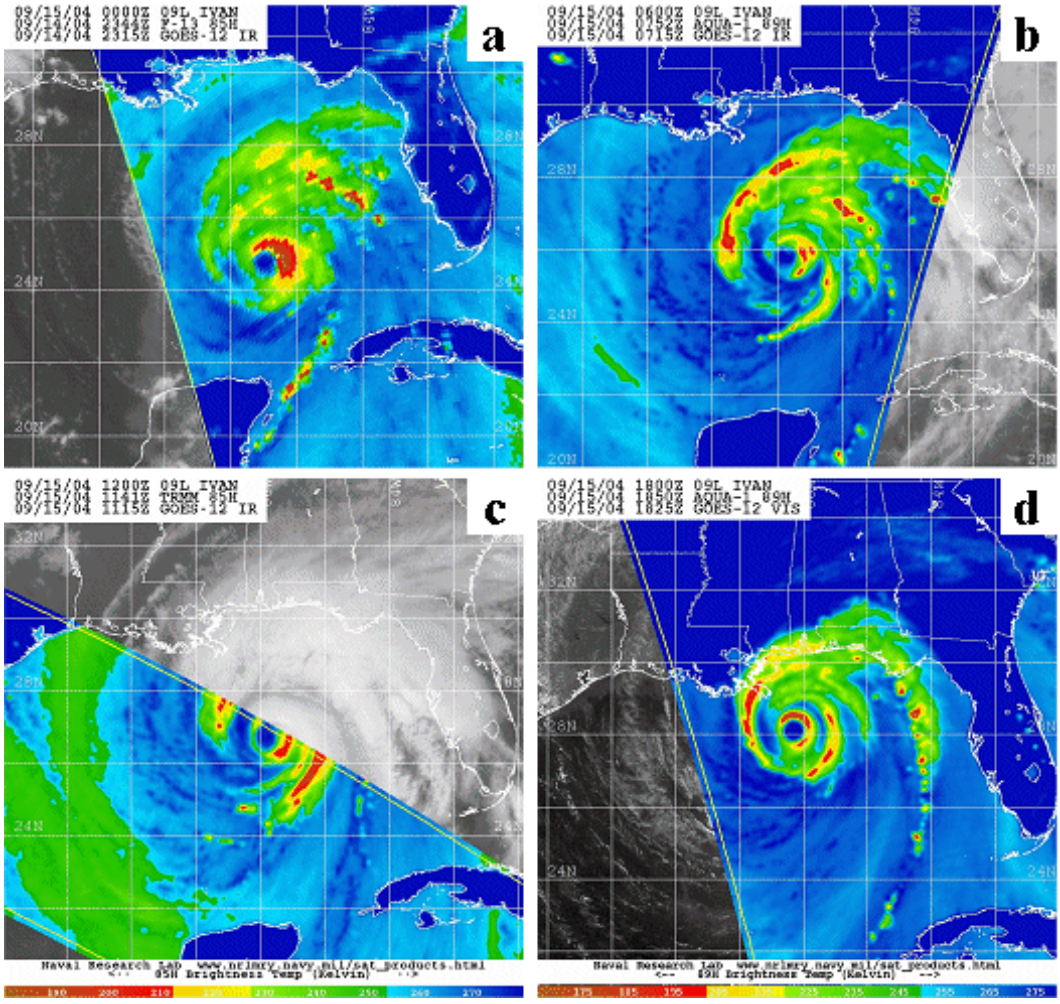

Figure 65 Microwave satellite imagery (85-89 GHz) for Hurricane Ivan from Aqua, TRMM, and DMSP polar orbiting platforms on (a) 14 September at 2344 UTC, (b) 15 September at 0752 UTC, (c) 15 September at 1141 UTC, and (d) 15 September at 1850 UTC (2004; from NRL 2007).

The azimuthal-average wind profiles in Fig. 66a prior to, following, and 6 h after the third eyewall replacement cycle (Hours 171, 192, and 198, respectively)

suggest an initial increase in the outer-core structure (R_{34}), but then minimal change during the 6 h after the replacement cycle. That is, the R_{34} initially increased by 59 km during this eyewall replacement cycle (blue arrow in Fig. 66a) and then decreased by 2 km 6 h after the cycle (red arrow in Fig. 66a), for a net increase of 57 km.

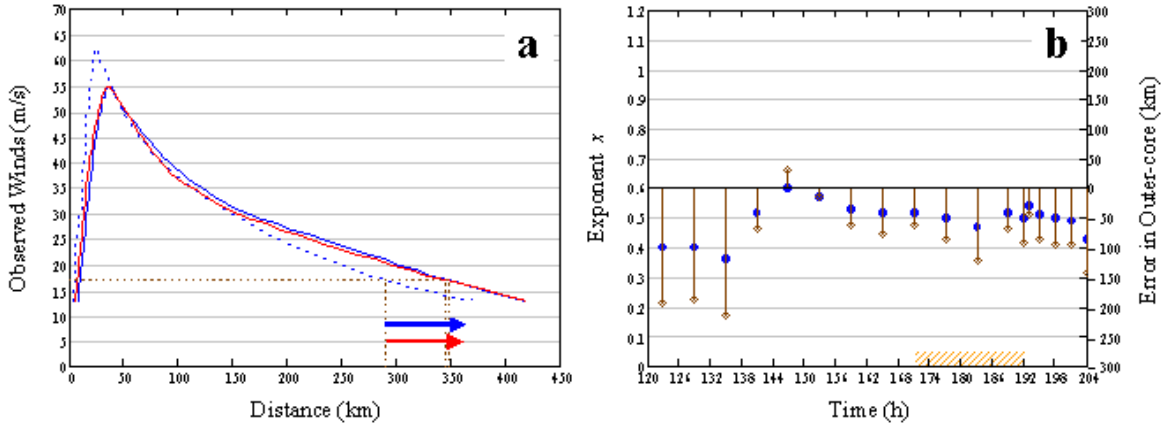

Figure 66 (a) Azimuthal-average wind profiles for Hurricane Ivan at Hour 171 (blue dashed line), Hour 192 (blue solid line) and Hour 198 (red solid line), and (b) observed values for exponent x in the modified Rankine vortex (blue circles) and the prediction error (stem plots) when the mean value for exponent $x = 0.58$ is applied in Eq. (20). The orange-hashed rectangle is the nominal period of the fourth eyewall replacement cycle.

As before, the exponent x values assuming a modified Rankine vortex suggest that Ivan had a larger outer-core structure prior to and during the fourth eyewall replacement cycle than the overall population of Atlantic tropical cyclones during 2003–2005 (Fig. 66b). Indeed, applying the overall mean value for exponent $x = 0.58$ in the modified Rankine vortex in Eq. (20) results in an under-prediction of R_{34} by 63–121 km prior to and during the fourth eyewall replacement cycle, as depicted by the stem plots in Fig. 66b. Individual exponent values for Hours 171, 192, and 198 were $x = 0.52$, $x = 0.50$, and $x = 0.50$, respectively. Contrary to the previous case studies, nearly the same exponent x following the secondary eyewall replacement as before the eyewall replacement would indicate a larger R_{34} when R_{max} increases, which is consistent with the 59 km increase. It is not clear why this eyewall replacement cycle was not followed by a sharpening of the radial profile.

Microwave satellite imagery at 0752 UTC and 1141 UTC 15 September (∼Hours 201.5 and 205 of the analysis, Figs. 65b–c) indicates a narrowing of the

convection in the eyewall with formation of two or three well-defined spiral rainbands surrounding the eyewall that extended outward to 3.5 degrees. A good correlation again exists between the direction of ΔKE_{anom} and changes in the R_{max} from 192 h and 216 h (Fig. 62b). Microwave satellite imagery at 1850 UTC 15 September ($\sim$Hour 212.5 of the analysis, Fig. 65d) appears to indicate the formation of another new secondary eyewall as Ivan approaches the southern Alabama coast. As the new partial eyewall formed, the R_{max} initially increased by 19 km, followed by a decrease by 14 km as the storm approached Alabama (Fig. 62b). From 195 h to 216 h, Ivan slowly weakened in intensity (V_t decreased 6 m s^{-1} in 21 h), and the outer-core structure (R_{34}) experienced small fluctuations of approximately 24 km or less (Fig. 62a).

In summary, four complete secondary eyewall replacement cycles occurred during the life cycle of Ivan from 2230 UTC 6 September to 2230 UTC 15 September. During all of the eyewall replacement cycles except the fourth, this tropical cyclone intensified with V_t increases of 2 m s^{-1}, 16 m s^{-1} and 13 m s^{-1}, respectively (Figs. 56a, 57a and 62a). In each case, the R_{max} approximately doubled (12 km, 12 km, 23 km, and 20 km increases, respectively). Inward (outward) ΔKE_{anom} was generally associated with a decrease (increase) of the R_{max} radius. Indeed, the correlation coefficient of 0.642 indicates a linear relationship between ΔKE_{anom} and R_{max}. An increase in radial inflow variance was observed when convective asymmetries in or near the eyewall were present, but increases in the R_{34} value did not generally follow within 6 h of the increased variance as with Frances (Figs. 56a, 57a and 62a).

The azimuthal-average wind profiles prior to, following, and 6 h after the four eyewall replacement cycles (Figs. 59, 60, 63, and 66) suggest that the R_{34} generally increased during secondary eyewall replacement, and that a time-lagged response was only present during the second eyewall replacement cycle. The range of exponent x values was 0.24–0.60, where the smaller (larger) values occurred prior to (after) a secondary eyewall replacement cycle. The exception was the fourth eyewall replacement cycle when the exponent x value remain nearly constant. Indeed, the exponent x increased from 0.40 to 0.52, 0.42 to 0.53, and 0.36 to 0.60 during the first three eyewall replacement cycles, respectively. Again with the exception of the fourth eyewall replacement, the eyewall replacement occurred when a flatter-than-average radial wind profile existed, and was followed by a sharper radial profile. Only in the fourth eyewall replacement would an assumption that the same wind profile shape would ex-

ist be appropriate. The influence of land interaction on the second and third eyewall replacement cycles will be further explored in a later section of this chapter.

d. *Katrina (2005)*

Katrina became a named storm by 0600 UTC 23 August over the western North Atlantic in the vicinity of 24.5°N, 76.5°W. This tropical cyclone had a northwestward track for about 24 h before turning westward. It continued on a westward track and strengthened into a hurricane at 1800 UTC 25 August as the storm made landfall over southern Florida near Miami. Hurricane Katrina re-emerged over the Gulf of Mexico by 0600 UTC 26 August and continued on a west-southwestward track for approximately 30 h prior to taking a northwestward track. Katrina had a northwestward track across the central Gulf of Mexico for 36 h before turning northward and making landfall along the southeastern Louisiana coast at approximately 1200 UTC 29 August. H*Wind analyses for Katrina became available at 0730 UTC 24 August and at regular increments for the remainder of the storm life cycle.

At 0730 UTC 27 August (hereafter referred to as Hour 0 of the analysis), Katrina had a tangential wind speed (V_t) of 42 m s^{-1} with azimuthal-average R_{max} and R_{34} values of 15 km and 267 km, respectively. Microwave satellite imagery at 0420 UTC 27 August (∼3 h prior to Hour 0 of the analysis, Fig. 67a) depicted a small eyewall with strong convection in the southern quadrant of the eyewall, and two spiral rainbands with strong convection to the east and south of the storm center that extended outward to 3 degrees. Enhanced convection was observed in the spiral rainbands that were interacting with western Cuba. During the first 6 h, a contraction of the R_{max} (3 km decrease) and inner eyewall (2 km decrease) radius occurred in the presence of weak inward ΔKE_{anom} (Fig. 68b).

Microwave satellite imagery at 2052 UTC 27 August (∼Hour 13.5 of the analysis, Fig. 67b) suggests that a secondary eyewall had formed and was in the process of replacing the convectively void original eyewall. Microwave satellite imagery at 0324 UTC 28 August (∼Hour 20 of the analysis, Fig. 67c) indicates that the broad, convectively active secondary eyewall had replaced the original eyewall and two weak spiral rainbands extending outward to 2 degrees. During this eyewall replacement cycle (orange hashed rectangles from Hour 0 to Hour 14 in Fig. 68), the R_{max} had more than tripled (increased from 16 km to 53 km) and inner eyewall more than doubled (increased from 6 km to 15 km) from 6 h to 14 h.

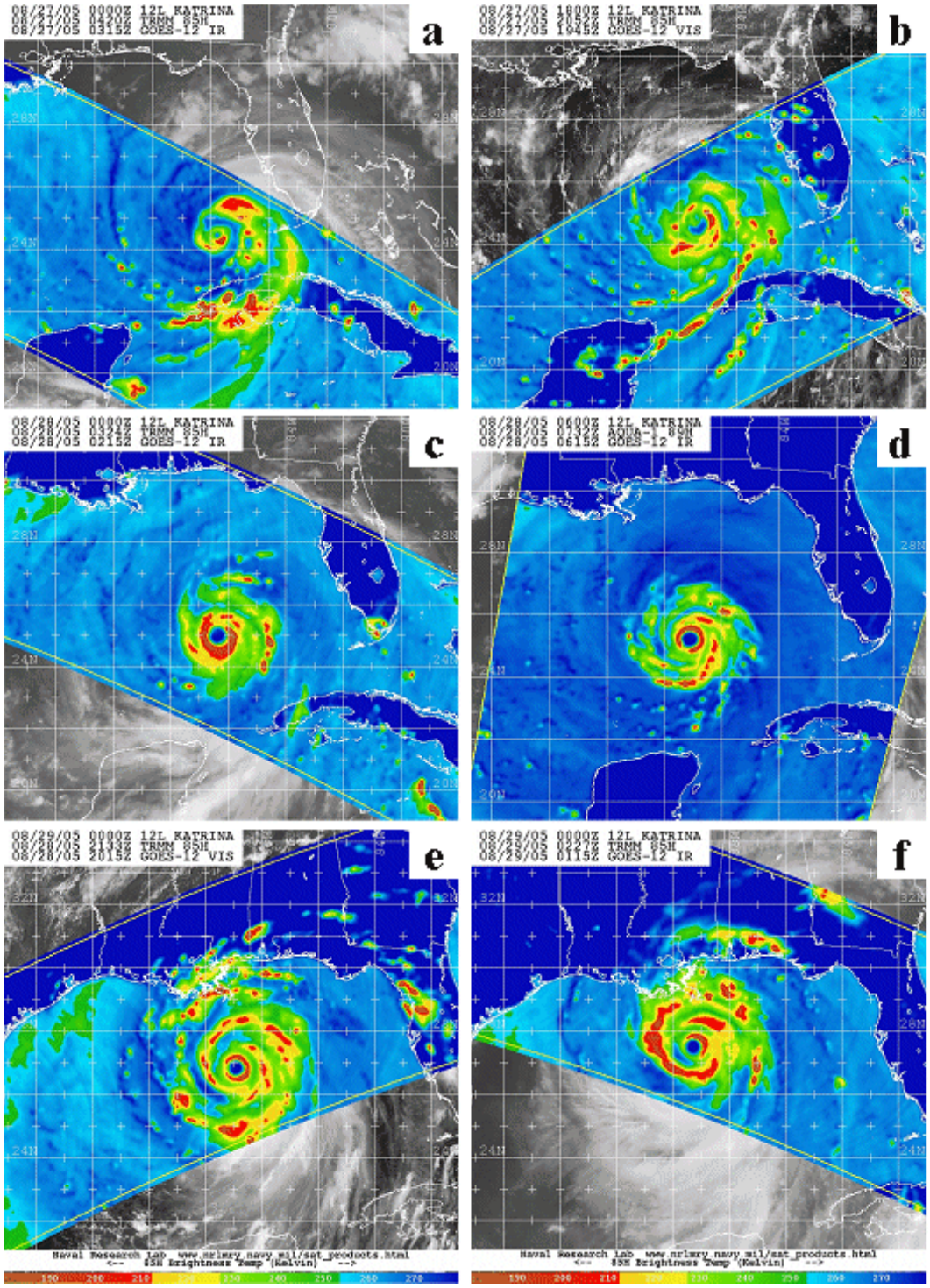

Figure 67 Microwave satellite imagery (85-89 GHz) for Hurricane Katrina from Aqua and TRMM polar orbiting platforms on (a) 27 August at 0420 UTC, (b) 27 August at 2052 UTC, (c) 28 August at 0324 UTC, (d) 28 August at 0732 UTC, (e) 28 August at 2133 UTC, and (f) 29 August at 0227 UTC (2005; from NRL 2007).

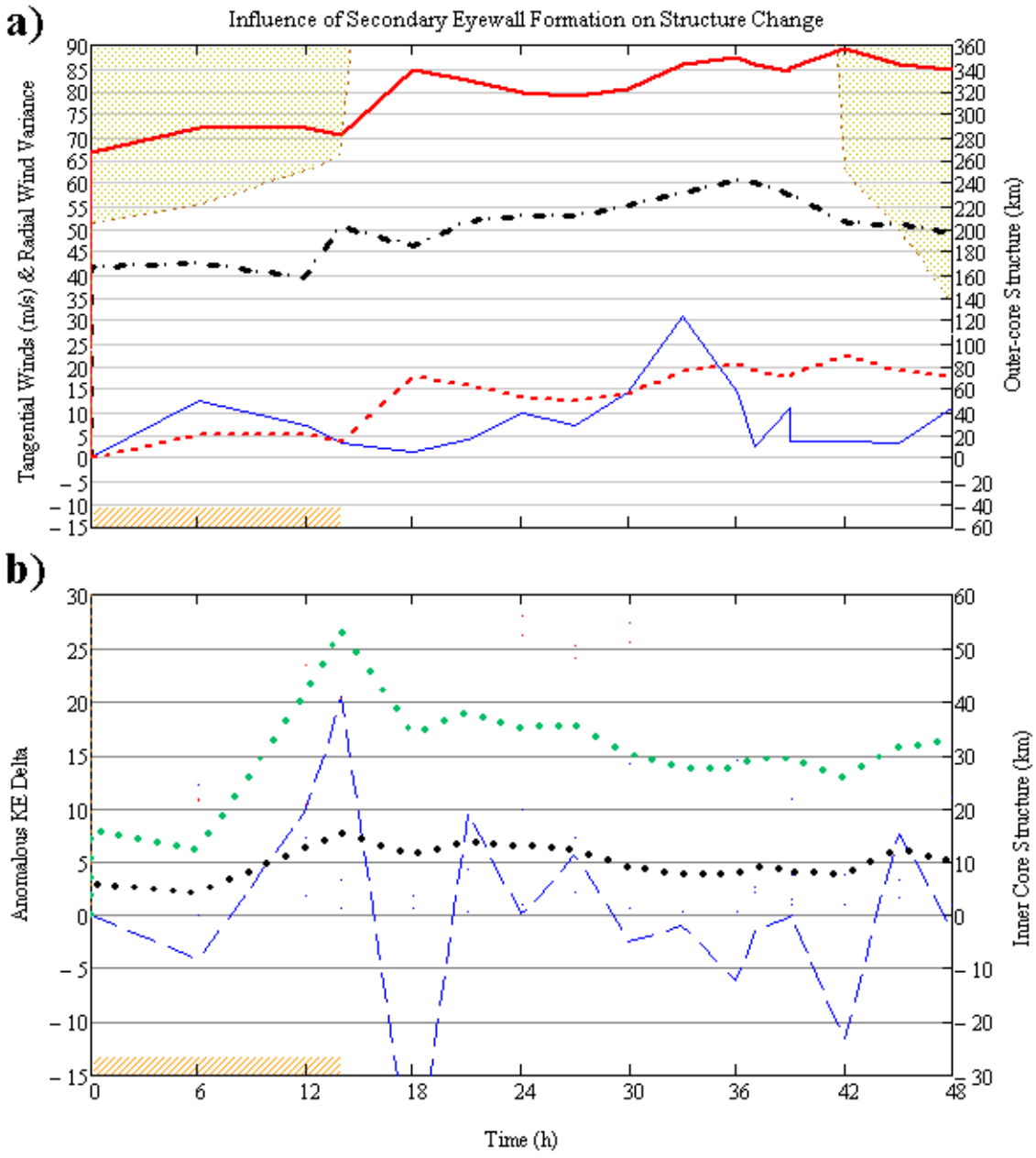

Figure 68 Time series of structure changes as in Fig. 48, except for Hurricane Katrina (2005) from 27 August at 0730 UTC (Hour 0) to 29 August at 0730 UTC (Hour 48), and the shaded region indicates land interaction within the R_{34} radius, where distance from storm center is on the right ordinate.

This rapid expansion of the inner-core structure was coincident with very strong outward ΔKE_{anom} (Fig. 68b). During the later part of this eyewall replacement cycle, a very rapid increase in V_t from 40 m s^{-1} to 51 m s^{-1} occurred in just 2 h (Fig. 68a). As with the rapid intensification during Frances' first eyewall replacement cycle, microwave satellite imagery suggests that convective asymmetries existed in the eyewall and surrounding spiral rainbands (Fig. 67b). Following secondary eyewall replacement, R_{max} and the inner eyewall radius contracted in the presence of inward ΔKE_{anom} (Fig. 68b).

The azimuthal-average wind profiles in Fig. 69a prior to, following, and 4 h after this eyewall replacement cycle (Hours 0, 14, and 18, respectively) suggest that a time lag exists between changes in the inner-core structure (R_{max}) and changes in the outer-core structure (R_{34}). Whereas the R_{max} increased by 37 km during this eyewall replacement cycle and then was followed by a decrease of 19 km 4 h after the cycle, the R_{34} increased by 19 km during this eyewall replacement cycle (blue arrow in Fig. 69a) and continued to increase by an additional 52 km 4 h after the cycle (red arrow in Fig. 69a). The peripheral land interaction with western Cuba (at a distance of 205 km or greater) during this eyewall replacement cycle appeared to have a minimal affect on the inner- and outer-core structures.

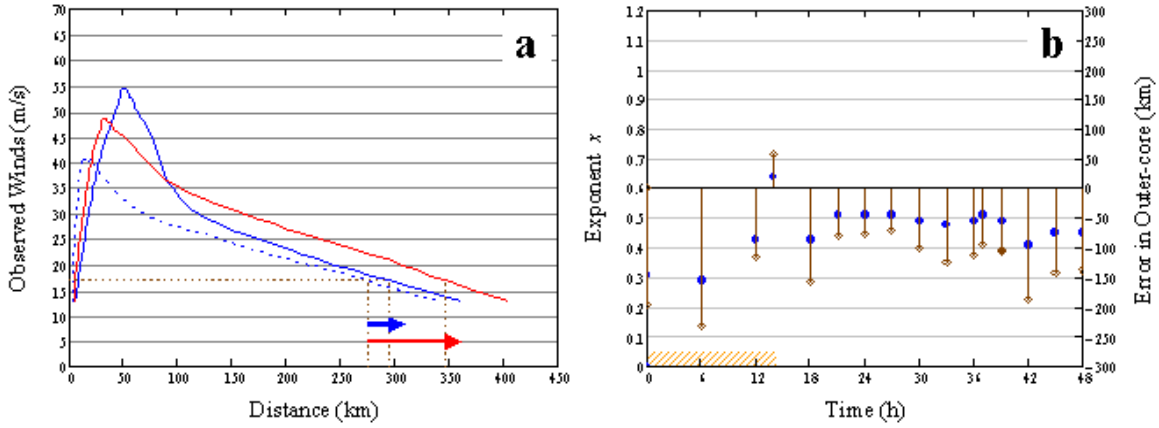

Figure 69 (a) Azimuthal-average wind profiles for Hurricane Katrina at Hour 0 (blue dashed line), Hour 14 (blue solid line) and Hour 18 (red solid line), and (b) observed values for exponent x in the modified Rankine vortex (blue circles) and the prediction error (stem plots) when the mean value for exponent $x = 0.58$ is applied in Eq. (20). The orange-hashed rectangle is the nominal period of the eyewall replacement cycle.

The exponent x values assuming a modified Rankine vortex suggest that Katrina had a larger outer-core structure prior to and during this eyewall replacement cycle than the overall population of Atlantic tropical cyclones during 2003–2005 (Fig. 69b). Indeed, applying the overall mean value for exponent $x = 0.58$ in the modified Rankine vortex in Eq. (20) results in an under-prediction of R_{34} by 116–230 km prior to and during this eyewall replacement cycle, as depicted by the stem plots in Fig. 69b. The mean modified Rankine vortex exponent x during the life cycle of Katrina was 0.46 with individual values of $x = 0.31$, $x = 0.64$, and $x = 0.43$ at Hours 0, 14, and 18, respectively. As with three of the four Ivan cases, this time evolution with a sharpening of the radial profile of tangential winds following the eyewall replacement indicates a conceptual model of constant radial profile shapes would not apply. This time variability in the profile shapes suggests that accurately predicting the change in R_{34} with a fixed value for exponent x during secondary eyewall replacement may not be plausible.

Hurricane Katrina's intensity (V_t) decreased by 4 m s^{-1} between 14 h and 18h, and then rapidly intensified (increase of 15 m s^{-1} in 18 h) through Hour 36 to a peak intensity of 61 m s^{-1} (Fig. 68a). Microwave satellite imagery at 0732 UTC 28 August (∼Hour 24 of the analysis, Fig. 67d) indicated increased organization of the symmetric eyewall and a narrowing of the eyewall convection. Of the spiral rainbands present, the one extending east and south of the storm center had the best organized strong convection. From 14 h to 42 h, R_{max} and the inner eyewall decreased to 26 km and 8 km, respectively, while the R_{34} continued to expand to a size of 356 km (Fig. 68). During this period, temporary increases in the R_{max} generally appear to be associated with the presence of outward ΔKE_{anom} (Fig. 68b).

A large spike in the radial inflow variance was observed around Hour 33 just prior to the peak intensity of Katrina. At this time, two convectively active spiral rainbands that were wrapped tightly around the primary eyewall in all quadrants as depicted by microwave satellite imagery at 2133 UTC 28 August (∼Hour 38 of the analysis, Fig. 67e). As with Ivan, it is not always observed that an increase in radial inflow variance is associated with a subsequent increase in the R_{34} radius. As Katrina approached the Gulf Coast between 36h and 48 h, the storm intensity (V_t) steadily weakened from 61 m s^{-1} to 49 m s^{-1} (Fig. 68a). Although the tropical cyclone intensity was decaying, the outer-core structure (R_{34}) only fluctuated in size by 17 km. Microwave satellite imagery at 0227 UTC 29 August (∼Hour 43 of the analysis,

Fig. 67f) suggests that broad, strong convection in the spiral rainbands may have been forming a new secondary eyewall. Perhaps, as a result of the formation of this partial secondary eyewall, the R_{max} expanded by 7 km (Fig. 68b).

In summary, one complete secondary eyewall replacement cycle occurred from 0730 UTC 27 August to 0730 UTC 29 August when Katrina was over the Gulf of Mexico. During this eyewall replacement cycle, Katrina had a V_t increase of 9 m s^{-1} (Fig. 68a). The R_{max} tripled (37 km increase) during the beginning of this eyewall replacement cycle, but then a contraction occurred at the end of the cycle (Fig. 68b). Inward (outward) ΔKE_{anom} was generally associated with a decrease (increase) of the R_{max} radius. Indeed, the correlation coefficient of 0.775 indicates a linear relationship between ΔKE_{anom} and R_{max}. An increase in radial inflow variance was observed when convective asymmetries in or near the eyewall were present, but an increase in the R_{34} value did not follow within 6 h of the increased variance as observed with Frances (Fig. 68a).

The azimuthal-average wind profiles prior to, following, and 4 h after this eyewall replacement cycle (Fig. 69) suggests that the R_{34} did have a time-lagged increase following secondary eyewall replacement. The range of exponent x values was 0.29–0.64, where the smaller (larger) values occurred prior to (after) the secondary eyewall replacement cycle. Indeed, the exponent x increased from 0.31 to 0.64 during this eyewall replacement cycle, which indicates a sharpening of the radial profile following the eyewall replacement. However, the tripling of R_{max} plus the intensification still led to an increase in R_{34} to 356 km. This outward expansion was a factor in the damage along the Gulf coast well to the east of the Katrina landfall position.

e. *Wilma (2005)*

Wilma became a named storm by 0600 UTC 17 October over the western Caribbean Sea in the vicinity of 17.3°N, 79.6°W. This tropical cyclone had a southward, and then south-southwestward track for 30 h before strengthening into a hurricane at 1200 UTC 18 October. After reaching hurricane intensity, Wilma moved slowly northwestward and made landfall over the northeastern Yucatan Peninsula at approximately 0200 UTC 22 October. Hurricane Wilma re-emerged over the Gulf of Mexico at approximately 0130 UTC 23 October and headed more quickly on a northeastward track before making a second landfall over southern Florida at approximately 1100 UTC 24 October. This storm re-emerged over the western North Atlantic at ap-

proximately 1430 UTC 24 October and moved parallel to the east coast of the United States before eventually heading eastward across the northern Atlantic at about 46°N. H*Wind analyses for Wilma became available at 1800 UTC 17 October and at regular increments until 1930 UTC 24 October as the storm moved away from land and across the North Atlantic.

At 0730 UTC 18 October (hereafter referred to as Hour 0 of the analysis), Wilma had a tangential wind speed (V_t) of 23 m s^{-1} with azimuthal-average R_{max} and R_{34} values of 17 km and 132 km, respectively. During the first 12 h of the analysis, Wilma had a small R_{max} and inner eyewall that expanded period by 2 km and 8 km, respectively (Fig. 70b). Microwave satellite imagery at 1857 UTC 18 October (∼Hour 11.5 of the analysis, Fig. 71a) indicates the presence of very strong convection around a small eyewall with three loosely organized spiral rainbands extending outward to 4 degrees. As Wilma became more organized, the intensity (V_t) steadily increased by 4 m s^{-1} and the R_{34} increased by 101 km during the first 12 h (Fig. 70a).

Microwave satellite imagery at 0125 UTC and 0709 UTC 19 October (∼Hours 18 and 23.5 of the analysis, Figs. 71b–c) indicates very strong symmetric convection over the eyewall with three loosely organized spiral rainbands that continued to extend up to 4 degrees from the storm center. One rainband at approximately 2 degrees east of the center had more broad, organized convection than the other rainbands. From 12 h to 24 h, an explosive intensification from 27 m s^{-1} to 61 m s^{-1} was observed, which is a V_t increase of 34 m s^{-1} in just 12 h (Fig. 70a). This explosive intensification coincided with a contraction of R_{max} and the inner eyewall by 13 km each to extremely small values of 6 km and 2 km, respectively (Fig. 70b). During the period from 12 h to 24 h, the outer-core structure (R_{34}) contracted by 28 km, and thus was not in agreement with the expectations from the empirical wind distribution in Fig. 1 or the axisymmetric models that suggest an increase in outer winds (R_{34}) during intensification (Fig. 70a). However, it should be noted that the R_{34} had a large increase (108 km) in the 12 h after rapid intensification, which suggests a time lag in the outer-core structure change during explosive intensification.

Microwave satellite imagery at 1400 UTC and 1740 UTC 19 October (∼Hours 29.5 and 34 of the analysis, Figs. 71d–e) indicates the formation of a secondary eyewall with three spiral rainbands, two of which had very strong, organized convection extending outward to 3.5 degrees.

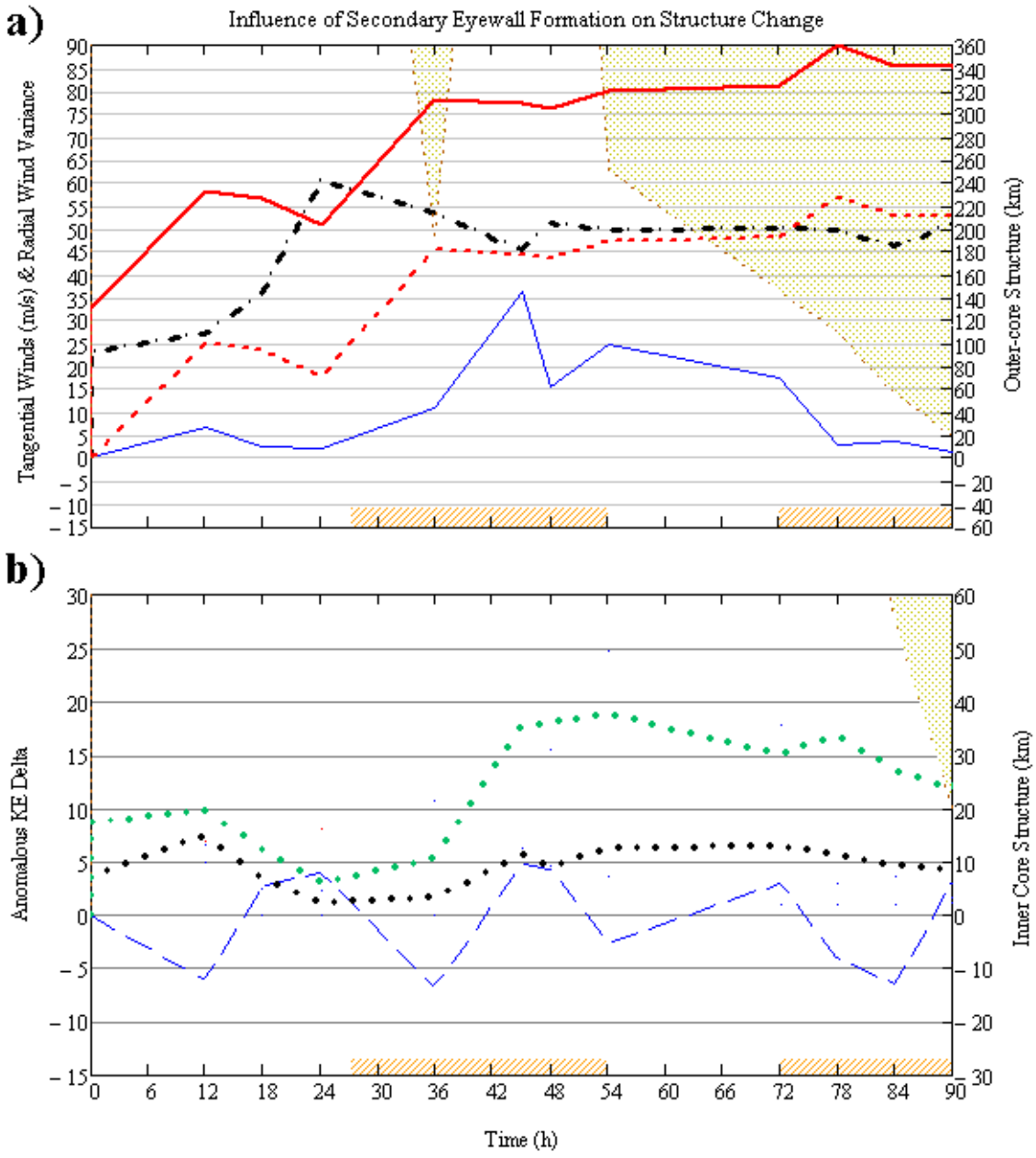

Figure 70 Time series of structure changes as in Fig. 48, except for Hurricane Wilma (2005) from 18 October at 0730 UTC (Hour 0) to 22 October at 0130 UTC (Hour 90), and the shaded region indicates land interaction within the R_{34} radius, where distance from storm center is on the right ordinate.

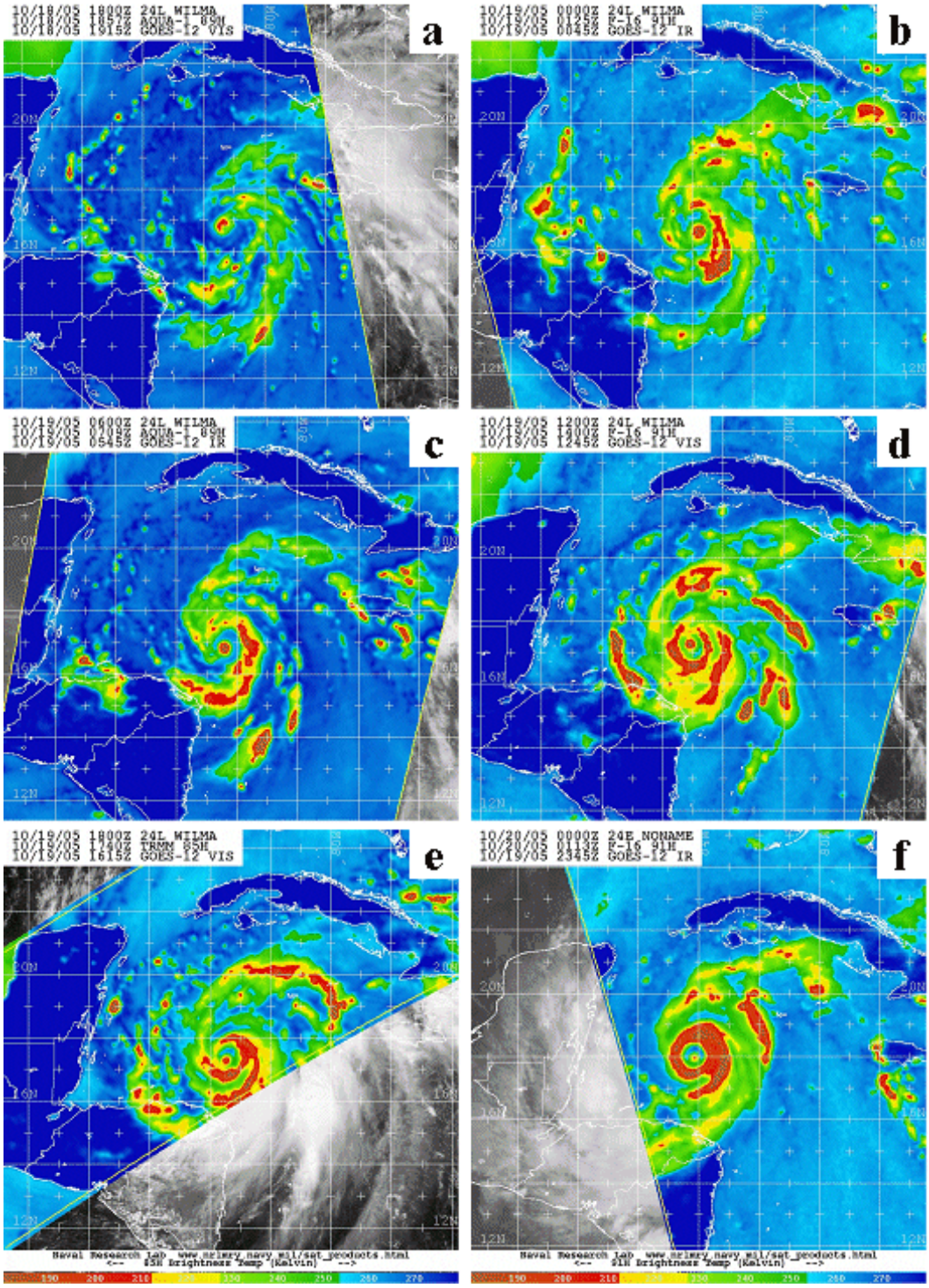

Figure 71 Microwave satellite imagery (85-91 GHz) for Hurricane Wilma from Aqua, TRMM, and DMSP polar orbiting platforms on (a) 18 October at 1857 UTC, (b) 19 October at 0125 UTC, (c) 19 October at 0709 UTC, (d) 19 October at 1400 UTC, (e) 19 October at 1740 UTC, and (f) 20 October at 0113 UTC (2005; from NRL 2007).

The secondary eyewall developed broad, strong convection while the convection in the primary eyewall diminished as evidenced by microwave satellite imagery at 0113 UTC and 1347 UTC 20 October (∼Hours 41.5 and 54.5 of the analysis, Figs. 71f and 72a). Microwave satellite imagery at 1845 UTC 20 October (∼Hour 59.5 of the analysis, Fig. 72b) depicts a secondary eyewall that had all but replaced the primary eyewall, although a small remnant of the original eyewall was still evident. Whereas the convection in the new eyewall narrowed and became more symmetric, the convection in the spiral rainbands weakened.

During the first eyewall replacement cycle (orange hashed rectangles from Hour 27 to Hour 54 in Fig. 70), R_{max} and the inner eyewall both increased by approximately five-fold (increased from 6 km to 38 km and from 2 km to 13 km, respectively). This rapid expansion of the R_{max} coincided with weak outward ΔKE_{anom} and a strong variance of the radial inflow (Fig. 70). As the secondary eyewall became the dominant eyewall (see Fig. 72b), organized spiral rainband convection weakened and the storm intensity (V_t) initially weakened (decreased from 61 m s^{-1} to 45 m s^{-1}). However, a brief period of rapid intensification of 6 m s^{-1} in 3 h (Fig. 70a) occurred at the end of the first eyewall replacement cycle.

The azimuthal-average wind profiles in Fig. 73a prior to, following, and 18 h after the first eyewall replacement cycle (Hours 24, 54, and 72, respectively) suggest an initial increase in the outer-core structure (R_{34}), and then minimal change 18 h after the replacement cycle. Whereas the R_{max} increased by 32 km during this eyewall replacement cycle and then was followed by a decrease of 8 km 18 h after the cycle, the R_{34} increased by 108 km during this eyewall replacement cycle (blue arrow in Fig. 73a) and then remained essentially constant 18 h after the cycle (red arrow in Fig. 73a) for a net increase of 109 km. The brief interaction of the outer-core structure within 195 km of northeastern Honduras appears to have had minimal impact on the R_{34} radius.

The exponent x values assuming a modified Rankine vortex suggest that Wilma had a larger outer-core structure prior to and during the first eyewall replacement cycle than the overall population of Atlantic tropical cyclones during 2003–2005 (Fig. 73b). Indeed, applying the overall mean value for exponent $x = 0.58$ in the modified Rankine vortex in Eq. (20) results in an under-prediction of R_{34} by 71–238 km prior to and during the first eyewall replacement cycle, as depicted by the stem plots in Fig. 73b.

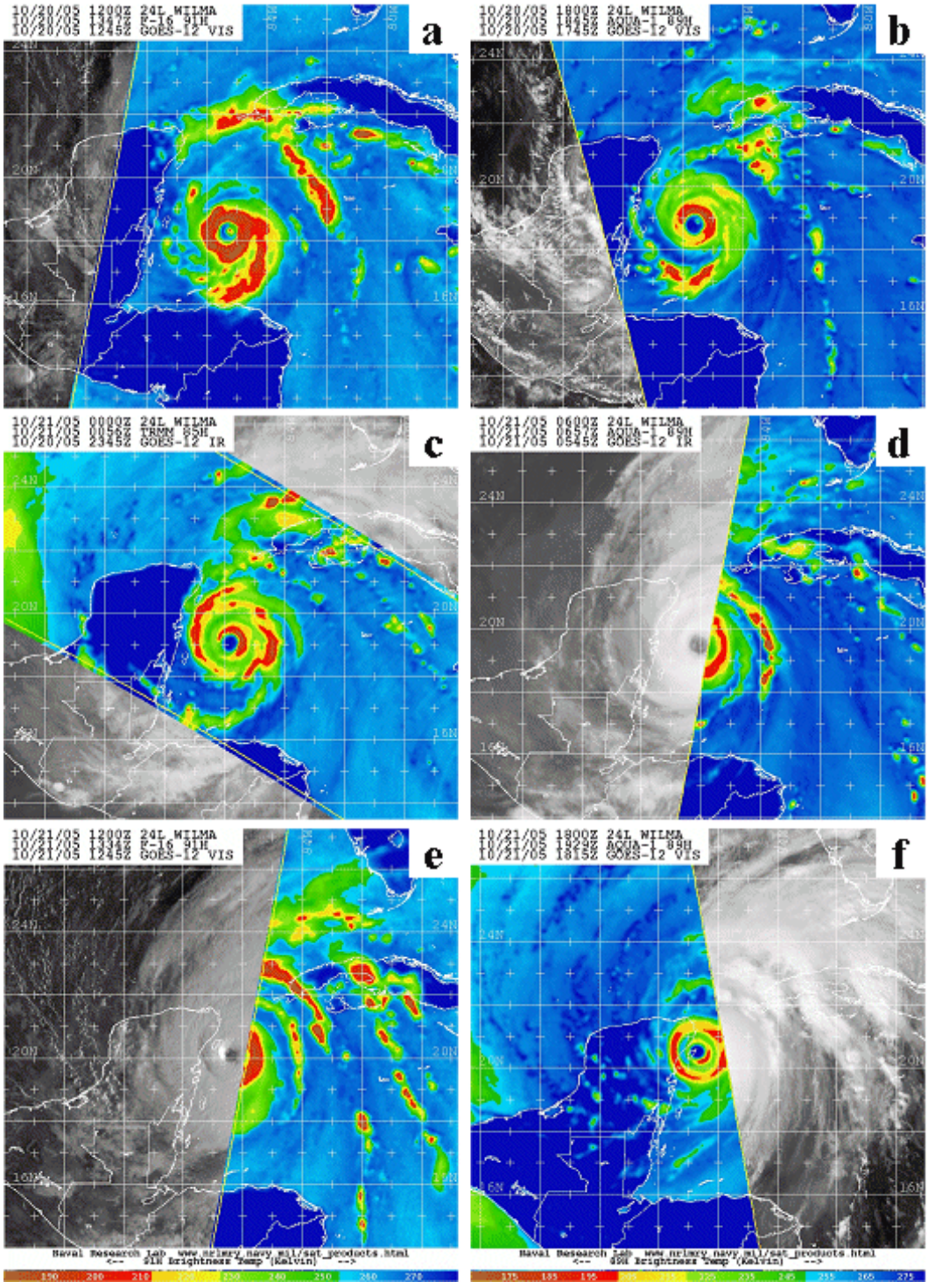

Figure 72 Microwave satellite imagery (85-91 GHz) for Hurricane Wilma from Aqua, TRMM, and DMSP polar orbiting platforms on (a) 20 October at 1347 UTC, (b) 20 October at 1845 UTC, (c) 21 October at 0056 UTC, (d) 21 October at 0657 UTC, (e) 21 October at 1334 UTC, and (f) 21 October at 1929 UTC (2005; from NRL 2007).

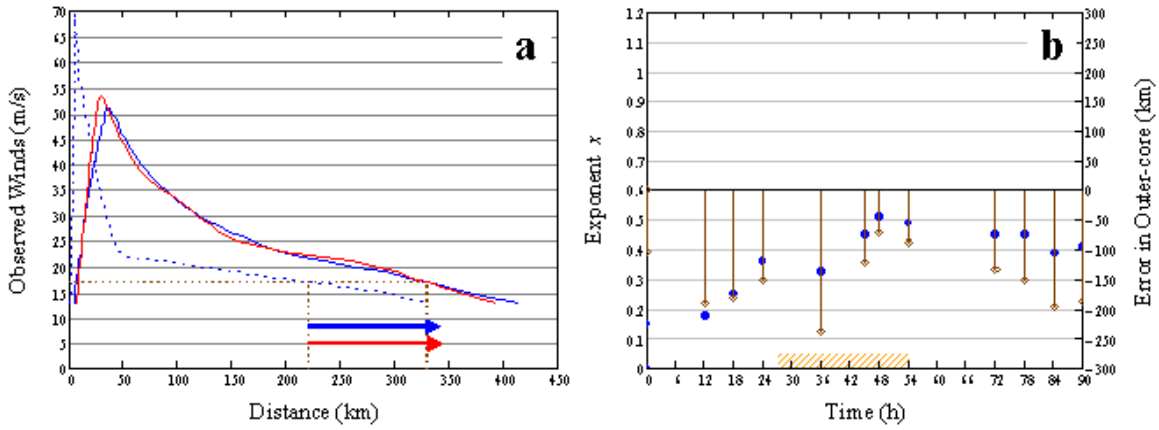

Figure 73 (a) Azimuthal-average wind profiles for Hurricane Wilma at Hour 24 (blue dashed line), Hour 54 (blue solid line) and Hour 72 (red solid line), and (b) observed values for exponent x in the modified Rankine vortex (blue circles) and the prediction error (stem plots) when the mean value for exponent $x = 0.58$ is applied in Eq. (20). The orange-hashed rectangle is the nominal period of the first eyewall replacement cycle.

The mean modified Rankine vortex exponent x during the first 114 h of Wilma's life cycle was 0.35 with individual values of $x = 0.36$, $x = 0.49$, and $x = 0.45$ at Hours 24, 54, and 72, respectively. As with the fourth case study of Ivan, this secondary eyewall replacement was not followed by a sharpening of the wind profile. However, Wilma had a greater intensity and sharper wind profile prior to eyewall replacement than is typically observed for Atlantic hurricanes. This time variability in the profile shapes again suggests that accurately predicting the change in the R_{34} with a fixed value for exponent x during secondary eyewall replacement may not be plausible.

Microwave satellite imagery at 0056 UTC and 0657 UTC 21 October (∼Hours 65.5 and 71.5 of the analysis, Figs. 72c–d) indicates the formation of a new secondary eyewall with one convectively active spiral rainband extending outward to 2.5 degrees in the north and east quadrants. As Wilma approached the northeastern Yucatan Peninsula, the secondary eyewall had developed strong, symmetric convection, as evidenced by microwave satellite imagery at 1334 UTC and 1929 UTC 21 October (∼Hours 78 and 84 of the analysis, Figs. 72e–f). Microwave satellite imagery at 0739 UTC and 1631 UTC 22 October (∼Hours 96 and 105 of the analysis, Figs. 74a–b) depicts a sequence of events in which the primary eyewall moved completely over land and dissipated, whereas three quadrants of the secondary eyewall remained over water and

retained strong convection, which allowed the secondary eyewall to become the dominant eyewall.

During the second eyewall replacement cycle (orange hashed rectangles from Hour 72 to Hour 90 in Fig. 70; Hours 91 to 114 not shown in figure due to the storm center being over land), R_{max} and the inner eyewall increased from 30 km to 49 km and 13 km to 34 km, respectively, from 72 h to 114 h. As the storm center moved over land, V_t decreased from 50 m s^{-1} to 23 m s^{-1} (Fig. 70a). Land interaction impacts will be further explored in a later section of this chapter. Following this eyewall replacement cycle, R_{max} and the inner eyewall radius contracted to 45 km and 19 km, respectively (not shown).

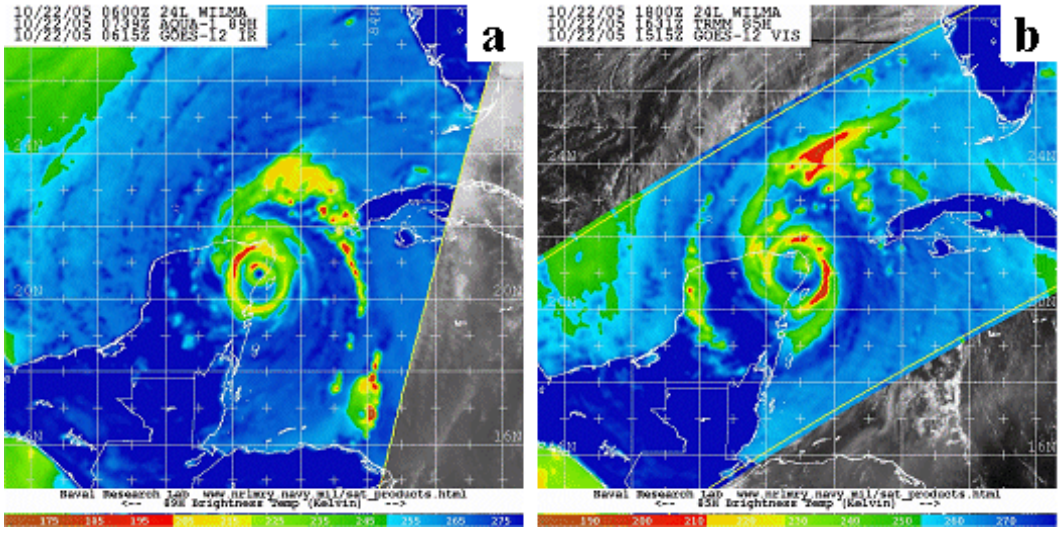

Figure 74 Microwave satellite imagery (85-89 GHz) for Hurricane Wilma from Aqua and TRMM polar orbiting platforms on (a) 22 October at 0739 UTC, and (b) 22 October at 1631 UTC (2005; from NRL 2007).

The azimuthal-average wind profiles in Fig. 75a prior to, following, and 6 h after the second eyewall replacement cycle (Hours 72, 114, and 120, respectively) suggest that a time lag existed between changes in the inner-core structure (R_{max}) and changes in the outer-core structure (R_{34}). Whereas the R_{max} increased by 19 km during this eyewall replacement cycle and then was followed by a decrease of 4 km 6 h after the cycle, the R_{34} initially decreased by 11 km during this eyewall replacement cycle (blue arrow in Fig. 75a) and then increased by 16 km 6 h after the cycle (red arrow in Fig. 75a) for a net increase of 5 km.

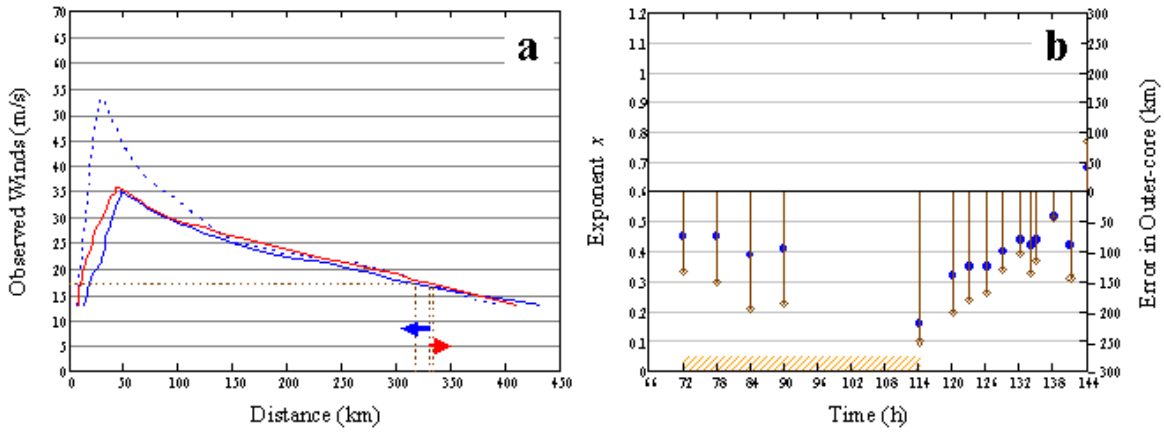

Figure 75 (a) Azimuthal-average wind profiles for Hurricane Wilma at Hour 72 (blue dashed line), Hour 114 (blue solid line) and Hour 120 (red solid line), and (b) observed values for exponent x in the modified Rankine vortex (blue circles) and the prediction error (stem plots) when the mean value for exponent $x = 0.58$ is applied in Eq. (20). The orange-hashed rectangle is the nominal period of the second eyewall replacement cycle.

Once again, the exponent x values assuming a modified Rankine vortex suggest that Wilma had a larger outer-core structure prior to and during the second eyewall replacement cycle than the overall population of Atlantic tropical cyclones during 2003–2005 (Fig. 75b). Indeed, applying the overall mean value for exponent x = 0.58 in the modified Rankine vortex in Eq. (20) results in an under-prediction of R_{34} by 87–252 km prior to and during the second eyewall replacement cycle, as depicted by the stem plots in Fig. 75b. Individual exponent values for Hours 72, 114, and 120 were $x = 0.45$, $x = 0.16$, and $x = 0.32$, respectively. As with the first eyewall replacement, the wind profile did not sharpen following the replacement cycle and this time variability in the profile shapes suggests that accurately predicting the change in the R_{34} with a fixed value for exponent x during secondary eyewall replacement may not be plausible. Contrary to all previous case studies, this eyewall replacement cycle resulted in a decrease in the modified Rankine vortex exponent x, and thus suggests a broadening of the R_{34} in association with land interaction. The impacts of land interaction will be further explored in a later section of this chapter.

In summary, two complete secondary eyewall replacement cycles occurred from 0730 UTC 18 October to 0130 UTC 23 October during the life cycle of Wilma. During each eyewall replacement cycle, this tropical cyclone weakened with V_t decreases

of 16 m s^{-1} and 27 m s^{-1}, respectively (Fig. 70a). Contrary to the previously discussed case studies except Ivan's fourth cycle, the intensity of Wilma decreased during eyewall replacement. However, Wilma was an unusually strong tropical cyclone prior to the first eyewall replacement cycle and made landfall during the second cycle. In both eyewall replacements, the R_{max} increased in value by 32 km and 19 km, respectively (Fig. 70b). Contrary to previous case studies, inward (outward) ΔKE_{anom} was poorly correlated (0.094) with a decrease (increase) of the R_{max} radius. An increase in radial inflow variance was observed when convective asymmetries in or near the eyewall were present, but increases in the R_{34} size were not always observed within 6 h of the increased variance (Fig. 70a).

The azimuthal-average wind profiles prior to, following, and after the two Wilma eyewall replacement cycles (Figs. 73 and 75) indicate that the R_{34} experienced an expansion following secondary eyewall replacement. The range of exponent x values was 0.15–0.51, where the smaller (larger) values occurred prior to (after) a non-landfalling secondary eyewall replacement cycle. Indeed, the exponent x increased from 0.36 to 0.49 during the first eyewall replacement cycle. By contrast, the exponent x decreased from 0.45 to 0.16 during the second eyewall replacement cycle, and thus suggests an relative expansion of the outer-core structure during landfall. The effects of landfall on structure will be further explored in a later section of this chapter. The observed variability of exponent x for Wilma demonstrates again that accurate prediction of the R_{34} change using a fixed value for exponent x of the modified Rankine vortex during secondary eyewall replacement may not be plausible.

2. Partial Replacement Cycle

For the purposes of this research, partial eyewall replacement is defined as an outer convectively active spiral rainband only partially encircles the storm eyewall. Detection of a partial eyewall replacement is via microwave satellite imagery from the NASA TRMM and Aqua research satellites, and the DMSP polar-orbiting platforms. While some of the changes in the inner-core structure are similar to complete eyewall replacement (as described in Chapter IV.A.1 above), a common feature of the partial eyewall replacement is that the intense convection of the encircling spiral rainbands may cause an expansion of the primary eyewall without a complete replacement. These expansions of the inner-core structure may be associated with PV asymmetries that

result from asymmetric convection near the eyewall, as shown by Wang (2008b) in a high-resolution numerical modeling study (see Chapter I.B.3).

a. *Emily (2005)*

Emily became a named storm at 0000 UTC 12 July over the central North Atlantic in the vicinity of 11.2°N, 46.7°W. This tropical cyclone had a westward track for 48 h before strengthening into a hurricane at 0000 UTC 14 July. After reaching hurricane intensity, Emily had a west-northwestward track across the Caribbean Sea, passed south of Jamaica on 16 July, and made landfall over the east coast of the Yucatan Peninsula at approximately 0600 UTC 18 July. Hurricane Emily re-emerged over the western Gulf of Mexico 6 h later, continued on a west-northwestward track, and then made a second landfall at approximately 1200 UTC 20 July over northeastern Mexico about 80 km south of Brownsville, Texas. H*Wind analyses for Emily became available at 1330 UTC 13 July and at regular increments until 1130 UTC 20 July as the storm approached landfall over northern Mexico.

At 1930 UTC 14 July (hereafter referred to as Hour 0 of the analysis), Emily had a tangential wind speed (V_t) of 39 m s^{-1} with azimuthal-average R_{max} and R_{34} values of 18 km and 124 km, respectively. During the first 6 h of the analysis, Emily experienced rapid intensification (increased by 7 m s^{-1}) with a storm intensity of 46 m s^{-1} (Fig. 76a). During this 6 h period, the R_{34} increased by 36 km while the R_{max} and inner eyewall each decreased by 6 km (Fig. 76). From 6 h to 12 h, Emily's intensity decreased by 9 m s^{-1} as the R_{max} increased by 6 km (Fig. 76b), and the R_{34} also decreased by 31 km (Fig. 76a). Coincidently, an increase in radial inflow variance suggests Emily had developed asymmetric convection near the eyewall (Fig. 76a).

Microwave satellite imagery at 0136 UTC 15 July (∼Hour 6 of the analysis, Fig. 77a) indicates the presence of intense convection over the eyewall of Emily with very strong, asymmetric convection in the spiral rainband that extends outward to 1 degree in the north quadrant. By 1627 UTC 15 July (∼Hour 21 of the analysis, Fig. 77b), strong convection was observed in the northern half of the eyewall with intense banded convection extending outward to 2 degrees in the north and east quadrants. Satellite imagery suggests the presence of a secondary eyewall that partially encircled the primary eyewall.

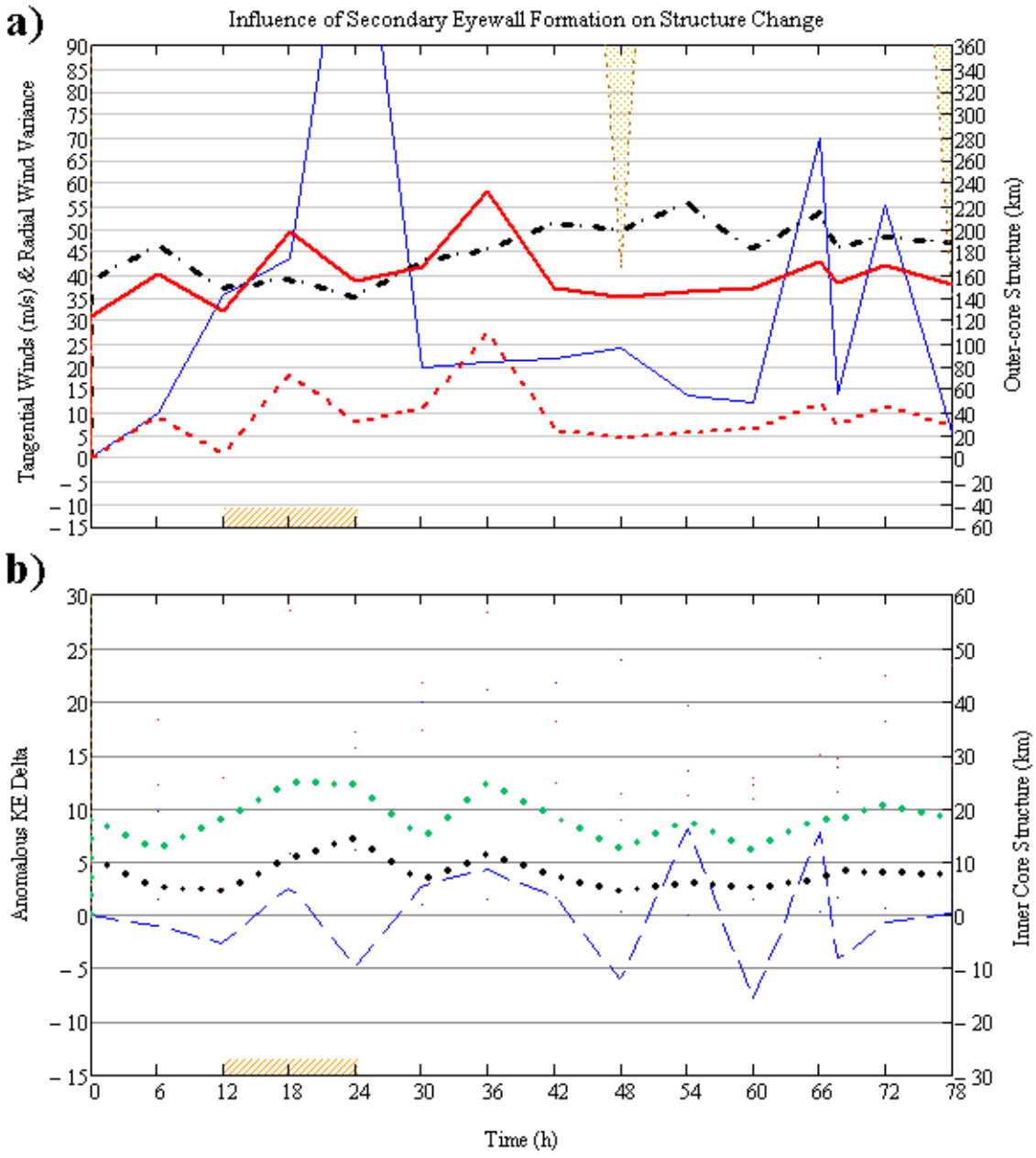

Figure 76 Time series of structure changes as in Fig. 48, except for Hurricane Emily (2005) from 14 July at 1930 UTC (Hour 0) to 18 July at 0130 UTC (Hour 78), and the shaded region indicates land interaction within the R_{34} radius, where distance from storm center is on the right ordinate.

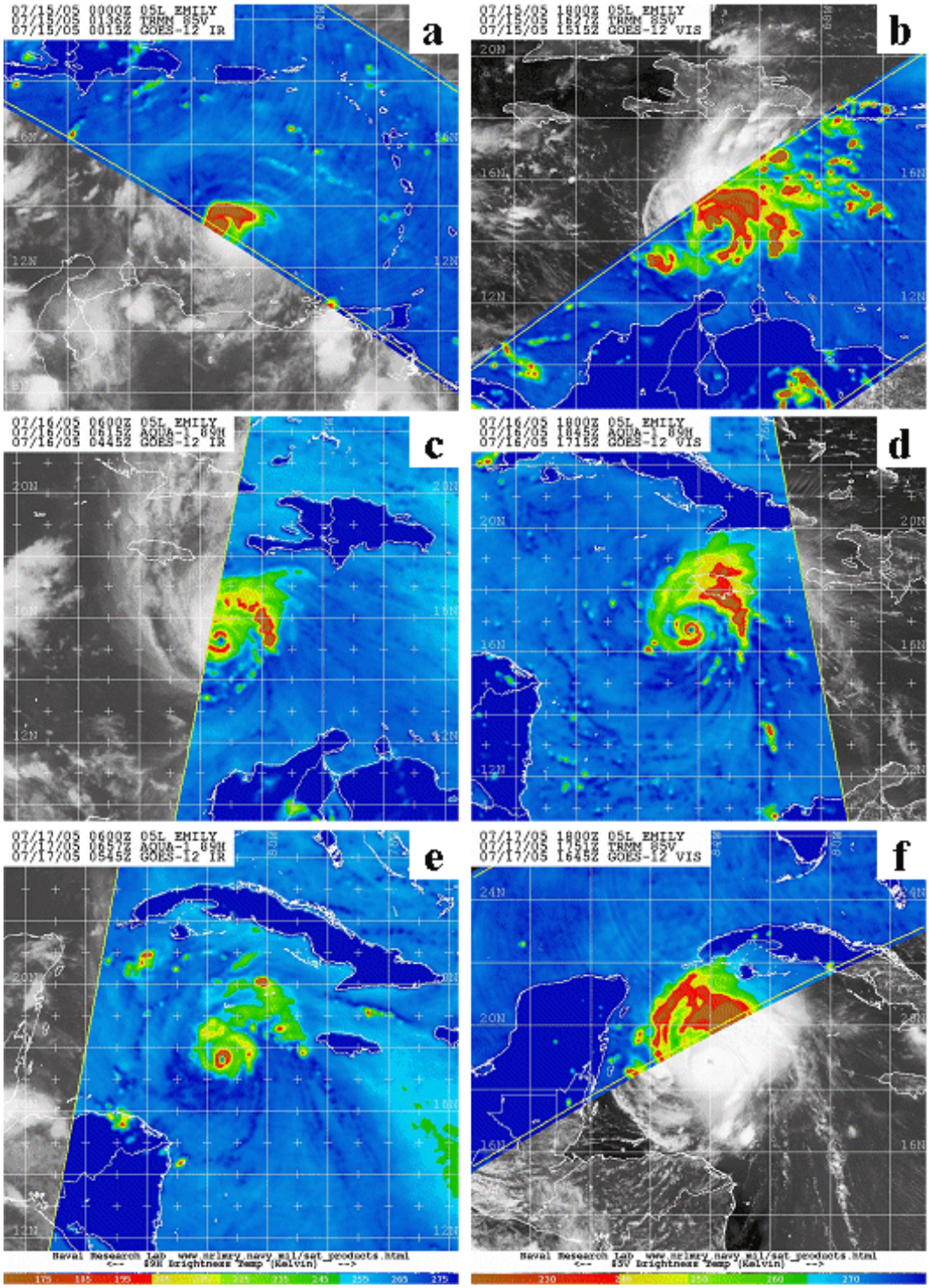

Figure 77 Microwave satellite imagery (85-89 GHz) for Hurricane Emily from Aqua and TRMM polar orbiting platforms on (a) 15 July at 0136 UTC, (b) 15 July at 1627 UTC, (c) 16 July at 0615 UTC, (d) 16 July at 1845 UTC, (e) 17 July at 0657 UTC, and (f) 17 July at 1751 UTC (2005; from NRL 2007).

Microwave satellite imagery at 0615 UTC 16 July (∼Hour 35 of the analysis, Fig. 77c) indicates the presence of a more symmetric eyewall with strong convection and one convectively active spiral rainband extending outward to 1.5 degrees in the north and east quadrants. This microwave imagery suggests that this tropical cyclone has returned to one dominant eyewall, but does not clearly resolve whether the remaining eyewall was the primary or secondary eyewall.

During the partial eyewall replacement cycle (orange hashed rectangles from Hour 12 to Hour 24 in Fig. 76), the R_{max} increased by 6 km (increased from 18 km to 24 km) and the inner eyewall more than doubled (increased from 5 km to 14 km) from 12 h to 24 h. This expansion of the inner-core structure was coincident with a weak outward ΔKE_{anom} (Fig. 76b). Following partial eyewall replacement, R_{max} and the inner eyewall radius contracted to approximately their pre-eyewall replacement sizes in the presence of inward ΔKE_{anom} (Fig. 76b). During the partial eyewall replacement, Emily's intensity (V_t) remained nearly constant during the first 12 h (Hour 33 to Hour 45), and then decreased from 55 m s^{-1} to 45 m s^{-1} by Hour 63 (Fig. 76a). A large increase in the radial inflow variance was observed in association with intense, asymmetric convection in and near the primary eyewall during the partial eyewall replacement cycle (Figs. 76a and 77b).

The azimuthal-average wind profiles in Fig. 78a prior to, following, and 6 h after the partial eyewall replacement cycle (Hours 12, 24, and 30, respectively) suggest an initial increase in the outer-core structure (R_{34}), and then a smaller change during the 6 h after the replacement cycle. While the R_{max} increased by 6 km during the partial eyewall replacement cycle and then decreased by 10 km 6 h after the cycle, the R_{34} increased by 29 km during the partial eyewall replacement cycle (blue arrow in Fig. 78a) and continued to increase by an additional 10 km 6 h after the cycle (red arrow in Fig. 78a). This suggests that the R_{34} had a time-lagged response to changes that occurred in the inner-core structure.

The exponent x values assuming a modified Rankine vortex suggest that Emily had a larger outer-core structure prior to and during the partial eyewall replacement cycle than the overall population of Atlantic tropical cyclones during 2003–2005 (Fig. 78b). Indeed, applying the overall mean value for exponent $x = 0.58$ in the modified Rankine vortex in Eq. (20) results in an under-prediction of R_{34} by 53–98 km prior to and during the partial eyewall replacement cycle, as depicted by the stem plots in Fig. 78b. The mean modified Rankine vortex exponent x during the life

cycle of Emily was 0.43 with individual values of $x = 0.39$, $x = 0.39$, and $x = 0.37$ at Hours 12, 24, and 30, respectively. As with the fourth case of Ivan, nearly the same exponent x following the partial eyewall replacement as before the replacement cycle would indicate a larger R_{34} when R_{max} increases, which is consistent with the 29 km increase in R_{34}.

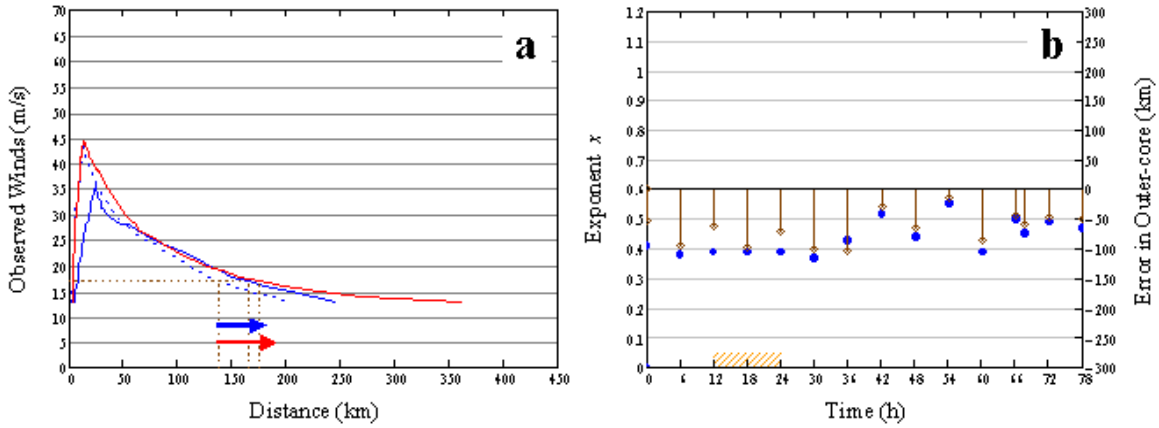

Figure 78 (a) Azimuthal-average wind profiles for Hurricane Emily at Hour 12 (blue dashed line), Hour 24 (blue solid line) and Hour 30 (red solid line), and (b) observed values for exponent x in the modified Rankine vortex (blue circles) and the prediction error (stem plots) when the mean value for exponent $x = 0.58$ is applied in Eq. (20). The orange-hashed rectangle is the nominal period of the partial eyewall replacement cycle.

Following a large spike in radial inflow variance at Hour 24, Emily experienced rapid intensification (V_t increased by 21 m s^{-1}) from 24 h to 54 h and reached a peak intensity of 56 m s^{-1} (Fig. 76a). As with Frances, the observed convective asymmetries from 21 h to 48 h in or near the eyewall of Emily suggest that axisymmetrization may be a potential mechanism for rapid storm intensification during secondary eyewall replacement (see Figs. 77b–d). As Emily passed 165 km to the south of Jamaica microwave satellite imagery at 1845 UTC 16 July (~Hour 47.5 of the analysis, Fig. 77d) indicates the presence of a well-defined eyewall with explosive convection over Jamaica along the spiral rainband that extended over the island. By 0657 UTC 17 July (~Hour 59.5 of the analysis, Fig. 77e), a more symmetric eyewall with strong convection existed, but without significant, organized convection outside of the eyewall. Although Emily's intensity (V_t) decreased by 11 m s^{-1} from 54 h to

60 h, the presence of a more symmetric eyewall was followed by a 9 m s^{-1} V_t increase from 60 h to 66 h (Fig. 76a).

From 24 h to 36 h, the R_{34} increased and reached a peak value of 233 km (Fig. 76a). After reaching the peak outer-core structure size, the R_{34} decreased by 85 km from 36 h to 42 h, and then fluctuated between 141 km and 171 km for the remainder of the life cycle, as depicted in Fig. 76a. Microwave satellite imagery at 1751 UTC 17 July (∼Hour 70.5 of the analysis, Fig. 77f) indicates an increased amount of intense convection in the north and east quadrants between 0.5 and 2.5 degrees from the storm center. With the return of asymmetric convection, spikes in the radial inflow variance were observed at Hours 66 and 72 (Fig. 76a). After Hour 24, the significant fluctuations in R_{max} and inner eyewall of Emily appear to be positively correlated with ΔKE_{anom} (Fig. 76b). These expansions of the inner-core structure are hypothesized to be associated with PV asymmetries that result from asymmetric convection near the eyewall (see Figs. 77c, d, and f). The effects of asymmetric convection will be further explored in a later section of this chapter.

In summary, one partial eyewall replacement cycle occurred from 1930 UTC 14 July to 0130 UTC 18 July while Emily was over the Caribbean Sea. Following the partial eyewall replacement cycle, Emily had a V_t increase of 21 m s^{-1} (Fig. 76a). The R_{max} increased by 6 km during the beginning of the partial eyewall replacement cycle, but then contracted by 10 km at the end of the cycle (Fig. 76b). Inward (outward) ΔKE_{anom} was generally associated with a decrease (increase) of the R_{max} radius. Indeed, the correlation coefficient of 0.460 indicates a weak linear relationship between ΔKE_{anom} and R_{max}, although with greater variance than for Frances, Ivan, or Katrina. An increase in radial inflow variance was observed when convective asymmetries in or near the eyewall were present, but the increase in R_{34} did not follow within 6 h of the increased variance as had been observed with Frances (Fig. 76a).

The azimuthal-average wind profiles prior to, following, and 6 h after the partial eyewall replacement cycle (Fig. 78) suggest that R_{34} did have a time-lagged increase following partial eyewall replacement. The range of values for the modified Rankine vortex exponent x was 0.37–0.55, where the smaller (larger) values generally occurred prior to (after) Hour 30. Although the exponent x remained nearly constant (0.37–0.39) during the partial eyewall replacement cycle, an increase of R_{max} plus the intensification still led to a temporary increase in R_{34} to 233 km. The expansions of the inner-core structure for this case study are believed to be associated with PV

asymmetries that result from asymmetric convection near the eyewall and will be further explored in a later section of this chapter.

b. *Rita (2005)*

Rita became a named storm by 0130 UTC 19 September over the western North Atlantic in the vicinity of 22.7°N, 73.2°W. This tropical cyclone had a west-northward track for approximately 36 h before strengthening into a hurricane as it passed between Florida and Cuba at 1400 UTC 20 September. After reaching hurricane intensity, Rita continued on a west-northwestward track across the Gulf of Mexico for 28 h, then turned northwestward across the central and western Gulf of Mexico, and finally made landfall near the Texas and Louisiana border at approximately 0800 UTC 24 September. H*Wind analyses for Rita became available at 1930 UTC 18 September and at regular increments until 1030 UTC 24 September as the storm approached landfall in the northern Gulf of Mexico.

At 1630 UTC 20 September (hereafter referred to as Hour 0 of the analysis), Rita had a tangential wind speed (V_t) of 35 m s^{-1} with azimuthal-average R_{max} and R_{34} values of 25 km and 225 km, respectively. Microwave satellite imagery at 1835 UTC 20 September (∼Hour 2 of the analysis, Fig. 79a) indicates the presence of a loosely organized eyewall with strong convection and one spiral rainband that extended outward to 2 degrees in the south and west quadrants. During the first 12 h of the analysis, Rita's intensity (V_t) initially declined by 3 m s^{-1} as the storm passed within 75 km of land, and then increased by 4 m s^{-1} as the distance from land increased to 165 km (Fig. 80a). During this period, R_{max} and the inner eyewall sizes temporarily increased by 17 km and 7 km, respectively, whereas the outer-core structure (R_{34}) only had small variations in size (Fig. 80).

At 0909 UTC and 1918 UTC 21 September (∼Hours 16.5 and 27 of the analysis, Figs. 79b–c), Rita's eyewall became more organized with strong, symmetric convection as evidenced by microwave satellite imagery. These satellite images also indicate the presence of at least two spiral rainbands with loosely organized convection extending outward to 2 degrees. In conjunction with the increased organization of Rita's eyewall, rapid intensification was observed between 12 h and 27 h with a V_t increase from 36 m s^{-1} to 58 m s^{-1} (22 m s^{-1} in 15 h, Fig. 80a). The R_{34} increased by 106 km during this same period. The ΔKE_{anom} appear to be positively correlated

with the inner-core structure (R_{max} and inner eyewall) changes through Hour 33 (Fig. 80b).

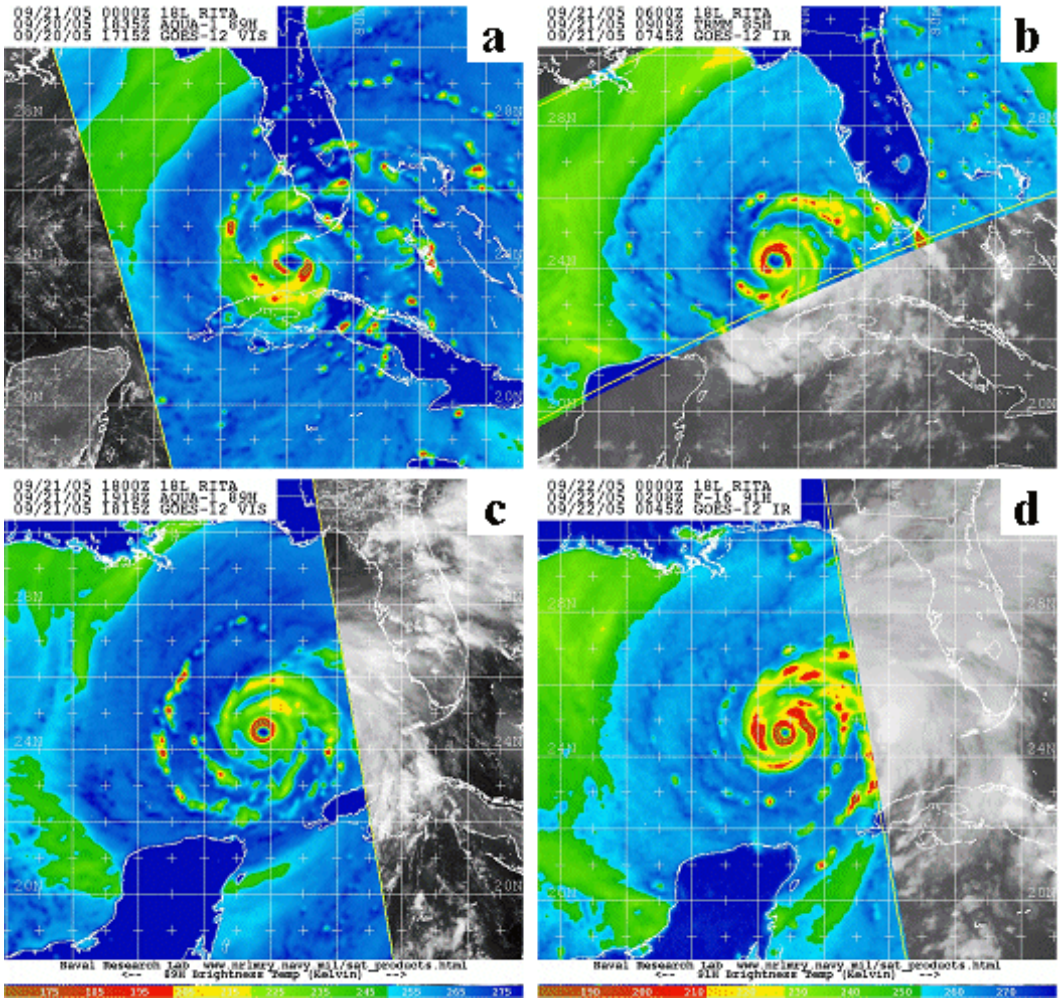

Figure 79 Microwave satellite imagery (85-91 GHz) for Hurricane Rita from Aqua, TRMM, and DMSP polar orbiting platforms on (a) 20 September at 1835 UTC, (b) 21 September at 0909 UTC, (c) 21 September at 1918 UTC, (d) 22 September at 0208 UTC (2005; from NRL 2007).

Microwave satellite imagery at 0208 UTC 22 September (∼Hour 33.5 of the analysis, Fig. 79d) indicates the presence of two spiral rainbands partially encircling the storm eyewall. The banded, inner-core convection in close proximity to the eyewall was intense and the northern rainband extends outward to 2.5 degrees in the east quadrant. At the point of Rita's peak intensity (Hour 33), a strong variance in the radial inflow was observed (Fig. 80a).

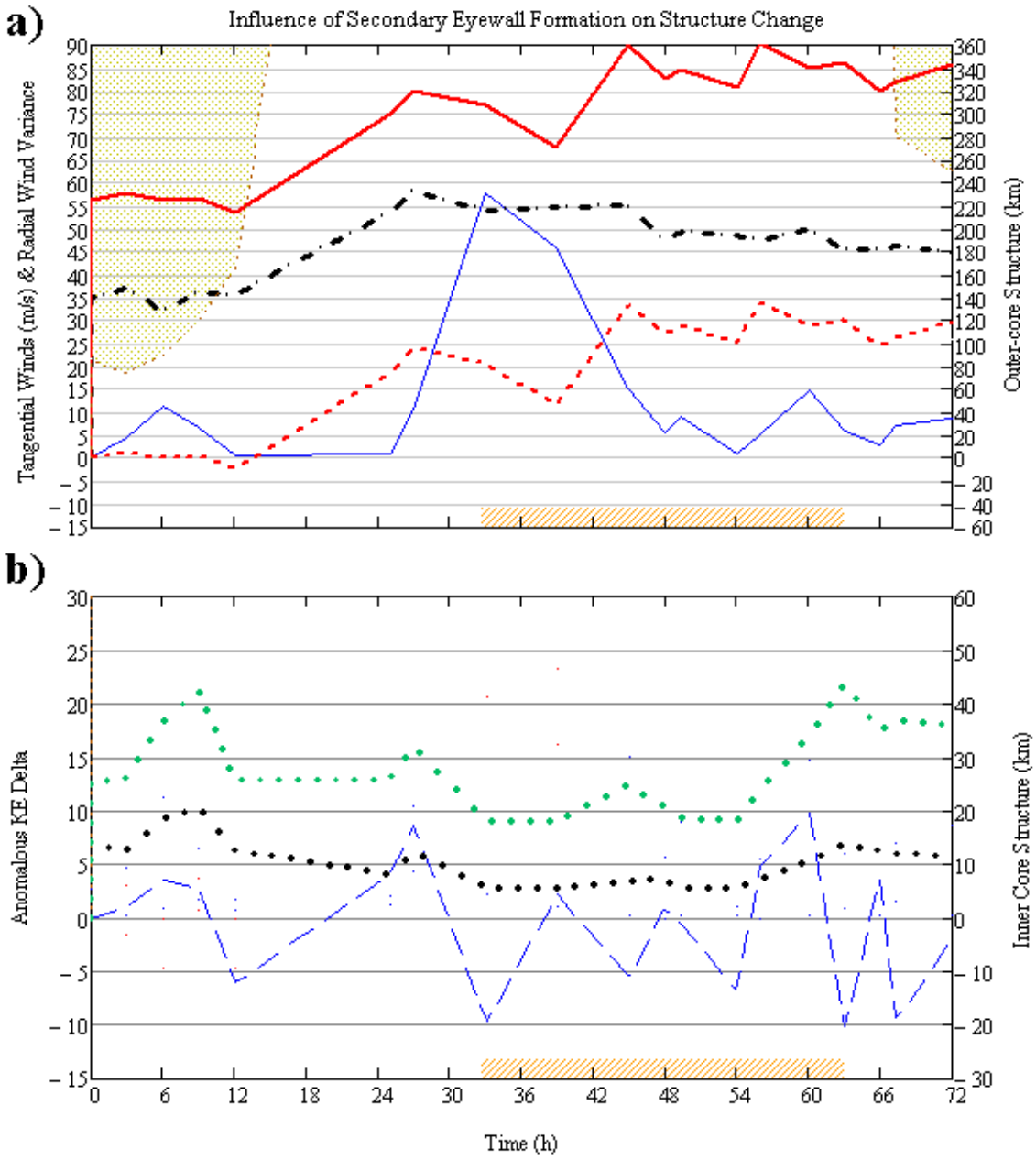

Figure 80 Time series of structure changes as in Fig. 48, except for Hurricane Rita (2005) from 20 September at 1630 UTC (Hour 0) to 23 September at 1630 UTC (Hour 72), and the shaded region indicates land interaction within the R_{34} radius, where distance from storm center is on the right ordinate.

A horizontal depiction of Hurricane Rita's storm-relative radial winds at 0130 UTC 22 September (Hour 33, Fig. 81) reveals a sharp gradient in the azimuthal distribution of the radial inflow. In the north-northwest quadrant near the R_{max} and the convection-free zone between spiral rainbands, Rita's maximum radial inflow was approximately 34 m s^{-1}, which is more than double the typically observed inflow of 15 m s^{-1}. Of greater interest was the approximate 2 m s^{-1} radial outflow in the east-southeast eyewall, which will be what the author termed an "eyewall burst". In this case, it appears that the interaction of strong spiral rainband convection in near proximity to the eyewall had the effect of creating a strong radial inflow that may have been a contributing factor in disrupting the symmetry of the eyewall and ultimately the storm structure.

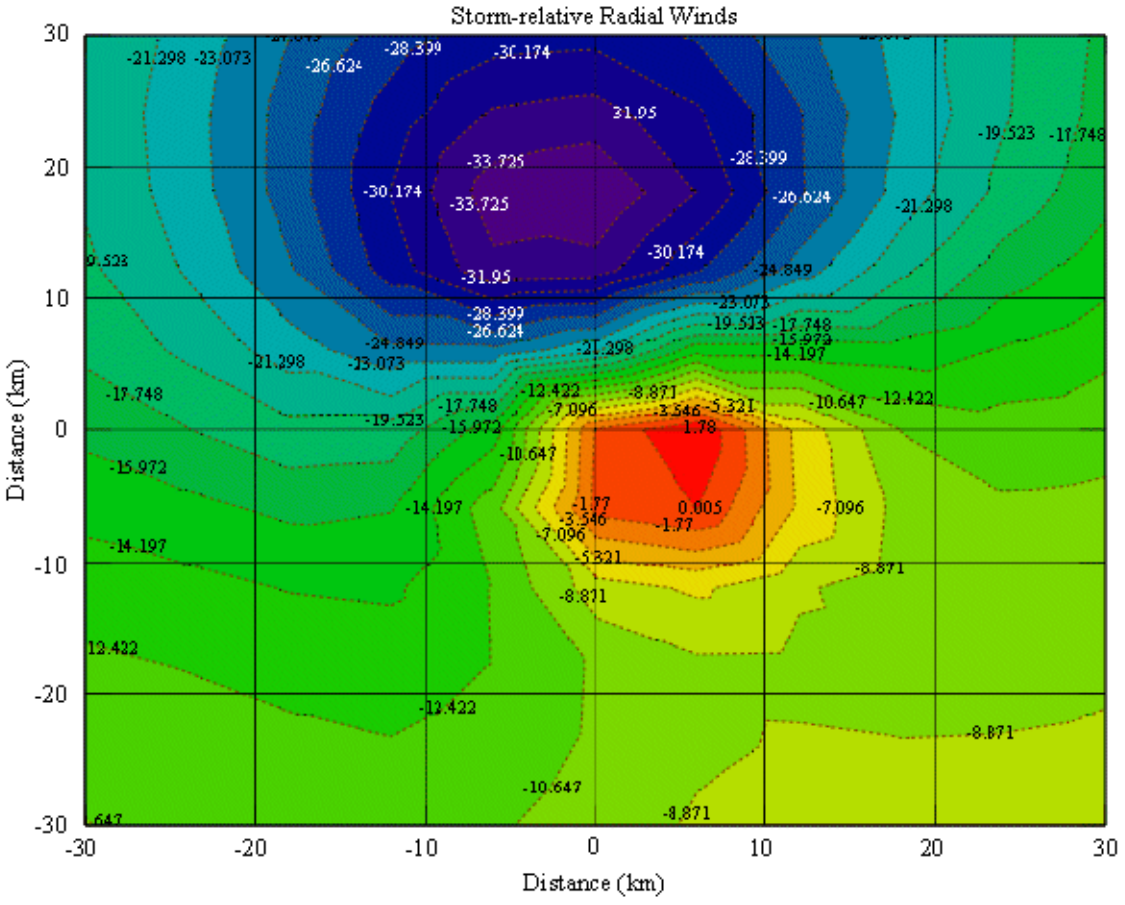

Figure 81 Horizontal depiction on a Cartesian grid of storm-relative radial winds (m s^{-1}) for Hurricane Rita on 22 September at 0130 UTC. Positive (negative) values are east (west) of the storm center on the abscissa and north (south) of the storm center on the ordinate.

Microwave satellite imagery at 0810 UTC 22 September (~Hour 39.5 of the analysis, Fig. 82a) indicates the presence of a developing secondary eyewall with strong convection in close proximity to the original eyewall. There are two spiral rainbands in the north quadrant, and the northernmost band extended eastward 5 degrees in the northeast quadrant. By 1442 UTC 22 September (~Hour 46 of the analysis, Fig. 82b), the secondary eyewall became more symmetric as evidenced by microwave satellite imagery. Convection in the two spiral rainbands was extremely strong between 2 degrees and 5.5 degrees in the northeast quadrant.

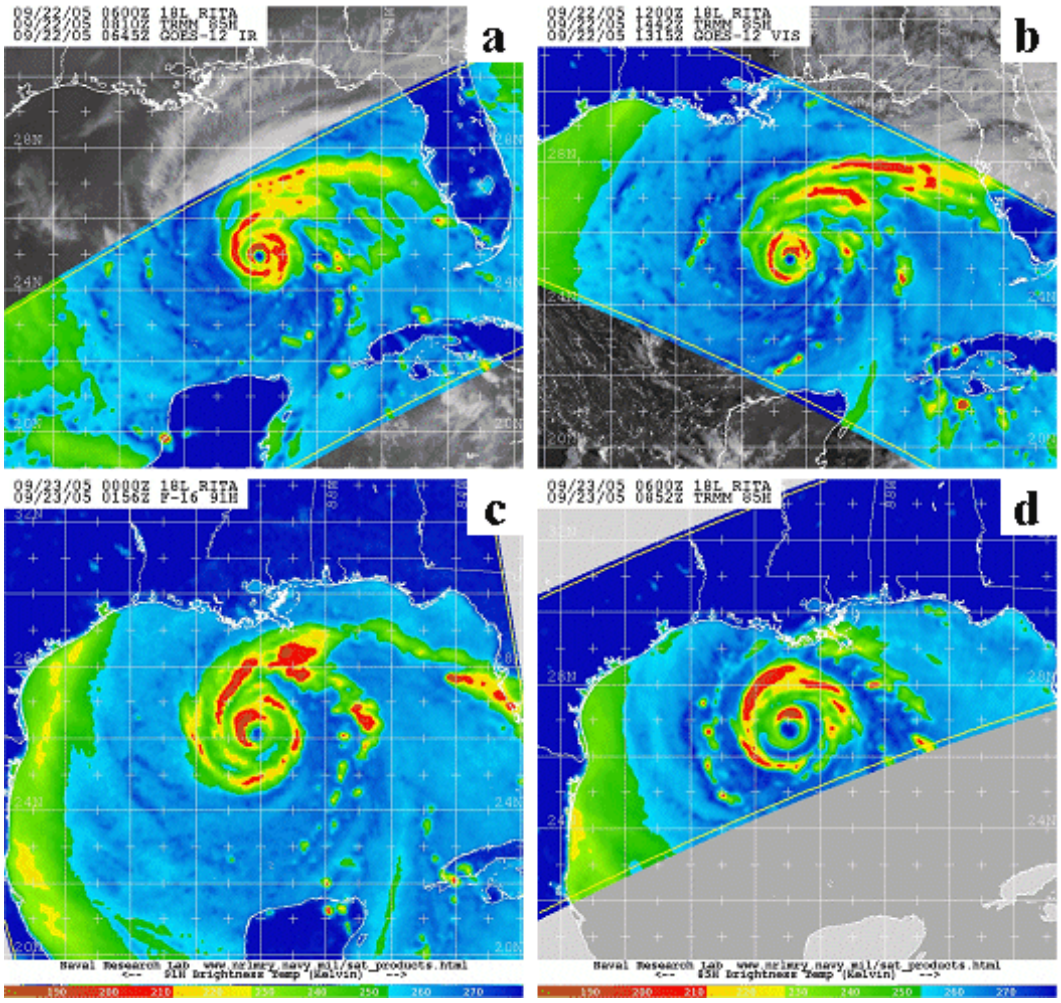

Figure 82 Microwave satellite imagery (85-91 GHz) for Hurricane Rita from TRMM and DMSP polar orbiting platforms on (a) 22 September at 0810 UTC, (b) 22 September at 1442 UTC, (c) 23 September at 0156 UTC, (d) 23 September at 0852 UTC (2005; from NRL 2007).

Microwave satellite imagery at 0156 UTC 23 September (∼Hour 57.5 of the analysis, Fig. 82c) suggests a broadening of the original eyewall, decreased symmetry in the secondary eyewall, and less convectively organized spiral rainbands in the northeast quadrant. The presence of a convectively asymmetric primary eyewall surrounded by a broad, convectively active secondary eyewall with no spiral rainbands was evident in the microwave satellite imagery at 0852 UTC 23 September (∼Hour 64.5 of the analysis, Fig. 82d).

During the partial eyewall replacement cycle (orange hashed rectangles from Hour 33 to Hour 63 in Fig. 80), R_{max} and the inner eyewall more than doubled (increased from 18 km to 44 km and from 5 km to 14 km, respectively) from 33 h to 63 h. This expansion of the inner-core structure was coincident with the outward ΔKE_{anom} (Fig. 80b). Following partial eyewall replacement, R_{max} and the inner eyewall radius contracted slowly in the presence of inward ΔKE_{anom} (Fig. 80b). During the partial eyewall replacement, Rita's intensity (V_t) remained nearly constant during the first 12 h (Hour 33 to Hour 45), and then decreased from 55 m s^{-1} to 45 m s^{-1} by Hour 63 (Fig. 80a).

The azimuthal-average wind profiles in Fig. 83a prior to, following, and 9 h after the partial eyewall replacement cycle (Hours 33, 63, and 72, respectively) suggest an initial increase in R_{34}, and then a continued increase during the 9 h after the replacement cycle. While R_{max} increased by 26 km during the partial eyewall replacement cycle and then decreased by 8 km 9 h after the cycle, R_{34} increased by 31 km during the partial eyewall replacement cycle (blue arrow in Fig. 83a) and continued to increase by an additional 21 km 9 h after the cycle (red arrow in Fig. 83a). As with Emily, this suggests that the R_{34} had a time-lagged response to changes that occurred in the inner-core structure.

The exponent x values assuming a modified Rankine vortex suggest that Rita had a larger outer-core structure prior to and during the partial eyewall replacement cycle than the overall population of Atlantic tropical cyclones during 2003–2005 (Fig. 83b). Indeed, applying the overall mean value for exponent $x = 0.58$ in the modified Rankine vortex in Eq. (20) results in an under-prediction of R_{34} by 60–226 km prior to and during the partial eyewall replacement cycle, as depicted by the stem plots in Fig. 83b. The mean modified Rankine vortex exponent x during the life cycle of Rita was 0.41 with individual values of $x = 0.40$, $x = 0.47$, and $x = 0.42$ at Hours 33, 63, and 72, respectively. As in the fourth case of Ivan, nearly the same exponent x existed

after the partial eyewall replacement as before, which would indicate a larger R_{34} when R_{max} increases, and thus is consistent with the 31 km increase in R_{34} in this case.

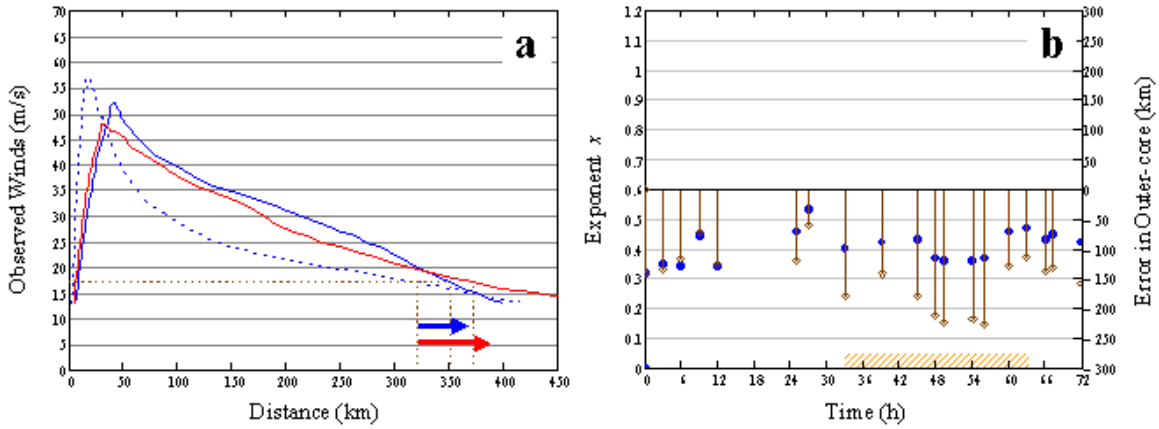

Figure 83 (a) Azimuthal-average wind profiles for Hurricane Rita at Hour 33 (blue dashed line), Hour 63 (blue solid line) and Hour 72 (red solid line), and (b) observed values for exponent x in the modified Rankine vortex (blue circles) and the prediction error (stem plots) when the mean value for exponent $x = 0.58$ is applied in Eq. (20). The orange-hashed rectangle is the nominal period of the partial eyewall replacement cycle.

In summary, one partial eyewall replacement cycle occurred from 1630 UTC 20 September to 1630 UTC 23 September while Rita was over the Gulf of Mexico. Prior to the partial eyewall replacement cycle, Rita had a V_t increase of 22 m s^{-1} (Fig. 80a). The R_{max} increased by 26 km toward the end of the partial eyewall replacement cycle, but then contracted by 8 km at the end of the cycle (Fig. 80b). Inward (outward) ΔKE_{anom} was generally associated with a decrease (increase) of the R_{max} radius. Indeed, the correlation coefficient of 0.399 indicates a weak linear relationship between ΔKE_{anom} and R_{max}, although with greater variance than for Frances, Ivan, or Katrina. An increase in radial inflow variance was observed when convective asymmetries in or near the eyewall were present, and then an increase in the R_{34} value appeared to follow beyond 6 h after the increased radial inflow variance (Fig. 80a).

The azimuthal-average wind profiles prior to, following, and 9 h after the partial eyewall replacement cycle (Fig. 83) suggests a time-lagged increase in R_{34} following partial eyewall replacement. The range of exponent x values was 0.32–0.53, where the smaller values generally occurred prior to Hour 12 and during partial eyewall

replacement. Although the exponent x remained nearly constant (0.40–0.47) during the partial eyewall replacement cycle, an increase of R_{max} still led to an increase in R_{34} to 360 km. The expansions of the inner-core structure for this case study are believed to be associated with PV asymmetries that result from asymmetric convection near the eyewall and will be further explored in a later section of this chapter.

c. *Ivan (2004)*

The life cycle of Hurricane Ivan was discussed in Chapter IV.A.1.c. The analysis period of partial secondary eyewall replacement for Ivan will be from 2230 UTC 6 September (Hour 0) to 0730 UTC 7 September (Hour 9) as this storm moved across the central North Atlantic toward the Lesser Antilles. Recall, at 2230 UTC 6 September (Hour 0 of the analysis), Ivan had a tangential wind speed (V_t) of 33 m s^{-1} with azimuthal-average R_{max} and R_{34} values of 12 km and 170 km, respectively (Fig. 56). Microwave satellite imagery at 1712 UTC 6 September (∼5.5 h prior to Hour 0 of the analysis, Fig. 55a) indicates a lack of convection in the southern eyewall with strong convection north of the storm center, which may be the formation of a secondary eyewall with asymmetric convection. Note that there are striking similarities in the microwave satellite signatures between Emily and Ivan during partial eyewall replacement (1627 UTC 15 July and 1712 UTC 6 September, respectively, Figs. 77b and 55a). Microwave satellite imagery at 0528 UTC 7 September (∼Hour 7 of the analysis, Fig. 55b) suggests that Ivan has returned to one dominant eyewall, but does not clearly resolve whether the remaining eyewall was the primary or secondary eyewall.

During the partial eyewall replacement cycle (orange hashed rectangles from Hour 0 to Hour 3 in Fig. 56), R_{max} and the inner eyewall both increased by approximately four-fold (increased from 12 km to 45 km and from 6 km to 24 km, respectively). Following partial eyewall replacement, R_{max} and the inner eyewall radius contracted to approximately their pre-eyewall replacement sizes (Fig. 56b). During the partial eyewall replacement, Ivan's intensity (V_t) initially decreased by 3 m s^{-1}, and then rapidly increased by 12 m s^{-1} in 6 h to an intensity of 42 m s^{-1} (Fig. 56a).

The azimuthal-average wind profiles in Fig. 84a prior to, following, and 6 h after the partial eyewall replacement cycle (Hours 0, 3, and 9, respectively) suggest an initial increase in the outer-core structure (R_{34}), and then a smaller change during the 6 h after the replacement cycle. While the R_{max} increased by 33 km during the

partial eyewall replacement cycle and then decreased by 27 km 6 h after the cycle, the R_{34} increased by 55 km during the partial eyewall replacement cycle (blue arrow in Fig. 84a) and continued to increase by an additional 13 km 6 h after the cycle (red arrow in Fig. 84a). This suggests that the R_{34} had a time-lagged response to changes that occurred in the inner-core structure.

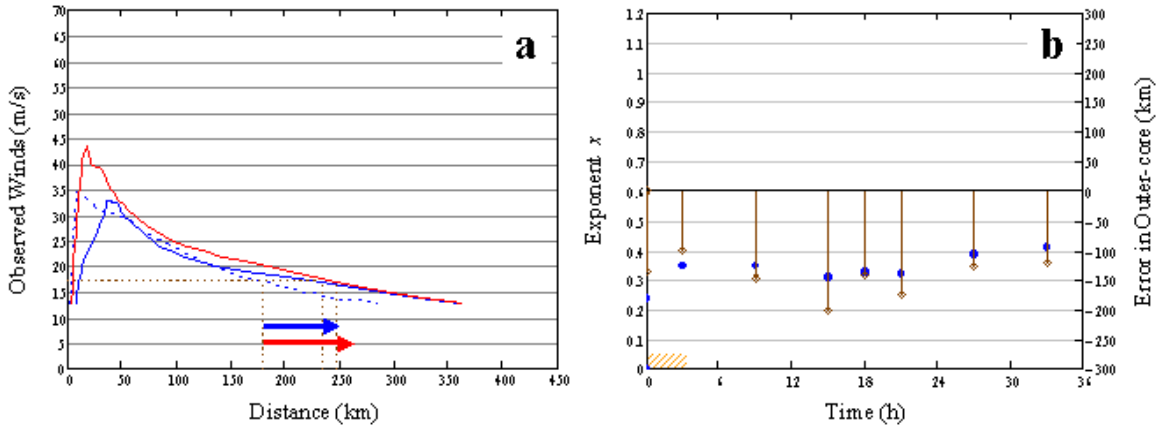

Figure 84 (a) Azimuthal-average wind profiles for Hurricane Ivan at Hour 0 (blue dashed line), Hour 3 (blue solid line) and Hour 9 (red solid line), and (b) observed values for exponent x in the modified Rankine vortex (blue circles) and the prediction error (stem plots) when the mean value for exponent $x = 0.58$ is applied in Eq. (20). The orange-hashed rectangle is the nominal period of the partial eyewall replacement cycle.

The exponent x values assuming a modified Rankine vortex suggest that Ivan had a larger outer-core structure prior to and during the partial eyewall replacement cycle than the overall population of Atlantic tropical cyclones during 2003–2005 (Fig. 84b). Indeed, applying the overall mean value for exponent $x = 0.58$ in the modified Rankine vortex in Eq. (20) results in an under-prediction of R_{34} by 100–136 km prior to and during the partial eyewall replacement cycle, as depicted by the stem plots in Fig. 84b. Individual exponent values for Hours 0, 3, and 9 were $x = 0.24$, $x = 0.35$, and $x = 0.35$, respectively. As with the second case of secondary eyewall replacement for this tropical cyclone in Chapter IV.A.1.c, the wind profile sharpened and V_t increased following the partial eyewall replacement.

In summary, one partial eyewall replacement cycle occurred from 2230 UTC 6 September to 0730 UTC 7 September while Ivan was over the central North Atlantic. Following the partial eyewall replacement cycle, Ivan had a V_t increase of 12 m s^{-1}

(Fig. 56a). The R_{max} increased by 33 km during the beginning of the partial eyewall replacement cycle, but then contracted by 27 km at the end of the cycle (Fig. 56b). The azimuthal-average wind profiles prior to, following, and 6 h after the partial eyewall replacement cycle (Fig. 84) suggest that R_{34} did have a time-lagged increase following partial eyewall replacement. Although the wind profile sharpened (an increase in the exponent x) during the partial eyewall replacement cycle, an increase of R_{max} plus the intensification still led to an increase in R_{34} to 247 km (a 68 km increase). The expansions of the inner-core structure for this case study are believed to be associated with PV asymmetries that result from asymmetric convection near the eyewall and will be further explored in a later section of this chapter.

3. Conclusions for Secondary Eyewall Formation

The analyses of individual case studies of complete and partial secondary eyewall replacement have revealed two modes of tropical cyclone structure changes. These two modes are represented by the conceptual radial wind profiles in Fig. 85.

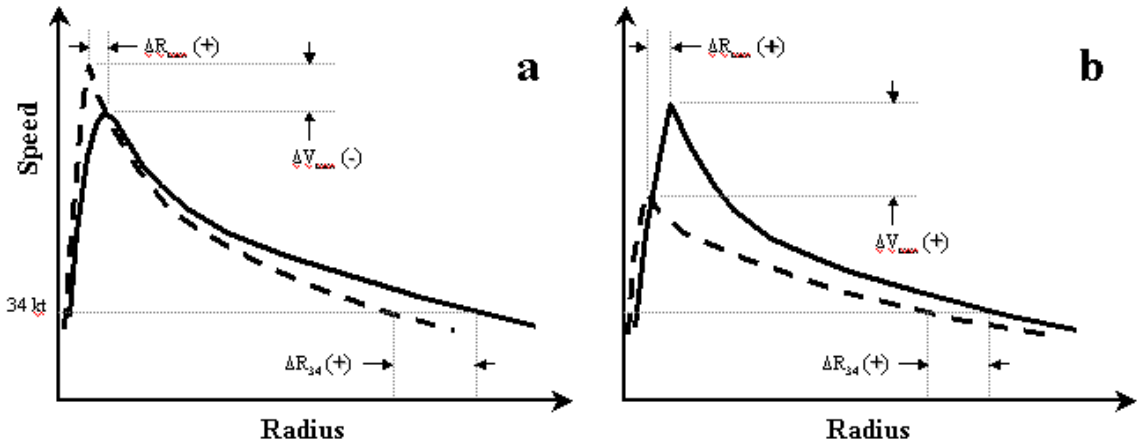

Figure 85 Conceptual radial profiles of tangential winds for tropical cyclones during complete or partial secondary eyewall replacement. The dashed and solid curves represent the azimuthal-average wind profiles at time (t) and $t+\Delta t$, respectively.

The first mode (Fig. 85a) was observed during complete and partial secondary eyewall replacement for Stage IIa and Stage III of the life cycle as defined in Fig. 9. This mode was specifically observed for complete eyewall replacement in the one Fabian (2003) case, the fourth Ivan (2004) case, and the first Wilma (2005) case (the second Wilma case was not used since the eyewall was over land). Additionally, this first

mode was observed for the partial eyewall replacement cases of Emily (2005) and Rita (2005). For this mode, the R_{max} increases and V_{max} (denoted as maximum tangential wind speed, V_t, in the discussions of Chapters III and IV) decreases in association with a complete or partial eyewall replacement cycle. The outer-core structure (R_{34}) also expands during the complete or partial eyewall replacement cycle, which includes a small and time-lagged R_{34} increase following the inner-core (R_{max}) change. This first mode is consistent with the traditional explanation for concentric eyewall replacement by Willoughby et al. (1982) as presented in Chapter I.A.3.

In these first mode cases (Fig. 85a), the average decrease in V_t was 7 m s^{-1} with a range of 6 m s^{-1} to 11 m s^{-1}. The R_{max} approximately doubled during these first mode cases, except for the Fabian eyewall replacement cycle that had a three-fold R_{max} increase and for the first Wilma eyewall replacement cycle that had a five-fold R_{max} increase. The average R_{max} increase was 28 km with a range from 6 km to 56 km.

The average R_{34} increase for these first mode cases (Fig. 85a) was 59 km with a range from 20 km to 109 km. The R_{34} increases for the first mode were generally larger than those of the second mode (discussed below) since the exponent x remains nearly constant. Indeed, the average exponent x increase was only 0.08 with a range of -0.02 to 0.21 during these first mode cases. Applying Eq. (20) to the partial eyewall replacement of Rita, the V_t decrease by 10 m s^{-1} has a 1-to-1 impact on the right side of the equation, whereas the 26 km increase in R_{max} with an exponent $x = 0.47$ has an approximate 2.4-to-1 impact. Thus, the R_{max} increase compensates for the V_t decrease and the resultant effect is a R_{34} increase of 52 km. These R_{34} increases are considerable outward expansions, especially when a tropical cyclone is approaching landfall.

Except for the partial eyewall replacement of Ivan, the second mode (Fig. 85b) was only observed during complete secondary eyewall replacement and for Stage IIa of the life cycle as defined in Fig. 9. This mode was specifically observed for both Frances (2004) cases, the first three Ivan (2004) cases, the one Katrina (2005) case, and the Ivan (2004) partial eyewall replacement case. For this mode, the R_{max} and V_{max} both increase in association with a eyewall replacement cycle. The outer-core structure (R_{34}) also expands during this eyewall replacement cycle, and often continues to expand in a time-lagged response of 6 h or more following the inner-core (R_{max}) change.

For the second mode (Fig. 85b), the observed average increase in V_t was 8 m s^{-1} with a range of 2 m s^{-1} to 13 m s^{-1}. Rapid intensification occurred during an eyewall replacement cycle when strong spiral rainband convection was in close proximity to the secondary eyewall. This was the case for the first eyewall replacement of Frances (Figs. 50c–e), the second and third eyewall replacements of Ivan (Figs. 58e–f and 61c–e), the eyewall replacement of Katrina (Figs. 67b–c), and the partial eyewall replacement of Ivan (Figs. 55a–b). Although, these convective asymmetries were not present or were much weaker for the remainder of the case studies in the second mode, the cases with convective asymmetries suggest that the process of axisymmetrization may be a potential mechanism for rapid storm intensification during eyewall replacement. The R_{max} doubled or tripled (e.g., Hurricane Katrina) during eyewall replacement for the second mode. The observed average R_{max} increase was 23 km with a range from 12 km to 37 km, which is very similar to the first mode.

The observed average R_{34} increase during eyewall replacement for the second mode (Fig. 85b) was 45 km with a range from 7 km to 99 km. The largest R_{34} increases occurred when rapid intensification (i.e., large V_t increases) was combined with a R_{max} increase. Indeed, this is consistent with Eq. (20) since increases in V_t and R_{max} on the left side of the equation are expected to result in an increase in R_{34} on the right side. However, the other unknown in Eq. 20 is the exponent x, which in the pre-eyewall replacement period for Katrina was equal to 0.31. If this exponent also applied after the eyewall replacement and using the Hour 18 values of V_t = 46 m s^{-1} and R_{max} = 34 km, the resulting R_{34} would be 807 km, which would be a 539 km increase in the outer-core radius. In reality, the observed R_{34} increase was limited to 71 km, which still represents a considerable outward expansion in less than 24 h for a tropical cyclone approaching landfall. This R_{34} increase of 539 km did not occur because the exponent for the outer profile during the eyewall replacement was much larger (0.64 versus 0.31), which implies a more rapid decrease in wind with radius. During eyewall replacement for all cases in the second mode (Fig. 85b), the post-replacement exponent x on average was increased by 0.19 with a range between 0.07 and 0.33. The smallest change in exponent x (0.07 increase) occurred for Ivan's second eyewall replacement, and R_{34} increased by 99 km in 18 h and then continued to increase by 120 km in 24 h. Thus, a "flatter-than-average" outer wind profile existed prior to the second mode of secondary eyewall formation that then became "sharper-than-average" following secondary eyewall formation. This time change in

the profile shapes demonstrates that accurately predicting the change in the R_{34} with a fixed value for exponent x during eyewall replacement is not plausible.

For all cases of complete and partial eyewall replacement with the exception of Wilma, the outward (inward) ΔKE_{anom} was correlated with an expansion (contraction) of the R_{max} radius. Indeed, the correlation coefficients for the Fabian, Frances, Ivan, and Katrina cases (0.709, 0.743, 0.642, and 0.775, respectively) suggest a linear relationship between ΔKE_{anom} and R_{max}. Additionally, the correlation coefficients for the Emily and Rita cases (0.460, and 0.399, respectively) suggest a positive correlation between the ΔKE_{anom} and the R_{max} changes, albeit with a larger spread in the values. Large increases in the radial inflow variance were often observed when strong asymmetric spiral rainband convection existed in close proximity to the primary or secondary eyewall. However, an increase in the R_{34} value was not always observed 6 h or more after the increased radial inflow variance.

The formation of a secondary eyewall was frequently observed as a tropical cyclone approached land, e.g., for Ivan at Hours 92, 164.5, and 212.5 (Figs. 58d, 64a, and 65d, respectively) as the storm center approached land within 130 km, 150 km, and 240 km, respectively. Additional examples include Hour 43 of Katrina (Fig. 67f) and Hour 65.5 of Wilma (Fig. 72c) where these storm centers experienced land interaction within 230 km and 180 km, respectively. The impacts of tropical cyclone land interaction will be further explored in a later section of this chapter.

B. ASYMMETRIC CONVECTION

As was discussed in Chapter 1, the presence of asymmetric convection in the near-core environment increases the asymmetric potential vorticity that leads to VRW generation in the process of axisymmetrization. Thus, strong convection outside the eyewall in the near-core environment is expected to have the effect of expanding the eyewall and the R_{max}. As the inner-core structure expands, the tropical cyclone intensity is expected to weaken in response. In this section, the observed changes in tropical cyclone structure will be analyzed using western North Atlantic storms from 2003 and 2004.

1. Fabian (2003)

The life cycle of Hurricane Fabian was discussed in Chapter IV.A.1.a. The analysis period of asymmetric convection for Fabian will be from 1330 UTC 1 September (Hour 0) to 1930 UTC 4 September (Hour 78) as this storm moved on a west-northwestward track across the central North Atlantic. At 1330 UTC 1 September (Hour 0 of the analysis), Fabian had a tangential wind speed (V_t) of 50 m s^{-1} with azimuthal-average R_{max} and R_{34} values of 27 km and 232 km, respectively. Microwave satellite imagery at 0201 UTC 1 September (∼11.5 h prior to Hour 0 of the analysis, Fig. 86a) indicates strong convection around a symmetric eyewall with one disorganized spiral rainband extending outward to 3 degrees in the north and east quadrants. Fabian reached its first peak intensity (V_t) of 54 m s^{-1} at Hour 10.5 (Fig. 87a). From 0 h to 12 h, there was a net increase of 24 km in the outer-core structure (R_{34}). At 0243 UTC 2 September (∼Hour 13 of the analysis, Fig. 86b), intense convection was present in the north and east quadrants of the eyewall as evidenced by microwave satellite imagery. One spiral rainband with organized strong convection extended outward from the eyewall to about 1 degree in the north and east quadrants.

From 10.5 h to 24 h, Fabian's intensity (V_t) weakened by 4 m s^{-1} while the R_{34} continued to expand by an additional 20 km to a size of 274 km (Fig. 87). Microwave satellite imagery at 1015 UTC 2 September (∼Hour 21 of the analysis, Fig. 86c) indicates strong, broad convection near the northern eyewall extended outward to 1.5 degrees. As in the previous case studies, a large spike in the radial inflow variance from 24 h to 30 h appears to be associated with the presence of asymmetric convection (Fig. 87a). During this first period of asymmetric convection (Hour 18 to Hour 36 in Fig. 87), R_{max} and the inner eyewall expanded by approximately 50 percent (increased from 25 km to 38 km, and 6 km to 10 km, respectively) from 24 h to 36 h. This expansion of the inner-core structure was coincident with an outward ΔKE_{anom} (Fig. 87b). This expansion is also consistent with the expectation that the presence of asymmetric convection in the near-core environment increases the asymmetric potential vorticity, and thus leads to an expansion of the R_{max} and eyewall radius.

Microwave satellite imagery at 0146 UTC and 0957 UTC 3 September (∼Hours 36.5 and 44.5 of the analysis, Figs. 86d–e) suggests that near-core convection along the northern eyewall had merged to form a broad asymmetric convective eyewall with sporadic disorganized convection outside of the eyewall.

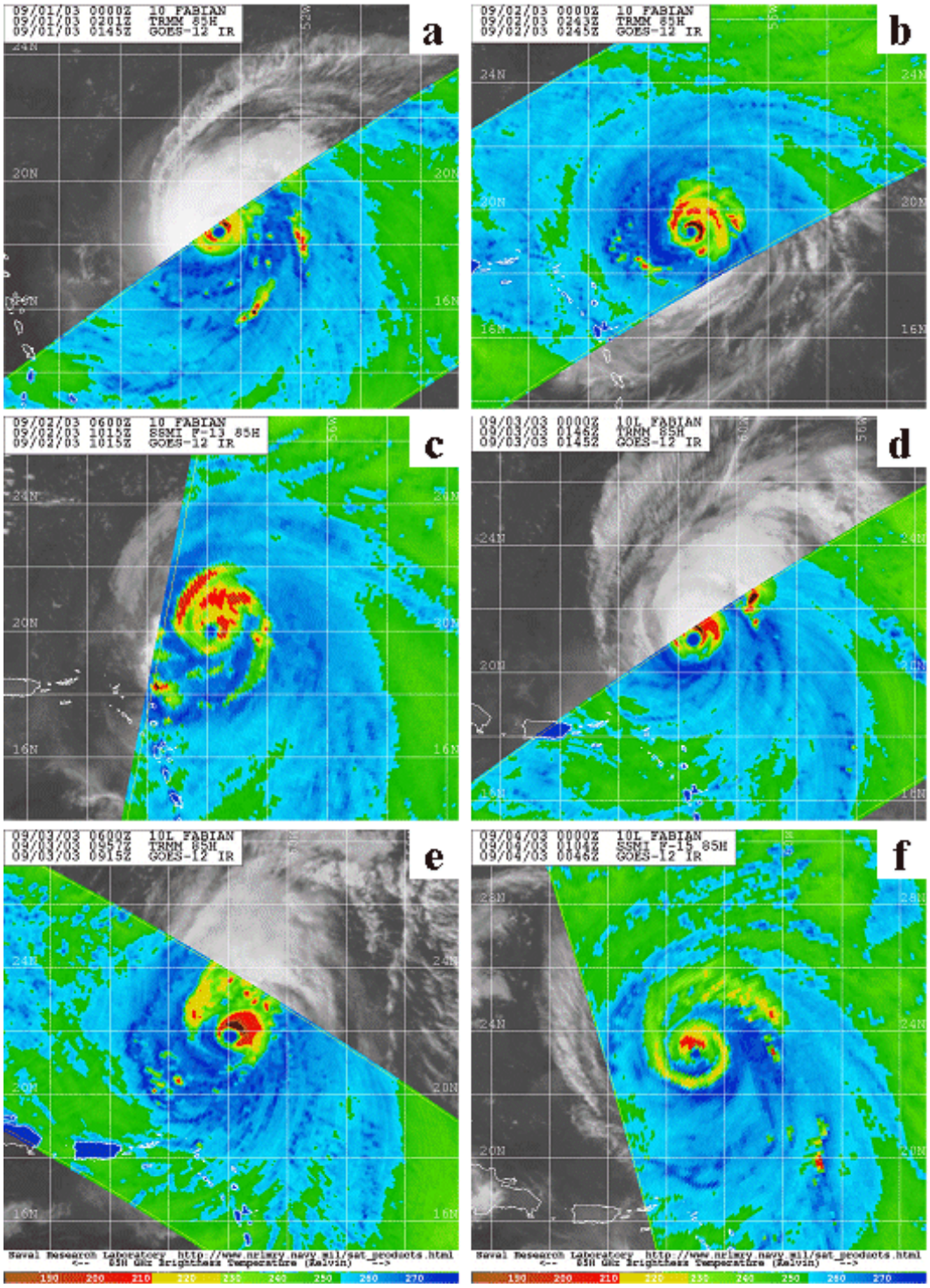

Figure 86 Microwave satellite imagery (85 GHz) for Hurricane Fabian from TRMM and DMSP polar orbiting platforms on (a) 1 September at 0201 UTC, (b) 2 September at 0243 UTC, (c) 2 September at 1015 UTC, (d) 3 September at 0146 UTC, (e) 3 September at 0957 UTC, and (f) 4 September at 0104 UTC (2003; from NRL 2007).

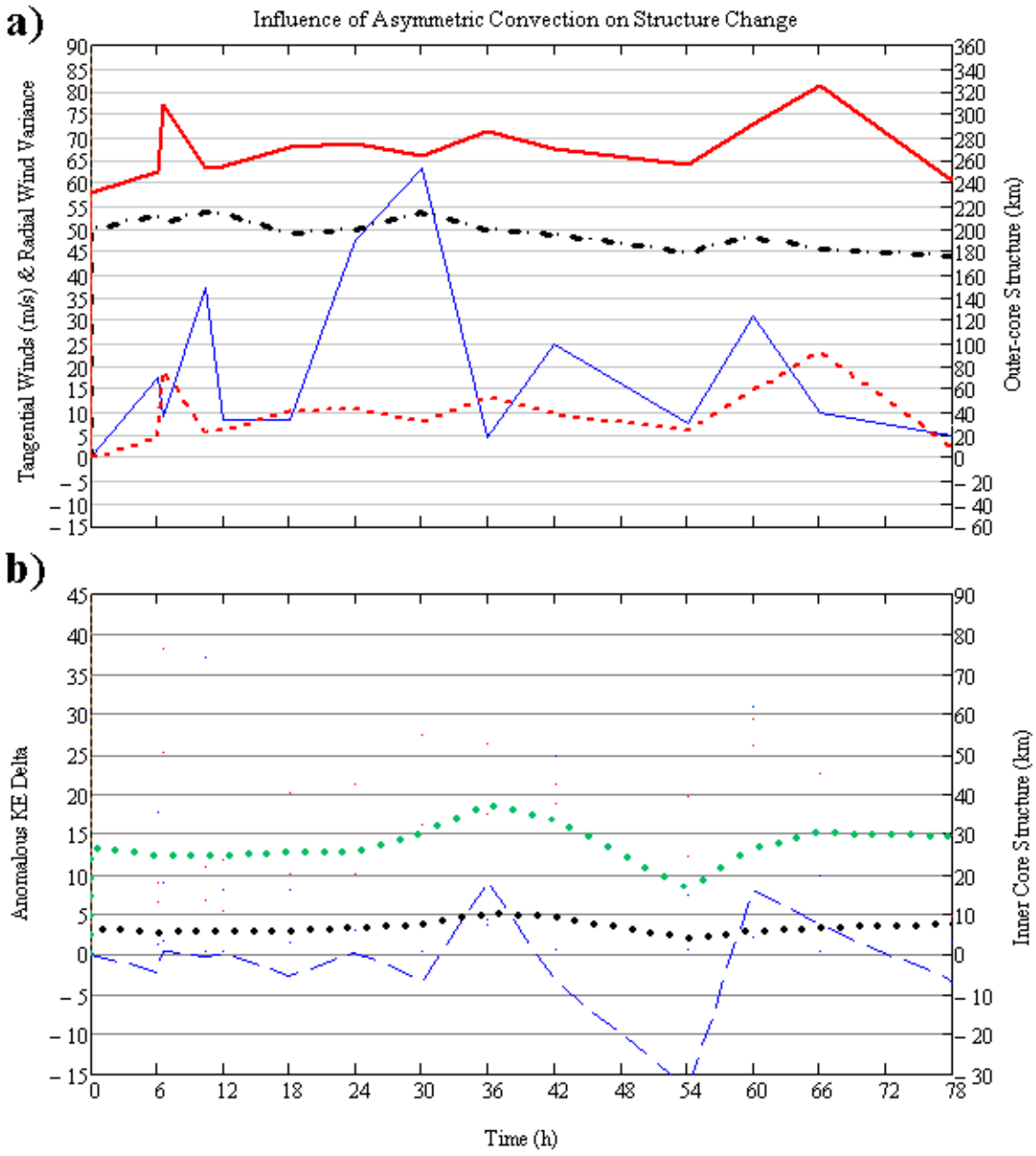

Figure 87 Time series of structure changes as in Fig. 48, except for Hurricane Fabian (2003) from 1 September at 1330 UTC (Hour 0) to 4 September at 1930 UTC (Hour 78).

As the near-core asymmetric convection diminished, R_{max} and the inner eyewall radius contracted to 21 km and 6 km, respectively, in the presence of an inward ΔKE_{anom} (Fig. 87b). As Fabian's inner-core structure changed in response to the presence of asymmetric convection, the intensity (V_t) initially increased to 54 m s^{-1} (a 5 m s^{-1} increase) by Hour 30, and then decreased to 45 m s^{-1} by Hour 54 (Fig. 87a). The initial increase in V_t as the inner-core structure expands is inconsistent with the expected response of a decrease in V_t as the eyewall expands.

The azimuthal-average wind profiles in Fig. 88a prior to, following, and 6 h after this inner-core structure response to asymmetric convection (Hours 18, 36, and 42, respectively) suggest an initial small increase in the outer-core structure (R_{34}), and then a decrease during the 6 h after the inner-core structure response. The R_{max} increased by 13 km in association with the asymmetric convection but then decreased by 4 km in the subsequent 6 h. Similarly, the R_{34} increased by 7 km during the inner-core structure response (blue arrow in Fig. 88a) but then decreased by 15 km 6 h after the inner-core structure response (red arrow in Fig. 88a), which resulted in a net decrease of 8 km.

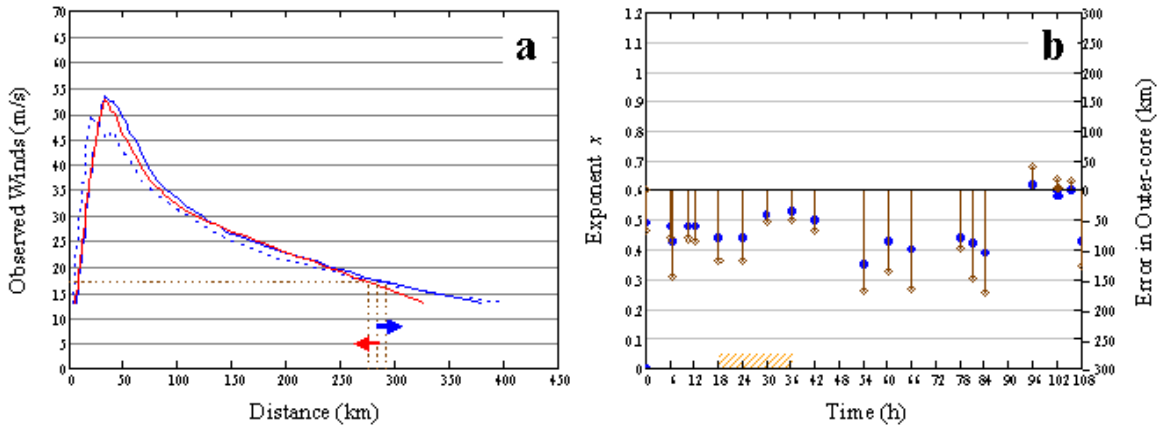

Figure 88 (a) Azimuthal-average wind profiles for Hurricane Fabian at Hour 18 (blue dashed line), Hour 36 (blue solid line) and Hour 42 (red solid line), and (b) observed values for exponent x in the modified Rankine vortex (blue circles) and the prediction error (stem plots) when the mean value for exponent $x = 0.58$ is applied in Eq. (20). The orange-hashed rectangle is the nominal first period of asymmetric convection associated inner-core structure changes.

The exponent x values assuming a modified Rankine vortex suggest that Fabian had a larger outer-core structure prior to and during this inner-core structure response to asymmetric convection than the overall population of Atlantic tropical cyclones during 2003–2005 (Fig. 88b). Indeed, applying the overall mean value for exponent x = 0.58 in the modified Rankine vortex in Eq. (20) results in an under-prediction of R_{34} by 50–118 km prior to and during this inner-core structure response to asymmetric convection, as depicted by the stem plots in Fig. 88b. Recall, the mean modified Rankine vortex exponent x during the life cycle of Fabian was 0.48 (see Chapter IV.A.1.a). Individual exponent values for Hours 18, 36, and 42 were x = 0.44, x = 0.53, and x = 0.50, respectively. The larger exponent x at Hour 36 compared to Hour 18 suggests that the wind profile sharpened following this inner-core structure response to asymmetric convection.

Microwave satellite imagery at 0104 UTC (∼Hour 59.5 of the analysis, Figs. 86f) indicates strong, asymmetric convection existed in the northern eyewall with strong convection in one spiral rainband in close proximity (∼1 degree) to the eyewall. Although less pronounced, a spike in the radial inflow variance around 60 h again appears to be associated with the presence of asymmetric convection (Fig. 87a).

During this second period of asymmetric convection (Hour 54 to Hour 66 in Fig. 87), R_{max} and the inner eyewall expanded by approximately 75 percent (increased from 17 km to 30 km and from 4 km to 7 km, respectively) from 54 h to 66 h. As with the previous case, this expansion of the inner-core structure was coincident with an outward ΔKE_{anom} (Fig. 87b), which is consistent with the expectation that the presence of asymmetric convection in the near-core environment leads to an increase in R_{max} and the eyewall radius. As Fabian's inner-core structure changed in response to the presence of asymmetric convection, the intensity (V_t) initially increased to 54 m s^{-1} (a 3 m s^{-1} increase) by Hour 60, and then decreased to 46 m s^{-1} by Hour 84 (Fig. 87a). As with the previous case, the initial increase in V_t as the inner-core structure expanded is inconsistent with the expected response of a decrease in V_t as the eyewall expands.

The azimuthal-average wind profiles in Fig. 89a prior to, following, and 12 h after this inner-core structure response to asymmetric convection (Hours 54, 66, and 78, respectively) suggest an initial increase in the outer-core structure (R_{34}), and then a decrease during the 12 h after the inner-core structure response. The R_{max} increased by 13 km in association with the asymmetric convection and then decreased by 4 km

in the subsequent 12 h. Similarly, the R_{34} increased by 70 km during the inner-core structure response (blue arrow in Fig. 89a) and then decreased by 85 km 12 h after the inner-core structure response (red arrow in Fig. 89a), which is a net decrease of 15 km.

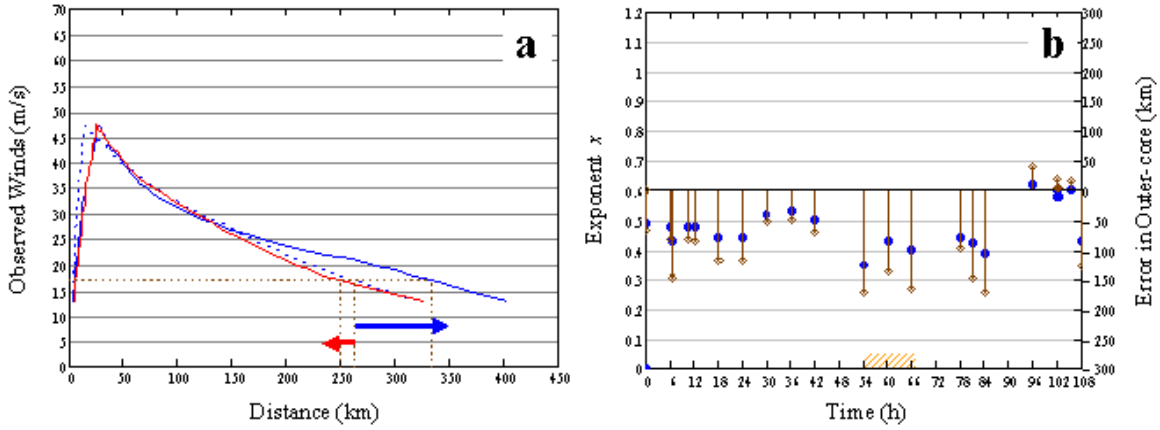

Figure 89 (a) Azimuthal-average wind profiles for Hurricane Fabian at Hour 54 (blue dashed line), Hour 66 (blue solid line) and Hour 78 (red solid line), and (b) observed values for exponent x in the modified Rankine vortex (blue circles) and the prediction error (stem plots) when the mean value for exponent $x = 0.58$ is applied in Eq. (20). The orange-hashed rectangle is the nominal second period of asymmetric convection associated inner-core structure changes.

The exponent x values assuming a modified Rankine vortex suggest that Fabian had a larger outer-core structure prior to and during this inner-core structure response to asymmetric convection than the overall population of Atlantic tropical cyclones during 2003–2005 (Fig. 89b). Indeed, applying the overall mean value for exponent x = 0.58 in the modified Rankine vortex in Eq. (20) results in an under-prediction of R_{34} by 136–171 km prior to and during this inner-core structure response to asymmetric convection, as depicted by the stem plots in Fig. 89b. Individual exponent values for Hours 54, 66, and 78 were $x = 0.35$, $x = 0.40$, and $x = 0.44$, respectively. As with the first case of asymmetric convection in Fabian, the larger exponent x at Hour 66 compared to Hour 54 suggests that the wind profile sharpened following this inner-core structure response to asymmetric convection.

In summary, two periods of asymmetric convection occurred during the life cycle of Fabian from 1330 UTC 1 September to 0130 UTC 6 September. During these two

periods of asymmetric convection, this tropical cyclone intensified with V_t increases of 5 m s^{-1} and 3 m s^{-1}, respectively (Fig. 87a). The R_{max} increased by 50–75 percent during these two periods of asymmetric convection (13 km increases for each period). Inward (outward) ΔKE_{anom} was generally associated with a decrease (increase) in R_{max}. Indeed, the correlation coefficient of 0.709 indicates a linear relationship between ΔKE_{anom} and R_{max}. Additionally, an increase in radial inflow variance was observed when convective asymmetries were present in or near the eyewall.

The azimuthal-average wind profiles prior to, following, and 6–12 h after these two periods of asymmetric convection (Figs. 88 and 89) suggest that R_{34} initially increased but then had a larger decrease, which thus resulted in a net decrease in R_{34}. The range of exponent x values was 0.35–0.62, where the smaller (larger) values occurred prior to (after) the inner-core structure response to asymmetric convection. Indeed, the exponent x increased from 0.44 to 0.53 and 0.35 to 0.40 during these two periods of asymmetric convection, respectively. As with the cases of secondary eyewall formation, the inner-core response to asymmetric convection occurred when a flatter-than-average tangential wind profile existed, and was followed by a sharper wind profile. The role that vertical wind shear plays in these convective asymmetries and resultant structure changes will be discussed in Chapter IV.D.

2. Isabel (2003)

Isabel became a named storm by 0600 UTC 6 September over the central North Atlantic in the vicinity of 14.0°N, 32.7°W. This tropical cyclone had a west-southwestward track for 12 h prior to moving west-northwestward. Isabel reached hurricane strength at 1200 UTC 7 September and continued on a west-northwestward track across the North Atlantic for 60 h before heading westward. After 0600 UTC 13 September, Hurricane Isabel moved on a west-northwestward track for 54 h before turning north-northwestward and making landfall near Cape Hatteras, North Carolina at approximately 1800 UTC 18 September. H*Wind analyses for Isabel became available at 1930 UTC 12 September and at regular increments until 1630 UTC 18 September as the storm approached landfall.

At 1930 UTC 12 September (hereafter referred to as Hour 0 of the analysis), Isabel had a tangential wind speed (V_t) of 60 m s^{-1} with azimuthal-average R_{max} and R_{34} values of 26 km and 217 km, respectively. Microwave satellite imagery at 2126 UTC 12 September (∼Hour 2 of the analysis, Fig. 90a) indicates a broad convective

eyewall with the strongest, broadest convection in the southern eyewall and minimal spiral rainband activity surrounding the eyewall. As in the Fabian cases, a spike in the radial inflow variance from 6 h to 12 h appears to be associated with the presence of asymmetric convection (Fig. 91a).

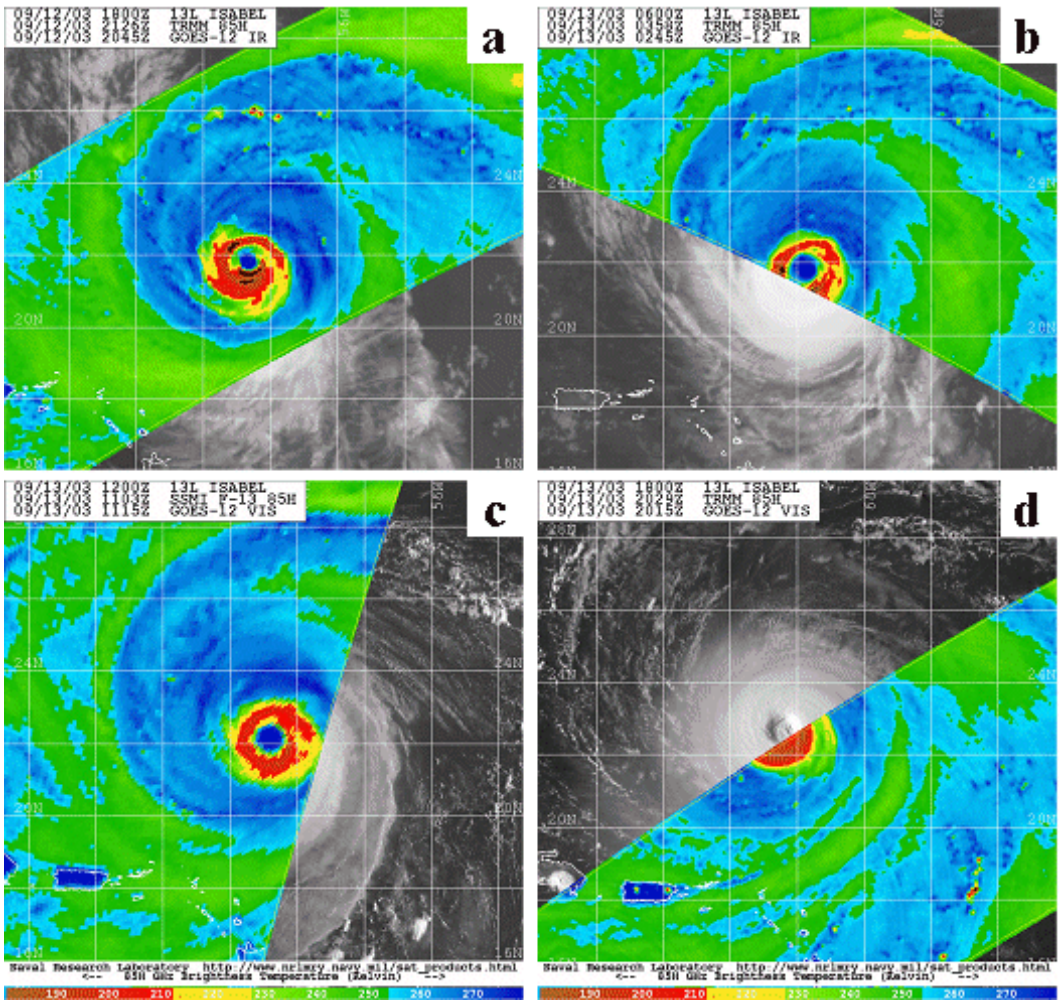

Figure 90 Microwave satellite imagery (85 GHz) for Hurricane Isabel from TRMM and DMSP polar orbiting platforms on (a) 12 September at 2126 UTC, (b) 13 September at 0358 UTC, (c) 13 September at 1103 UTC, and (d) 13 September at 2029 UTC (2003; from NRL 2007).

During this first period of asymmetric convection (Hour 0 to Hour 12 in Fig. 91) in Isabel, R_{max} and the inner eyewall doubled (increased from 26 km to 51 km and from 4 km to 10 km, respectively) from 0 h to 12 h. This expansion of the inner-core structure was coincident with an outward ΔKE_{anom} (Fig. 91b).

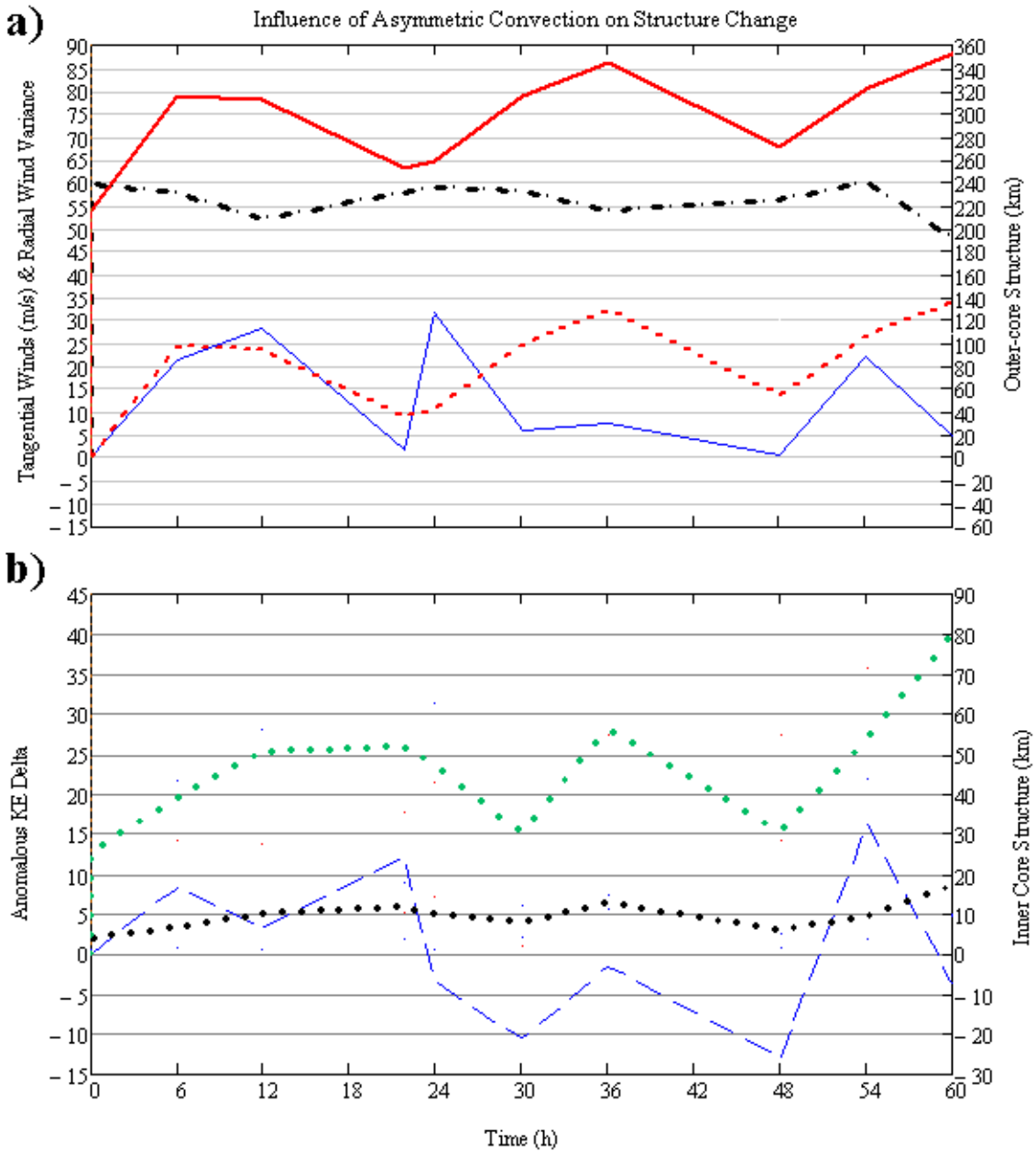

Figure 91 Time series of structure changes as in Fig. 48, except for Hurricane Isabel (2003) from 12 September at 1930 UTC (Hour 0) to 15 September at 0730 UTC (Hour 60).

This expansion is also consistent with the expectation that asymmetric convection in the near-core environment leads to an increase in the R_{max} and eyewall radius. In contrast to the two cases of asymmetric convection for Fabian, the intensity (V_t) decreased from 60 m s^{-1} to 52 m s^{-1} from 0 h to 12 h (Fig. 91a), but thus is consistent with the expected V_t decrease when the eyewall expands.

The azimuthal-average wind profiles in Fig. 92a prior to, following, and 10 h after this inner-core structure response to asymmetric convection (Hours 0, 12, and 22, respectively) suggest an initial increase in the outer-core structure (R_{34}), but then a decrease during the 10 h after the inner-core structure response. The R_{max} increased by 25 km in association with the asymmetric convection and then had a slight increase during the subsequent 10 h. The R_{34} increased by 100 km during the inner-core structure response (blue arrow in Fig. 92a), but then decreased by 64 km 10 h after the inner-core structure response (red arrow in Fig. 92a), and thus had a net increase of 36 km.

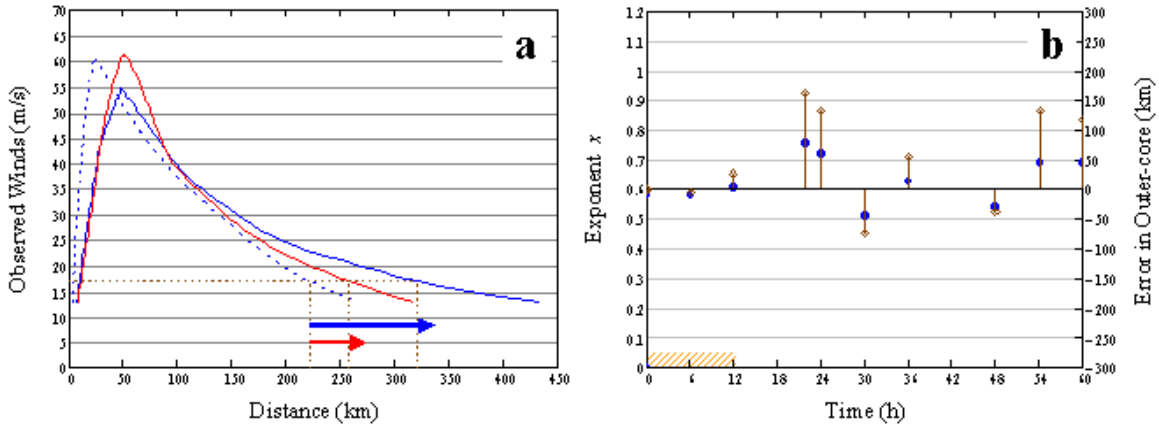

Figure 92 (a) Azimuthal-average wind profiles for Hurricane Isabel at Hour 0 (blue dashed line), Hour 12 (blue solid line) and Hour 22 (red solid line), and (b) observed values for exponent x in the modified Rankine vortex (blue circles) and the prediction error (stem plots) when the mean value for exponent $x = 0.58$ is applied in Eq. (20). The orange-hashed rectangle is the nominal first period of asymmetric convection associated inner-core structure changes.

The exponent x values assuming a modified Rankine vortex suggest that Isabel had a similar outer-core structure prior to and during this inner-core structure response to asymmetric convection to the overall population of Atlantic tropical cyclones during

2003–2005 (Fig. 92b). Indeed, applying the overall mean value for exponent $x = 0.58$ in the modified Rankine vortex in Eq. (20) results in an accurate prediction of the R_{34} prior to and only a small over-prediction (26 km) during this inner-core structure response to asymmetric convection, as depicted by the stem plots in Fig. 92b. The mean modified Rankine vortex exponent x during the first 60 h of Isabel's life cycle was 0.63 with individual values of $x = 0.58$, $x = 0.61$, and $x = 0.76$ at Hours 0, 12, and 22, respectively. The larger exponent x at Hour 22 compared to Hour 0 suggests that the wind profile sharpened (albeit time-lagged) following this inner-core structure response to asymmetric convection.

Microwave satellite imagery at 0358 UTC, 1103 UTC, and 2029 UTC 13 September (∼Hours 8.5, 15.5, and 25 of the analysis, Fig. 90b–d) indicates the development of a highly symmetric annular structure with a broad, convectively active eyewall with no spiral rainbands. As Isabel's eyewall became more symmetric, the inner-core structure (R_{max}) contracted to 30 km (decreased by 22 km) by Hour 30 (Fig. 91b). In conjunction with the decrease in R_{max}, the storm intensity (V_t) increased from 52 m s^{-1} to 59 m s^{-1} (Fig. 91a), which is consistent with the expected V_t increase when the eyewall contracts. The inner-core contraction from 24 h to 30 h coincided with an inward ΔKE_{anom} (Fig. 91b).

Microwave satellite imagery at 0439 UTC 14 September (∼Hour 33 of the analysis, Fig. 93a) indicates that Isabel's eyewall was becoming less symmetric with a broader southern eyewall and with the development of near-core spiral rainbands. As with the first case of Isabel, a spike in the radial inflow variance was observed around 24 h as the convective asymmetries depicted in Fig. 93a were developing. During this second period of asymmetric convection (Hour 30 to Hour 36 in Fig. 91), R_{max} and the inner eyewall nearly doubled (increased from 30 km to 56 km and from 8 km to 13 km, respectively) from 30 h to 36 h. In contrast to the first case, this expansion of the inner-core structure was coincident with a decreased inward ΔKE_{anom} (Fig. 91b). As with other cases of asymmetric convection, this expansion is consistent with the expectation that the presence of asymmetric convection in the near-core environment leads to an increase in R_{max} and the eyewall radius. As with the first case of Isabel, the intensity (V_t) decreased from 58 m s^{-1} to 54 m s^{-1} from 30 h to 36 h (Fig. 91a), which is consistent with the expected V_t decrease when the eyewall expands.

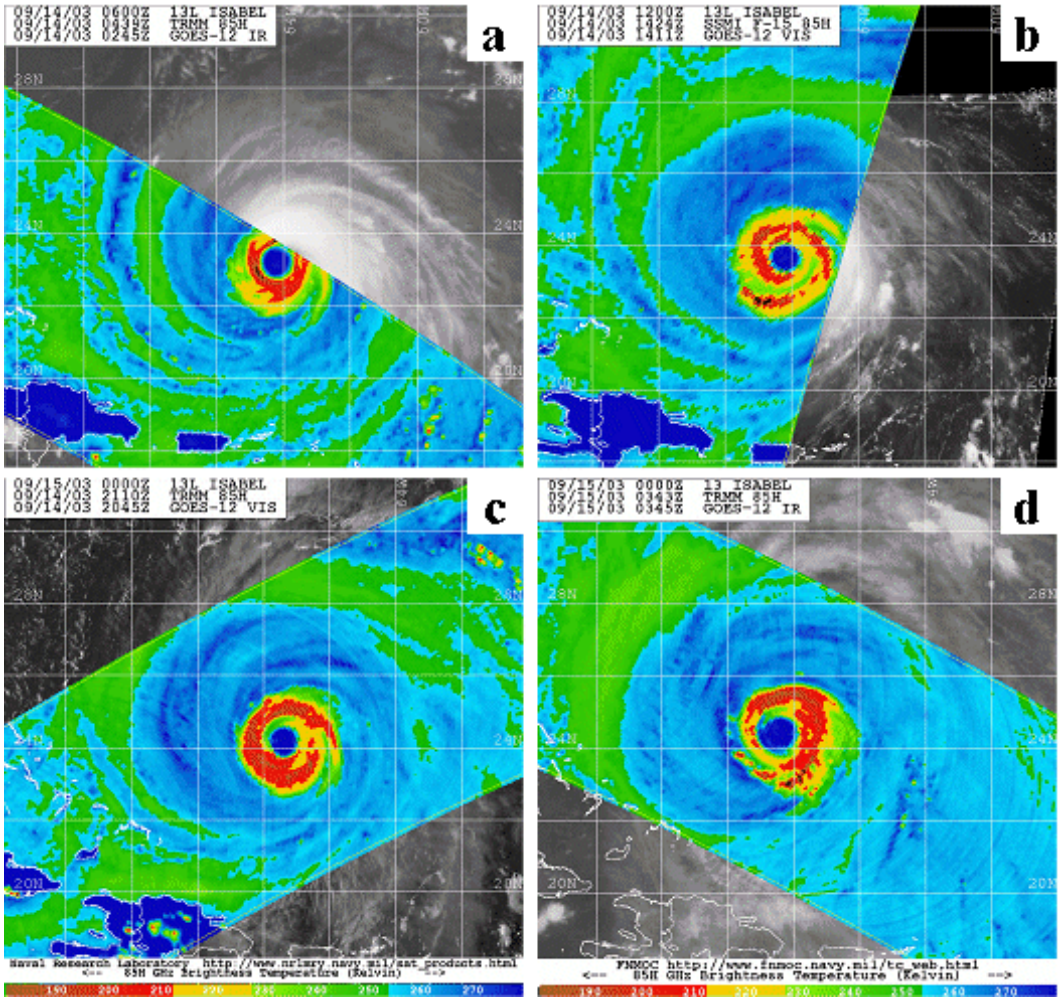

Figure 93 Microwave satellite imagery (85 GHz) for Hurricane Isabel from TRMM and DMSP polar orbiting platforms on (a) 14 September at 0439 UTC, (b) 14 September at 1424 UTC, (c) 14 September at 2110 UTC, and (d) 15 September at 0343 UTC (2003; from NRL 2007).

The azimuthal-average wind profiles in Fig. 94a prior to, following, and 12 h after this inner-core structure response to asymmetric convection (Hours 30, 36, and 48, respectively) suggest an initial increase in the outer-core structure (R_{34}), and then a decrease during the 12 h after the inner-core structure response. The R_{max} increased by 26 km in association with the asymmetric convection and then decreased by 25 km in the subsequent 12 h. The R_{34} increased by 31 km during the inner-core structure response (blue arrow in Fig. 94a), but then decreased by 79 km 12 h after the inner-core structure response (red arrow in Fig. 94a), and thus had a net decrease of 48 km.

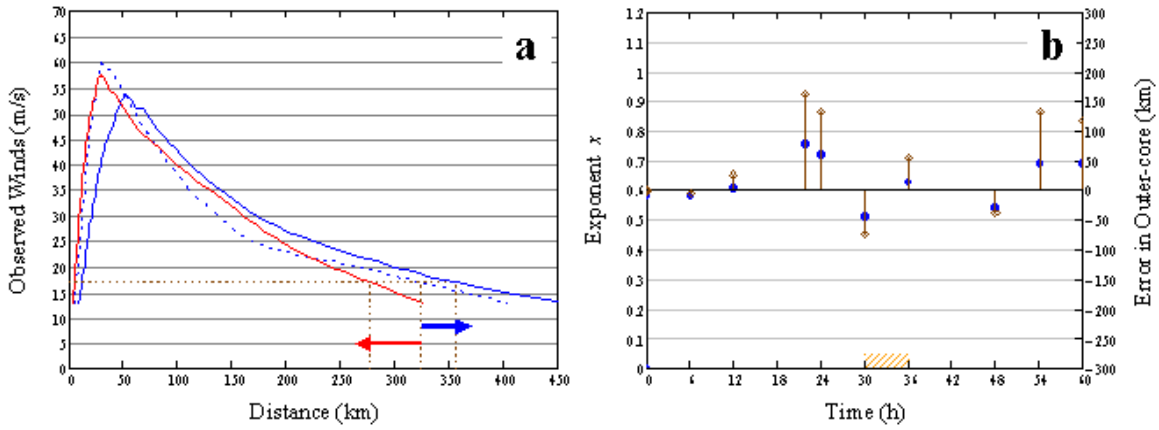

Figure 94 (a) Azimuthal-average wind profiles for Hurricane Isabel at Hour 30 (blue dashed line), Hour 36 (blue solid line) and Hour 48 (red solid line), and (b) observed values for exponent x in the modified Rankine vortex (blue circles) and the prediction error (stem plots) when the mean value for exponent $x = 0.58$ is applied in Eq. (20). The orange-hashed rectangle is the nominal second period of asymmetric convection associated inner-core structure changes.

The exponent x values assuming a modified Rankine vortex suggest that Isabel had a similar outer-core structure prior to and during this inner-core structure response to asymmetric convection to the overall population of Atlantic tropical cyclones during 2003–2005 (Fig. 94b). Indeed, applying the overall mean value for exponent $x = 0.58$ in the modified Rankine vortex in Eq. (20) results in an under-prediction of R_{34} by 73 km prior to and an over-prediction by 55 km during this inner-core structure response to asymmetric convection, as depicted by the stem plots in Fig. 94b. Individual exponent values for Hours 30, 36, and 48 were $x = 0.51$, $x = 0.63$, and $x = 0.54$, respectively. The larger exponent x at Hour 36 compared to Hour 30 again suggests that the wind profile sharpened following this inner-core structure response to asymmetric convection.

As Isabel became more symmetric with near-core spiral rainbands as depicted by microwave satellite imagery at 1424 UTC 14 September (~Hour 43 of the analysis, Fig. 93b), the storm inner-core structure (R_{max}) once again contracted. An inward ΔKE_{anom} between 36 h and 48 h was associated with the R_{max} and inner eyewall contraction of 25 km and 7 km, respectively (Fig. 91b). As the storm inner-core structure became more symmetric and the eyewall contracted, V_t increased by 6 m s^{-1},

and thus returned to a storm intensity of 60 m s^{-1} by Hour 54 (Fig. 91a). As before, an increase of V_t when the eyewall contracts was expected.

Microwave satellite imagery at 2110 UTC 14 September (∼Hour 49.5 of the analysis, Fig. 93c) indicates that Isabel's eyewall was asymmetric with broad, strong convection in the southern eyewall and weak convection in the eastern eyewall. An increased convective asymmetry of Isabel's inner-core structure was evident in the microwave satellite imagery at 0343 UTC 15 September (∼Hour 56 of the analysis, Fig. 93d). Whereas the northern and eastern eyewalls had broad, strong convection, the western and southern eyewalls had weaker convection. As in other cases of convective asymmetry, a spike in the radial inflow variance at 54 h suggests an association with the asymmetric convection (Fig. 91a).

During this third period of asymmetric convection (Hour 48 to Hour 60 in Fig. 91), R_{max} and the inner eyewall had a 1.5-fold expansion (increased from 31 km to 79 km and from 6 km to 17 km, respectively) from 48 h to 60 h. As with the first case, this expansion of the inner-core structure was coincident with an outward ΔKE_{anom} (Fig. 91b). Similar to the other cases of asymmetric convection, this expansion is consistent with the expectation that the presence of asymmetric convection in the near-core environment leads to an increase in R_{max} and the eyewall radius. As with the other cases of Isabel, the intensity (V_t) decreased from 60 m s^{-1} to 49 m s^{-1} from 54 h to 60 h (Fig. 91a), which is consistent with the expected V_t decrease when the eyewall expands.

The azimuthal-average wind profiles in Fig. 95a prior to, following, and 6 h after this inner-core structure response to asymmetric convection (Hours 48, 60, and 66, respectively) suggest an initial increase in the outer-core structure (R_{34}), and then a continued small increase during the 6 h after the inner-core structure response. The R_{max} increased by 48 km in association with the asymmetric convection and then decreased by 15 km 6 h after. By contrast, R_{34} increased by 82 km during the inner-core structure response (blue arrow in Fig. 95a) and then continued to increase by an additional 7 km 6 h after the inner-core structure response (red arrow in Fig. 95a), which is a net increase of 89 km.

The exponent x values assuming a modified Rankine vortex suggest that Isabel had a smaller outer-core structure during this inner-core structure response to asymmetric convection than the overall population of Atlantic tropical cyclones during

2003–2005 (Fig. 95b). Indeed, applying the overall mean value for exponent $x = 0.58$ in the modified Rankine vortex in Eq. (20) results in an under-prediction of R_{34} by 37 km prior to and an over-prediction by 118–132 km during this inner-core structure response to asymmetric convection, as depicted by the stem plots in Fig. 95b. Individual exponent values for Hours 48, 60, and 66 were $x = 0.54$, $x = 0.69$, and $x = 0.61$, respectively. The larger exponent x at Hour 60 compared to Hour 48 again suggests that the wind profile sharpened following this inner-core structure response to asymmetric convection.

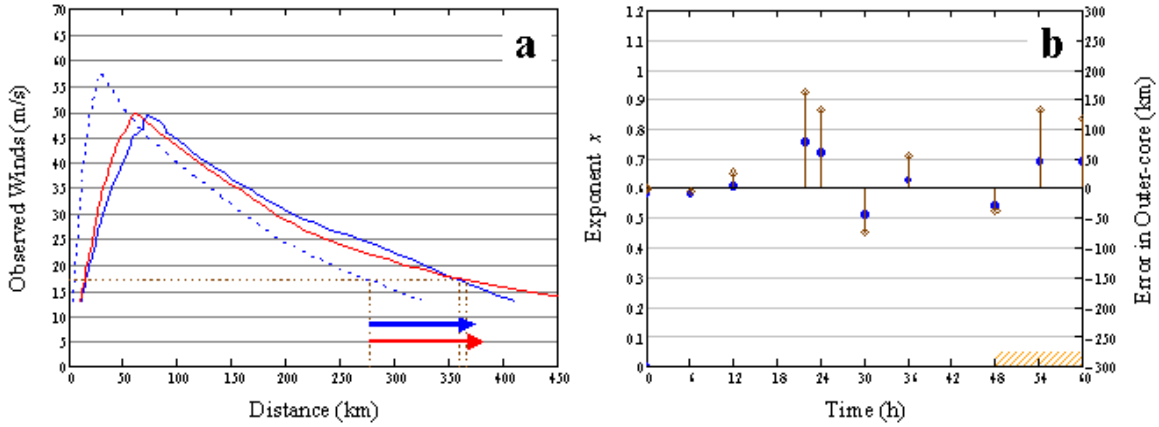

Figure 95 (a) Azimuthal-average wind profiles for Hurricane Isabel at Hour 48 (blue dashed line), Hour 60 (blue solid line) and Hour 66 (red solid line), and (b) observed values for exponent x in the modified Rankine vortex (blue circles) and the prediction error (stem plots) when the mean value for exponent $x = 0.58$ is applied in Eq. (20). The orange-hashed rectangle is the nominal third period of asymmetric convection associated inner-core structure changes.

In summary, three periods of asymmetric convection occurred during the life cycle of Isabel from 1930 UTC 12 September to 0730 UTC 15 September. During each period of asymmetric convection, this tropical cyclone weakened with V_t decreases of 8 m s^{-1}, 4 m s^{-1}, and 11 m s^{-1}, respectively (Fig. 91a). In contrast to the Fabian cases, the decreases in V_t in the first two cases of Isabel were followed by intensification as the eyewall contracted in response to increasing structure symmetry (Fig. 91a). The R_{max} increased by 150–200 percent during all three periods of asymmetric convection (increased by 25 km, 26 km and from 48 km, respectively). Inward (outward) ΔKE_{anom} was generally associated with a decrease (increase) of the R_{max} radius. Indeed, the

correlation coefficient of 0.556 indicates a linear relationship between ΔKE_{anom} and R_{max}. In addition, an increase in radial inflow variance was observed when convective asymmetries were present in or near the eyewall.

The azimuthal-average wind profiles prior to, following, and 10–12 h after the first two periods of asymmetric convection (Figs. 92 and 94) suggest that R_{34} initially increased and then decreased following the inner-core response response to asymmetric convection. During the first two periods of asymmetric convection, V_t decreased as R_{max} increased, and then V_t increased as R_{max} decreased following the inner-core response to asymmetric convection. By contrast, the third period of asymmetric convection (Fig. 95) was consistent with the first mode of secondary eyewall formation in Fig. 85a in which R_{34} increases during the inner-core (R_{max}) expansion and then is followed by a smaller time-lagged expansion after the inner-core increase. The role that vertical wind shear played in the transition of Isabel from an annular structure to a more asymmetric structure from Hour 48 and beyond will be discussed in Chapter IV.D. The range of exponent x values was 0.51–0.76, where the smaller (larger) values occurred prior to (after) the inner-core structure response to asymmetric convection. Indeed, the exponent x increased from 0.58 to 0.61, 0.51 to 0.63, and 0.54 to 0.69 during the three periods of asymmetric convection, respectively. As with the cases of secondary eyewall formation, the inner-core response to asymmetric convection occurred when a flatter-than-average radial wind profile existed, and was followed by a sharper radial profile.

3. Jeanne (2004)

Jeanne became a named storm by 1200 UTC 14 September as it passed over the Lesser Antilles in the vicinity of 16.4°N, 62.7°W. This tropical cyclone had a west-northwestward track prior to making landfall over Puerto Rico at approximately 1600 UTC 15 September. Jeanne re-emerged over water at 0000 UTC 16 September and moved westward to make a second landfall along the northern coast of the Dominican Republic as it reached hurricane strength at 1200 UTC 16 September. After moving along the northern coast of the Dominican Republic (with the storm center over land), Jeanne re-emerged as a tropical depression over the western North Atlantic (north of Haiti) at about 1800 UTC 17 September. Jeanne quickly regained tropical storm strength and moved west-northwestward for about 12 h, and then northward for 60 h before regaining hurricane strength at 1800 UTC 20 September northeast of the Ba-

hamas in the vicinity of 27.5°N. Jeanne then moved eastward in a broad clockwise loop for 54 h before moving westward and eventually making landfall over southern Florida at approximately 0400 UTC 26 September. H*Wind analyses for Jeanne became available at 1930 UTC 14 September, but were only available in irregular increments until 0730 UTC 24 September. After 0730 UTC 24 September, the analyses were available in regular increments until 0330 UTC 26 September as the storm approached landfall along the east coast of Florida.

At 1930 UTC 22 September (hereafter referred to as Hour 0 of the analysis), Jeanne had a tangential wind speed (V_t) of 35 m s^{-1} with azimuthal-average R_{max} and R_{34} values of 31 km and 217 km, respectively. As Jeanne completed a clockwise loop and began a westward track, microwave satellite imagery at 2327 UTC 22 September (∼Hour 4 of the analysis, Fig. 96a) indicates a convectively weak, symmetric eyewall and one spiral rainband with sporadic convection extending outward to 2 degrees in the north quadrant. At Hour 10.5 of the analysis, stronger convection was present in the eyewall and strong convection was present just outside the eyewall, as evidenced by microwave satellite imagery at 0559 UTC 23 September (Fig. 96b). Microwave satellite imagery at 1800 UTC 23 September (∼Hour 22.5 of the analysis, Fig. 96c) depicts a weakening of convection in the eyewall and strengthening convection in a spiral rainband in the northeast quadrant about 1 degree from the storm center. As the storm continued to evolve, the strong convection in the spiral rainband migrated to the south quadrant while convection in the eyewall continued to weaken, which is evident in the microwave satellite imagery at 0009 UTC 24 September (∼Hour 28.5 of the analysis, Fig. 96d).

Microwave satellite imagery at 0503 UTC 24 September (∼Hour 33.5 of the analysis, Fig. 97a) indicates weak convection in the eyewall and spiral rainbands as this tropical cyclone crossed over its previous northward track, which is a region of lower sea-surface temperatures due to mixing forced by the tropical cyclone circulation. During the first 36 h, Jeanne's intensity (V_t) decreased by 6 m s^{-1} to 29 m s^{-1} (Fig. 98a). During this same period, R_{34}, R_{max}, and the inner eyewall radius increased by 117 km, 18 km, and 4 km, respectively (Fig. 98). Although there are no data points between Hours 0 and 36 in Fig. 98, it is likely that the increase in R_{max} was in response to the asymmetric spiral rainband convection observed in Figs. 96c–d. Microwave satellite imagery at 1146 UTC and 1435 UTC 24 September (∼Hours 40.5 and 43 of the analysis, Figs. 97b–c) indicates intense convection existed in a spiral

rainband near the weakened eyewall. During this period of asymmetric convection (Hour 42 to Hour 48 in Fig. 98), R_{max} and the inner eyewall expanded by approximately 30 percent (increased from 48 km to 63 km), and 15 percent (increased from 13 km to 15 km), respectively. As with the other cases of asymmetric convection, this expansion of the inner-core structure was coincident with an outward ΔKE_{anom} (Fig. 98b), which is consistent with the expectation that asymmetric convection in the near-core environment leads to an increase in R_{max} and the eyewall radius.

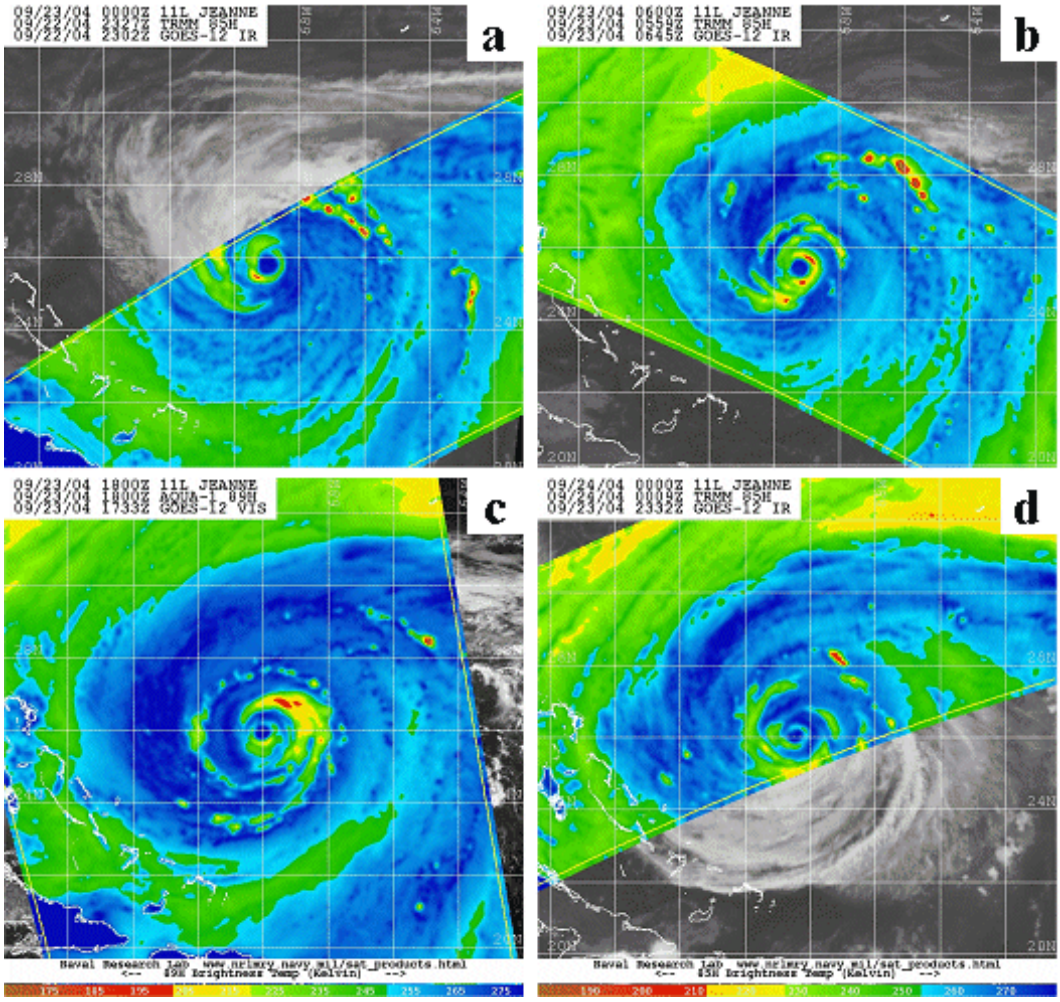

Figure 96 Microwave satellite imagery (85-89 GHz) for Hurricane Jeanne from Aqua and TRMM polar orbiting platforms on (a) 22 September at 2327 UTC, (b) 23 September at 0559 UTC, (c) 23 September at 1800 UTC, and (d) 24 September at 0009 UTC (2004; from NRL 2007).

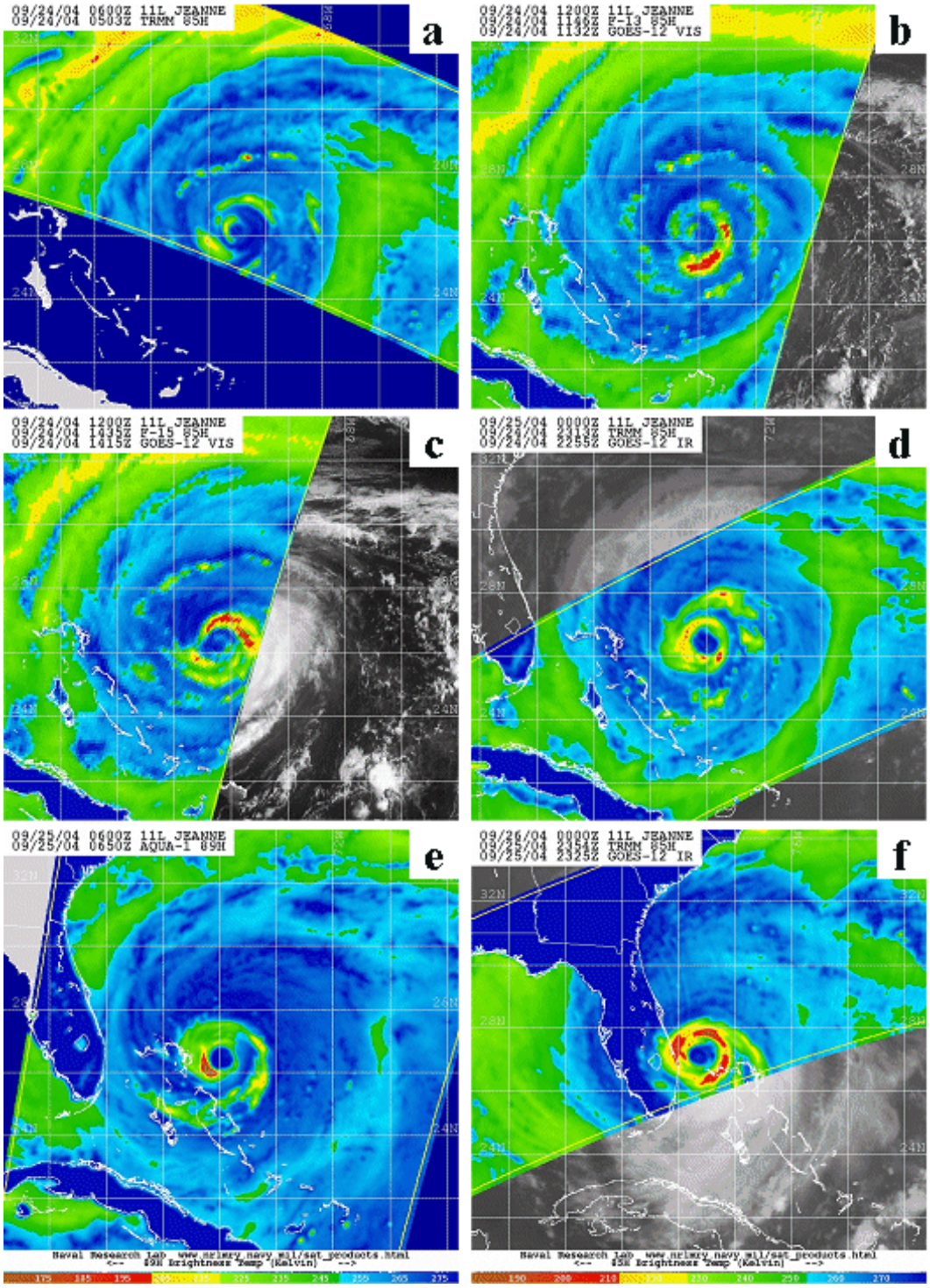

Figure 97 Microwave satellite imagery (85-89 GHz) for Hurricane Jeanne from Aqua, TRMM, and DMSP polar orbiting platforms on (a) 24 September at 0503 UTC, (b) 24 September at 1146 UTC, (c) 24 September at 1435 UTC, (d) 24 September at 2313 UTC, (e) 25 September at 0650 UTC, and (f) 25 September at 2354 UTC (2004; from NRL 2007).

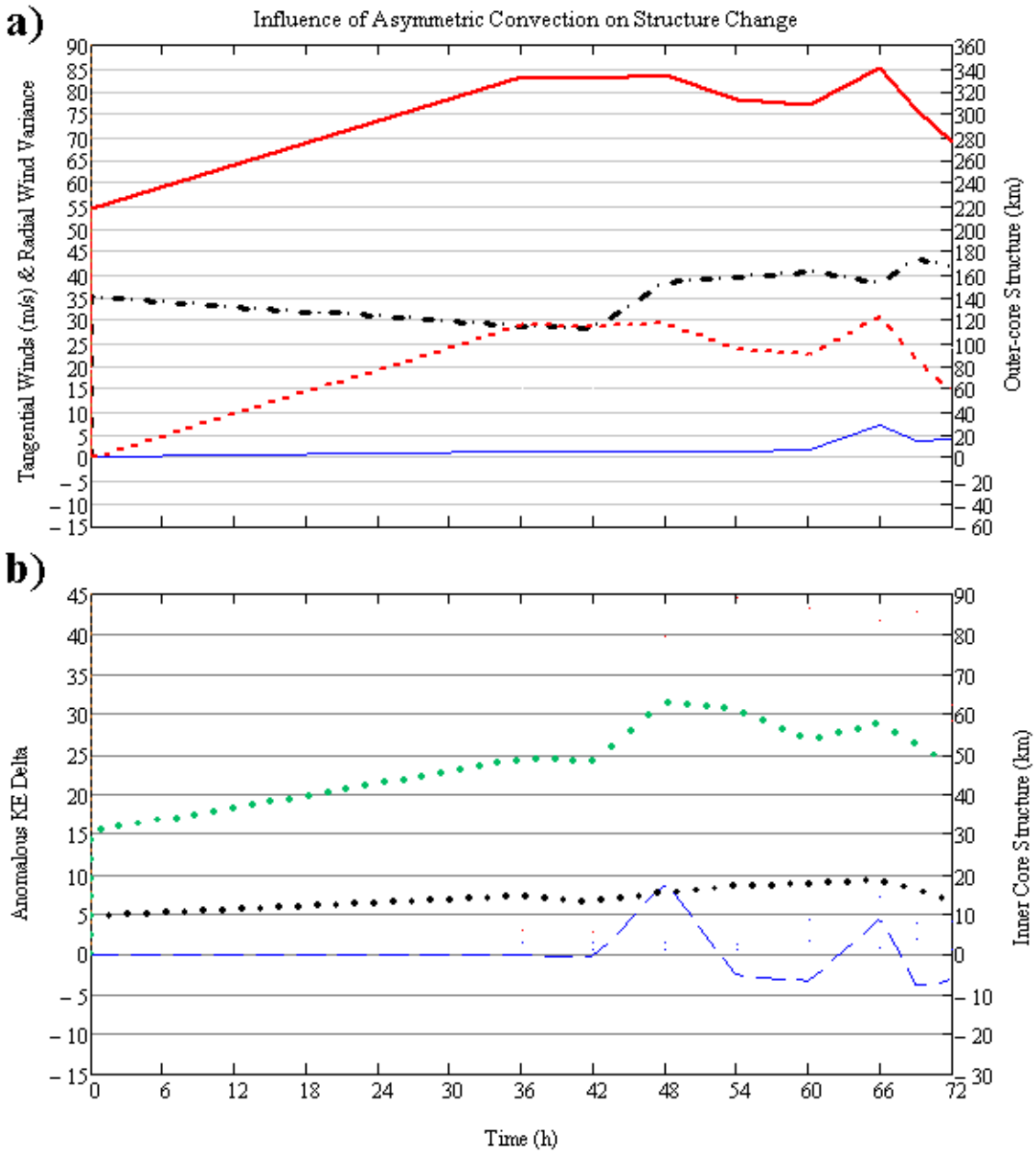

Figure 98 Time series of structure changes as in Fig. 48, except for Hurricane Jeanne (2004) from 22 September at 1930 UTC (Hour 0) to 25 September at 1930 UTC (Hour 72).

As the inner-core structure changed in response to the presence of asymmetric convection, the intensity (V_t) rapidly increased to 38 m s^{-1} (a 10 m s^{-1} increase in 6 h) by Hour 48, and then continued to increase by an additional 3 m s^{-1} through Hour 60 (Fig. 98a).

Microwave satellite imagery at 2313 UTC 24 September (∼Hour 51.5 of the analysis, Fig. 97d) suggests greater symmetry in the strong convection around a larger eyewall. Whereas Figs. 97b–c seem to suggest secondary eyewall formation, the lack of a significant inner eyewall expansion during the increase in R_{max} is inconsistent with the eyewall replacement cases in the previous section (Fig. 98b). However, this rapid intensification is consistent with the hypothesis in the last section that the process of axisymmetrization of asymmetric convection and PV is a potential mechanism for rapid storm intensification.

The azimuthal-average wind profiles in Fig. 99a prior to, following, and 6 h after this inner-core structure response to asymmetric convection (Hours 42, 48, and 54, respectively) suggest a small initial decrease in the outer-core structure (R_{34}), and then a larger decrease during the 6 h after the inner-core structure response. The R_{max} increased by 15 km in association with the asymmetric convection and then decreased by 2 km in the subsequent 6 h. The R_{34} decreased by 3 km during the inner-core structure response (blue arrow in Fig. 99a) and then decreased an additional 24 km 6 h after the inner-core structure response (red arrow in Fig. 99a), which is a net decrease of 27 km.

The exponent x values assuming a modified Rankine vortex suggest that Jeanne had a larger outer-core structure prior to and during this inner-core structure response to asymmetric convection than the overall population of Atlantic tropical cyclones during 2003–2005 (Fig. 99b). Indeed, applying the overall mean value for exponent $x = 0.58$ in the modified Rankine vortex in Eq. (20) results in an under-prediction of R_{34} by 88–221 km prior to and during this inner-core structure response to asymmetric convection, as depicted by the stem plots in Fig. 99b. The mean modified Rankine vortex exponent x during the life cycle of Jeanne was 0.42 with individual values of $x = 0.25$, $x = 0.47$, and $x = 0.50$ at Hours 42, 48, and 54, respectively. As with other cases of asymmetric convection, the larger exponent x at Hour 48 compared to Hour 42 suggests that the wind profile sharpened following this inner-core structure response to asymmetric convection.

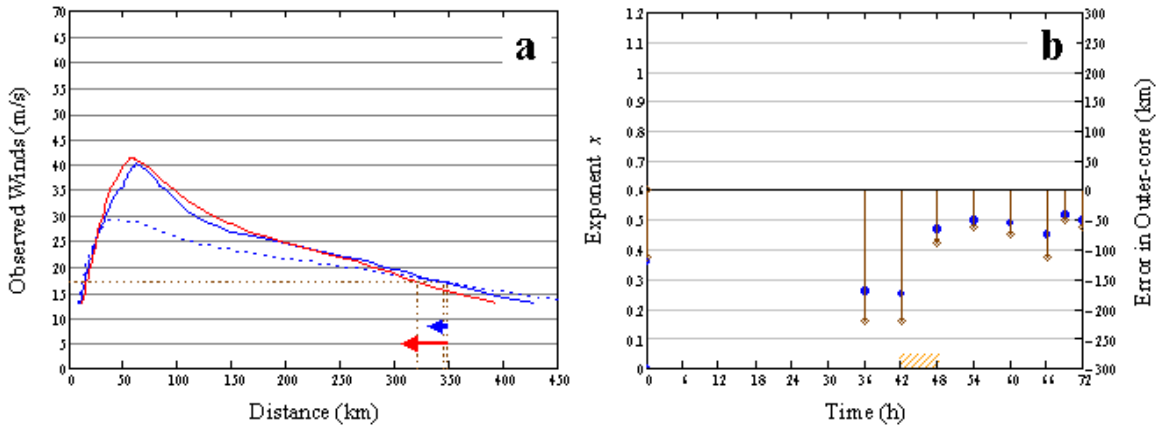

Figure 99 (a) Azimuthal-average wind profiles for Hurricane Jeanne at Hour 42 (blue dashed line), Hour 48 (blue solid line) and Hour 54 (red solid line), and (b) observed values for exponent x in the modified Rankine vortex (blue circles) and the prediction error (stem plots) when the mean value for exponent $x = 0.58$ is applied in Eq. (20). The orange-hashed rectangle is the nominal period of asymmetric convection associated inner-core structure changes.

From 48 h to 60 h, R_{max} decreased by 9 km (Fig. 98b). Microwave satellite imagery at 0650 UTC 25 September (∼Hour 60.5 of the analysis, Fig. 97e) indicates intense, asymmetric convection existed in the southwestern eyewall, and one spiral rainband with disorganized convection extended to 1.5 degrees in the east and south quadrants. From 60 h and 66 h, R_{max} increased by 4 km and V_t increased by 5 m s^{-1}as Jeanne crossed the Gulf Stream and reached a peak intensity of 43 m s^{-1} (Fig. 98). Intense, symmetric convection in the eyewall is evident in the microwave satellite imagery at 2354 UTC 25 September (∼Hour 76.5 of the analysis, Fig. 97f) as the storm approached landfall along the east coast of Florida. As the eyewall convection became more symmetric, R_{max} decreased by 5 km from 66 h to 72 h (Fig. 98b).

In summary, one period of asymmetric convection was analyzed from 1930 UTC 22 September to 1930 UTC 25 September during the life cycle of Jeanne. During this period of asymmetric convection, this tropical cyclone intensified with a V_t increase of 10 m s^{-1} (Fig. 98a). The R_{max} increased by 30 percent during this period of asymmetric convection (increase of 15 km). Outward ΔKE_{anom} was generally associated with an increase in R_{max} radius. Indeed, the correlation coefficient of 0.968 indicates a strong linear relationship between ΔKE_{anom} and R_{max}. Contrary to other cases in

which convective asymmetries in or near the eyewall were present, an increase in radial inflow variance was not observed in this case.

The azimuthal-average wind profiles prior to, following, and 6 h after the period of asymmetric convection (Fig. 99) suggest a small decrease in R_{34}. The inner-core structure (R_{max}) response to asymmetric convection (Fig. 99) was similar to the second mode of secondary eyewall formation in Fig. 85b in which the intensity (V_t) significantly increases when the inner-core (R_{max}) increases. The range of exponent x values was 0.25–0.52, where the smaller (larger) values occurred prior to (after) the inner-core structure response to asymmetric convection. Indeed, the exponent x increased from 0.25 to 0.47 during the period of asymmetric convection. As with the cases of secondary eyewall formation, the inner-core response to asymmetric convection occurred when a flatter-than-average radial wind profile existed, and was followed by a sharper radial profile.

4. Conclusions for Asymmetric Convection

The analyses of individual case studies of asymmetric convection have revealed two modes of tropical cyclone structure changes. These two modes are represented by the conceptual radial wind profiles in Fig. 100.

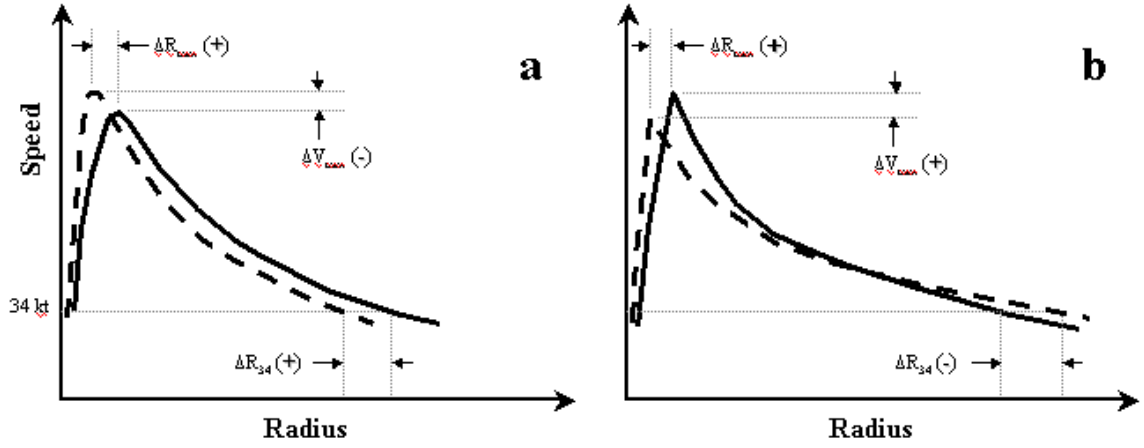

Figure 100 Conceptual radial profiles of tangential winds for tropical cyclones during asymmetric convection. The dashed and solid curves represent the azimuthal-average wind profiles at time (t) and $t + \Delta t$, respectively.

The first mode (Fig. 100a) was observed during periods of asymmetric convection for Stage IIa of the life cycle as defined in Fig. 9. This mode was best illustrated

for the cases during the annular phase of Isabel (2003). For this mode, the R_{max} increases in association with asymmetric convection, but V_{max} decreases. The outer-core structure (R_{34}) expands during the inner-core response to asymmetric convection, but then generally has a time-lagged decrease in R_{34} following the inner-core (R_{max}) expansion. For the first mode (Fig. 100a), the average decrease in V_t was 8 m s^{-1} with a range of 4 m s^{-1} to 11 m s^{-1}. The R_{max} increased by 150–200 percent in the presence of asymmetric convection with an average R_{max} increase of 33 km and a range from 25 km to 48 km.

The average R_{34} increase during the inner-core response to asymmetric convection for the first mode (Fig. 100a) was 26 km with a range from −48 km to 89 km. Whereas there are similarities with the first mode of the conceptual model for secondary eyewall formation in Fig. 85a, the time-lagged response in this mode is a contraction even though V_t generally increases following the inner-core expansion. The R_{34} increases for this mode were generally smaller than those for the first mode of the conceptual model for secondary eyewall formation (Fig. 85a) since the exponent x has a larger increase. Indeed, the average exponent x increase was only 0.09 with a range of 0.03 to 0.18 during asymmetric convection. As discussed in the section on secondary eyewall formation, these R_{34} increases may be significant when a tropical cyclone is approaching landfall.

The second mode (Fig. 100b) was only observed during periods of asymmetric convection for Stage IIa and Stage III of the life cycle as defined in Fig. 9. This mode was specifically observed for the two Fabian (2003) cases and the Jeanne (2004) case. For this mode, R_{max} and V_{max} both increase in association with the presence of asymmetric convection. The R_{max} and V_{max} increases are generally smaller than for the second mode of the conceptual model for secondary eyewall formation in Fig. 85b. In this case, the outer-core structure (R_{34}) actually has a small net decrease during the inner-core response to the asymmetric convection.

For the second mode (Fig. 100b), the average V_t increase was 6 m s^{-1} with a range from 3 m s^{-1} to 10 m s^{-1}. Rapid intensification occurred during the inner-core response to asymmetric convection for Jeanne (the only case of Stage IIa) when strong spiral rainband convection was in close proximity to the convectively weak eyewall (Figs. 97b–c). As with the second mode for secondary eyewall formation cases, this rapid intensification is consistent with the hypothesis in Chapter IV.A that the process of axisymmetrization may be a potential mechanism for rapid storm intensification

during the inner-core response to asymmetric convection. The R_{max} increased by approximately 50 percent in the presence of asymmetric convection, with an average R_{max} increase of 14 km and a range from 13 km to 15 km.

For the second mode (Fig. 100b), the average R_{34} decrease during the inner-core response to asymmetric convection was 17 km with a range from -8 km to -27 km. This is inconsistent with Eq. (20) assuming a fixed value of the exponent x since V_t and R_{max} increases on the left side of the equation are expected to result in a R_{34} increase on the right side. However, the other unknown in Eq. 20 is the exponent x, which in the pre-asymmetric convection inner-core response for Jeanne was equal to 0.25. If this exponent also applied after the asymmetric convection inner-core response and using the Hour 54 values of $V_t = 39$ m s^{-1} and $R_{max} = 61$ km, the resulting R_{34} would be 1628 km, which would be a 1281 km increase in the outer-core radius. In reality, the observed R_{34} decreased by 27 km. This R_{34} increase of 1281 km did not occur because the exponent for the outer profile during the asymmetric convection inner-core response was much larger (0.47 versus 0.25), which implies a more rapid decrease in wind with radius. During asymmetric convection inner-core response for all cases in the second mode (Fig. 100b), the post-response exponent x on average was increased by 0.13 with a range between 0.06 and 0.25. In these second mode cases, tropical cyclones have a "flatter-than-average" profile prior to the response to asymmetric convection, and then have a "sharper-than-average" profile after the response to asymmetric convection. This time variability in the profile shapes demonstrates that accurately predicting the change in the R_{34} with a fixed value for exponent x during asymmetric convection is not plausible.

For all of these cases of asymmetric convection, outward (inward) ΔKE_{anom} are correlated with expansion (contraction) of R_{max}. Indeed, the correlation coefficients during the life cycles of Fabian, Isabel, and Jeanne (0.709, 0.556, and 0.968, respectively) suggest a linear relationship between ΔKE_{anom} and R_{max}. As in the last section, large increases in the radial inflow variance were often observed when strong asymmetric spiral rainband convection existed in close proximity to the eyewall. For example, the spikes in radial inflow variance at Hours 11, 24, 42, 60, and 84 of Fabian (Fig. 87a) occurred while asymmetric convection was present in the eyewall or in close proximity to the eyewall (see Figs. 86b–f and 47b). The imbalance in radial inflow at Hours 6 and 54 of Isabel (Fig. 91a) also occurred while asymmetric convection was present in the eyewall (see Figs. 90a–b and 93d). As Hurricane Jeanne looped and

crossed its previous path, the effect of decreased sea-surface temperature was apparent by the absence of strong eyewall convection. This sea-surface cooling was a result of entrainment mixing that occurred beneath Jeanne's eye during its first pass over the same location (see Fig. 97a). By contrast, eyewall convection exploded as Jeanne crossed over the Gulf Stream near the east coast of Florida (see Fig. 97f).

C. LAND INTERACTION

1. Peripheral Interaction

For the purposes of this research, peripheral land interaction is defined as sustained interaction (12 h or longer) of one or more quadrants of a mature storm's outer-core structure with a continent or large island. The outer-core structure is defined as the region of the storm structure from 110 km to the R_{34} radius. Of the tropical cyclones during 2003–2005 in the North Atlantic basin, only three storms meet these criteria for peripheral land interaction and have a sufficient number of H*Wind analyses for a meaningful discussion.

a. *Rita (2005)*

The life cycle of Hurricane Rita was discussed in Chapter IV.A.2.b. The analysis period of peripheral land interaction with Rita was from 1030 UTC 23 September (Hour 66) to 0430 UTC 24 September (Hour 84) as Rita approached the Texas and Louisiana coasts. At Hour 66, Rita had a tangential wind speed (V_t) of 45 m s^{-1} with azimuthal-average R_{max} and R_{34} values of 35 km and 322 km, respectively (Fig. 101). Rita interacted with the Louisiana and Texas coasts between 67 h and 84 h.

At Hour 67, the outer-core structure (R_{34}) began to interact with Louisiana at a distance of 330 km, and then the storm center moved progressively closer to land until it was within 80 km at Hour 84. From 66 h to 72 h, Rita's intensity (V_t) only experienced very small oscillations between 45 m s^{-1} and 46 m s^{-1}. Whereas V_t increased by 4 m s^{-1} (to 49 m s^{-1}) during the 3-h period after Hour 72, V_t decreased as the storm center moved from within 200 km to within 80 km of land from 75 h to 84 h, and thus decreased to an intensity of 41 m s^{-1} by Hour 84. The outer-core structure (R_{34}) increased by 21 km between 66 h and 72 h, and then decreased by 64 km in the subsequent 12-h period as the storm center moved increasingly closer to land. The increased frictional drag of peripheral land interaction likely weakened the

outer-core winds in the quadrants over land (LF and RF), which then propagated to the quadrants over water (LR and RR) and contributed to the R_{34} decrease in the azimuthal-average outer-core winds. The decrease in the R_{34} began just 6 h after this indicator of a peripheral land interaction was satisfied, which was likely a result of a significantly large area of the outer-core structure being over a contiguous land surface. It is hypothesized that the increased frictional drag during peripheral land interaction weakens the outer-core winds (and thus leads to azimuthal-average R_{34} decreases) after a sustained exposure of 6–18 hours, which may be the necessary duration of exposure of the tropical cyclone circulation over land and its larger roughness length.

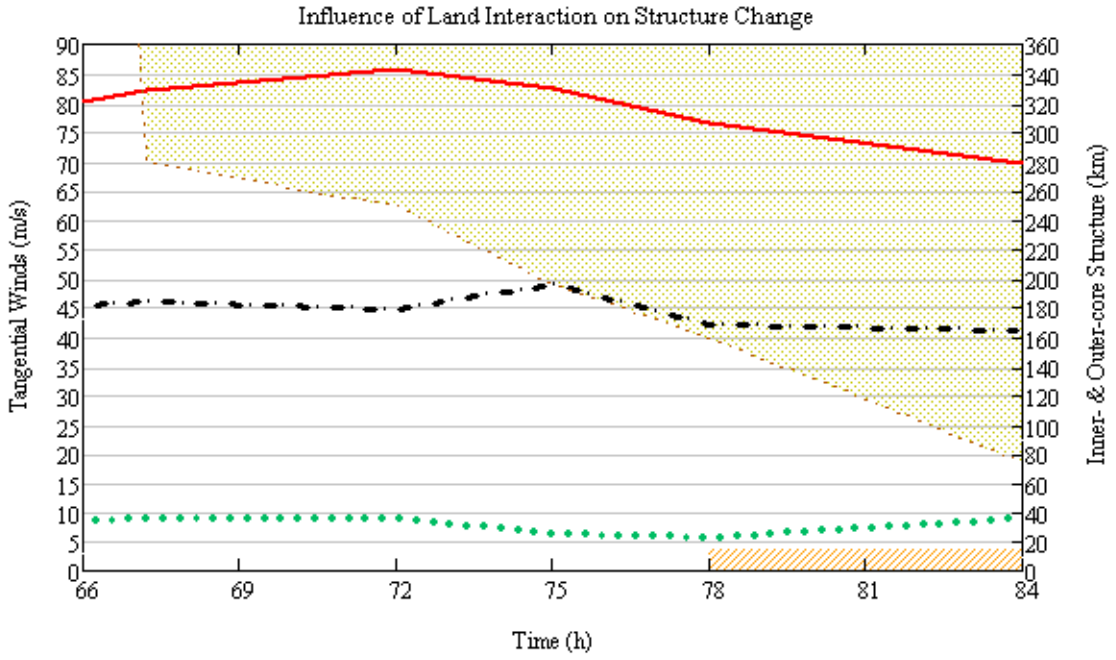

Figure 101 Time series of structure changes for Hurricane Rita (2005) from 23 September at 1030 UTC (Hour 66) to 24 September at 0430 UTC (Hour 84). The black dash-dot line is the azimuthal-average tangential winds (V_t). The red solid and green dotted lines are the azimuthal-average R_{34} and R_{max} radii, respectively, with the scale on the right ordinate. The shaded region indicates land interaction within the R_{34} radius, where distance from storm center is on the right ordinate. The orange-hashed rectangle is the nominal period of secondary eyewall formation.

Microwave satellite imagery at 0808 UTC 23 September (~2.5 h prior to Hour 66 of the analysis, Fig. 102a) indicates the presence of two spiral rainbands with fragmented convection that partially encircles the eyewall. Microwave satellite imagery

at 1345 UTC and 1907 UTC 23 September (~Hours 69.5 and 74.5 of the analysis, Figs. 102b–c) indicates a burst of strong convection in the Rita spiral rainband that intersects land, which appears to be coincident with the formation of a secondary eyewall. Microwave satellite imagery at 0144 UTC 24 September (~Hour 81 of the analysis, Fig. 102d) indicates a large area of intense, asymmetric convection along the spiral rainband over the Gulf Coast in close proximity to the eyewall. The strong convection in a spiral rainband that intersects land appears to have contributed to secondary eyewall formation.

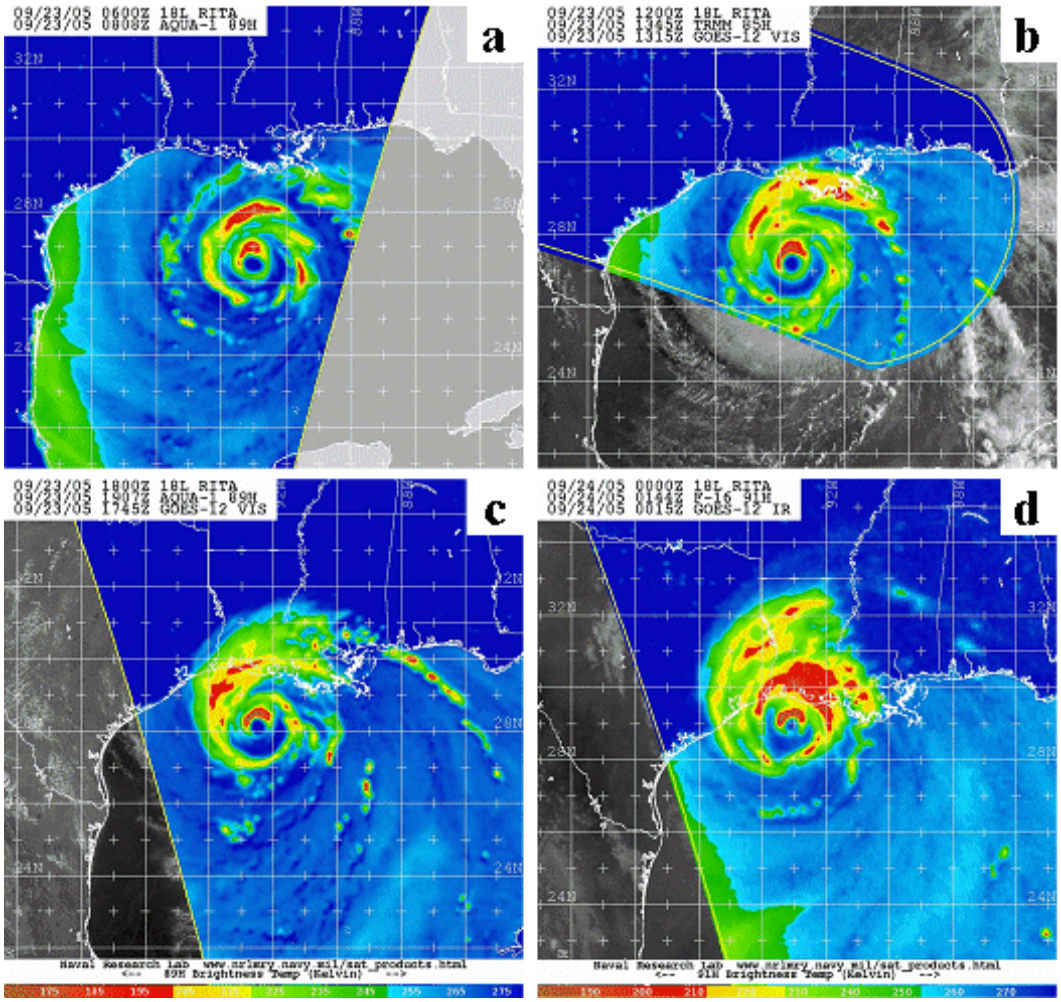

Figure 102 Microwave satellite imagery (85-91 GHz) for Hurricane Rita from Aqua, TRMM, and DMSP polar orbiting platforms on (a) 23 September at 0808 UTC, (b) 23 September at 1345 UTC, (c) 23 September at 1907 UTC, and (d) 24 September at 0144 UTC (2005; from NRL 2007).

The azimuthal-average wind profiles in Fig. 103a prior to, during, and 3 h after secondary eyewall formation (Hours 78, 84, and 87, respectively) suggest a rapidly changing wind profile as Rita made landfall near the Texas and Louisiana border. Whereas the R_{34} value decreased by 34 km (blue arrow in Fig. 103a) and then continued to decrease by an additional 31 km 3 h after secondary eyewall formation (red arrow in Fig. 103a) as Rita made landfall, the hurricane-force winds (R_{64}) experienced a net increase of 19 km just prior to landfall. This suggests that the wind profile sharpened following secondary eyewall formation in conjunction with peripheral land interaction. Indeed, individual exponent values in the modified Rankine vortex in Eq. (20) for Hours 78 and 84 were $x = 0.35$ and $x = 0.42$, respectively. Microwave satellite imagery at 0933 UTC 24 September (~Hour 89 of the analysis, Fig. 103b) indicates the presence of two eyewalls approximately 1.5 h after landfall, which is consistent with the wind analysis with two R_{max} radii in Fig. 103a.

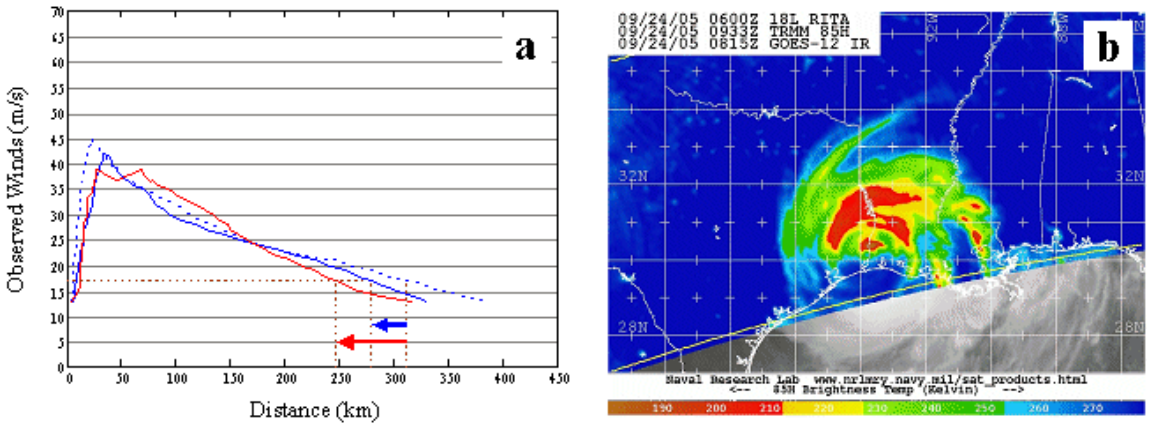

Figure 103 (a) Azimuthal-average wind profiles for Hurricane Rita at Hour 78 (blue dashed line), Hour 84 (blue solid line) and Hour 87 (red solid line), and (b) microwave satellite imagery (85 GHz) for Hurricane Rita from TRMM on 24 September at 0933 UTC (2005; from NRL 2007).

In summary, Hurricane Rita had a secondary eyewall formation in conjunction with peripheral land interaction during a period of approximately 15 h as Rita approached landfall along the Texas and Louisiana coasts. The R_{34} radius decreased when the storm center was within 250 km of land, or approximately 6 h after R_{34} was first over land and the peripheral land interaction is considered to begin (Fig. 101). This suggests that the frictional drag of peripheral land interaction requires some period of exposure (potentially 6–18 hours depending on the storm area over

land and the roughness length of the underlying land) before the gale-force wind radius (R_{34}) decreases in the quadrants over water (i.e., the quadrants used to calculate the azimuthal-average R_{34} value).

This case of peripheral land interaction for Rita suggests that the frictional convergence of the winds in the vicinity of a spiral rainband that intersects the land leads to enhanced strong convection that then advects around the eyewall with the spiral rainband and evidently contributes to the secondary eyewall formation by surrounding the eyewall with active spiral rainbands. The continuous peripheral land interaction as the front quadrants of Rita moved over land likely modified the outer-core structure (R_{34}) expansion in response to secondary eyewall formation. However, the net R_{64} increase of 19 km just prior to landfall may significantly impact the timing and coverage of hurricane warnings for coastal communities. As with the cases of secondary eyewall formation in Chapter IV.A, secondary eyewall formation in conjunction with peripheral land interaction occurred when a flatter-than-average radial wind profile existed, and was followed by a sharper radial profile.

b. *Ivan (2004)*

The life cycle of Hurricane Ivan was discussed in Chapter IV.A.1.c. The analysis period of peripheral land interaction with Ivan was from 2230 UTC 12 September (Hour 144) as Ivan approached the Yucatan Gap to 0430 UTC 15 September (Hour 198) as this storm moved over the central Gulf of Mexico. At Hour 144, Ivan had a tangential wind speed (V_t) of 58 m s^{-1} with azimuthal-average R_{max} and R_{34} values of 40 km and 335 km, respectively (Fig. 104). Ivan interacted with western Cuba and the northeastern Yucatan Peninsula between 146 h and 190 h.

At Hour 147, the outer-core structure (R_{34}) began to interact with western Cuba at a distance of 335 km, and then the storm center moved progressively closer to land until it was within 110 km at Hour 171 (Fig. 104). From 144 h to 171 h, Ivan's intensity (V_t) only had small oscillations between 58 m s^{-1} and 62 m s^{-1}. Following the point of farthest intrusion of western Cuba into the storm structure, V_t decreased by 8 m s^{-1} in 12 h. The outer-core structure (R_{34}) also decreased by 67 km between 165 h and 171 h, but R_{34} was quickly regained with an increase of 68 km in the subsequent 6-h period as the storm center moved a greater distance from land. The datasets at Hours 165 and 171 both had similar observational sources for the H*Wind analyses.

Thus, the rapid changes in R_{34} appear to be related to the storm center proximity to land rather than differences in observational types.

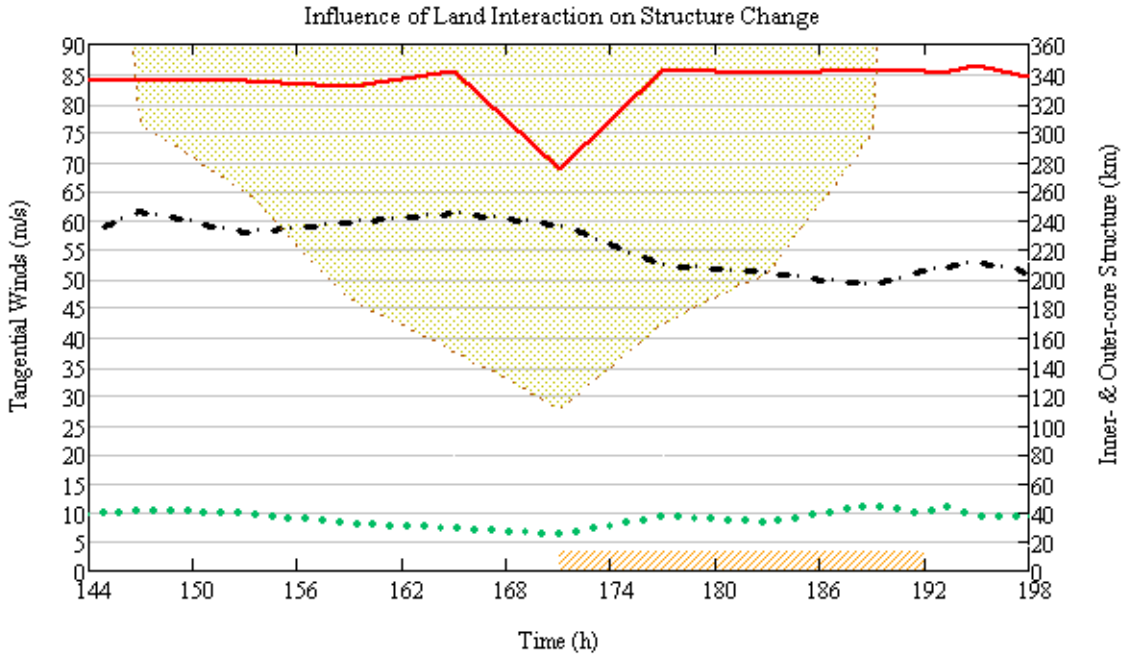

Figure 104 Time series of structure changes as in Fig. 101, except for Hurricane Ivan (2004) from 12 September at 2230 UTC (Hour 144) to 15 September at 0430 UTC (Hour 198).

It is noted that a secondary eyewall formation (see Chapter IV.A.1.c and Fig. 66a) had a role in the rapid expansion of the R_{34} following the largest land intrusion of western Cuba on the storm structure. Although the storm intensity (V_t) decreased by 9 m s^{-1}, the post-peripheral land interaction R_{34} had a similar magnitude as prior to land interaction. The azimuthal-average wind profiles in Fig. 105a prior to, following, and 6 h after secondary eyewall formation (Hours 171, 192, and 198, respectively) suggest an initial increase in the outer-core structure (R_{34}), but then minimal change during the 6 h after secondary eyewall formation as Ivan moved away from western Cuba. That is, the R_{34} initially increased by 59 km (blue arrow in Fig. 105a) and then decreased by 2 km 6 h after secondary eyewall formation in conjunction with peripheral land interaction (red arrow in Fig. 105a), for a net increase of 57 km. Microwave satellite imagery at 0710 UTC 14 September (~Hour 176.5 of the analysis, Fig. 105b) indicates the presence of two eyewalls following peripheral land interaction. As with Rita, the frictional convergence of winds over the land increased the strong

convection in Ivan's spiral rainband that intersected land, which may have played a role in the secondary eyewall formation. That is, this strong convection over land is advected cyclonically around the storm center in the spiral rainband analogous to the secondary eyewall formation in Fig. 61f. Contrary to the continuous peripheral land interaction with Rita, the limited peripheral land interaction with Ivan did not result in a sharpened wind profile following secondary eyewall formation in conjunction with peripheral land interaction. Recall from Chapter IV.A.1.c and Fig. 66b, individual exponent values in the modified Rankine vortex in Eq. (20) for Hours 171 and 192 were $x = 0.52$ and $x = 0.50$, respectively.

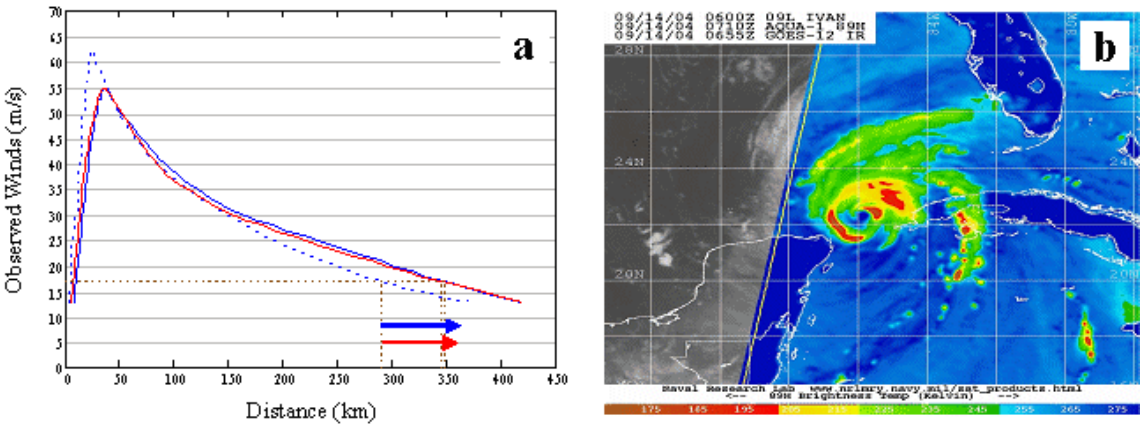

Figure 105 (a) Azimuthal-average wind profiles for Hurricane Ivan at Hour 171 (blue dashed line), Hour 192 (blue solid line) and Hour 198 (red solid line), and (b) microwave satellite imagery (89 GHz) for Hurricane Ivan from Aqua on 14 September at 0710 UTC (2004; from NRL 2007).

In summary, Hurricane Ivan experienced peripheral land interaction for a period of approximately 42 h as it passed through the Yucatan Gap. The R_{34} remained unaffected until the storm center moved to within 160 km of land and approximately 15 h after peripheral land interaction began (Fig. 104). This delayed effect suggests that the frictional drag during peripheral land interaction requires some period of exposure of the storm structure over land before the gale-force wind radius (R_{34}) is decreased in the quadrants over water that are used to calculate the azimuthal-average R_{34} value. As with Hurricane Rita, this case of peripheral land interaction for Ivan also suggests that the frictional convergence of the winds in the vicinity of a spiral rainband that intersects the land leads to enhanced strong convection that then advects around the eyewall with the spiral rainband. This sequence of events may increase the likelihood

of secondary eyewall formation with active spiral rainbands surrounding the eyewall, or by the strong convection causing a disruption in the eyewall as was suggested in the Rita partial eyewall replacement case in Chapter IV.A.2.b. Contrary to Rita, the wind profile of Ivan did not sharpen following secondary eyewall formation in conjunction with peripheral land interaction, which is likely a result of a smaller outer-core structure area of Ivan over land and the less continuous interaction of the storm structure with land.

c. *Wilma (2005)*

The life cycle of Hurricane Wilma was discussed in Chapter IV.A.1.e. The analysis period of peripheral land interaction with Wilma was from 1030 UTC 23 October (Hour 123) to 0730 UTC 24 October (Hour 144) as Wilma moved across the Gulf of Mexico and approached a second landfall over southern Florida. At Hour 123 (following landfall on the Yucatan Peninsula), Wilma had a tangential wind speed (V_t) of 34 m s^{-1} with azimuthal-average R_{max} and R_{34} values of 49 km and 342 km, respectively (Fig. 106). Thus, Wilma interacted with the Yucatan Peninsula, western Cuba, and southern Florida between 123 h and 144 h.

At Hour 123, the outer-core structure (R_{34}) interacted with the northeastern Yucatan Peninsula at a distance of 115 km following landfall over the peninsula and a secondary eyewall replacement cycle, and then the storm center moved progressively away from land until the distance was 205 km at Hour 129. From 123 h to 132 h, Wilma's intensity (V_t) only had small oscillations between 32 m s^{-1} and 35 m s^{-1} (Fig. 106). After Hour 132, V_t increased from 35 m s^{-1} to 47 m s^{-1} (a rapid intensification of 12 m s^{-1} in 12 h) as the storm center moved away from land (160 km to 220 km, Fig. 106). The outer-core structure (R_{34}) remained constant between 123 h and 126 h, and then decreased by 48 km in the subsequent 18-h period as the storm center moved across the Gulf of Mexico toward Florida. As with the other cases in this section, the frictional drag of peripheral land interaction between 150–200 km of the storm center appears to have weakened the outer-core winds, and thus led to an azimuthal-average R_{34} decrease.

Microwave satellite imagery at 1536 UTC 23 October (∼Hour 128 of the analysis, Fig. 107a) indicates strengthening of the convection in the outer eyewall and a weakened inner eyewall. As Wilma moves to the northeast and interacts with western Cuba, microwave satellite imagery at 1917 UTC 23 September and 0204 UTC 24

September (∼Hours 132 and 138.5 of the analysis, Figs. 107b–c) indicates increased convection in the spiral rainbands that intersect western Cuba and a subsequent increase in the strong convection of the new, broad eyewall. The increased organization of strong convection in the eyewall along with convective asymmetries resulting from peripheral land interaction may be contributing factors to Wilma's rapid intensification given the lack of sustained contraction of the R_{max} radius.

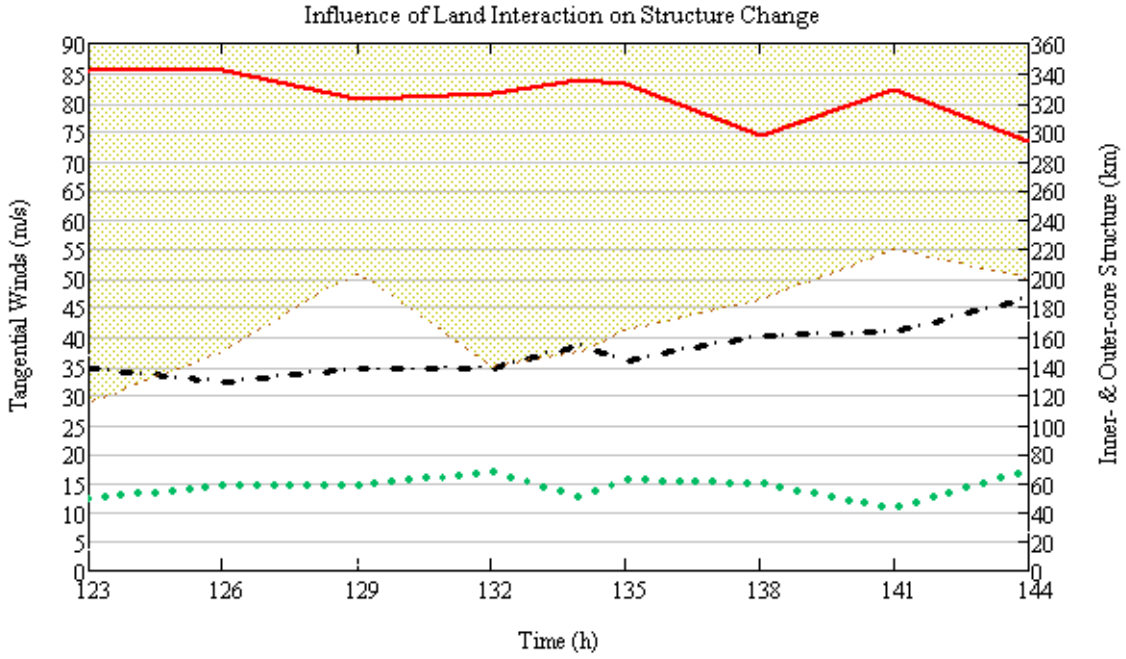

Figure 106 Time series of structure changes as in Fig. 101, except for Hurricane Wilma (2005) from 23 October at 1030 UTC (Hour 123) to 24 October at 0730 UTC (Hour 144).

As Wilma approached the south Florida coast, microwave satellite imagery at 0726 UTC 24 September (∼Hour 144 of the analysis, Fig. 107d) again depicts an increase in spiral rainband convection to the north and east of the eyewall. In contrast to the Ivan and Rita cases, another secondary eyewall formation does not occur as Wilma interacts with the Florida coast. Two factors are hypothesized to contribute to the absence of a secondary eyewall formation as Wilma approached landfall over Florida: (i) Wilma's R_{max} was 60+ km as it approached land, while the R_{max} values for Ivan and Rita were 25–30 km; and (ii) the translation speed for Wilma was approximately 20 kt as it approached land, while the translation speeds for Ivan and Rita were 10 kt or less.

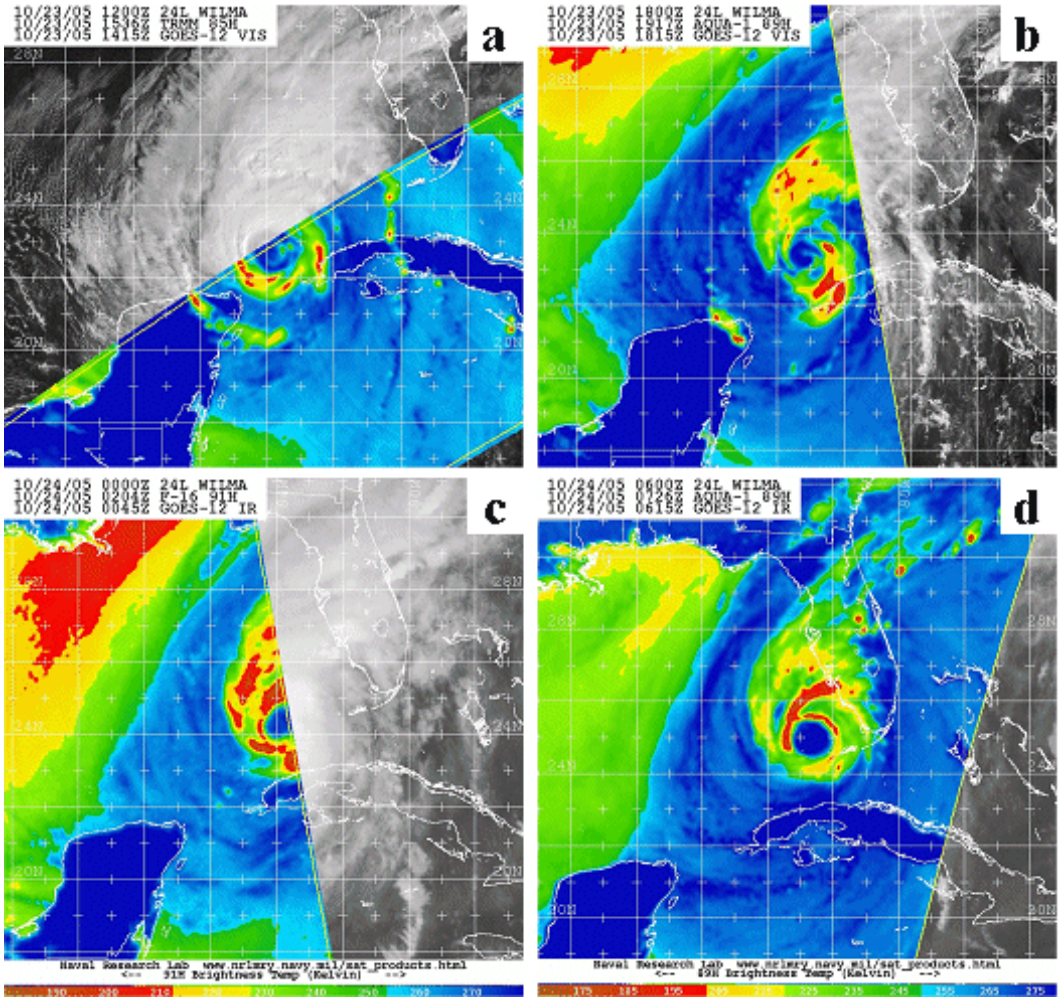

Figure 107 Microwave satellite imagery (85-91 GHz) for Hurricane Wilma from Aqua, TRMM, and DMSP polar orbiting platforms on (a) 23 October at 1536 UTC, (b) 23 October at 1917 UTC, (c) 24 October at 0204 UTC, and (d) 24 October at 0726 UTC (2005; from NRL 2007).

The azimuthal-average wind profiles in Fig. 108a at Hours 123, 132, and 144, respectively, suggest minimal change in the outer-core structure (R_{34}) through Hour 132, and then a R_{34} decrease from 132 h to 144 h. The R_{max} increased by 18 km (to 67 km) by Hour 132 and then experienced oscillations before increasing to 69 km at Hour 144. By contrast, R_{34} remained nearly constant at 339 km during the R_{max} increase (solid blue line in Fig. 108a) and then decreased by 62 km (to 277 km) as Wilma approached the Florida coast (red arrow in Fig. 108a). This R_{34} decrease as V_t increased by 12 m s^{-1} from 132 h to 144 h suggests a significant sharpening of

Wilma's wind profile as it crossed the Gulf of Mexico. Indeed, individual exponent values in the modified Rankine vortex in Eq. (20) for Hours 123, 132, and 144 were x = 0.35, x = 0.44, and x = 0.68, respectively (Fig. 108b).

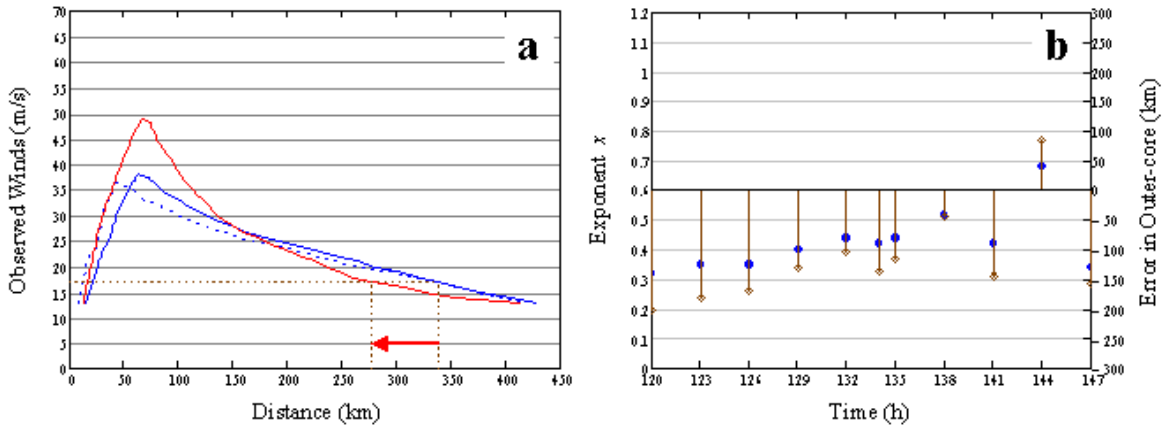

Figure 108 (a) Azimuthal-average wind profiles for Hurricane Wilma at Hour 123 (blue dashed line), Hour 132 (blue solid line) and Hour 144 (red solid line), and (b) observed values for exponent x in the modified Rankine vortex (blue circles) and the prediction error (stem plots) when the mean value for exponent x = 0.58 is applied in Eq. (20).

In summary, Hurricane Wilma experienced peripheral land interaction over an extended period between landfall over the Yucatan Peninsula until landfall over southern Florida. As Wilma left the Yucatan Peninsula and moved over the Gulf of Mexico, R_{34} generally decreased as peripheral land interaction continued between 140–220 km of the storm center (Fig. 106). As before, this suggests that the frictional drag of peripheral land interaction may have contributed to a decrease in the gale-force wind radius (R_{34}) when an extended duration of outer-core structure interaction with land has occurred. As with the previous cases in this section, Wilma's spiral rainbands developed enhanced convection where they interacted with land. In addition, the enhanced asymmetric convection in these spiral rainbands may have been a contributing factor in Wilma's rapid intensification through the process of axisymmetrization as hypothesized in Chapter IV.A. Wilma did not experience another secondary eyewall formation as it approached landfall over southern Florida. The large R_{max} of 60+ km and Wilma's translation speed of approximately 20 kt are hypothesized to be contributing factors as to why a secondary eyewall formation was not observed.

2. Near-core Interaction

For the purposes of this research, near-core land interaction is defined as total or partial intrusion of the inner-core structure of a mature storm with a continent or large island. The inner-core structure is defined as the region from the eye to 110 km. Three storms during 2003–2005 in the North Atlantic basin will be discussed that meet these criteria for near-core land interaction and have a sufficient number of H*Wind analyses.

a. *Charley (2004)*

Charley became a named storm by 0600 UTC 10 August in the vicinity of 12.9°N, 65.4°W as it passed through the eastern Caribbean Sea. This tropical cyclone had a west-northwestward track across the central Caribbean Sea prior to strengthening into a hurricane by 1800 UTC 11 August. After reaching hurricane strength, Charley moved northwestward and made landfall over western Cuba around 0500 UTC 13 August. Charley re-emerged over the Gulf of Mexico at approximately 0630 UTC 13 August and moved northward across the Gulf Stream prior to making a second landfall over southwest Florida at approximately 2000 UTC 13 August. Charley briefly re-emerged over the western North Atlantic before it made a final landfall in northeastern South Carolina at around 1600 UTC 14 August. H*Wind analyses for Charley became available at 1930 UTC 10 August and at regular increments until 1645 UTC 14 August as the storm made its final landfall in South Carolina.

The discussion in this section will focus on near-core and peripheral land interaction with Charley from 1930 UTC 12 August (hereafter referred to as Hour 0 of the analysis) to 1930 UTC 13 August (Hour 24) as this storm made landfall in southwest Florida. At Hour 0, Charley had a tangential wind speed (V_t) of 36 m s^{-1} with azimuthal-average R_{max} and R_{34} values of 18 km and 123 km, respectively (Fig. 109). Charley interacted with western Cuba between 3 h and 15 h and southwest Florida after 21 h.

At Hour 3, the outer-core structure (R_{34}) began to interact with western Cuba at a distance of 110 km, and then the storm center moved progressively closer to land until it made landfall at approximately Hour 9.5 (Fig. 109). As Charley approached the western Cuba coast, microwave satellite imagery at 1900 UTC 12 August ($\sim$0.5 h prior to Hour 0 of the analysis, Fig. 110a) indicates strong convection

in the spiral rainband to the north and east of the eyewall as the rainband interacts with Cuba. Charley's intensity (V_t) increased by 5 m s^{-1} (to 41 m s^{-1}) during the first 6 h, and then rapidly decreased to 18 m s^{-1} as the eye moved over land. While Charley's eye was over land, microwave satellite imagery at 0432 UTC 13 August (∼Hour 9 of the analysis, Fig. 110b) depicts a lack of spiral rainband convection. As Charley reemerged over the waters of the Gulf of Mexico following its brief 1.5 h duration over land, microwave satellite imagery at 0710 UTC 13 August (∼Hour 11.5 of the analysis, Fig. 110c) indicates a return of strong convection in the spiral rainband in the northwest quadrant. As Charley makes a second landfall in southwest Florida, microwave satellite imagery at 2105 UTC 13 August (∼Hour 25.5 of the analysis, Fig. 110d) suggests that Charley had formed a secondary eyewall as it moved across the warm waters of the Gulf Stream. In addition, a lesser quality SSM/I microwave satellite image at 1513 UTC 13 August (∼Hour 19.5 of the analysis, not shown) suggests an increase in spiral rainband convection that encircles 75 percent of the eyewall as the rainband begins to interact with the Florida coast.

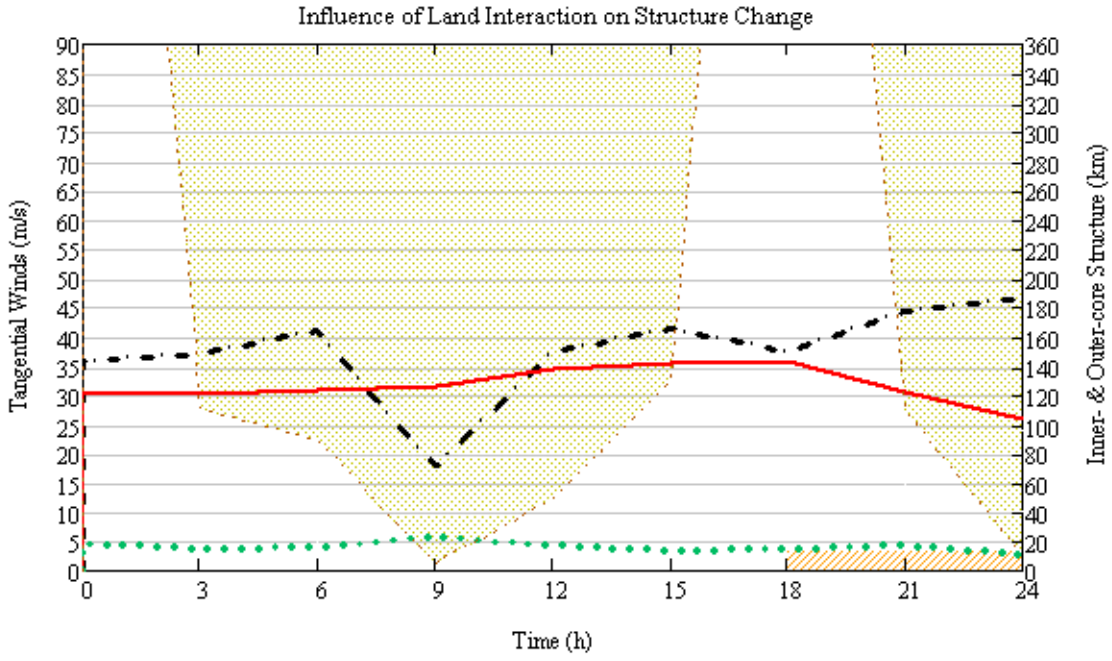

Figure 109 Time series of structure changes as in Fig. 101, except for Hurricane Charley (2004) from 12 August at 1930 UTC (Hour 0) to 13 August at 1930 UTC (Hour 24).

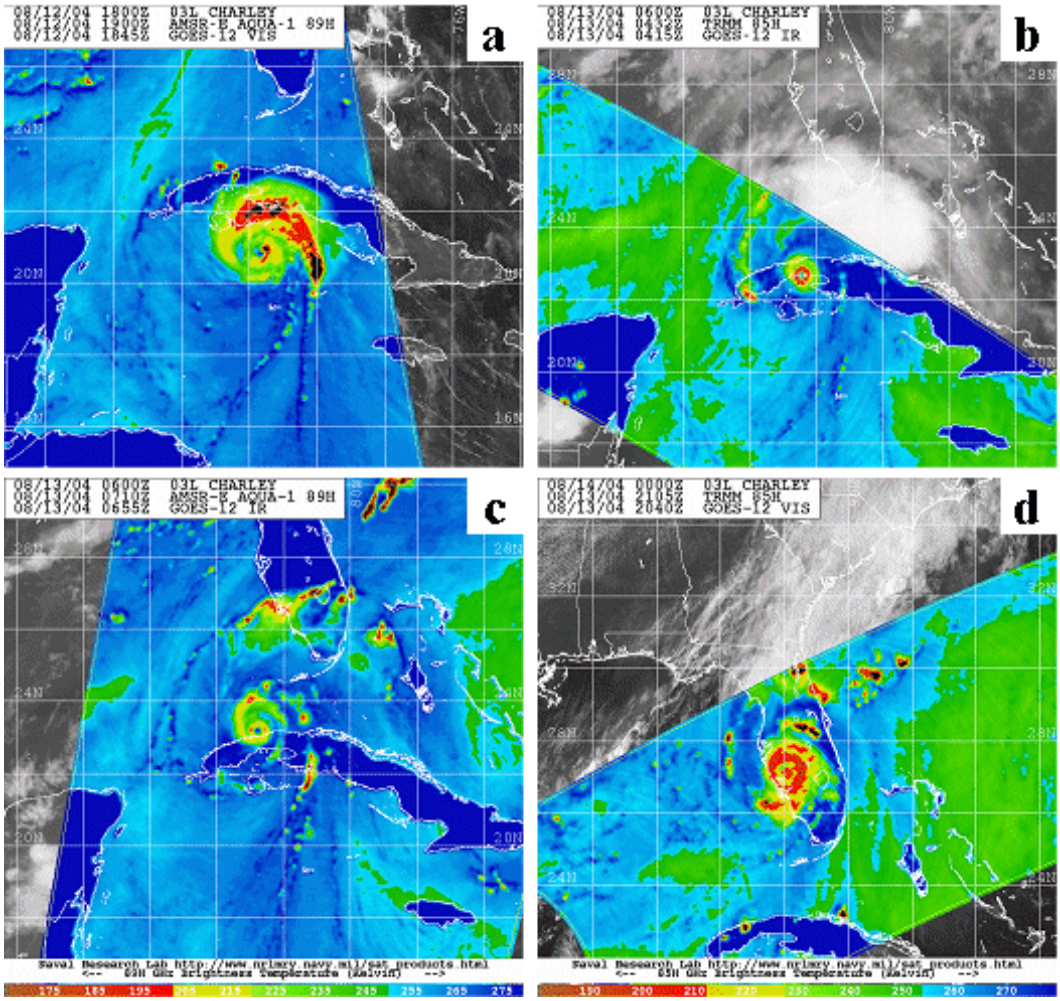

Figure 110 Microwave satellite imagery (85-89 GHz) for Hurricane Charley from Aqua and TRMM polar orbiting platforms on (a) 12 August at 1900 UTC, (b) 13 August at 0432 UTC, (c) 13 August at 0710 UTC, and (d) 13 August at 2105 UTC (2004; from NRL 2007).

The outer-core structure (R_{34}) increased by 22 km between 3 h and 15 h as Charley interacted with and made landfall over Cuba. The R_{34} increase during land interaction is similar to Ivan in Chapter IV.C.1.b, which is partially explained by decreased frictional drag as result of a smaller outer-core structure area of Charley over land and the less continuous interaction of the storm structure with land. As Charley approaches the landmass of Florida, the effects of frictional drag on the outer-core winds become more apparent. The azimuthal-average wind profiles in Fig. 111a prior to, during, and 3 h after secondary eyewall formation (Hours 18, 21, and 24,

respectively) suggest a rapidly changing wind profile as Charley made landfall over southwest Florida. Whereas the R_{34} value decreased by 14 km (blue arrow in Fig. 111a) and then continued to decrease by an additional 36 km 3 h after secondary eyewall formation (red arrow in Fig. 111a) as Charley made landfall, the hurricane-force winds (R_{64}) experienced a net increase just prior to landfall. The increase in R_{64} is in part a result of Charley's rapid intensification (9 m s^{-1} in 6 h) as this storm approached the Florida coast. Such a R_{64} increase just prior to landfall may significantly impact the timing and coverage of hurricane warnings for coastal communities.

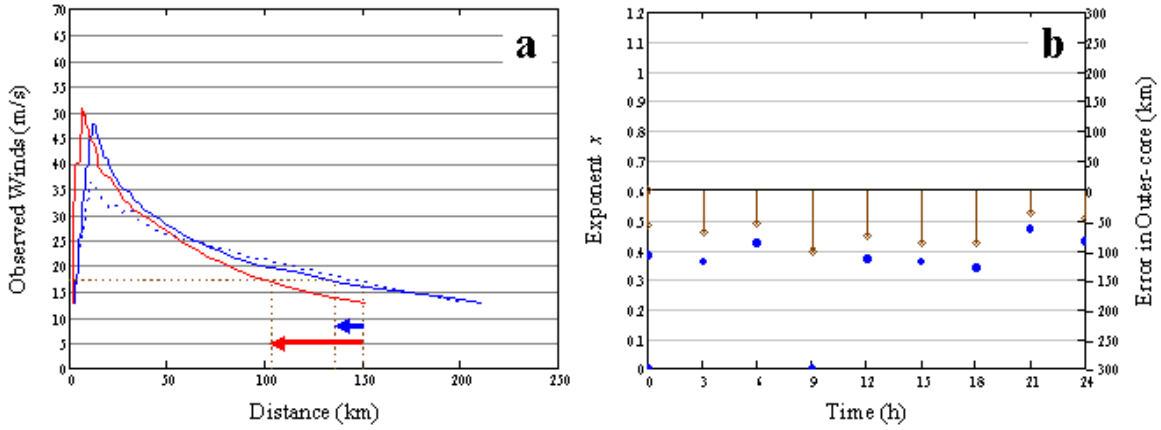

Figure 111 (a) Azimuthal-average wind profiles for Hurricane Charley at Hour 18 (blue dashed line), Hour 21 (blue solid line) and Hour 24 (red solid line), and (b) observed values for exponent x in the modified Rankine vortex (blue circles) and the prediction error (stem plots) when the mean value for exponent $x = 0.58$ is applied in Eq. (20).

Based on the statistical results in Fig. 42b, a greater probability of larger (smaller) R_{34} radii is expected in the right (left) quadrants of the tropical cyclone during rapid intensification. Although the V_t and R_{64} increased, the wind profile sharpened following secondary eyewall formation in conjunction with land interaction. Indeed, individual exponent values in the modified Rankine vortex in Eq. (20) for Hours 18, 21, and 24 were $x = 0.34$, $x = 0.47$, and $x = 0.43$, respectively (Fig. 111b).

In summary, Hurricane Charley experienced land interaction for 15 h of the 24 h analysis as this storm passed over western Cuba and approached the Florida coast. The R_{34} gradually increased in size until the storm center moved to within ~160 km of Florida and as the right quadrants began to interact with land (Fig. 109). As with the cases of peripheral land interaction of Hurricanes Rita and Ivan

in Chapter IV.C.1, this case of near-core land interaction for Charley also suggests that the frictional convergence of the winds in the vicinity of a spiral rainband that intersects the land leads to enhanced strong convection that then advects around the eyewall with the spiral rainband. This sequence of events may increase the likelihood of secondary eyewall formation with active spiral rainbands surrounding the eyewall, or by the strong convection causing a disruption of the flow in the eyewall as was suggested in the Rita partial eyewall replacement case in Chapter IV.A.2.b.

Similar to Rita, the wind profile of Charley sharpened following secondary eyewall formation in conjunction with land interaction. This suggests that the frictional drag of land interaction in the RF quadrants of Charley likely modified the outer-core structure (R_{34}) in response to secondary eyewall formation. As with the cases of secondary eyewall formation in Chapter IV.A, secondary eyewall formation in conjunction with near-core land interaction occurred when a flatter-than-average tangential wind profile with radius existed, but was then followed by a sharper radial profile.

b. *Ivan (2004)*

The life cycle of Hurricane Ivan was discussed in Chapter IV.A.1.c. The analysis period of near-core land interaction will be from 1030 UTC 10 September (Hour 84) to 0430 UTC 13 September (Hour 150) as Ivan moved across the Caribbean Sea and passed south of the island of Jamaica without making landfall. Ivan interacted with the island of Jamaica between 87 h and 123 h. At Hour 84, Ivan had a tangential wind speed (V_t) of 53 m s^{-1} with azimuthal-average R_{max} and R_{34} values of 21 km and 198 km, respectively (Fig. 112).

At Hour 87, the outer-core structure (R_{34}) began to interact with Jamaica at a distance of 220 km, and then the storm center moved progressively closer to land until it was within 55 km at Hour 105 (Fig. 112). As Ivan moved progressively closer to Jamaica from 84 h to 99 h, a secondary eyewall replacement cycle occurred and the intensity (V_t) decreased from 53 m s^{-1} to 47 m s^{-1}. However, V_t increased rapidly by 16 m s^{-1} in 12 h after the closest approach of the storm center to Jamaica. Even though the outer-core structure (R_{34}) increased by 136 km between 87 h and 117 h, such a non-landfalling, near-core land interaction with a large island is not likely the cause of this large increase in the outer-core structure.

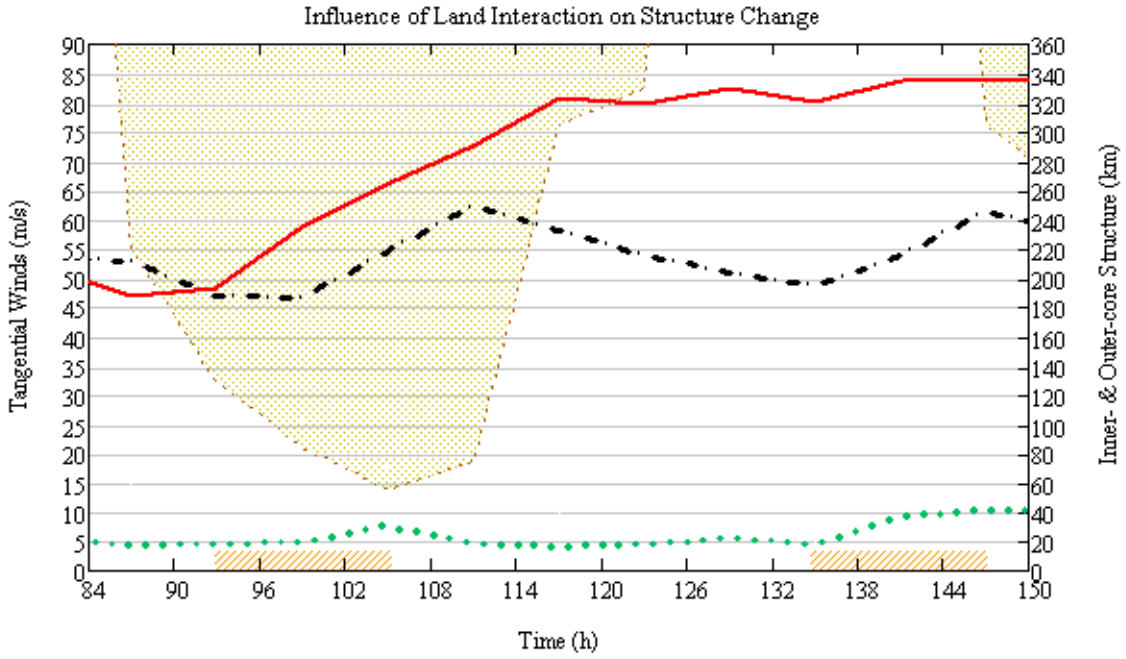

Figure 112 Time series of structure changes as in Fig. 101, except for Hurricane Ivan (2004) from 10 September at 1030 UTC (Hour 84) to 13 September at 0430 UTC (Hour 150).

Rather, it is suggested that the secondary eyewall formation (see Chapter IV.A.1.c and Fig. 60a) had the more important role in the rapid expansion of the R_{34}. The azimuthal-average wind profiles in Fig. 113a prior to, during, and 6 h after secondary eyewall formation (Hours 87, 105, and 111, respectively) suggest an initial increase in the outer-core structure (R_{34}), and then an additional increase during the 6 h after secondary eyewall formation as Ivan moved away from Jamaica. That is, the R_{34} initially increased by 76 km (blue arrow in Fig. 113a) and then increased by an additional 23 km 6 h after secondary eyewall formation (red arrow in Fig. 113a), for a net increase of 99 km. This near-core land interaction with Ivan did not result in a significant sharpened wind profile following secondary eyewall formation. As indicated in Chapter IV.A.1.c and Fig. 60b, the individual exponent values in the modified Rankine vortex in Eq. (20) for Hours 87 and 105 were $x = 0.46$ and $x = 0.53$, respectively.

Microwave satellite imagery at 1348 UTC 11 September (~Hour 111.5 of the analysis, Fig. 113b) indicates the presence of very strong convection in the spiral rainband as it interacts with Jamaica. As with previous cases of land interaction, the

frictional convergence of winds over the land is considered to have increased the strong convection in the spiral rainbands that intersected land. Following the interaction with Jamaica and enhanced spiral rainband convection, Ivan developed a subsequent secondary eyewall by Hour 135 (Figs. 112 and 61a–c). Again, it is suggested that the asymmetric strong convection in Ivan's spiral rainband that intersected land may have played a role in the secondary eyewall formation. That is, this strong convection over land is considered to advect cyclonically around the storm center in the spiral rainband.

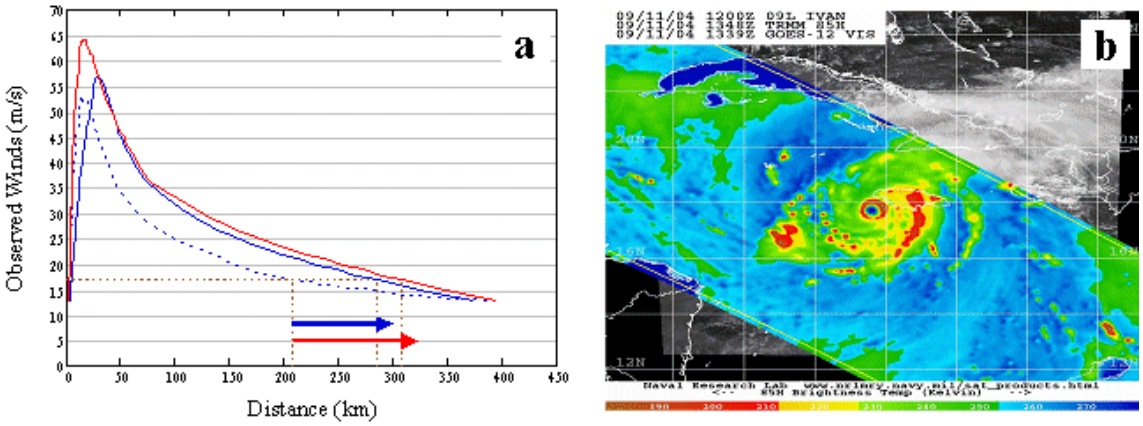

Figure 113 (a) Azimuthal-average wind profiles for Hurricane Ivan at Hour 87 (blue dashed line), Hour 105 (blue solid line) and Hour 111 (red solid line), and (b) microwave satellite imagery (85 GHz) for Hurricane Ivan from TRMM on 11 September at 1348 UTC (2004; from NRL 2007).

In summary, Hurricane Ivan experienced near-core land interaction for a period of approximately 16 h as it passed south of Jamaica. The R_{34} did increase during the near-core land interaction, but the continued R_{34} increase is not consistent with the effects of frictional drag associated with non-landfalling, near-core land interaction and may be the result of limited exposure of the storm structure to the frictional drag. However, the frictional convergence of the winds in the vicinity of a spiral rainband that did intersect the land led to enhanced strong convection that then advected around the eyewall with the spiral rainband. This sequence of events may increase the likelihood of secondary eyewall formation with active spiral rainbands surrounding the eyewall, or by the strong convection causing a disruption in the eyewall as was suggested in the Rita partial eyewall replacement case in Chapter IV.A.2.b.

c. *Wilma (2005)*

The life cycle of Hurricane Wilma was discussed in Chapter IV.A.1.e. The analysis period of near-core land interaction will be from 0730 UTC 21 October (Hour 72) to 1330 UTC 23 October (Hour 126) as Wilma made landfall over the Yucatan Peninsula and then re-emerged over the central Gulf of Mexico. At Hour 72, Wilma had a tangential wind speed (V_t) of 50 m s^{-1} with azimuthal-average R_{max} and R_{34} values of 30 km and 329 km, respectively (Fig. 114). Wilma had a near-core interaction with the northeastern Yucatan Peninsula between 78 h and 122 h.

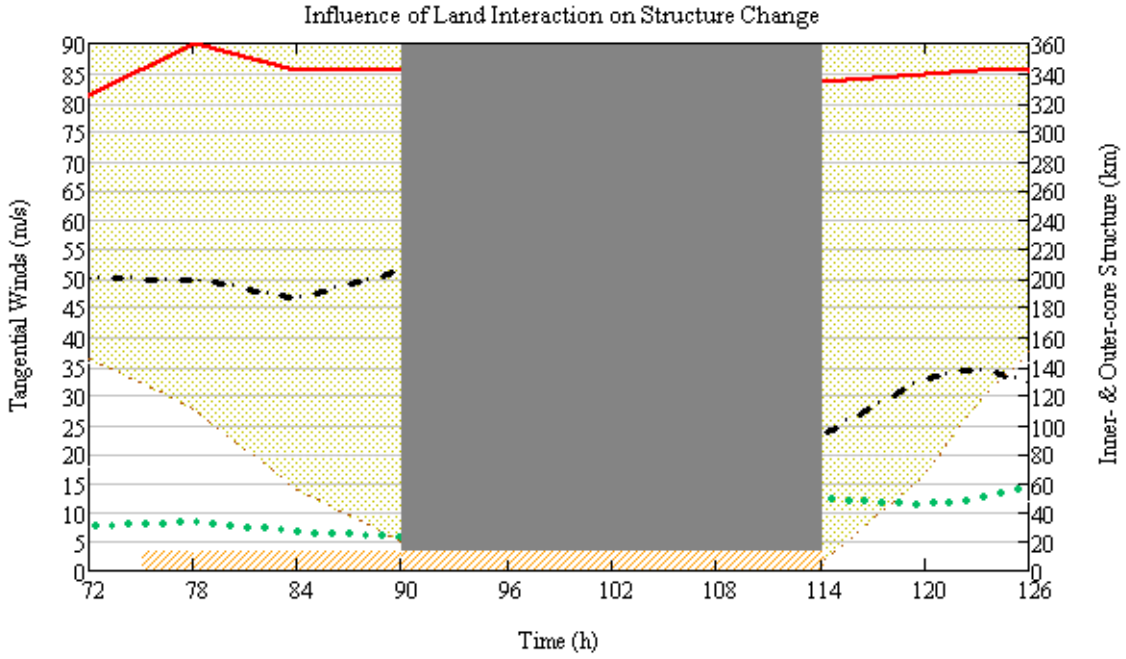

Figure 114 Time series of structure changes as in Fig. 101, except for Hurricane Wilma (2005) from 21 October at 0730 UTC (Hour 72) to 23 October at 1330 UTC (Hour 126). The gray area represents the period in which H*Wind analyses are not available as a result of landfall.

At Hour 72, the outer-core structure (R_{34}) was interacting with the Yucatan Peninsula at a distance of 145 km, and then the storm center moved progressively closer to land until it made landfall at approximately Hour 90.5 (Fig. 114). From 72 h to 90 h as Wilma moved progressively closer to the northeastern Yucatan Peninsula and experienced a secondary eyewall replacement cycle, the intensity (V_t) fluctuated between 46 m s^{-1} and 52 m s^{-1}. During landfall over the Yucatan Peninsula, V_t

decreased rapidly by 29 m s^{-1} in 24 h, but reintensified to 35 m s^{-1} as Wilma moved back over the waters of the Gulf of Mexico. By contrast, the outer-core structure (R_{34}) remained fairly constant with a size greater than 320 km, and thus suggests that near-core land interaction with a less continuous landmass may have a minimal impact on an already large outer-core structure.

Indeed, the azimuthal-average wind profiles in Fig. 115a prior to, during, and 6 h after secondary eyewall formation (Hours 72, 114, and 120, respectively) suggest minimal change in the outer-core structure (R_{34}) during Wilma's eyewall replacement cycle preceding landfall over the Yucatan Peninsula. That is, the R_{34} initially decreased by 11 km (blue arrow in Fig. 115a) and then increased by 16 km 6 h after secondary eyewall formation in conjunction with near-core land interaction (red arrow in Fig. 115a), for a net increase of 5 km. Whereas Ivan's structure experienced a considerable increase during near-core land interaction (see Chapter IV.C.2.b), Wilma's already large R_{34} value may have been a limiting factor for additional size increases. In contrast to the other cases of land interaction in Chapter IV.C, the near-core land interaction with Wilma resulted in a significantly flattened wind profile following secondary eyewall formation. Recall from Chapter IV.A.1.e and Fig. 75b, individual exponent values in the modified Rankine vortex in Eq. (20) for Hours 72 and 114 were $x = 0.45$ and $x = 0.16$, respectively.

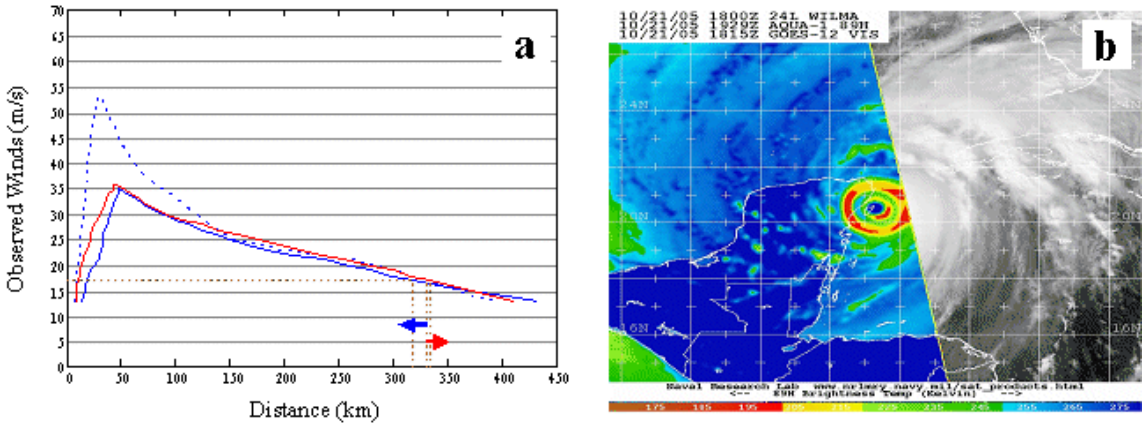

Figure 115 (a) Azimuthal-average wind profiles for Hurricane Wilma at Hour 72 (blue dashed line), Hour 114 (blue solid line) and Hour 120 (red solid line), and (b) microwave satellite imagery (89 GHz) for Hurricane Wilma from Aqua on 21 October at 1929 UTC (2005; from NRL 2007).

Microwave satellite imagery at 1929 UTC 21 October (∼Hour 84 of the analysis, Fig. 115b) indicates the presence of very strong convection in the secondary eyewall that remains partially over water as Wilma approaches landfall over the extreme northwestern tip of the Yucatan Peninsula. As with the landfall of Charley (Chapter IV.C.2.a), the strong convection in the spiral rainbands of Wilma appear to weaken (see Figs. 72e–f and 74a–b), except where the spiral rainbands intersect western Cuba well to the east of the storm center. The convection in the secondary eyewall continued to be quite strong despite landfall and became the dominant eyewall by the time Wilma re-emerged over the Gulf of Mexico (Figs. 74b and 114).

In summary, Hurricane Wilma experienced near-core land interaction for a period of approximately 44 h as it passed over the Yucatan Peninsula. The R_{34} remained nearly constant during the near-core land interaction (Fig. 114). This suggests that the frictional drag associated with near-core land interaction combined with a limited exposure of the storm structure over land (i.e., a peninsula as opposed to a continuous landmass) has a minimal impact on the outer-core structure. As with Ivan's third eyewall replacement in Chapter IV.A.1.c, the lack of a significant R_{34} increase during Wilma's eyewall replacement in conjunction with near-core land interaction may be the result of size limiting factors of the environment, since both of these storms already had very large R_{34} values prior to the secondary eyewall formation. In contrast to all other cases of near-core and peripheral land interaction, Wilma had a significantly flatter wind profile following near-core land interaction, but this resulted from the prior eyewall replacement that was not modified.

3. Conclusions for Land Interaction

The analyses of individual case studies of peripheral and near-core land interaction revealed that the frictional convergence of the winds in the vicinity of spiral rainbands that intersect the land led to enhanced strong convection that then advected around the eyewall with the spiral rainbands and may have contributed to the secondary eyewall formation by surrounding the eyewall with active spiral rainbands. This sequence of events may also increase the likelihood of secondary eyewall formation by the strong convection causing a disruption in the eyewall as was suggested in the Rita partial eyewall replacement case in Chapter IV.A.2.b. Secondary eyewall formation occurred during the peripheral land interaction for Ivan and Rita (Figs. 64a–c and 102b–d), and during near-core land interaction for Ivan, Wilma, and Charley (Figs.

58f, 61a–c, 72c–f, and 110d). The peripheral land interaction as Wilma approached landfall over southern Florida (see Chapter IV.C.1.c) is the only exception for the cases analyzed in this section. However, Wilma appears to be a special case. Wilma's large R_{max} of 60+ km and its fast translation speed of nearly 20 kt prior to this second case of land interaction, which are approximately twice as large as the other cases in which a secondary eyewall formed in conjunction with landfall. Thus, it is hypothesized that a large R_{max} and fast translation speed are contributing factors that may hinder secondary eyewall formation in tropical cyclones during peripheral and near-core land interaction.

The outer-core structure (R_{34}) decreased during continuous land interaction (e.g., along the coasts of the United States), and thus suggests that the frictional drag of land interaction with a sustained period of exposure also led to a decrease in the R_{34} quadrants over water (i.e., the quadrants used to calculate the azimuthal-average R_{34} value). For example, this type of land interaction was observed in the cases of peripheral land interaction for Rita and Wilma (Figs. 101 and 106), and in the case of near-core land interaction for Charley (Fig. 109). As with the cases of secondary eyewall formation in Chapter IV.A, secondary eyewall formation in conjunction with this type of land interaction occurred when a flatter-than-average radial wind profile initially existed, but was followed by a sharper radial profile. Although R_{34} decreased, it should be noted that a net increase in the radius of hurricane-force winds (R_{64}) was observed in Charley prior to landfall that may significantly impact the timing and coverage of hurricane warnings for coastal communities.

The evolution of tropical cyclone structure changes associated with continuous land interaction are illustrated in Fig. 116. As a tropical cyclone with a typical radial wind profile (Fig. 116b) of tangential wind with maximum speed (V_t) >33 m s^{-1} approaches a continuous landmass, an enhancement of convection occurs in the spiral rainband where it intersects with the land (Fig. 116a). This increased convection in the spiral rainband causes convective asymmetries that lead to a reduction of V_t, yet also an expansion of the eyewall (Fig. 116d) as was demonstrated in Chapter IV.B. In contrast to the expected R_{34} increase associated with a R_{max} increase, in conjunction with a V_t decrease as a result of the frictional drag of land interaction with a sustained period of exposure, a decrease in R_{34} occurs (Fig. 116d). Over time, the enhanced convection is rotated around the eyewall and begins to surround the eyewall (Fig. 116c).

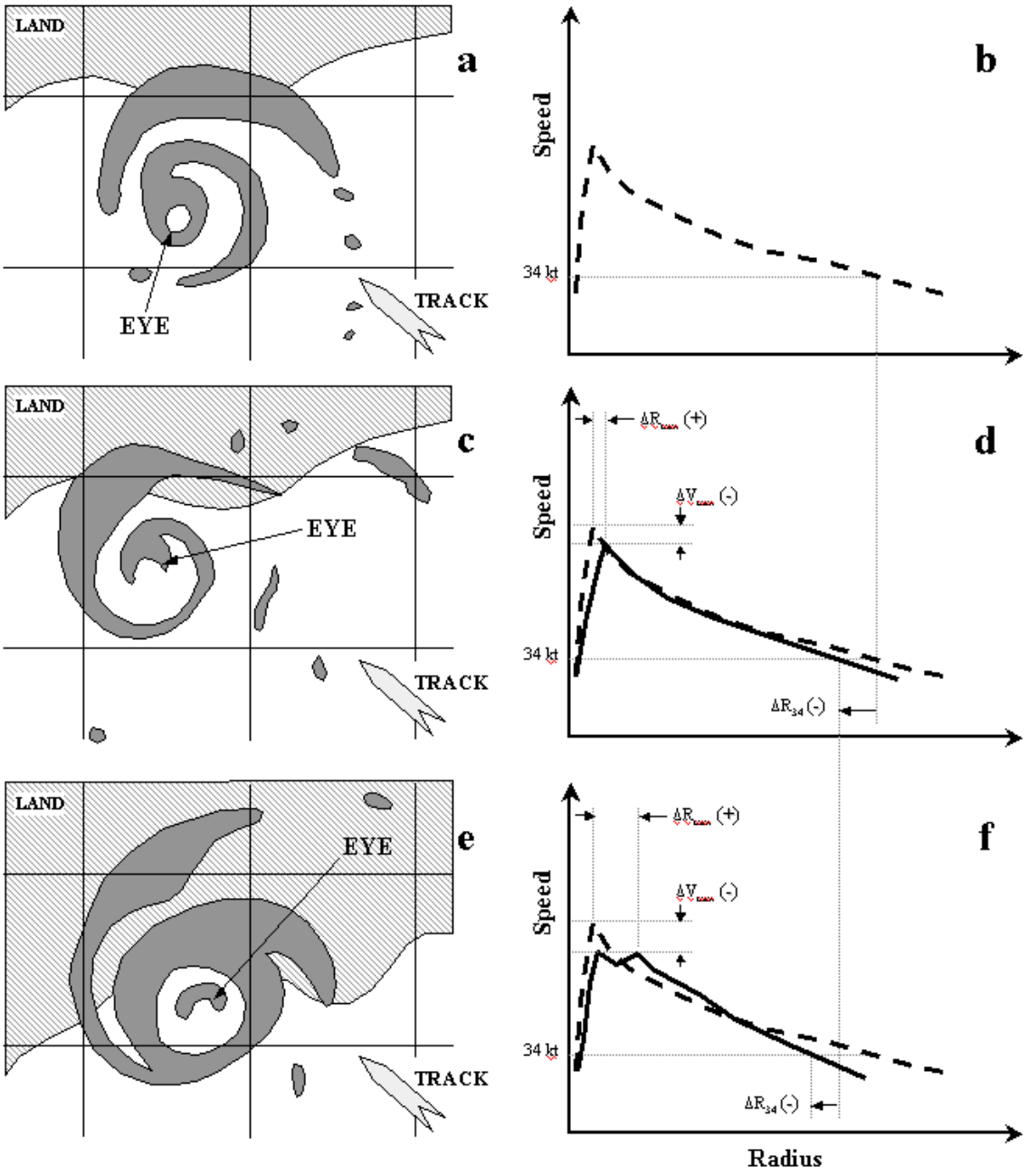

Figure 116 Schematic illustration of (a, c, and e) convection and (b, d, and f) radial profiles of tangential wind structure changes associated with continuous land interaction at time $t - \Delta t$, t, and $t + \Delta t$, respectively. The dashed curves (b, d, and f) represent the azimuthal-average wind profile at time $t - \Delta t$. The solid curves (d and f) represent the azimuthal-average wind profiles at time t and $t + \Delta t$, respectively.

This sequence of events increases the likelihood of secondary eyewall formation as a result of active spiral rainbands surrounding the eyewall or by the strong convection causing a disruption in the eyewall. As the tropical cyclone moves closer to landfall, a secondary eyewall may begin to form (Fig. 116e) and the original eyewall convection becomes less symmetric. This formation of a secondary eyewall may be reflected in the radial profile of the tangential wind (Fig. 116f) as with Hurricane Rita. Whereas the formation of a secondary eyewall was found to result in R_{34} increases in Chapter IV.A, the compensating V_t decreases during continuous land interaction as a result of the sustained frictional drag generally leads to R_{34} decreases during continuous land interaction.

By contrast, land interaction combined with a limited exposure of the storm structure over land (e.g., an island or a peninsula as opposed to a continuous landmass) had a minimal impact on the outer-core structure (R_{34}) of a tropical cyclone. For example, this type of land interaction was observed in the cases of peripheral and near-core land interaction for Ivan (Figs. 104 and 112), and in the case of near-core land interaction for Wilma (Fig. 114). As with Ivan's third eyewall replacement in Chapter IV.A.1.c, the lack of a significant R_{34} increase during Wilma's eyewall replacement in conjunction with near-core land interaction may be the result of size-limiting factors of the environment, since both of these storms already had very large R_{34} values prior to the secondary eyewall formation. Contrary to all other cases of near-core and peripheral land interaction, Wilma's near-core land interaction during eyewall replacement resulted in a significantly flatter wind profile following secondary eyewall replacement due to a significant decrease in V_t that resulted from the duration of inner-core exposure to frictional effects.

The evolution of tropical cyclone structure changes associated with land interaction of limited exposure are illustrated in Fig. 117. As a tropical cyclone with a typical radial wind profile (Fig. 117b) of tangential wind with maximum speed (V_t) >33 m s^{-1} approaches a smaller landmass, an enhancement of convection occurs in the spiral rainband where it intersects with the land (Figs. 117a and c). This increased convection in the spiral rainband causes convective asymmetries that lead to a reduction of V_t, yet also an expansion of the eyewall (Fig. 117d) as was demonstrated in Chapter IV.B. In this case, R_{34} increases in response to the R_{max} increase since the radial profile in the outer region is little affected by the limited exposure of the storm structure to land and its enhanced frictional drag.

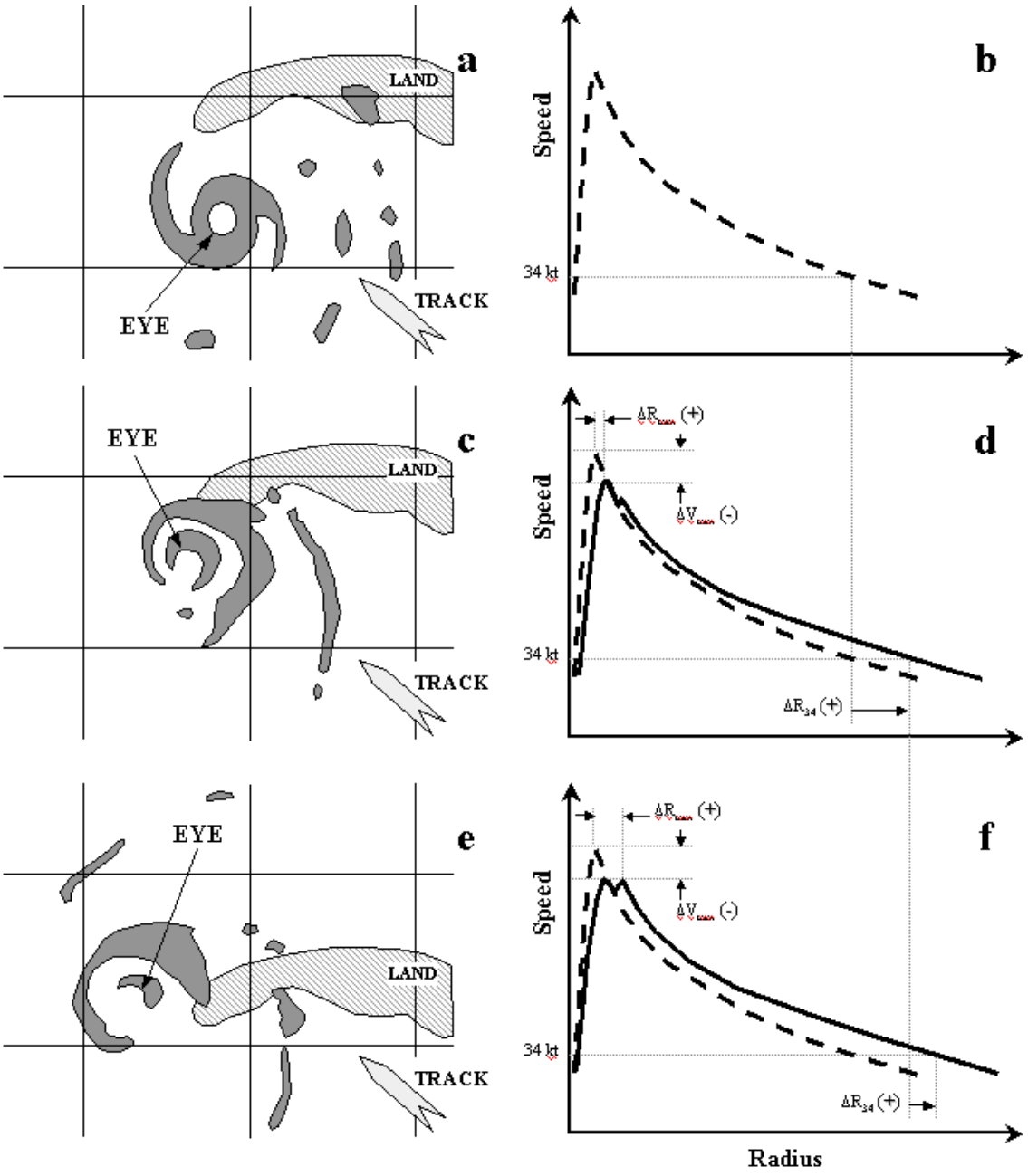

Figure 117 Schematic illustration of (a, c, and e) convection and (b, d, and f) radial profiles of tangential wind structure changes associated with land interaction of limited exposure at time $t - \Delta t$, t, and $t + \Delta t$, respectively. The dashed curves (b, d, and f) represent the azimuthal-average wind profile at time $t - \Delta t$. The solid curves (d and f) represent the azimuthal-average wind profiles at time t and $t + \Delta t$, respectively.

Over time, the enhanced convection is rotated around the eyewall and begins to surround the eyewall (Fig. 117c). This sequence of events increases the likelihood of secondary eyewall formation as a result of active spiral rainbands surrounding the eyewall or by the strong convection causing a disruption in the eyewall. As the tropical cyclone moves closer to landfall or moves past the land, a secondary eyewall may begin to form (Fig. 117e) and the original eyewall convection becomes less symmetric. This formation of a secondary eyewall may be reflected in the radial wind profile (Fig. 117f). As in the secondary eyewall cases described in Chapter IV.A, R_{34} continues to increase during cases of limited exposure to land since the outer wind profile is little affected by frictional drag. For the secondary eyewall formation cases associated with limited land interaction, the V_t often increases after an initial decrease. This increased V_t with a larger R_{max} and a similar outer wind structure can lead to a substantial R_{34} increase (compare Fig. 117f with Fig. 117b).

D. VERTICAL WIND SHEAR

As discussed in Chapter I, the presence of environmental vertical wind shear generally has a negative impact on tropical cyclone development. For the purposes of this research, the impacts of vertical wind shear are assessed for the large-scale interaction between a midlatitude baroclinic system and a tropical cyclone. Whereas the presence of vertical wind shear is inferred using infrared or water vapor satellite imagery, tropical cyclone structure changes are assessed by utilizing microwave satellite imagery. Of the tropical cyclones during 2003–2005 in the North Atlantic basin, three storms will be discussed that meet these criteria for vertical wind shear and have a sufficient number of H*Wind analyses.

1. Fabian (2003)

The life cycle of Hurricane Fabian was discussed in Chapter IV.A.1.a. The analysis period of vertical wind shear will be from 1330 UTC 2 September (Hour 24) to 0130 UTC 6 September (Hour 108) as Fabian moved across the western North Atlantic on a northwestward track (first case) followed by a northward track (second case). The first of two midlatitude baroclinic systems interacted with Hurricane Fabian on 3 September.

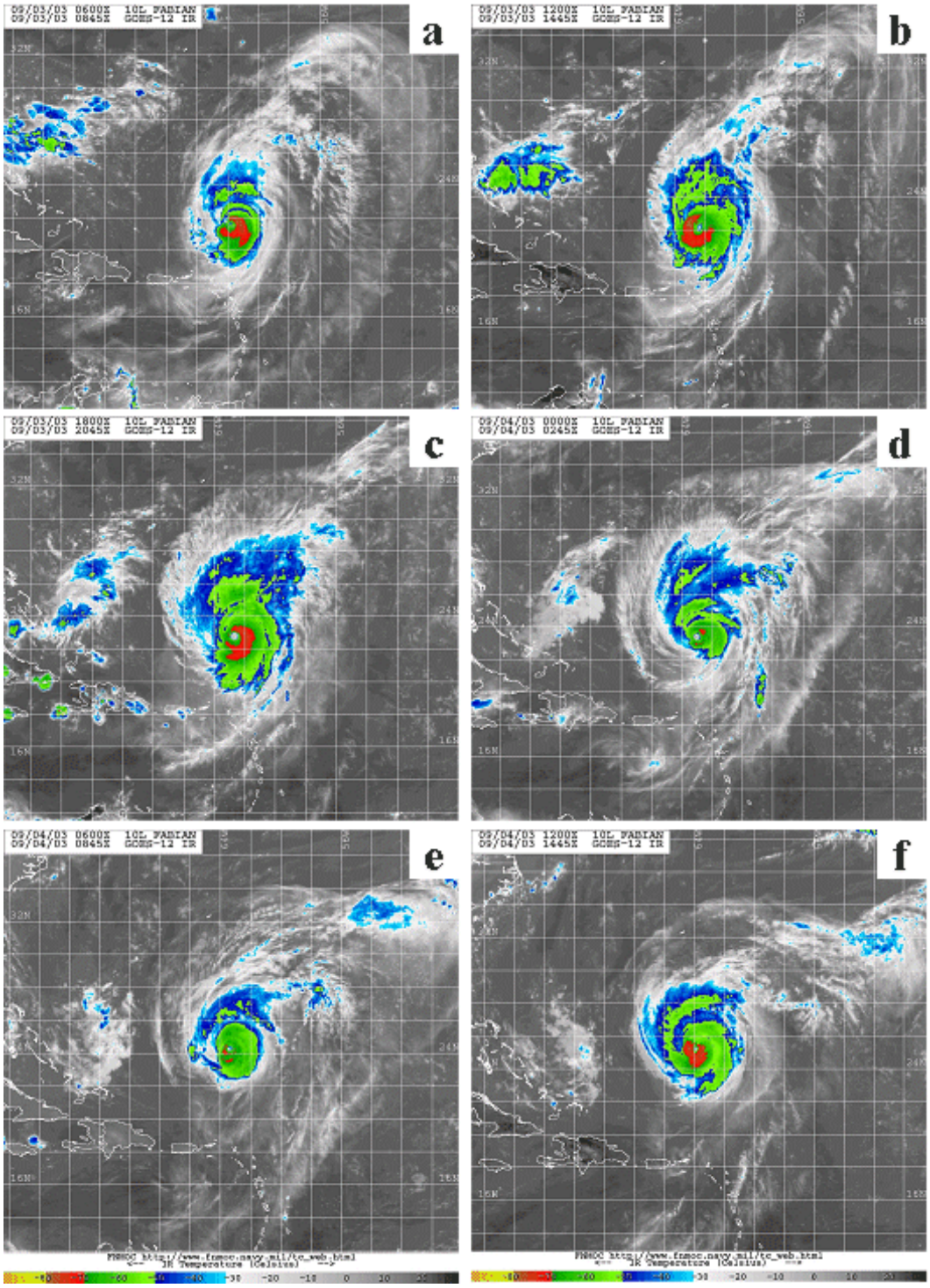

Figure 118 Infrared satellite imagery for Hurricane Fabian from the GOES-East platform on (a) 3 September at 0845 UTC, (b) 3 September at 1445 UTC, (c) 3 September at 2045 UTC, (d) 4 September at 0245 UTC, (e) 4 September at 0845 UTC, and (f) 4 September at 1445 UTC (2003; from NRL 2007).

Infrared satellite imagery at 0845 UTC and 1445 UTC 3 September (∼Hours 43.5 and 49.5 of the analysis, Fig. 118a–b) depicts the approach of a upper-level trough from the west with a flair up of deep convection along the southern extent of the trough. As this midlatitude trough approached Fabian, a north-south elongation of the cloud shield is evidenced by infrared satellite imagery at 0845 UTC, 1445 UTC, and 2045 UTC 3 September (∼Hours 43.5, 49.5, and 55.5 of the analysis, Figs. 118a–c). Microwave satellite imagery at 0957 UTC 3 September (∼Hour 42.5 of the analysis, Fig. 119b) suggests that the environmental vertical wind shear leads to asymmetric, strong convection in the downshear (northeast) side of Fabian's eyewall and in the northern quadrants of the storm.

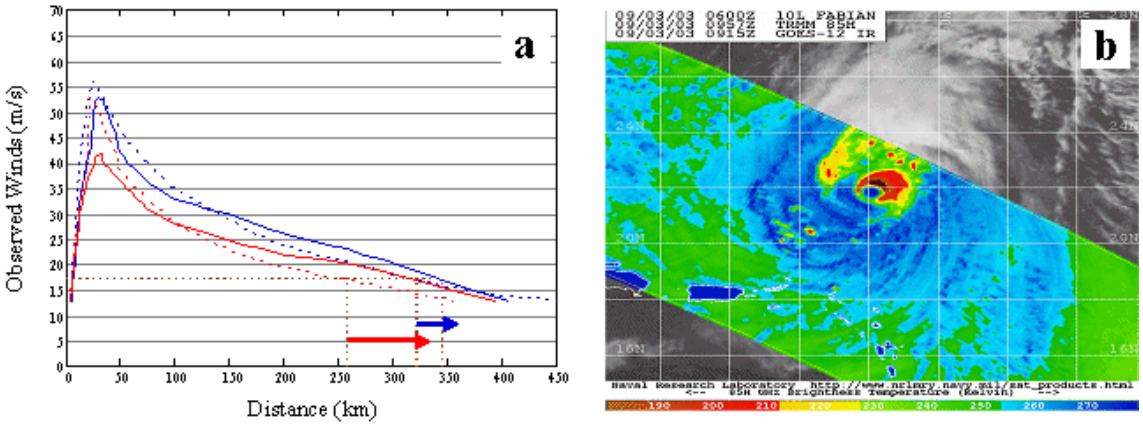

Figure 119 (a) Motion-relative wind profiles for Hurricane Fabian at Hour 24 (dashed lines) and Hour 66 (solid lines) for the RF and LR quadrants (blue and red lines, respectively), and (b) microwave satellite imagery (85 GHz) for Hurricane Fabian from TRMM on 3 September at 0957 UTC (2003; from NRL 2007).

Infrared satellite imagery at 0245 UTC, 0845 UTC, and 1445 UTC 4 September (∼Hours 61.5, 67.5, and 73.5 of the analysis, Figs. 118d–f) indicates a quick passage of the first midlatitude system and greater convective symmetry of Fabian's structure (see Fig. 86f). Whereas the motion-relative wind profiles in the RF and LR quadrants (Fig. 119a) prior to and after (Hours 24 and 66, respectively) suggest the influence of environmental vertical wind shear has led to greater asymmetry in the storm inner-core structure (R_{max}), the outer-core structure (R_{34}) became more symmetric. That is, although no significant differences are indicated in the R_{max} radii, the maximum tangential wind speed (V_t) in the LR quadrant decreased more rapidly than in the RF

quadrant. By contrast, a larger R_{34} increase occurred in the LR quadrant than in the RF quadrant (62 km versus 23 km). Intermediate wind profiles suggest that the R_{34} radii first increased on the downshear side (RF quadrant) of the tropical cyclone and later increased in the upshear side (LR quadrant) of the storm. These differences in the inner- and outer-core structures are also apparent in the microwave satellite imagery in Fig. 86f.

Infrared satellite imagery at 2045 UTC 4 September, and 0245 UTC and 0845 UTC 5 September (∼Hours 79.5, 85.5, and 91.5 of the analysis, Figs. 120a–c) depicts the approach of the second, stronger midlatitude trough. As this midlatitude system approaches from the west, the ridge between the first and second midlatitude troughs introduced an easterly vertical wind shear across Fabian as evidenced by the east-west elongation of the cloud shield. In conjunction with the changing environmental vertical wind shear, microwave satellite imagery (Figs. 47b–c) indicates a shift in Fabian's downshear convection from the north quadrants to the west quadrants (Fig. 121b). As the second midlatitude trough interacted with Fabian, a return to southerly vertical wind shear is evidenced by the elongation of Fabian's cloud shield in the north-south direction as depicted by infrared satellite imagery at 1445 UTC and 2045 UTC 5 September, and 0245 UTC 6 September (∼Hours 97.5, 103.5, and 109.5 of the analysis, Figs. 120d–f).

Whereas the motion-relative wind profiles in the RF and LR quadrants (Fig. 121a) prior to and after (Hours 78 and 108, respectively) depict the influence of environmental vertical wind shear has led to a size increase in the inner-core structure (R_{max}) associated with secondary eyewall formation as discussed in Chapter IV.A.1.a. Contrary to the first Fabian case, the decrease in V_t is similar for both the RF and LR quadrants of the storm. As with the first Fabian case, a larger R_{34} increase occurred in the LR quadrant than in the RF quadrant (115 km versus 70 km). Intermediate wind profiles for this case suggest that the increase of R_{34} in the LR quadrant was less than for the first case, perhaps because the downshear convection was located in the LF quadrant (Fig. 121b) and the circulation rotated the associated momentum from the LF to the LR quadrant.

In summary, Hurricane Fabian experienced environmental vertical wind shear due to the interactions with two midlatitude baroclinic systems. In the first interaction, greater inner-core structure asymmetry was realized as a result of a more rapid decrease of V_t in the LR quadrant than in the RF quadrant.

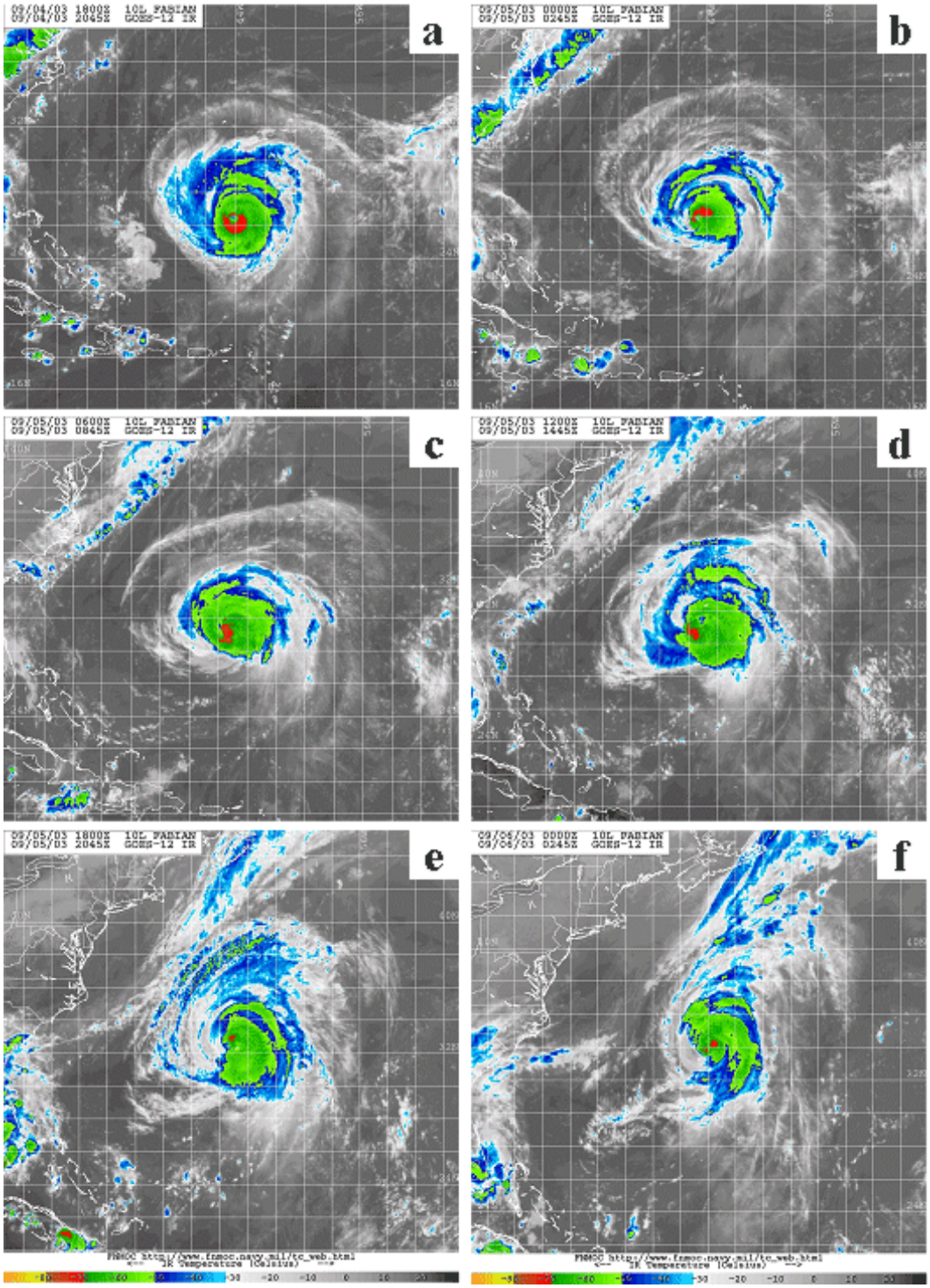

Figure 120 Infrared satellite imagery for Hurricane Fabian from the GOES-East platform on (a) 4 September at 2045 UTC, (b) 5 September at 0245 UTC, (c) 5 September at 0845 UTC, (d) 5 September at 1445 UTC, (e) 5 September at 2045 UTC, and (f) 6 September at 0245 UTC (2003; from NRL 2007).

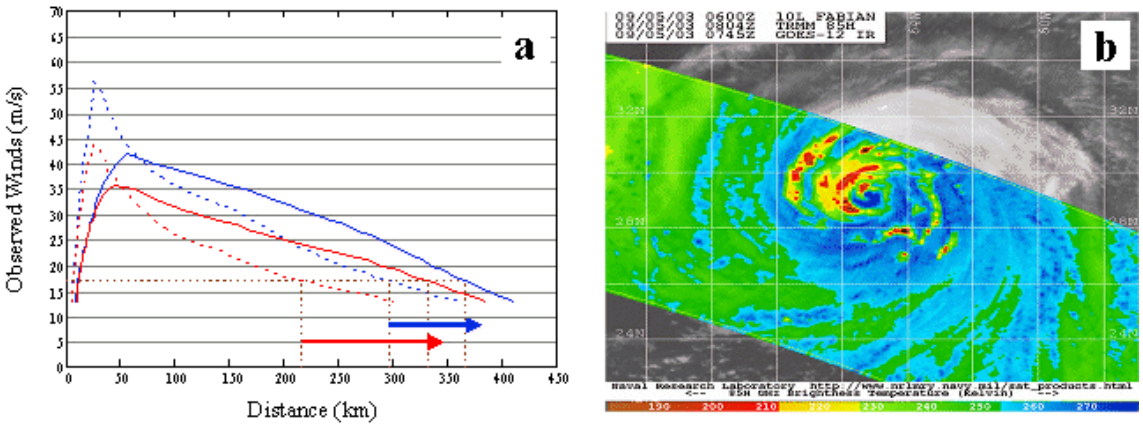

Figure 121 (a) Motion-relative wind profiles for Hurricane Fabian at Hour 78 (dashed lines) and Hour 108 (solid lines) for the RF and LR quadrants (blue and red lines, respectively), and (b) microwave satellite imagery (85 GHz) for Hurricane Fabian from TRMM on 5 September at 0804 UTC (2003; from NRL 2007).

In the second interaction, inner-core asymmetries already existed prior to the interaction with the second midlatitude system and the V_t decreases in the RF and LR quadrants were similar. These differences are hypothesized to be the result of the changing direction of vertical wind shear and a secondary eyewall formation in the second case that were not observed in the first case. For both interactions, the outer-core structure (R_{34}) became more symmetric. That is, a proportionally larger R_{34} increase occurred in the LR quadrant than in the RF quadrant (2.7 to 1 and 1.6 to 1, respectively), which thus reduced asymmetries that existed prior to the influence of environmental vertical wind shear. It is also hypothesized that the stronger winds were then advected from the RF quadrant to the LR quadrant in response to structural asymmetries that resulted from environmental vertical wind shear, and thus led to axisymmetrization of the outer-core structure.

2. Isabel (2003)

The life cycle of Hurricane Isabel was discussed in Chapter IV.B.2. The analysis period of vertical wind shear will be from 1930 UTC 14 September (Hour 48) to 1930 UTC 17 September (Hour 120, Fig. 122) as Isabel moved across the western North Atlantic on a west-northwestward track (first case) followed by a northwestward track (second case). A midlatitude baroclinic system interacted with Hurricane Isabel from 15 September to 17 September. Infrared satellite imagery at 0145 UTC 15 September

(∼Hour 54.5 of the analysis, Fig. 123a) indicates a highly symmetric cloud shield as Isabel reached a peak intensity (V_t) of 60 m s^{-1} during its annular phase (Fig. 122).

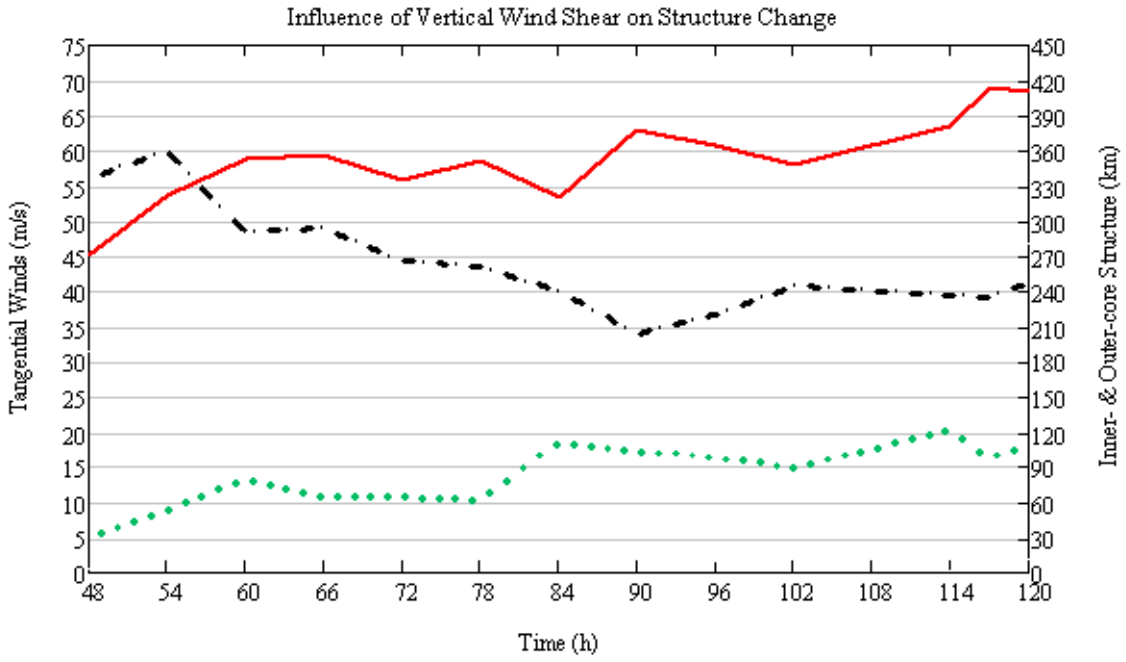

Figure 122 Time series of structure changes as in Fig. 101, except for Hurricane Isabel (2003) from 14 September at 1930 UTC (Hour 48) to 17 September at 1930 UTC (Hour 120).

Infrared satellite imagery at 0745 UTC, 1345 UTC, and 1945 UTC 15 September (∼Hours 60.5, 66.5, and 72.5 of the analysis, Figs. 123b–d) suggests a structural transition of Isabel from a highly symmetric, annular hurricane to an asymmetric system with a north-south elongation of the cloud shield as Isabel interacted with a midlatitude trough stalled along the east coast of the United States. Indeed, microwave satellite imagery at 1409 UTC and 2152 UTC 15 September (∼Hours 66.5 and 74.5 of the analysis, Figs. 124a–b) depicts an increase in structure asymmetry of Isabel, which contrasts with the structure depicted in Fig. 93. Infrared satellite imagery at 0145 UTC and 0745 UTC 16 September (∼Hours 78.5 and 84.5 of the analysis, Figs. 123e–f) indicates the shifting of the coldest cloud tops (an indication of the deepest, strongest convection) into the northeast quadrant. This downshear shift of the strongest convection is also evident in microwave satellite imagery at 0246 UTC 16 September (∼Hour 79.5 of the analysis, Fig. 124c).

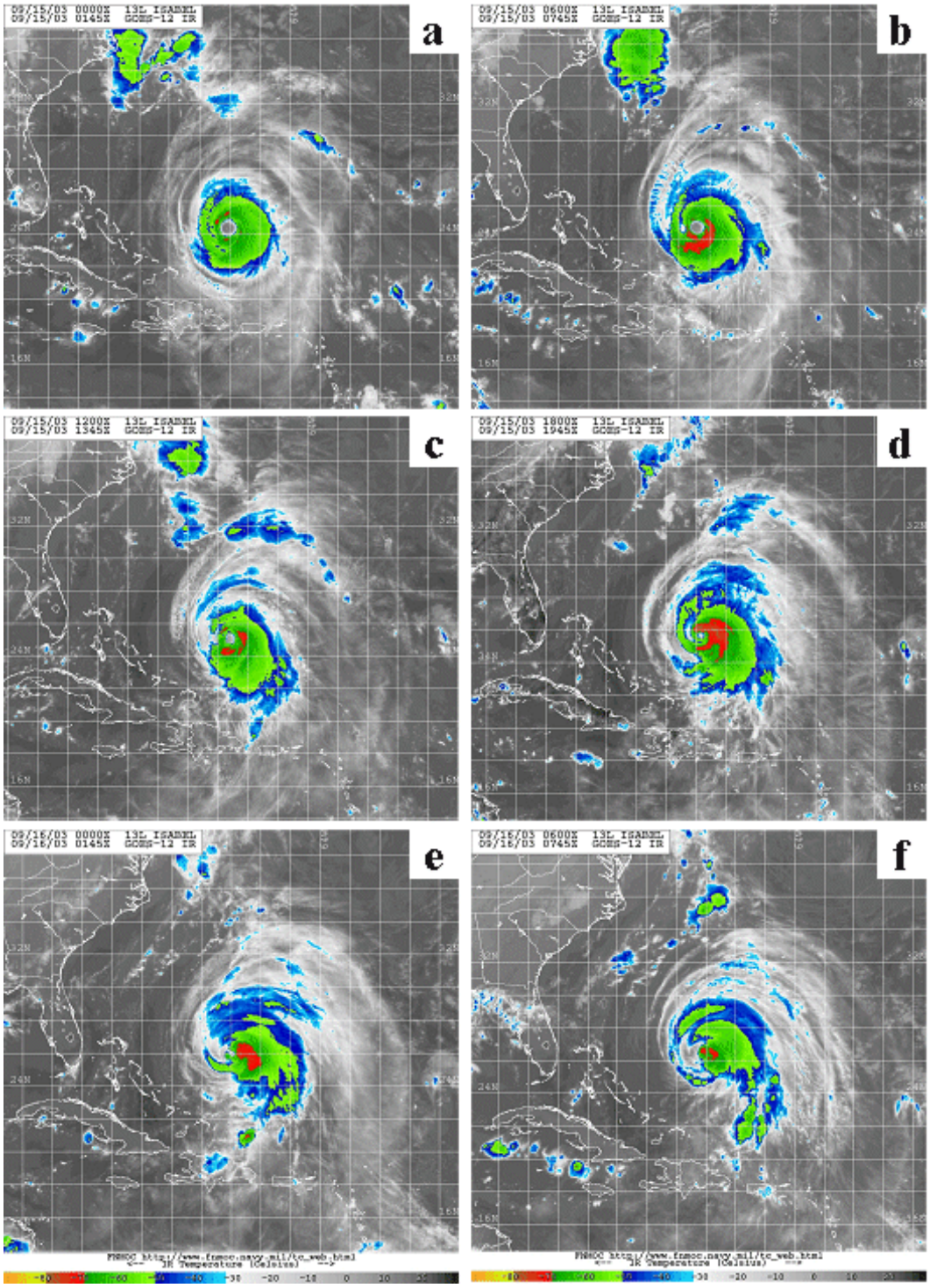

Figure 123 Infrared satellite imagery for Hurricane Isabel from the GOES-East platform on (a) 15 September at 0145 UTC, (b) 15 September at 0745 UTC, (c) 15 September at 1345 UTC, (d) 15 September at 1945 UTC, (e) 16 September at 0145 UTC, and (f) 16 September at 0745 UTC (2003; from NRL 2007).

During this interaction of southwesterly environmental vertical wind shear with Isabel between 54 h and 84 h, V_t decreased from 60 m s^{-1} to 40 m s^{-1} (Fig. 122).

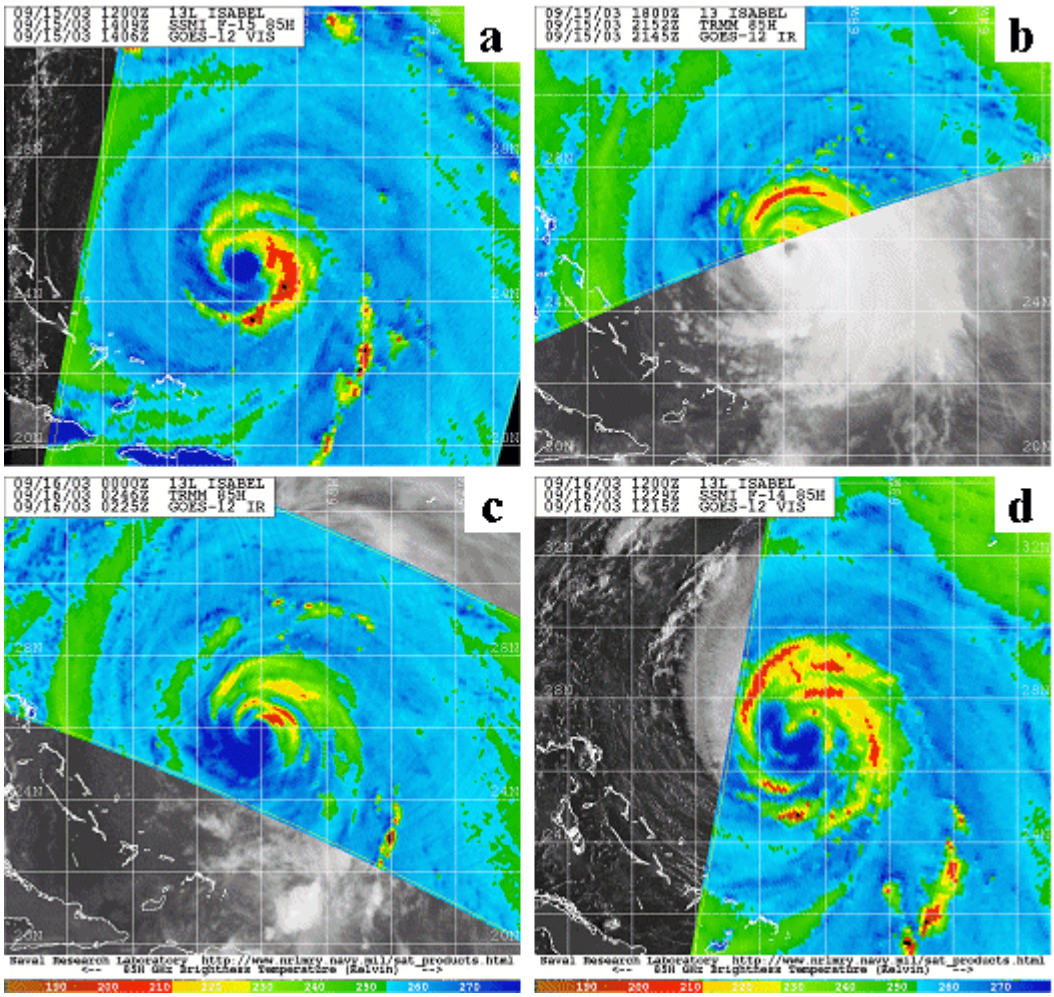

Figure 124 Microwave satellite imagery (85 GHz) for Hurricane Isabel from TRMM and DMSP polar orbiting platforms on (a) 15 September at 1409 UTC, (b) 15 September at 2152 UTC, (c) 16 September at 0246 UTC, and (d) 16 September at 1229 UTC (2003; from NRL 2007).

The motion-relative wind profiles in the RF and LR quadrants (Fig. 125a) prior to and during (Hours 48 and 84, respectively)depict the influence of environmental vertical wind shear has led to an increase in R_{max} and the transition from a highly symmetric structure to an asymmetric structure as depicted in Fig. 125b. That is, the RF and LR quadrants at Hour 48 were quite similar, but following the increase in vertical wind shear, V_t in the LR quadrant of Isabel decreased more rapidly than in the

RF quadrant. As with the two Fabian interactions, R_{34} increased in both the RF and LR quadrants (68 km and 53 km, respectively). These R_{34} increases may be attributed to the R_{max} increases in each quadrant since the slope of the profile remained similar, and thus more than offset the large V_t decreases that would have been expected to result in R_{34} decreases.

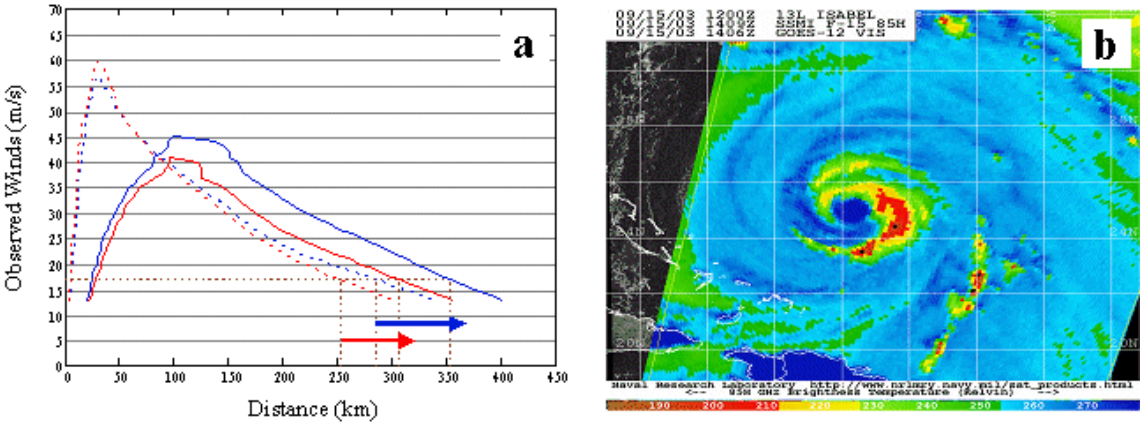

Figure 125 (a) Motion-relative wind profiles for Hurricane Isabel at Hour 48 (dashed lines) and Hour 84 (solid lines) for the RF and LR quadrants (blue and red lines, respectively), and (b) microwave satellite imagery (85 GHz) for Hurricane Isabel from DMSP on 15 September at 1409 UTC (2003; from NRL 2007).

Infrared satellite imagery at 1345 UTC and 1945 UTC 16 September and 0145 UTC and 0745 UTC 17 September (~Hours 90.5, 96.5, 102.5, and 108.5 of the analysis, Figs. 126a–d) indicates an increase in convection along the midlatitude trough as Isabel approaches the trough. However, an increase in symmetry of the cloud shield suggests a decrease in the influence of vertical wind shear on Isabel. Indeed, microwave satellite imagery at 1229 UTC and 2056 UTC 16 September (~Hours 89 and 97.5 of the analysis, Figs. 124d and 127a) depicts a return of strong, banded convection to the southern quadrants of this storm. From 90 h to 102 h, V_t increased from 34 m s^{-1} to 41 m s^{-1} and R_{max} decreased from 103 km to 89 km (Fig. 122). As Isabel interacts more directly with the midlatitude trough, microwave satellite imagery at 0150 UTC and 1146 UTC 17 September (~Hours 102.5 and 112.5 of the analysis, Figs. 127b–c) depicts a return of strong asymmetric convection to the northern quadrants that is then rotated around the storm center to the western quadrants.

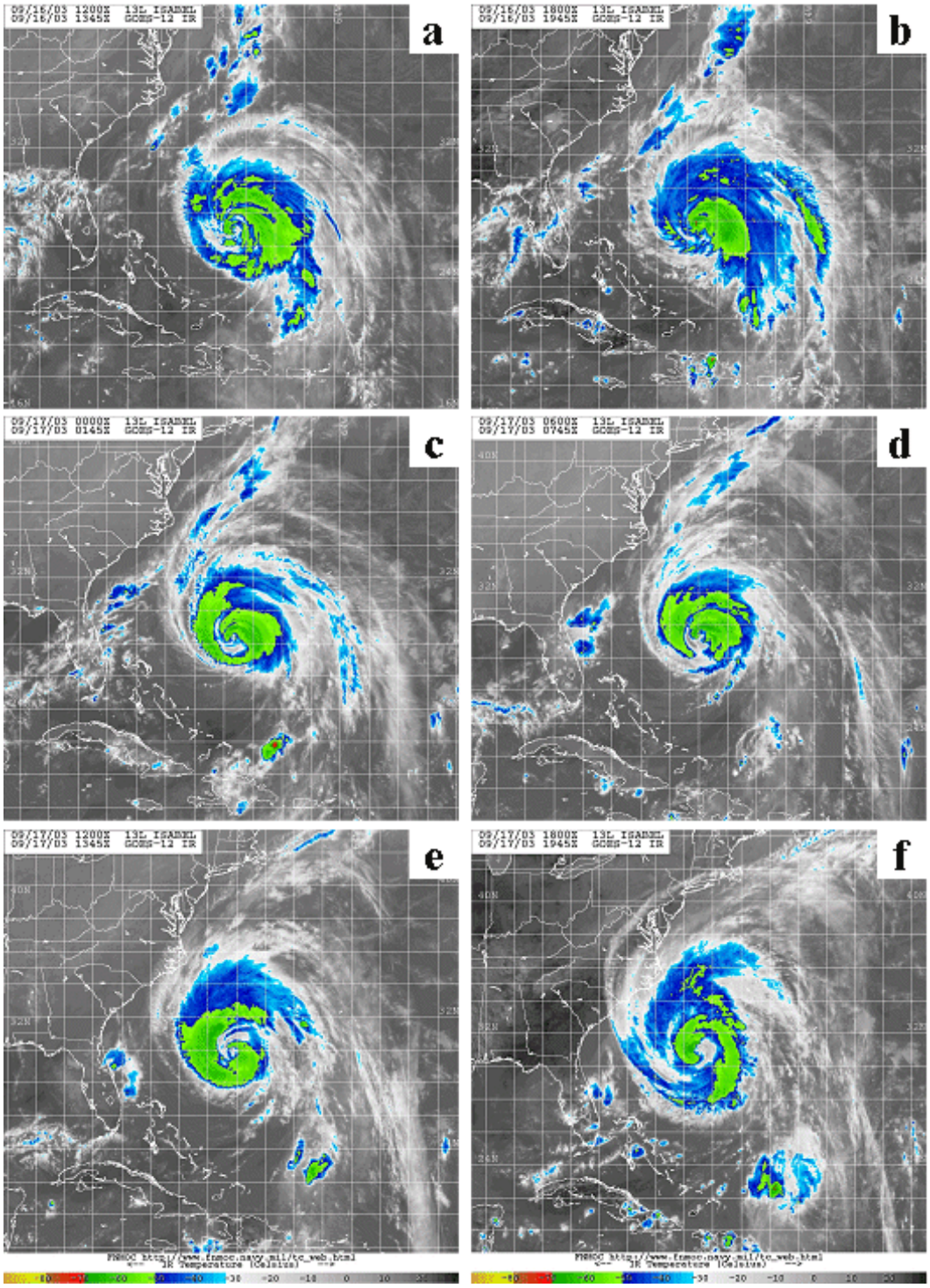

Figure 126 Infrared satellite imagery for Hurricane Isabel from the GOES-East platform on (a) 16 September at 1345 UTC, (b) 16 September at 1945 UTC, (c) 17 September at 0145 UTC, (d) 17 September at 0745 UTC, (e) 17 September at 1345 UTC, and (f) 17 September at 1945 UTC (2003; from NRL 2007).

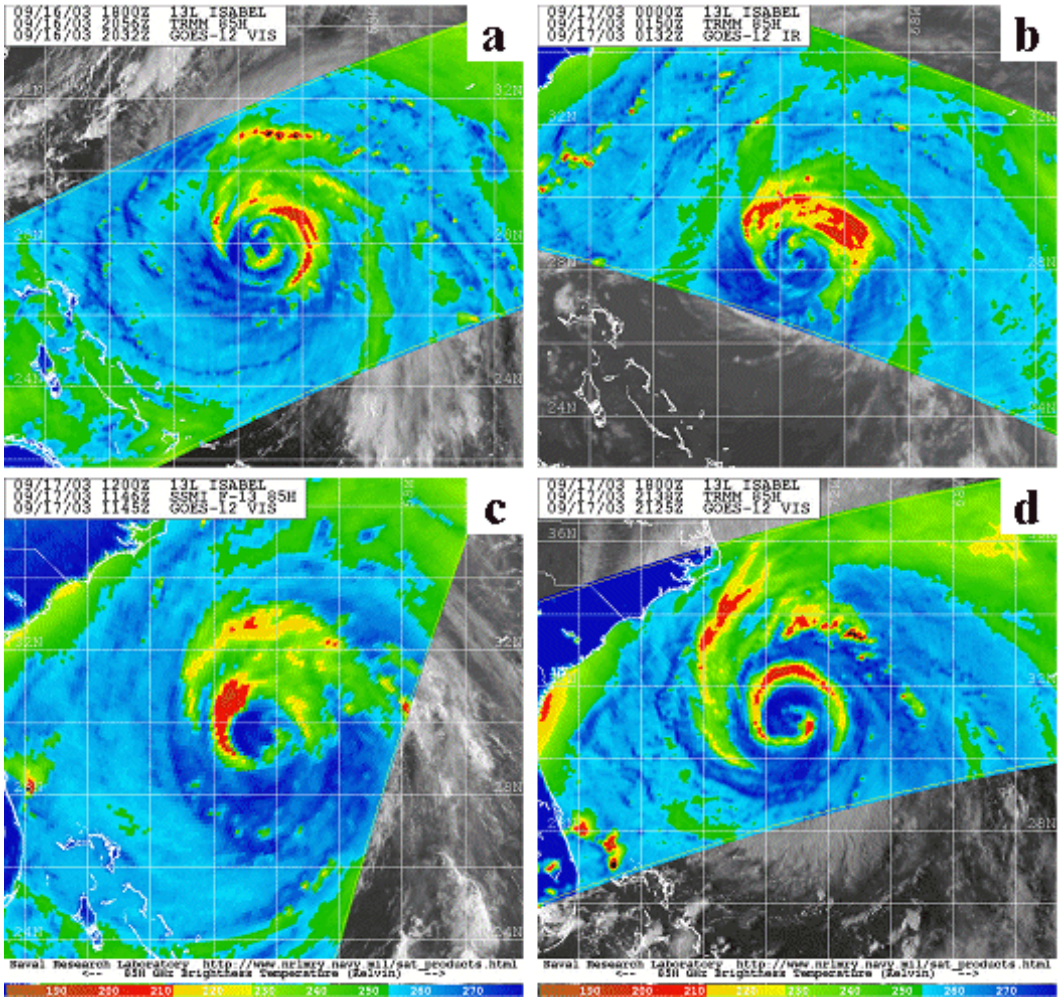

Figure 127 Microwave satellite imagery (85 GHz) for Hurricane Isabel from TRMM and DMSP polar orbiting platforms on (a) 16 September at 2056 UTC, (b) 17 September at 0150 UTC, (c) 17 September at 1146 UTC, and (d) 17 September at 2138 UTC (2003; from NRL 2007).

Infrared satellite imagery at 1345 UTC and 1945 UTC 17 September (∼Hours 114.5 and 120.5 of the analysis, Figs. 126e–f) suggests a weakening of the influence of the midlatitude trough on Isabel. Indeed, microwave satellite imagery at 2138 UTC 17 September (∼Hour 122 of the analysis, Fig. 127d) provides evidence of a decreasing influence of environmental vertical wind shear as strong, banded convection once again encircles the storm center.

The motion-relative wind profiles in the RF and LR quadrants (Fig. 128a) during and after (Hours 96 and 120, respectively) depict the influence of environmental vertical wind shear has led to a small increase in R_{max} and an increase in the storm intensity

(V_t). Following the increase of V_t, a return of asymmetric convection was observed as depicted by Fig. 128b. As with the first Isabel interaction, R_{34} increased in both the RF and LR quadrants (57 km and 40 km, respectively). By contrast to the first Isabel interaction, these R_{34} increases may be attributed to both the V_t and R_{max} increases in each quadrant.

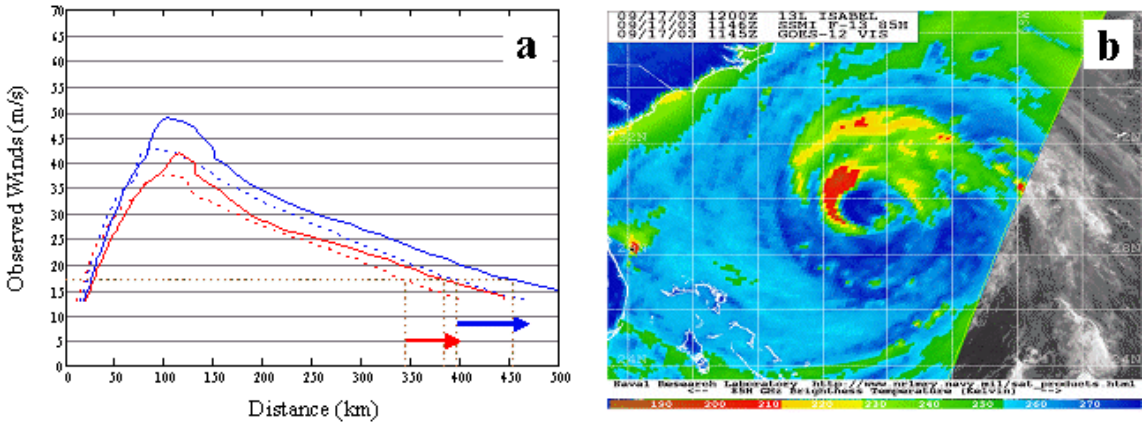

Figure 128 (a) Motion-relative wind profiles for Hurricane Isabel at Hour 96 (dashed lines) and Hour 120 (solid lines) for the RF and LR quadrants (blue and red lines, respectively), and (b) microwave satellite imagery (85 GHz) for Hurricane Isabel from DMSP on 17 September at 1146 UTC (2003; from NRL 2007).

In summary, Hurricane Isabel experienced environmental vertical wind shear due to the interaction with a midlatitude baroclinic system. In the first Isabel interaction, a highly symmetric structure was transformed into an asymmetric structure with a more rapid decrease of V_t in the LR quadrant than in the RF quadrant. This increase in southwesterly environmental vertical wind shear across Isabel was clearly the catalyst that triggered the structure change from a stable, symmetric annular hurricane to a storm with asymmetric convection. In the second Isabel interaction, the existing inner-core asymmetries continued, but with small V_t increases in both RF and LR quadrants. For both Isabel interactions, the inner- and outer-core structures (R_{max} and R_{34}, respectively) were significantly increased. Given the large V_t decreases (decreases of approximately 20 m s^{-1}), the R_{34} increases in the RF quadrant (68 km and 57 km, respectively) and LR quadrant (53 km and 40 km, respectively) may be directly attributed to the increases in R_{max}. In contrast to the Fabian interactions, the R_{34} radii of Isabel became more asymmetric in response to the environmental vertical

wind shear. However, Isabel may be considered a special case since this tropical cyclone had a highly symmetric annular structure prior to the influence of southwesterly environmental vertical wind shear.

3. Ophelia (2005)

Ophelia became a named storm by 0600 UTC 7 September at 27.9°N, 78.8°W in the western North Atlantic (north of the Bahamas). After moving north-northwestward for 12 h, Ophelia drifted southwestward for 24 h along the east coast of Florida. Ophelia strengthened into a hurricane by 1800 UTC 9 September, and then moved northeastward until 0000 UTC 11 September. Ophelia then made a tight clockwise loop for 30 h over the Atlantic east of Georgia, and then moved northwestward on 13 September. Ophelia moved northeastward along the outer banks of North Carolina on 14–15 September before heading back over the open waters of the western North Atlantic. H*Wind analyses for Ophelia became available at 0730 UTC 7 September and at regular increments until 1930 UTC 17 September.

The analysis period of vertical wind shear will be from 0730 UTC 8 September (hereafter referred to as Hour 0 of the analysis) to 0730 UTC 11 September (Hour 72) as Ophelia moved northeastward along the southeast coast of the United States during the portion of the life cycle when Ophelia first reached hurricane strength. At Hour 0, Ophelia had a tangential wind speed (V_t) of 22 m s^{-1} with azimuthal-average R_{max} and R_{34} values of 31 km and 79 km, respectively (Fig. 129).

Microwave satellite imagery at 0133 UTC 9 September (∼18 h of the analysis, Fig. 130a) indicates strong convection near the storm center in the southwest quadrant and an absence of convection farther from the center. Water vapor satellite imagery at 2045 UTC 8 September, and 0245 UTC and 0845 UTC 9 September (∼Hours 13.5, 19.5, and 25.5 of the analysis, Figs. 131a–c) depicts the movement of a midlatitude system across the Midwest toward the east coast of the United States. During the first 24 h of the analysis, Ophelia only experienced small changes in intensity and structure. Strong convection near the storm center only resulted in a R_{max} decrease of 3 km while the R_{34} increased by 20 km (Fig. 129). In conjunction with the R_{max} decrease, Ophelia's intensity (V_t) increased by 2 m s^{-1}.

Water vapor satellite imagery at 1445 UTC and 2045 UTC 9 September, and 0245 UTC, 0845 UTC, 1445 UTC, and 2045 UTC 10 September (∼Hours 31.5, 37.5, 43.5,

49.5, 55.5, and 61.5 of the analysis, Figs. 131d-f and 132a–c) indicates a deepening of the midlatitude trough and an increased interaction with Ophelia as suggested by the elongation of atmospheric moisture to the northeast of the storm center. In conjunction with the increasing vertical wind shear associated with the midlatitude trough, microwave satellite imagery at 1523 UTC 9 September, and 0121 UTC, 0659 UTC, and 1743 UTC 10 September (∼Hours 32, 42, 47.5, and 58 of the analysis, Figs. 130b–e) depicts an increase in strong convection in the downshear (or northeast) quadrant of the storm. During this interaction of southwesterly environmental vertical wind shear with Ophelia, V_t increased from 23 m s^{-1} to 32 m s^{-1} and R_{max} temporarily increased from 28 km to 68 km before decreasing to 43 km (Fig. 129).

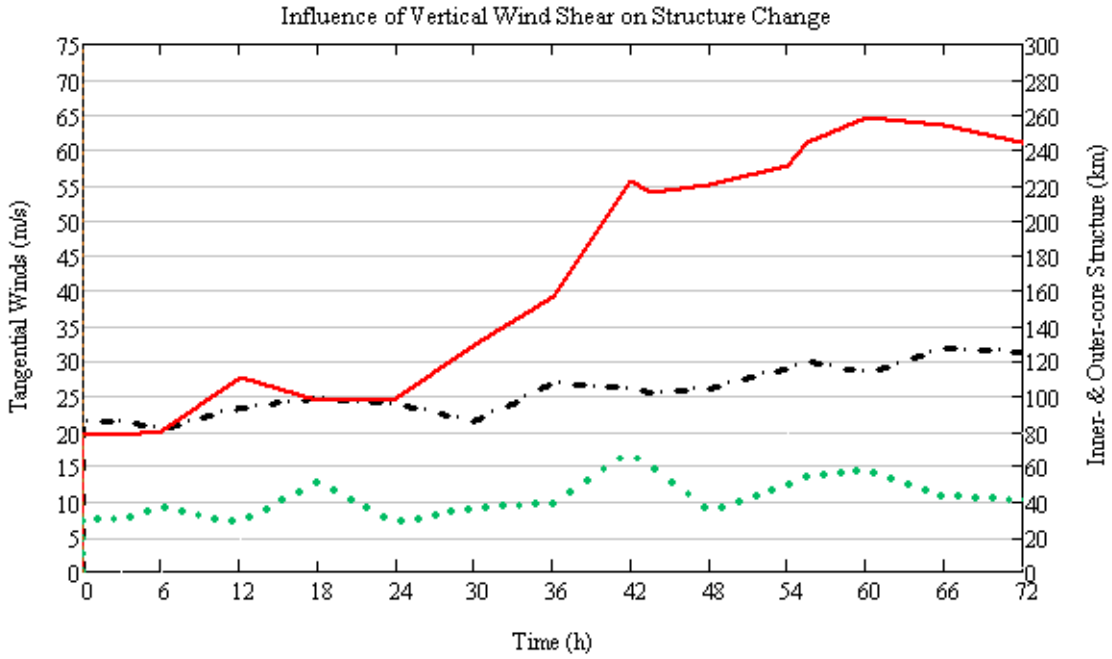

Figure 129 Time series of structure change for Hurricane Ophelia (2005) from 8 September at 0730 UTC (Hour 0) to 11 September at 0730 UTC (Hour 72) as in Fig. 51.

The motion-relative wind profiles in the RF and LR quadrants (Fig. 133a) during and after (Hours 12 and 66, respectively) depict the influence of environmental vertical wind shear has led to an increase in R_{max} and an increase in the storm intensity (V_t). As with the two Fabian interactions, R_{34} increases occurred in both RF and LR quadrants (83 km and 144 km, respectively).

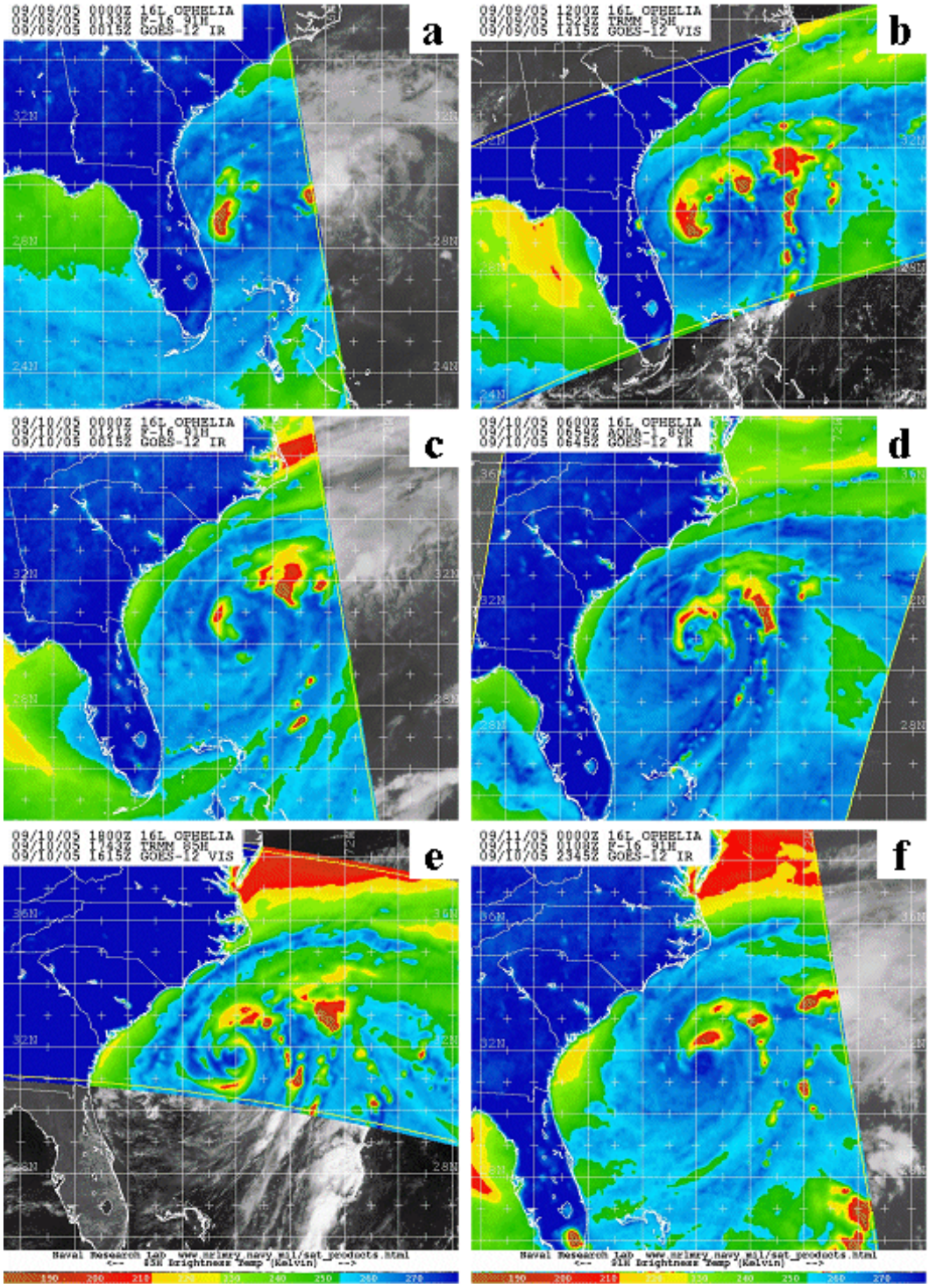

Figure 130 Microwave satellite imagery (85-91 GHz) for Hurricane Ophelia from Aqua, TRMM, and DMSP polar orbiting platforms on (a) 9 September at 0133 UTC, (b) 9 September at 1523 UTC, (c) 10 September at 0121 UTC, (d) 10 September at 0659 UTC, (e) 10 September at 1743 UTC, and (f) 11 September at 0108 UTC (2005; from NRL 2007).

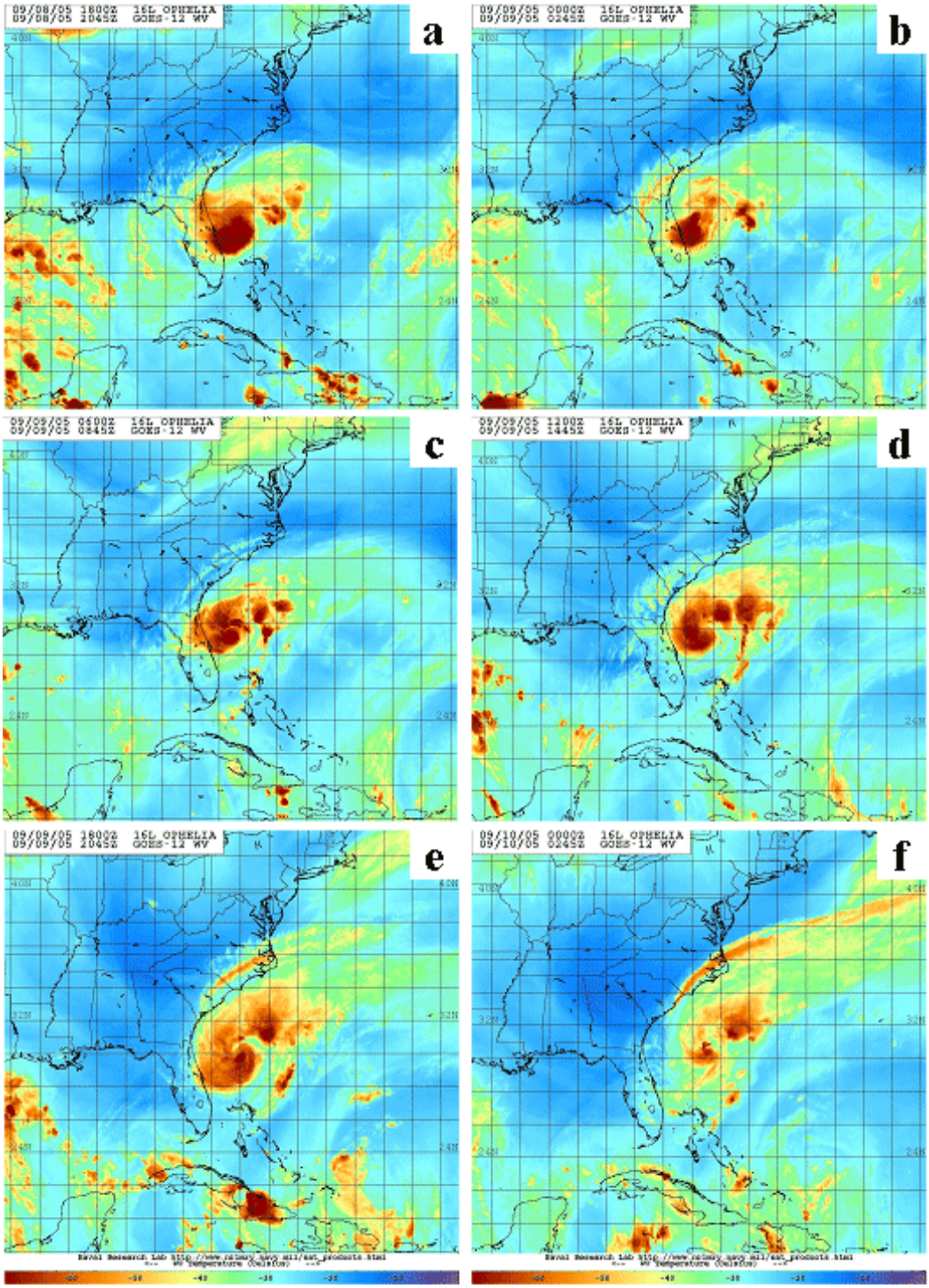

Figure 131 Water vapor satellite imagery for Hurricane Ophelia from the GOES-East platform on (a) 8 September at 2045 UTC, (b) 9 September at 0245 UTC, (c) 9 September at 0845 UTC, (d) 9 September at 1445 UTC, (e) 9 September at 2045 UTC, and (f) 10 September at 0245 UTC (2005; from NRL 2007).

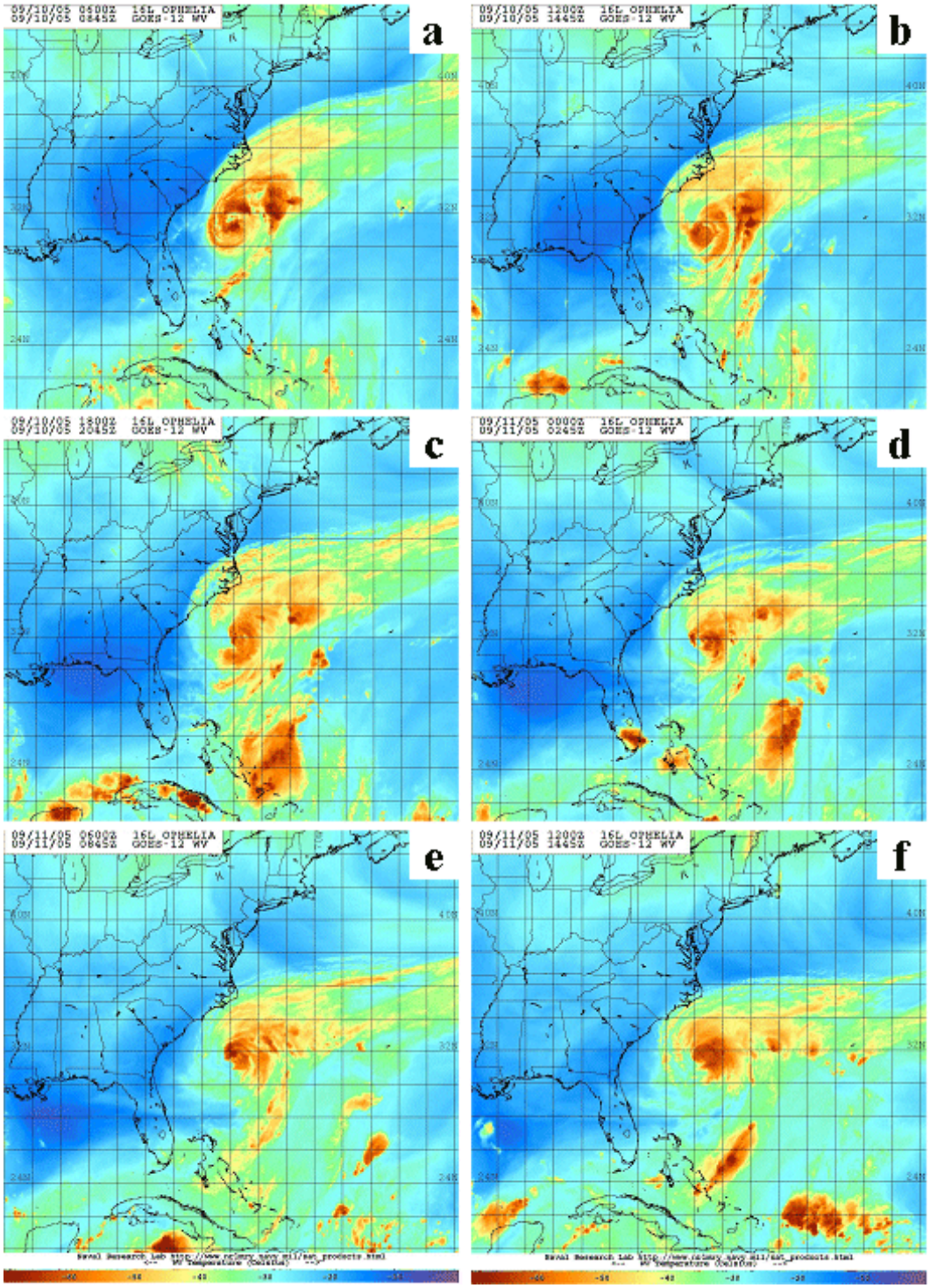

Figure 132 Water vapor satellite imagery for Hurricane Ophelia from the GOES-East platform on (a) 10 September at 0845 UTC, (b) 10 September at 1445 UTC, (c) 10 September at 2045 UTC, (d) 11 September at 0245 UTC, (e) 11 September at 0845 UTC, and (f) 11 September at 1445 UTC (2005; from NRL 2007).

As with the Fabian interactions, intermediate wind profiles suggest a delayed increase of R_{34} in the LR quadrant, perhaps as the momentum associated with convection was advected around the storm center (Fig. 133b). These R_{34} increases may be attributed to both the V_t and R_{max} increases in each quadrant, since the slope of each profile remained similar following the R_{34} increases.

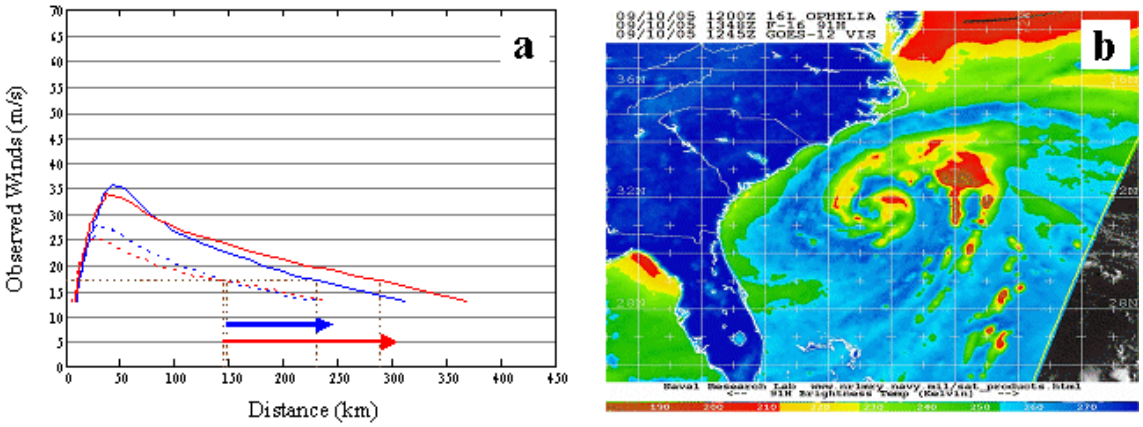

Figure 133 (a) Motion-relative wind profiles for Hurricane Ophelia Hour 12 (dashed lines) and Hour 66 (solid lines) for the RF and LR quadrants (blue and red lines, respectively), and (b) microwave satellite imagery (91 GHz) for Hurricane Ophelia from DMSP on 10 September at 1348 UTC (2005; from NRL 2007).

Water vapor satellite imagery at 0245 UTC, 0845 UTC, and 1445 UTC 11 September (∼Hours 67.5, 73.5, and 79.5 of the analysis, Figs. 132d–f) indicates the movement of the midlatitude baroclinic system farther to the east of Ophelia. In response to the changing direction of environmental vertical wind shear, microwave satellite imagery at 0108 UTC 11 September (∼Hour 65.5 of the analysis, Fig. 130f) depicts a shift in the convection away from the storm center to the east-northeast of the center. During this period, the inner- and outer-core structures of Ophelia stop increasing in size and begin decreasing slowly (Fig. 129) as this storm begins to move in a tight clockwise loop before heading toward the North Carolina coast.

In summary, Hurricane Ophelia experienced environmental vertical wind shear due to the interaction with a midlatitude baroclinic system. As with the Fabian interactions, Ophelia had a proportionally larger R_{34} increase in the LR quadrant than in the RF quadrant (1.7 to 1), which resulted in a larger outer-core structure in the LR quadrant from the increase in vertical wind shear. It is hypothesized that stronger

winds are advected around the storm center from the RF quadrant to the LR quadrant as a delayed response to structural asymmetries resulting from environmental vertical wind shear, and thus leads to axisymmetrization of the outer-core structure. In contrast to the Fabian interactions, the inner-core structure of Ophelia did not become more asymmetric as a result of vertical wind shear. Also unlike the two Fabian interactions and the first Isabel interaction, V_t increased for Ophelia which may have been the result of a weaker, smaller tropical cyclone being strengthened by enhanced outflow from the storm center as the baroclinic trough approached.

4. Conclusions for Vertical Wind Shear

The analyses of individual tropical cyclone case studies of environmental vertical wind shear have revealed that the interactions with midlatitude baroclinic systems resulted in increases in the R_{max} and R_{34}. As expected, convection was enhanced in the downshear quadrant of the tropical cyclone under the influence of vertical wind shear, e.g., for Fabian at Hours 42.5 and 102.5, Isabel at Hours 79.5 and 102.5, and Ophelia at Hour 47.5 (Figs. 119b, 47b, 124, 127b, and 130d, respectively). With the exceptions of the second Isabel interaction and the Ophelia interaction, V_t decreased when vertical wind shear was present. As hypothesized in Chapter IV.A, axisymmetrization of the storm structure may have played a role in the Isabel and Ophelia V_t increases. In the case of Ophelia, the V_t increase may have also been the result of a weaker, smaller tropical cyclone being strengthened by enhanced outflow from the storm center as a baroclinic trough approached.

In all cases, increases of R_{max} was accompanied by R_{34} increases since the slope of the profile was similar before and after the influence of environmental vertical wind shear, i.e., minimal changes in the exponent x of the modified Rankine vortex in Eq. (20) occurred. Whereas the R_{max} increases in the RF and LR quadrants were similar, the changes to R_{34} in the RF and LR quadrants were quite different. The range of R_{34} increases were 23–83 km for the RF quadrant and 40–144 km for the LR quadrant. That is, on average a larger R_{34} increase occurred in the LR quadrant than in the RF quadrant following the influence of vertical wind shear. Indeed, for the two Fabian interactions and the Ophelia interaction, the ratios of R_{34} increases for the LR quadrant compared to the RF quadrant were 2.7 to 1, 1.6 to 1, and 1.7 to 1, respectively. These larger R_{34} increases in the LR quadrant generally resulted in a reduction of asymmetries that existed in the outer-core structure prior to the influence of environmental

vertical wind shear. It is hypothesized that stronger winds associated with enhanced convection were advected cyclonically around the storm center from the RF quadrant to the LR quadrant in a delayed response, and thus led to axisymmetrization of the outer-core structure.

Whereas the outer-core structure asymmetries for the two Fabian interactions and the Ophelia interaction were reduced, the Isabel interaction was the exception in that outer-core structure asymmetries increased. Isabel may be considered a special case since this tropical cyclone had a highly symmetric annular structure prior to the influence of southwesterly environmental vertical wind shear. This increase in southwesterly environmental vertical wind shear across Isabel was clearly the catalyst that triggered the structure change from a stable, symmetric annular hurricane to a storm with asymmetric convection. For both Isabel interactions, R_{max} and R_{34} had considerable increases. In contrast to the Fabian and Ophelia interactions, the smaller R_{34} increases in the LR quadrant (53 km and 40 km, respectively) compared to the RF quadrant (68 km and 57 km, respectively) increased the asymmetries of the outer-core structure.

Environmental vertical wind shear appears to influence tropical cyclone structure in two ways. Similar to the findings on asymmetric convection in Chapter IV.B, the downshear convective asymmetries in the eyewall and spiral rainbands result in an expansion of inner-core structure (R_{max}). In turn, the R_{max} increase results in a R_{34} increase, and thus represents the primary factor in outer-core structure (R_{34}) increases. The enhanced outflow from the storm may be a second factor that influences storm structure during environmental vertical wind shear, since the R_{34} increases associated with asymmetric convection for the cases in this section are larger than for the cases in Chapter IV.B. That is, the cases in this section suggest a more favorable environment for sustained outer-core structure (R_{34}) increases, and thus results in the potential of a larger outer-core structure. By contrast to the cases of asymmetric convection in Chapter IV.B, R_{max} and R_{34} increases associated with tropical cyclone interaction with environmental vertical wind shear are often sustained following that interaction, i.e., the R_{max} and R_{34} radii generally did not decrease following the storm interaction with environmental vertical wind shear.

The evolution of tropical cyclone structure changes associated with environmental vertical wind shear are illustrated in Fig. 134.

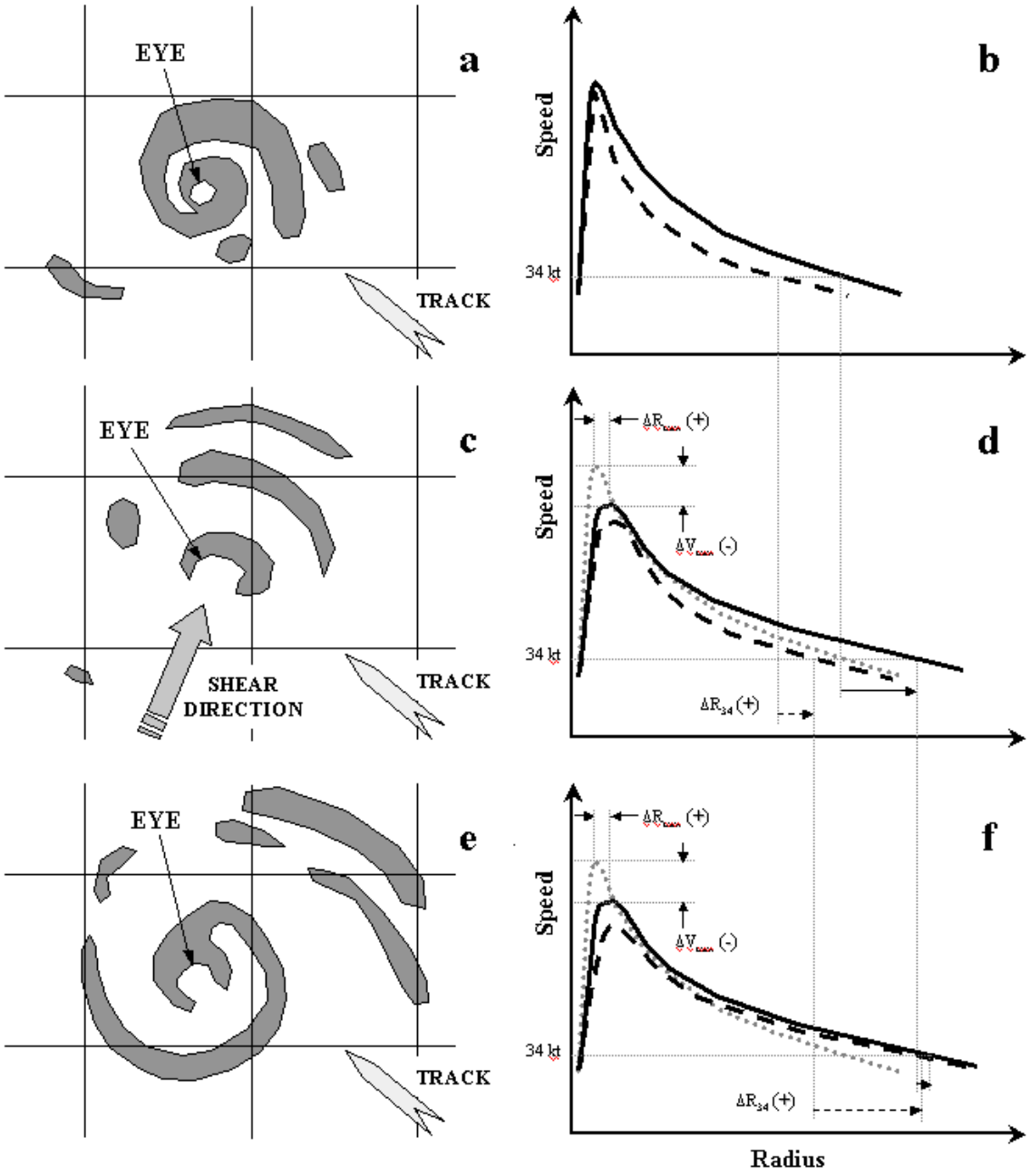

Figure 134 Schematic illustration of (a, c, and e) convection and (b, d, and f) radial profiles of tangential wind structure changes associated with environmental vertical wind shear at time $t - \Delta t$, t, and $t + \Delta t$, respectively. The dashed curves (b, d, and f) represent the azimuthal-average wind profile at time $t - \Delta t$. The solid and dashed curves (b, d, and f) represent the radial profiles of tangential wind for the RF and LR quadrants, respectively. The gray, dotted curves (d and f) represent wind profile of the RF quadrant at time $t - \Delta t$.

In Figs. 134a–b, a tropical cyclone with typical convection and radial wind profiles prior to the presence of environmental vertical wind shear is illustrated. As a midlatitude baroclinic trough introduces vertical wind shear across the storm structure, convection is enhanced (suppressed) in the downshear (upshear) portion of the eyewall and spiral rainbands (Fig. 134c). As with the cases of asymmetric convection of the first mode in Fig. 100a of Chapter IV.B, the inner-core structure (R_{max}) increases and V_t decreases in response to increasing convective asymmetries. As expected, an increase in R_{34} accompanied the R_{max} increase (Fig. 134d). However, the R_{34} increase is initially larger in the RF quadrant (downshear) than in the LR quadrant (upshear) of the storm (Fig. 134d). As the midlatitude baroclinic system moved away from the tropical cyclone and the environmental vertical wind shear decreased, the convective structure tended to become more symmetric (Fig. 134e). The outer-core structure (R_{34}) also becomes more symmetric as depicted by the radial profiles of tangential wind in Fig. 134f. This symmetry in the outer-core structure is achieved by a greater R_{34} increase in the LR quadrant than in the RF quadrant. By contrast, the inner-core tangential wind speed (V_t) is generally smaller in the LR quadrant than the RF quadrant following the effects of environmental vertical wind shear.

V. CONCLUSIONS

A. SUMMARY

Hurricanes are among the most costly natural disasters in the United States as a result of strong winds (Pielke and Landsea 1998) and flooding (Elsberry 2002). In recent years, the landfall of large hurricanes in densely populated areas along the Gulf Coast of the United States has increased the awareness that tropical cyclone structure plays an important role in the destructive potential of a storm (Powell and Reinhold 2007). The tropical cyclone structure change can be quite large over relatively short periods of time. While prediction of tropical cyclone motion has steadily improved over the past two decades, comparatively lesser progress has been made toward the understanding of intensity or structure change until recent work such as Montgomery and Smith (2013). Without a complete understanding of these structure variations, accurate wind and surge forecasting for tropical cyclone damage potential will remain elusive.

In the Unites States, the emergency management community requires warnings of when sustained (one-minute average) surface winds exceeding gale-force ($\geq$34 kt) winds will arrive at a location in advance of a tropical cyclone. That is, the objective is to give the public sufficient time to complete all disaster preparedness activities prior to the onset of gale-force winds and the often coincident heavy precipitation, so that these activities (including evacuation or moving to a secure shelter) are completed safely. While an accurate understanding of structure change for landfalling cyclones is a concern to populated coastal regions, they are equally important to commercial shipping vessels, and the airplanes and warships of the United States Air Force and Navy and those of its allies.

The mechanisms leading to structure change in a tropical cyclone can be categorized as internal, external, or both. Vortex Rossby waves are a prime example of an internal mechanism since their horizontal propagation is limited by the stagnation radius where the radial group velocity goes to zero (Wang 2002a). Environmental flow, vertical wind shear, upper-tropospheric troughs, sea-surface temperature, ocean heat content, sea spray, and frictional drag (e.g., land) are all examples of external mechanisms that can affect tropical cyclone structure. Some external mechanisms directly impact tropical cyclone structure (e.g., vertical wind shear) while others affect the structure indirectly through intensity change (e.g., sea-surface temperature).

Changes to tropical cyclone structure by spiral rainbands and asymmetric convection can be categorized as both internal and external mechanisms.

The unique dataset used in this dissertation to study outer wind structure change is from the NOAA-AOML H*Wind (Powell and Houston 1996, Powell et al. 1996, 1998). The H*Wind grid is centered on the storm and has a horizontal grid spacing of approximately 6 km in a domain of 920 km by 920 km. The H*Wind analyses incorporate all available surface observations, such as ships, buoys, coastal platforms, surface aviation reports, and reconnaissance aircraft data adjusted to the surface (NOAA 2007). Observations that are fit to the analysis framework include data transmitted from NOAA P-3 research aircraft equipped with the SFMR flown by the HRD, and the AFRES C-130 reconnaissance aircraft flight-level winds. Additional sources of data include remotely sensed winds from the polar-orbiting satellite platforms of SSM/I and ERS, the microwave imagers of QuikScat and TRMM, and GOES drift winds from the geostationary satellites. All data are processed to conform to the common height of 10 m and an averaging period of 1-minute maximum sustained wind speed. More information on the techniques and limitations of the H*Wind analyses is found in Chapter II.

An original software program, referred to as TC-SAT, was written to analyze tropical cyclone structure using a Windows GUI and more than 13,000 lines of Visual Basic code. The software was designed to utilize the raw H*Wind analyses to produce the types of analyses required for this research and future work on tropical cyclone structure. The software GUI was designed to allow the user maximum flexibility in extracting available H*Wind analyses and producing analyses of choice. Greater detail on the various analyses available from TC-SAT is found in Chapter II.

Elsberry and Stenger (2008) tested these simple conceptual ideas of outer wind structure changes (discussed in Chapter I) through application of the tropical cyclone life cycle intensity change definitions of Elsberry et al. (2007) displayed in Fig. 9. The Elsberry et al. (2007) formation Stage I is limited to V_{max} less than 34 kt. Storm intensification from 34 kt to the first intensity peak (or end of this stage) is defined as Stage II. After the first intensity peak, if the storm intensity decays by at least 10 kt and then re-intensifies by at least 10 kt, it is defined as a decay and re-intensification cycle that is labeled as Stage IIa. If the re-intensification criterion of Stage IIa is not met, the storm is decaying and classified as Stage III. In addition, Stage II is subdivided into rapid or non-rapid intensification, and Stage IIa is subdivided into a

decay followed by either a rapid or a non-rapid intensification. Rapid intensification is defined here as an increase equal to or greater than 15 kt in 12 h. A 12-h interval was selected to better capture rapid intensification events during storm intensity cycles and exclude intensity fluctuations that occur over shorter periods of time.

Histograms of 12-h axisymmetric outer wind structure changes in terms of R_{34} values are shown in Figs. 11–13. After eliminating all cases that involve landfall, or where insufficient analyses were available to compute the 12-h structure change, 400 cases remained to evaluate R_{34} structure variability during the 2003–2005 Atlantic tropical cyclone seasons. A considerable fraction of R_{34} changes over 12 h during the intensification or re-intensification phases are decreases rather than the increases that would be expected from the simple conceptual models discussed in Chapter I. Similarly, a considerable fraction of R_{34} increases over 12 h are found during the decay phases when decreases might have been expected from the simple conceptual model. However, Merrill (1984, 1988) had suggested that the radii of the surface closed isobars increase during the decay phase and the Knaff et al. (2008) model has a latitudinal dependence that may predict R_{34} increases at latitudes greater the 25°N where decay is expected. Thus, these axisymmetric (and quadrant-by-quadrant, not shown) R_{34} changes are more complicated than the simple conceptual model that directly correlates R_{34} changes to intensity changes.

These life cycle histograms may indicate two possibilities: (i) structure change is random and unpredictable; or (ii) identifiable internal and external mechanisms exist that lead to the observed structure changes. Through analysis of individual storm cases as in Fig. 3, structure change mechanisms have been studied to demonstrate the second possibility applies in the majority of the cases with large changes. Through examination of tropical cyclones that undergo similar structure changes, it was possible to isolate the most probable mechanism(s) that lead to the changes observed.

A characterization the observed variability in the R_{max}, V_{max}, and R_{34} was conducted that can also provide bounds to perturb tropical cyclone vortex initial conditions in an ensemble model (the second goal of this research). Few research projects have attempted to quantitatively assess the observed variability of these three instrumental parameters in order to synthetically represent a tropical cyclone in the initial conditions of a numerical weather prediction model. Understanding the variability of these three parameters is essential to building an ensemble capability that will improve tropical cyclone structure forecasting.

The predictability of a numerical weather model is primarily limited by: (i) uncertainty in the physical laws that govern atmospheric motions resulting from numerical approximations and sub-grid parameterizations; (ii) uncertainty in the specification of initial conditions arising from systematic and random errors in the observations, inhomogeneity in coverage and lack of sufficient density to represent spatial and temporal scales being resolved in the model, and errors in the approximations of the data assimilation system; (iii) uncertainty in the specification of lateral boundary condition updates for a limited-area model that result from the coarser mesh model having poorer horizontal and vertical resolution, significantly different physical parameterizations, or inadequate handling of the interface between the two grids; and (iv) uncertainty caused by the ability of the model to resolve topography within the domain, or the interaction of topography with the model lateral boundaries (Thompson 1957; Warner et al. 1997; Zhu and Thorpe 2006). Lorenz (1963) identified the chaotic nature of weather prediction that causes a numerical modeling system to be sensitive to the initial conditions. As such, Lorenz (1963) theorized that there is a near-total loss in model predictive skill after a period of 7 to 14 days.

The data-sparse regions of the vast oceanic areas suggest the need to synthetically represent the structure of a tropical cyclone in the initial conditions of a numerical prediction model. While many past numerical simulation studies have attempted to accurately represent the initial tropical cyclone vortex with approximations such as the modified Rankine profile, these methods are limited by their deterministic nature. In reality, tropical cyclone vortex structure has a considerable amount of variability that can not be adequately described by a simple deterministic approach. Instead, capturing the uncertainty of a tropical cyclone structure, intensity, and track requires an ensemble approach, a viewpoint consistent with Nguyen et al. (2008) and Shin and Smith (2008).

Stenger and Elsberry (2008) documented the observed variability of the R_{34} outer-core radius of tropical cyclones in the western North Atlantic from 2003 through 2005 using Saffir-Simpson categories of hurricanes and the tropical cyclone life cycle intensity change definitions of Elsberry et al. (2007) displayed in Fig. 9. In Fig. 21, the H*Wind R_{34} wind radii are plotted for each Saffir-Simpson storm category and for each Cartesian quadrant. The box plot widths are proportional to the sample size used to compute the statistics. All land interaction cases within the R_{34} wind radii have been identified and eliminated from the plots. In addition, all trivial "zeros"

have been eliminated from the plots, i.e., cases with a maximum wind speed less than tropical storm strength (<34 kt).

The most rapid R_{34} size increase relative to a prior life cycle stage in Fig. 22 is noted during the Stage IIa (S-IIA) intensity decay (D) phase, which occurs when the intensity temporarily decreases before again increasing in a secondary eyewall formation (Fig. 9c). This result is consistent with the findings of Terwey and Montgomery (2008) in their idealized high-resolution numerical simulation of secondary eyewall replacement. Their numerical study appeared to predict an outer wind radii increase during the S-II (D) phase of storm development.

Whether the re-intensification is non-rapid (N) or rapid (R) during Stage IIa (S-IIA) does not affect the R_{34} size, although the R_{34} value is slightly smaller in the SW quadrant (Fig. 22). During the decay Stage III (S-III), most of the Atlantic tropical cyclones will be moving toward the northeast. Therefore, the most relevant R_{34} comparison is between the SE and NW quadrants where the background southwesterly steering flow is expected to be adding to or opposing the vortex flow, respectively. Indeed, the median R_{34} value in the SE quadrant is slightly larger than in the NW quadrant, but the more significant difference may be the larger fraction of small (<200 km) R_{34} values in the NW quadrant. In the SE quadrant, this is inconsistent with the size decrease during the decay stage implied by the modified Rankine vortex, but is consistent with the forecaster rule-of-thumb that an expansion of the tropical cyclone R_{34} wind radii will occur during the decay phase of the tropical cyclone.

The observed variability of V_t, R_{max}, and R_{34} of tropical cyclones in the western North Atlantic from 2003 through 2005 were assessed in a motion-relative coordinate system. In motion-relative coordinates, the vortex structure in the LF, RF, RR, and LR quadrants can be directly compared without the added contribution from the storm motion.

Objective analyses of the 10 m surface wind speed based on the H*Wind program for the different stages of the life cycle (Fig. 9) of Atlantic tropical cyclones during the 2003–2005 hurricane season were conducted. The primary focus was on the outer-core structure changes or size changes represented by the R_{34} radius. Contrary to the simple conceptual model that intensification is accompanied by increases in R_{34}, about 30 percent of intensifying cyclones had decreasing values of R_{34} (Fig. 12). During the decay stage (Fig. 13b), about one half of the cyclones had decreases in R_{34} and about

one quarter had increases in R_{34}, which then differs from the forecaster rule of thumb that tropical cyclones expand in size during the decay. Box plots of the R_{34} radii document significantly larger R_{34} values progressing from the Tropical Storm stage to the Category 1 hurricanes and then to the Category 2 hurricanes (Fig. 21). Further intensification does not lead to significantly larger R_{34} values; indeed, a small sample of Category 5 hurricanes appears to have smaller R_{34} values.

Various assessments of the characterizations of the inner-core vortex in terms of R_{max} and V_t, and the outer-core vortex in terms of R_{34} have been made for different stages of the life cycle. Although with considerable scatter, the R_{max} and V_t have the expected relationship that smaller R_{max} values are associated with larger V_t near the center, and especially for rapid intensification cases. The relationship of the R_{34} to the V_t and R_{max} is more complex and varies with stage of development. For the Stage II intensification and for R_{34} <150 km, the R_{34} has little association with V_t, but has larger R_{34} values for larger R_{max}. For R_{34} >150 km, larger R_{34} values are associated with larger V_t, but not larger R_{max}. During the decay and re-intensification Stage IIa, the above relationship for R_{34} <150 km are generally valid. For R_{34} >150 km, larger R_{34} values were associated with larger R_{max} values, which may be associated with a secondary eyewall formation. Although the Stage III decay had the largest correlation between V_t and R_{34}, this sample had different characteristics for R_{34} <150 km and R_{34} >150 km.

An assessment of the azimuthal-average values for exponent x in the modified Rankine vortex of Eq. (20) for the different stages of the life cycle (Figs. 26, 30, 34, 38, 42, and 46) yield a mean value of 0.56–0.58, whereas the standard deviation decreases from 0.21 to 0.13 as the storm progresses from Stage II ($\sim$0.21) to Stage IIa decay and non-rapid intensification (0.17), and then to Stage IIa rapid intensification and Stage III decay (0.13). For the Stage II and Stage IIa periods of the life cycle, the right (left) quadrant outer-core structures (as measured using R_{34}) were generally larger (smaller), whereas the LF (RR) quadrant had the largest (smallest) R_{34} values for the Stage III decay. Nearly 100 percent of the outer-core structure asymmetries can be accounted for by the addition or subtraction of the average tropical cyclone motion vector during Stage IIa decay. For the Stage II non-rapid intensification, and Stage IIa non-rapid and rapid intensification, only a portion (80 percent, 60 percent and 70 percent, respectively) of the outer-core structure asymmetries can be explained by the addition or subtraction of the storm motion vector. The greatest amount of

outer-core structure asymmetries were observed for Stage II rapid intensification since only 40 percent of the asymmetries can be explained by the addition or subtraction of the storm motion vector. The smaller mean and the ∼30 percent reduction in the standard deviation for the right quadrants compared to the left quadrants for the rapid intensification phases of Stage II and Stage IIa indicate a greater probability of larger R_{34} sizes on the right side of the tropical cyclone for these stages of the life cycle and may be a contributing factor in rapid intensification. Greater detail on the observed variability of V_t, R_{max} and R_{34} of tropical cyclones in the western North Atlantic is found in Chapter III and Appendix E.

In summary, the large variability between the Atlantic tropical cyclone inner- and outer-core structure characteristics make the use of simple wind profile relationships inadequate to represent the overall structure in all stages of the life cycle. In order to make significant improvements in the forecast of tropical cyclone intensity and track, future work will require investment in ensemble techniques to better capture the observed variability and uncertainty of the inner- and outer-core storm structures in the initial conditions of numerical weather prediction models.

In Chapter IV, individual storm analysis has been applied by examining cases of large R_{34} changes that may be explainable in terms of the internal or external mechanisms that have been proposed for structure changes (see Chapter I). The main objective of this research has been to better understand the internal and external mechanisms that lead to significant variability in tropical cyclone wind structure, especially in the outer-core region. Secondary eyewall formation and enhanced asymmetric near-core convection have been found to be two internal mechanisms that lead to large structure changes. Upper-tropospheric trough interaction and the associated vertical wind shear, and peripheral and near-core land interaction, have been found to be two external mechanisms of interest in structure change. Although it has not been possible to fully isolate the impact each of these mechanisms has on structure change in this observational study, this research is a first step in using special observations to gain a better understanding of which mechanism contributed to cases with significant tropical cyclone structure variations.

The analyses of individual case studies of complete and partial secondary eyewall replacement have revealed two modes of tropical cyclone structure changes. These two modes are represented by the conceptual radial wind profiles in Fig. 85. The first mode (Fig. 85a) was observed during complete and partial secondary eyewall replacement

for Stage IIa and Stage III of the life cycle as defined in Fig. 9. For this mode, the R_{max} increases and V_{max} (denoted as maximum tangential wind speed, V_t, in the discussions of Chapters III and IV) decreases in association with a complete or partial eyewall replacement cycle. The outer-core structure (R_{34}) also expands during the complete or partial eyewall replacement cycle, which includes a small and time-lagged R_{34} increase following the inner-core (R_{max}) change. This first mode is consistent with the traditional explanation for concentric eyewall replacement as presented by Willoughby et al. (1982).

In these first mode cases (Fig. 85a), the average decrease in V_t was 7 m s^{-1} with a range of 6 m s^{-1} to 11 m s^{-1}. The R_{max} approximately doubled during these first mode cases, except for the Fabian eyewall replacement cycle that had a three-fold R_{max} increase and for the first Wilma eyewall replacement cycle that had a five-fold R_{max} increase. The average R_{max} increase was 28 km with a range from 6 km to 56 km.

The average R_{34} increase for these first mode cases (Fig. 85a) was 59 km with a range from 20 km to 109 km. The R_{34} increases for the first mode were generally larger than those of the second mode (an average 59 km versus 45 km) since the exponent x remains nearly constant. Indeed, the average exponent x increase was only 0.08 with a range of -0.02 to 0.21 during these first mode cases. Applying Eq. (20) to the partial eyewall replacement of Rita, the V_t decrease by 10 m s^{-1} has a 1-to-1 impact on the right side of the equation, whereas the 26 km increase in R_{max} with an exponent x = 0.47 has an approximate 2.4-to-1 impact. Thus, the R_{max} increase compensates for the V_t decrease and the resultant effect is a R_{34} increase of 52 km. These R_{34} increases are significant outward expansions, especially when a tropical cyclone is approaching landfall.

Except for the partial eyewall replacement of Ivan, the second mode (Fig. 85b) was only observed during complete secondary eyewall replacement and for Stage IIa of the life cycle as defined in Fig. 9. For this mode, the R_{max} and V_{max} both increase in association with a eyewall replacement cycle. The outer-core structure (R_{34}) also expands during this eyewall replacement cycle, and often continues to expand in a time-lagged response of 6 h or more following the inner-core (R_{max}) change.

For the second mode (Fig. 85b), the observed average increase in V_t was 8 m s^{-1} with a range of 2 m s^{-1} to 13 m s^{-1}. Rapid intensification occurred during an eyewall replacement cycle when strong spiral rainband convection was in close proximity to

the secondary eyewall. Although these convective asymmetries were not present or were much weaker for the remainder of the case studies in the second mode, the cases with convective asymmetries suggest that the process of axisymmetrization may be a potential mechanism for rapid storm intensification during eyewall replacement. The R_{max} doubled or tripled (e.g., Hurricane Katrina) during eyewall replacement for the second mode. The observed average R_{max} increase was 23 km with a range from 12 km to 37 km, which is very similar to the first mode.

The observed average R_{34} increase during eyewall replacement for the second mode (Fig. 85b) was 45 km with a range from 7 km to 99 km. The largest R_{34} increases occurred when rapid intensification (i.e., large V_t increases) was combined with a R_{max} increase. Indeed, this is consistent with Eq. (20) since increases in V_t and R_{max} on the left side of the equation are expected to result in an increase in R_{34} on the right side. However, the other unknown in Eq. 20 is the exponent x, which in the pre-eyewall replacement period for Katrina was equal to 0.31. If this exponent also applied after the eyewall replacement and using the Hour 18 values of $V_t = 46$ m s^{-1} and $R_{max} = 34$ km, the resulting R_{34} would be 807 km, which would be a 539 km increase in the outer-core radius. In reality, the observed R_{34} increase was limited to 71 km, which still represents a significant outward expansion in less than 24 h for a tropical cyclone approaching landfall. This R_{34} increase of 539 km did not occur because the exponent for the outer profile during the eyewall replacement was much larger (0.64 versus 0.31), which implies a more rapid decrease in wind with radius. During eyewall replacement for all cases in the second mode (Fig. 85b), the post-replacement exponent x on average was increased by 0.19 with a range between 0.07 and 0.33. The smallest change in exponent x (0.07 increase) occurred for Ivan's second eyewall replacement, and R_{34} increased by 99 km in 18 h and then continued to increase by 120 km in 24 h. Thus, a "flatter-than-average" outer wind profile existed prior to the second mode of secondary eyewall formation that then became "sharper-than-average" following secondary eyewall formation. This time change in the profile shapes demonstrates that accurately predicting the change in the R_{34} with a fixed value for exponent x during eyewall replacement is not plausible.

For all cases of complete and partial eyewall replacement with the exception of Wilma, the outward (inward) ΔKE_{anom} was correlated with an expansion (contraction) of the R_{max} radius. Indeed, the correlation coefficients for the Fabian, Frances, Ivan, and Katrina cases (0.709, 0.743, 0.642, and 0.775, respectively) suggest a linear

relationship between ΔKE_{anom} and R_{max}. Additionally, the correlation coefficients for the Emily and Rita cases (0.460, and 0.399, respectively) suggest a positive correlation between the ΔKE_{anom} and the R_{max} changes, albeit with a larger spread in the values. Large increases in the radial inflow variance were often observed when strong asymmetric spiral rainband convection existed in close proximity to the primary or secondary eyewall. However, an increase in the R_{34} value was not always observed 6 h or more after the increased radial inflow variance.

The analyses of individual case studies of asymmetric convection also revealed two modes of tropical cyclone structure changes. These two modes are represented by the conceptual radial wind profiles in Fig. 100. The first mode (Fig. 100a) was observed during periods of asymmetric convection for Stage IIa of the life cycle as defined in Fig. 9. This mode was best illustrated for the cases during the annular phase of Isabel (2003). For this mode, the R_{max} increased in association with asymmetric convection, but V_{max} decreased. The outer-core structure (R_{34}) expanded during the inner-core response to asymmetric convection, but then generally had a time-lagged decrease in R_{34} following the inner-core (R_{max}) expansion. For the first mode (Fig. 100a), the average decrease in V_t was 8 m s^{-1} with a range of 4 m s^{-1} to 11 m s^{-1}. The R_{max} increased by 150–200 percent in the presence of asymmetric convection with an average R_{max} increase of 33 km and a range from 25 km to 48 km.

The average R_{34} increase during the inner-core response to asymmetric convection for the first mode (Fig. 100a) was 26 km with a range from −48 km to 89 km. Whereas there are similarities with the first mode of the conceptual model for secondary eyewall formation in Fig. 85a, the time-lagged response in this mode was a contraction even though V_t generally increased following the inner-core expansion. The R_{34} increases for this mode were generally smaller than those for the first mode of the conceptual model for secondary eyewall formation (Fig. 85a) since the exponent x had a larger increase. Indeed, the average exponent x increase was only 0.09 with a range of 0.03 to 0.18 during asymmetric convection. As discussed in the section on secondary eyewall formation, these R_{34} increases may be significant when a tropical cyclone is approaching landfall.

The second mode (Fig. 100b) was only observed during periods of asymmetric convection for Stage IIa and Stage III of the life cycle as defined in Fig. 9. For this mode, R_{max} and V_{max} both increase in association with the presence of asymmetric convection. The R_{max} and V_{max} increases are generally smaller than for the second

mode of the conceptual model for secondary eyewall formation in Fig. 85b. In this case, the outer-core structure (R_{34}) actually has a small net decrease during the inner-core response to the asymmetric convection.

For the second mode (Fig. 100b), the average V_t increase was 6 m s^{-1} with a range from 3 m s^{-1} to 10 m s^{-1}. Rapid intensification occurred during the inner-core response to asymmetric convection for Jeanne (the only case of Stage IIa) when strong spiral rainband convection was in close proximity to the convectively weak eyewall (Figs. 97b–c). As with the second mode for secondary eyewall formation cases, this rapid intensification is consistent with the hypothesis in Chapter IV.A that the process of axisymmetrization may be a potential mechanism for rapid storm intensification during the inner-core response to asymmetric convection. The R_{max} increased by approximately 50 percent in the presence of asymmetric convection, with an average R_{max} increase of 14 km and a range from 13 km to 15 km.

For the second mode (Fig. 100b), the average R_{34} decrease during the inner-core response to asymmetric convection was 17 km with a range from -8 km to -27 km. This is inconsistent with Eq. (20) assuming a fixed value of the exponent x since V_t and R_{max} increases on the left side of the equation are expected to result in a R_{34} increase on the right side. However, the other unknown in Eq. 20 is the exponent x, which in the pre-asymmetric convection inner-core response for Jeanne was equal to 0.25. If this exponent also applied after the asymmetric convection inner-core response and using the Hour 54 values of $V_t = 39$ m s^{-1} and $R_{max} = 61$ km, the resulting R_{34} would be 1628 km, which would be a 1281 km increase in the outer-core radius. In reality, the observed R_{34} decreased by 27 km. This R_{34} increase of 1281 km did not occur because the exponent for the outer profile during the asymmetric convection inner-core response was much larger (0.47 versus 0.25), which implies a more rapid decrease in wind with radius. During asymmetric convection inner-core response for all cases in the second mode (Fig. 100b), the post-response exponent x on average was increased by 0.13 with a range between 0.06 and 0.25. In these second mode cases, tropical cyclones have a "flatter-than-average" profile prior to the response to asymmetric convection, and then have a "sharper-than-average" profile after the response to asymmetric convection. As with secondary eyewall formation, this time variability in the profile shapes demonstrates that accurately predicting the change in the R_{34} with a fixed value for exponent x during asymmetric convection is not plausible.

For all of these cases of asymmetric convection, outward (inward) ΔKE_{anom} were correlated with expansion (contraction) of R_{max}. Indeed, the correlation coefficients during the life cycles of Fabian, Isabel, and Jeanne (0.709, 0.556, and 0.968, respectively) suggest a linear relationship between ΔKE_{anom} and R_{max}. As with secondary eyewall formation, large increases in the radial inflow variance were often observed when strong asymmetric spiral rainband convection existed in close proximity to the eyewall. However, the increase in radial inflow variance was not found to have a good correlation to outer-core structure (R_{34}) changes.

The analyses of individual case studies of peripheral and near-core land interaction revealed that the frictional convergence of the winds in the vicinity of spiral rainbands that intersect the land led to enhanced strong convection that then advected around the eyewall with the spiral rainbands and may have contributed to the secondary eyewall formation by surrounding the eyewall with active spiral rainbands. This sequence of events may also increase the likelihood of secondary eyewall formation by the strong convection causing a disruption in the eyewall as was suggested in the Rita partial eyewall replacement case in Chapter IV.A.2.b. The peripheral land interaction as Wilma approached landfall over southern Florida (see Chapter IV.C.1.c) is the only exception for the cases analyzed in this section. However, Wilma appears to be a special case. Wilma's large R_{max} of 60+ km and its fast translation speed of nearly 20 kt prior to this second case of land interaction, which are approximately twice as large as the other cases in which a secondary eyewall formed in conjunction with landfall. Thus, it is hypothesized that a large R_{max} and fast translation speed are contributing factors that may hinder secondary eyewall formation in tropical cyclones during peripheral and near-core land interaction.

The outer-core structure (R_{34}) decreased during continuous land interaction (e.g., along the coasts of the United States), and thus suggests that the frictional drag of land interaction with a sustained period of exposure also led to a decrease in the R_{34} quadrants over water (i.e., the quadrants used to calculate the azimuthal-average R_{34} value). As with the cases of secondary eyewall formation in Chapter IV.A, secondary eyewall formation in conjunction with this type of land interaction occurred when a flatter-than-average radial wind profile initially existed, but was followed by a sharper radial profile. Although R_{34} decreased, it should be noted that a net radius of hurricane-force winds (R_{64}) increase was observed in Charley prior to landfall that may significantly impact the timing and coverage of hurricane warnings for coastal

communities. The evolutions of tropical cyclone structure changes associated with continuous land interaction are illustrated in Fig. 116 of Chapter IV.

By contrast, land interaction combined with a limited exposure of the storm structure over land (e.g., an island or a peninsula as opposed to a continuous landmass) had a minimal impact on the outer-core structure (R_{34}) of a tropical cyclone. As with Ivan's third eyewall replacement (see Chapter IV.A.1.c), the lack of a significant R_{34} increase during Wilma's eyewall replacement in conjunction with near-core land interaction may be the result of size-limiting factors of the environment, since both of these storms already had very large R_{34} values prior to the secondary eyewall formation. Contrary to all other cases of near-core and peripheral land interaction, Wilma's near-core land interaction during eyewall replacement resulted in a significantly flatter wind profile following secondary eyewall replacement due to a significant decrease in V_t that resulted from the duration of inner-core exposure to frictional effects. The evolutions of tropical cyclone structure changes associated with land interaction of limited exposure are illustrated in Fig. 117 of Chapter IV.

The analyses of individual tropical cyclone case studies of environmental vertical wind shear have revealed that the interactions with midlatitude baroclinic systems resulted in increases in the R_{max} and R_{34}. As expected, convection was enhanced in the downshear quadrant of the tropical cyclone under the influence of vertical wind shear. With the exceptions of the second Isabel interaction and the Ophelia interaction, V_t decreased when vertical wind shear was present. As hypothesized in Chapter IV.A, axisymmetrization of the storm structure may have played a role in the Isabel and Ophelia V_t increases. In the case of Ophelia, the V_t increase may have also been the result of a weaker, smaller tropical cyclone being strengthened by enhanced outflow from the storm center as a baroclinic trough approached.

In all cases, increases of R_{max} played the primary role in the R_{34} increases since the slope of the profile was similar before and after the influence of environmental vertical wind shear, i.e., minimal changes in the exponent x of the modified Rankine vortex in Eq. (20) occurred. Whereas the R_{max} increases in the RF and LR quadrants were similar, the changes to R_{34} in the RF and LR quadrants were quite different. The range of R_{34} increases were 23–83 km for the RF quadrant and 40–144 km for the LR quadrant. That is, on average a larger R_{34} increase occurred in the LR quadrant than in the RF quadrant following the influence of vertical wind shear. Indeed, for the two Fabian interactions and the Ophelia interaction, the ratios of R_{34} increases for the LR

quadrant compared to the RF quadrant were 2.7 to 1, 1.6 to 1, and 1.7 to 1, respectively. These larger R_{34} increases in the LR quadrant generally resulted in a reduction of asymmetries that existed in the outer-core structure prior to the influence of environmental vertical wind shear. It is hypothesized that stronger winds associated with enhanced convection were advected cyclonically around the storm center from the RF quadrant to the LR quadrant in a delayed response, and thus led to axisymmetrization of the outer-core structure.

Whereas the outer-core structure asymmetries for the two Fabian interactions and the Ophelia interaction were reduced, the Isabel interaction was the exception in that outer-core structure asymmetries increased. Isabel may be considered a special case since this tropical cyclone had a highly symmetric annular structure prior to the influence of southwesterly environmental vertical wind shear. This increase in southwesterly environmental vertical wind shear across Isabel was clearly the catalyst that triggered the structure change from a stable, symmetric annular hurricane to a storm with asymmetric convection. For both Isabel interactions, R_{max} and R_{34} had significant increases. In contrast to the Fabian and Ophelia interactions, the smaller R_{34} increases in the LR quadrant (53 km and 40 km, respectively) compared to the RF quadrant (68 km and 57 km, respectively) increased the asymmetries of the outer-core structure.

Environmental vertical wind shear appears to influence tropical cyclone structure in two ways. Similar to the findings on asymmetric convection in Chapter IV.B, the downshear convective asymmetries in the eyewall and spiral rainbands result in an expansion of inner-core structure (R_{max}). In turn, the R_{max} increase results in a R_{34} increase, and thus represents the primary factor in outer-core structure (R_{34}) increases. The enhanced outflow from the storm may be a second factor that influences storm structure during environmental vertical wind shear, since the R_{34} increases associated with asymmetric convection for the cases in Chapter IV.D are larger than for the cases in Chapter IV.B. That is, the cases in Chapter IV.D suggest a more favorable environment for sustained outer-core structure (R_{34}) increases, and thus results in the potential of a larger outer-core structure. By contrast to the cases of asymmetric convection in Chapter IV.B, R_{max} and R_{34} increases associated with tropical cyclone interaction with environmental vertical wind shear were often sustained following that interaction, i.e., the R_{max} and R_{34} radii generally did not decrease following the storm interaction with environmental vertical wind shear. The evolution of tropical cyclone

structure changes associated with environmental vertical wind shear are illustrated in Fig. 134 of Chapter IV.

In summary, secondary eyewall formation, asymmetric convection, land interaction, and environmental vertical wind shear were all found to be conditions that initiate mechanisms that result in structure change of tropical cyclones. All four mechanisms were found to result in inner-core structure (R_{max}) increases and intensity (V_t) decreases, except for the second mode of secondary eyewall formation and asymmetric convection where V_t increases were observed. With the exception of the second mode of asymmetric convection and continuous land interaction, the outer-core structure (R_{34}) was found to increase when one of the four mechanisms was present. The largest R_{34} increases were observed for both modes of secondary eyewall formation, for land interaction combined with a limited exposure of the storm structure over land and the eye over water, and for mature tropical cyclones exposed to environmental vertical wind shear. In some cases, R_{34} increased by as much as 100 km in 12 h which has significant implications on preparedness when the storm is headed toward landfall.

B. FUTURE WORK

This research has been a first step in understanding the internal and external mechanisms that lead to structure change in tropical cyclones, and to characterize the variability of key tropical cyclone parameters to aid in ensemble development. While much information may be gleaned from the current research, more work is required to fully understand the dynamics and physics of the observed structure changes resulting from the mechanism explored in this research.

The understanding of the internal and external mechanisms that lead to structure change in tropical cyclones and the characterization of the variability of key tropical cyclone parameters to aid ensemble development provided by the current research should be expanded. Since the 2005 Atlantic hurricane season, the SFMR equipment has been installed on the AFRES C-130 reconnaissance aircraft. Therefore, nearly all flights into hurricanes since 2005 will include SFMR data in the H*Wind analyses. Increasing the current dataset will lead to a better statistical sampling of the "true" structure variability of Atlantic hurricanes.

The assessment of ΔKE_{anom} (see Appendix D for more details) for secondary eyewall formation and asymmetric convection in Chapter IV indicated a good correla-

tion with the observed outer-core structure (R_{34}) changes. The fundamental question that must first be answered: "Can the current numerical weather prediction models accurately simulate deviations in KE from the standard tropical cyclone wind profile?" If the current numerical weather prediction models are able to adequately simulate these deviations, modeling simulations need to be conducted to better understand the time correlation between when positive (negative) anomalous KE appears in the various conical regions of the tropical cyclone structure and when R_{34} increases (decreases) occur. A better understanding of the potential outward (inward) ΔKE_{anom} may prove useful in alerting operational forecaster to when significant R_{34} increases (decreases) may be expected. This information becomes invaluable in warning coastal population when a tropical cyclone is expected to make landfall.

A good correlation between the increase in radial inflow asymmetries and outer-core structure (R_{34}) changes was not found in this research. However, it was noted that the increase in radial inflow asymmetries appeared to be linked to increases in strong convection in the spiral rainbands near the storm eyewall. In the case of the partial eyewall replacement of Rita in Chapter IV.A.2.b, it appears that this increase in radial inflow asymmetry may have triggered imbalances in the eyewall that resulted in what is termed here an "eyewall burst" (i.e., storm-relative radial outflow) and the formation of a secondary eyewall. Idealized numerical modeling studies should be conducted to assess the role that radial inflow asymmetries may play in secondary eyewall formation. In addition, a better understanding of the relationship between radial inflow asymmetries and secondary eyewall formation may aid operational forecasters in predicting when a secondary eyewall formation and associated R_{34} increases are likely to occur, particularly as a tropical cyclone approaches landfall.

It was observed in this research that the right storm quadrants are larger during rapid intensification of tropical cyclones. Whereas the size increases of the outer-core structure (R_{34}) in the right quadrants may be explained by V_t increases in those quadrants using the modified Rankine vortex in Eq. (20), the internal or external mechanisms that lead to rapid intensification are not obvious. Again, idealized numerical modeling studies should be conducted to gain a better understanding to what role the larger right quadrants play in the rapid intensification of tropical cyclones. Operational forecasters may benefit from a better understanding of the internal or external mechanisms that lead to rapid intensification, especially when a tropical cyclone is threatening a populated area.

It was discovered during this research that a secondary eyewall often forms when a mature tropical cyclone interacts with land. The one exception was with Hurricane Wilma as it approached landfall in southern Florida. However, Wilma's eyewall radius and translation speed were both approximately twice as large as for other storms where a secondary eyewall formed. It was hypothesized that Wilma did not form a secondary eyewall (as it interacted with Florida) because of these two factors. An idealized numerical modeling study is proposed to determine whether these factors are indeed contributing factors to why a secondary eyewall formation was not observed. Again, understanding whether a secondary eyewall will form or not during landfall is crucial to accurately warning populated coastal regions.

Finally, the observed variability of V_t, R_{max}, and R_{34} of tropical cyclones in the western North Atlantic suggest that an ensemble approach to numerical weather modeling is required to fully capture the realm of possible outcomes of structure, intensity, and track in tropical cyclone forecasting. The first step in documenting the variability of the key parameters of V_t, R_{max}, and R_{34} has been accomplished in the current research. The next step is to develop an technique to perturb tropical cyclone vortices in the various members of an ensemble. This step will require the development of realistic tropical cyclone vortex perturbations that can be based on the parameter variabilities documented in this research. After these vortices are inserted into the initial conditions for the ensemble model members, a set of balance equations will be required to prevent spurious inertia-gravity waves from contaminating the solution of the numerical model during model spin-up.

THIS PAGE INTENTIONALLY LEFT BLANK

APPENDIX A. LIST OF STORMS

The 2003–2005 Atlantic tropical cyclone seasons offered a rare opportunity to evaluate a large number of storms of varied intensity and structure, and over a broad seasonal timeframe. Tables 7–9 list 2003–2005 tropical cyclones where H*Wind analyses were available for use in support of this research. All tables contain the storm name (NAME), the period of available analyses (PERIOD OF RECORD), the number of available analyses (# ANAL), the number of analyses incorporating rawinsonde data (# SONDE), the number of analyses incorporating aircraft flight-level reduced data (# ACFT), the number of analyses incorporating stepped frequency microwave radiometer data (# SFMR), and the maximum storm intensity recorded by the analyses (MAX WIND). Analyses from 2003 and 2005 eastern Pacific tropical systems are denoted by 'EP'. The investigation of an area of interest in the western Caribbean during 2005 is denoted by 'INV'..

Table 7 List of 2003 tropical cyclones with H*Wind analysis data.

NAME	PERIOD OF RECORD	# ANAL	# SONDE	# ACFT	# SFMR	MAX WIND
BILL	30JUN@1330 - 30JUN@2330	4	4	4	0	51
CLAUDETTE	9JUL@1330 - 15JUL@1730	20	15	20	0	75
SIX	21JUL@1930 - 21JUL@1930	1	0	1	0	32
ERIKA	15AUG@0130 - 16AUG@1030	8	8	8	0	59
FABIAN	1SEP@1330 - 6SEP@0130	22	22	20	7	123
GRACE	30AUG@1930 - 31AUG@1330	4	1	4	0	45
HENRI	4SEP@1930 - 6SEP@0730	7	2	7	0	48
ISABEL	11SEP@1730 - 18SEP@1630	28	27	25	11	129
LARRY	2OCT@1930 - 3OCT@1330	2	2	2	0	49
MINDY	10OCT@2146 - 10OCT@2146	1	1	1	0	40
ODETTE	5DEC@1630 - 7DEC@0130	5	5	5	1	57
JIMENA (EP)	31AUG@1800 - 2SEP@0130	7	0	7	0	59
LINDA (EP)	14SEP@2000 - 16SEP@1930	2	0	0	0	52

Table 8 List of 2004 tropical cyclones with H*Wind analysis data.

NAME	PERIOD OF RECORD	# ANAL	# SONDE	# ACFT	# SFMR	MAX WIND
ALEX	1AUG@1330 - 4AUG@0730	13	13	13	0	87
BONNIE	9AUG@1930 - 12AUG@1800	14	13	11	0	54
CHARLEY	10AUG@1930 - 14AUG@1645	27	26	25	0	123
FRANCES	29AUG@1930 - 6SEP@1630	35	34	22	16	123
GASTON	29AUG@0003 - 29AUG@0003	1	0	1	0	49
IVAN	6SEP@1930 - 23SEP@1930	51	50	38	18	138
JEANNE	14SEP@1930 - 26SEP@0330	18	16	14	8	96

Table 9 List of 2005 tropical cyclones with H*Wind analysis data.

NAME	PERIOD OF RECORD	# ANAL	# SONDE	# ACFT	# SFMR	MAX WIND
ARLENE	9JUN@0730 - 11JUN@1930	13	12	12	2	62
CINDY	3JUL@2230 - 6JUL@0130	5	5	3	4	67
DENNIS	5JUL@2230 - 10JUL@2230	29	28	24	9	117
EMILY	13JUL@1330 - 20JUL@1130	39	38	37	2	136
FRANKLIN	22JUL@0130 - 25JUL@1930	12	9	11	0	52
GERT	24JUL@1330 - 25JUL@0045	3	3	3	0	46
HARVEY	3AUG@1930 - 4AUG@1330	5	3	4	0	50
IRENE	12AUG@1930 - 14AUG@1930	5	4	5	1	64
KATRINA	24AUG@0730 - 29AUG@1930	41	35	29	16	133
OPHELIA	7SEP@0730 - 17SEP@1930	60	59	47	17	79
PHILIPPE	19SEP@0130 - 19SEP@0730	2	1	2	0	64
RITA	18SEP@1930 - 24SEP@1030	38	35	28	17	136
STAN	2OCT@0703 - 4OCT@1330	4	4	4	0	76
TAMMY	5OCT@1330 - 5OCT@2230	3	0	2	0	44
WILMA	17OCT@1800 - 24OCT@1930	32	32	27	6	141
BETA	28OCT@1930 - 28OCT@1930	1	1	1	0	43
INV (W CAR)	18NOV@1930 - 18NOV@1930	1	0	1	0	39
ADRIAN (EP)	19MAY@1930 - 19MAY@1930	1	0	1	0	70

APPENDIX B. COMPUTING CRITICAL RADII

The H*Wind analyses provide wind data on an approximate 6 km^2 Cartesian grid with each analysis containing more than 25 thousand gridpoints. The distance of a H*Wind intensity threshold of interest (or critical wind radii) from a tropical cyclone's center is determined by dividing each H*Wind analysis grid box into 16 subgrid boxes of equal area (as in Figure 135).

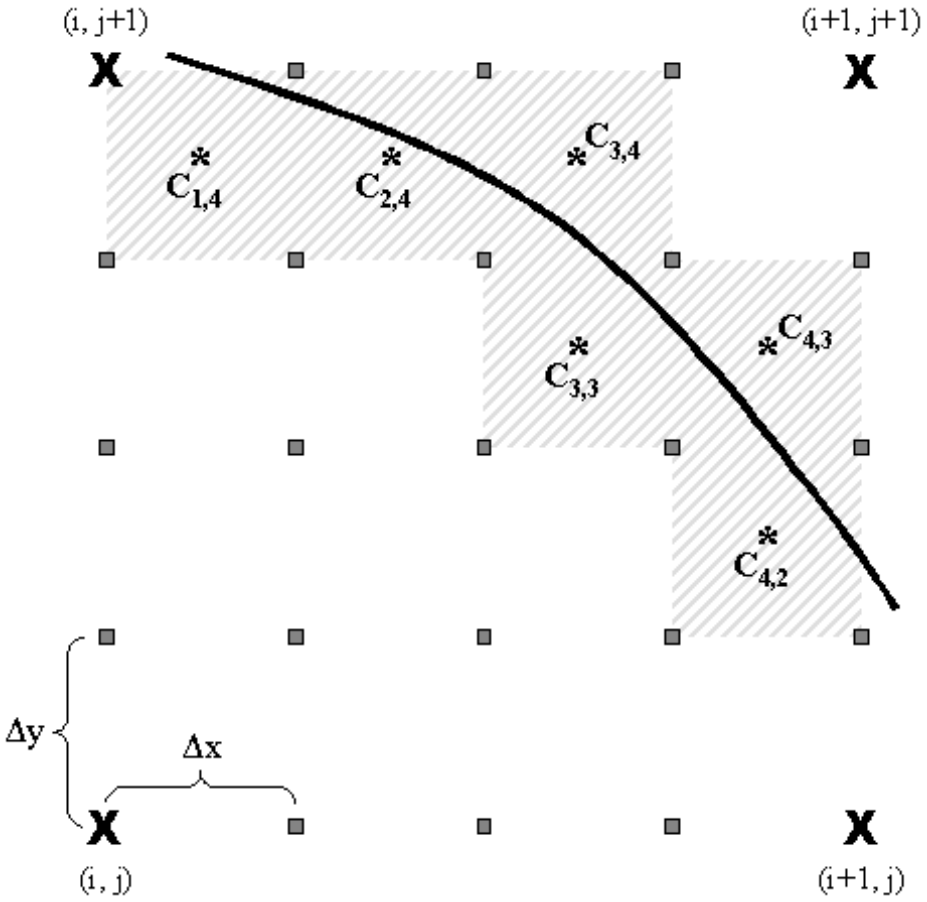

Figure 135 Computing critical wind radii using a distance-weighted subgrid analysis technique. The solid line represents the critical wind radii of interest. The '**X**'s represent the H*Wind analysis gridpoints. The gray '■'s represent the subgrid corner points. The subgrid box centroids ($C_{k,l}$) are represented by '$*$'s. The shaded area highlights the subgrid boxes that the critical wind radii passes through.

The magnitude of the wind ($WSpd$) is computed at the corners of each subgrid box by using the following simple distance-weighted linear interpolation:

$$WSpd_{i+k\Delta x,j+l\Delta y} = a_1 b_1 WSpd_{i,j} + a_2 b_1 WSpd_{i+1,j} + a_1 b_2 WSpd_{i,j+1} + a_2 b_2 WSpd_{i+1,j+1}, \tag{21}$$

where the weights are given by

$$a_1 = 1 - \frac{k}{4},\ a_2 = \frac{k}{4},\ b_1 = 1 - \frac{l}{4},\ b_2 = \frac{l}{4}, \tag{22}$$

and the integers of k and l vary from $0 \rightarrow 4$.

Once each subgrid is defined with a wind magnitude, a simple logical check is performed to determine the existence of the "critical wind radii" within the boundaries of each subgrid box. If the critical threshold is present in a subgrid box, the distance of the subgrid box centroid ($C_{k,l}$) is calculated using

$$C_{k,l} = \sqrt{\left[dist_i + \left(k - \frac{1}{2}\right)\Delta x\right]^2 + \left[dist_j + \left(l - \frac{1}{2}\right)\Delta y\right]^2}, \tag{23}$$

where $dist_i$ and $dist_j$ are the x and y distances of the (i,j) gridpoint from the storm's center. The average distance to the critical wind radii for a given H*Wind analysis grid box is calculated by averaging the subgrid box centroids (shaded boxes in Figure 135) using

$$critical\ wind\ radius\ = \frac{\sum_{k=0}^{4}\sum_{l=0}^{4} C_{k,l}}{n}, \tag{24}$$

where n equals the number of subgrid box intersections.

APPENDIX C. TIME-WEIGHTED INTERPOLATION

The extended best track (EBT) dataset provides tropical cyclone critical wind radii data in 6-h increments for the Atlantic basin. In order to compare EBT critical wind radii with that of the H*Wind analyses, the EBT data is compared to the H*Wind time of interest (t_{HWND}) using a time-weighted linear interpolation according to the following equation:

$$EBTdist(t_{HWND}) = \frac{w_1 Dist(EBT)_{k-1} + w_2 Dist(EBT)_k}{d}, \tag{25}$$

where $d = 0.539612$ (conversion from nautical miles to kilometers), k is the EBT data time greater than t_{HWND}, $k-1$ is the EBT data time less than t_{HWND}, and the weights (w_1 and w_2) are calculated using

$$w_1 = ABS\left[\frac{t(EBT)_k - t_{HWND}}{t(EBT)_k - t(EBT)_{k-1}}\right],\ w_2 = 1 - w_1. \tag{26}$$

THIS PAGE INTENTIONALLY LEFT BLANK

APPENDIX D. ANOMALOUS KINETIC ENERGY DELTA

During the preliminary analysis of the H*Wind analyses for the Atlantic dataset, various diagnostics of tropical cyclone structure changes were examined. The decrease (increase) in the inner-core structure size (R_{max}) was generally found to be correlated with an inward (outward) radial delta of anomalous kinetic energy. This delta of anomalous kinetic energy (KE) per unit area (ΔKE_{anom}) is defined using a differential of time and space according to the following formula:

$$\Delta KE_{anom} = KE_{diff}\,(t) - KE_{diff}\,(t - \Delta t)\,, \tag{27}$$

where t and $t - \Delta t$ represent the current and previous analysis times, and KE_{diff} is defined as

$$KE_{diff} = KE_{anom}(\text{2.0-2.5 deg}) - KE_{anom}\,(\text{1.0–1.5 deg})\,. \tag{28}$$

The anomalous KE (KE_{anom}) is computed across the specified annular ring using

$$KE_{anom} = \frac{IKE_{obs} - IKE_{std}}{A}, \tag{29}$$

where IKE is computed according to Eq. (2), *obs* refers to the observed IKE value, *std* refers to the expected IKE value given by the standard modified Rankine vortex profile from Fig. 1 with an exponent $x = 0.5$, and A is the area of the annular ring. Thus, a negative (positive) ΔKE_{anom} value represents an inward (outward) radial delta of anomalous KE between these two rings for the given analysis time, and an inward (outward) ΔKE_{anom} is expected to be correlated with a decrease (increase) in R_{max} as a contraction (expansion) occurs in the inner-core structure.

THIS PAGE INTENTIONALLY LEFT BLANK

APPENDIX E. OBSERVED STRUCTURE VARIABILITY

Tables 10–21 contain the mean (μ, in km) and standard deviation (SD) for the R_{max} and R_{34} radial distances of 2003–2005 north Atlantic tropical cyclones into motion-relative coordinates: left front (LF), right front (RF), right rear (RR) and left rear (LR) quadrants. The data is parsed in accordance with the life cycle definitions provided in Chapter III and binned in 5 m s^{-1} increments using each quadrant's observed maximum tangential velocity (V_t, in m s^{-1}). Additionally, a multi-pass filter was used to eliminate wind fields in which land interaction (e.g., continents or large islands) occurred within the observation R_{34} radial distance and to eliminate spurious values caused by tropical cyclone interaction with very small islands. Caution must be used in interpreting the data since some bins contain a sample size (n) that is too small to be considered representative of the overarching population distribution. Regardless, the tables that follow are useful in understanding the large variability in structure of north Atlantic tropical cyclones.

Table 10 Rmax distance for Stage II - non-rapid intensification.

V_t		LF			RF			RR			LR		
min	max	n	μ	SD	n	μ	SD	n	μ	SD	n	μ	SD
17	21.9	3	75	13.3	10	76	36.3	10	59	41.6	2	81	0.7
22	26.9	18	41	27.4	31	49	37.4	33	53	36.5	16	44	23.4
27	31.9	14	38	20.1	22	46	36.0	23	46	37.3	16	38	25.0
32	36.9	15	47	23.6	15	42	14.9	16	40	15.0	12	42	17.7
37	41.9	2	24	26.9	2	28	20.5	2	26	18.4	2	22	16.3
42	46.9	1	26	-	1	19	-	1	8	-	1	12	-
47	51.9	0	-	-	0	-	-	0	-	-	0	-	-
52	56.9	4	19	5.0	3	19	3.8	3	18	5.8	4	16	3.7
57	61.9	5	21	5.9	4	19	10.4	4	21	2.9	5	19	5.4
62	66.9	4	27	2.9	4	31	7.3	4	29	6.7	4	24	5.9

Table 11 R34 distance for Stage II - non-rapid intensification.

V_t		LF			RF			RR			LR		
min	max	n	μ	SD	n	μ	SD	n	μ	SD	n	μ	SD
17	21.9	3	98	33.5	10	95	49.8	10	70	50.3	2	90	14.1
22	26.9	18	75	34.8	31	97	51.1	33	94	47.0	16	69	27.7
27	31.9	14	87	45.5	22	120	65.2	23	114	60.0	16	85	41.6
32	36.9	15	146	67.5	15	201	68.6	16	158	78.7	12	156	76.8
37	41.9	2	87	47.4	2	244	53.0	2	178	1.4	2	51	20.5
42	46.9	1	99	-	1	225	-	1	204	-	1	70	-
47	51.9	0	-	-	0	-	-	0	-	-	0	-	-
52	56.9	4	171	64.2	3	285	5.7	3	230	6.4	4	175	61.5
57	61.9	5	187	67.0	4	225	147.6	4	252	59.5	5	123	31.8
62	66.9	4	237	31.5	4	291	35.1	4	267	41.4	4	205	52.8

Table 12 Rmax distance for Stage II - rapid intensification.

V_t		LF			RF			RR			LR		
min	max	n	μ	SD	n	μ	SD	n	μ	SD	n	μ	SD
17	21.9	0	-	-	0	-	-	0	-	-	0	-	-
22	26.9	1	25	-	2	60	50.2	2	67	60.8	1	29	-
27	31.9	3	57	36.0	3	53	37.5	3	61	46.5	3	59	41.6
32	36.9	5	35	15.5	5	31	7.8	7	28	6.9	7	26	5.6
37	41.9	1	27	-	0	-	-	0	-	-	2	14	12.7
42	46.9	3	30	13.6	2	15	5.0	3	18	5.5	3	17	5.6
47	51.9	3	21	0.6	3	22	5.0	3	17	2.5	3	16	2.6
52	56.9	4	12	9.0	4	16	2.4	4	17	5.4	5	14	4.7
57	61.9	0	-	-	0	-	-	0	-	-	0	-	-
62	66.9	1	26	-	1	25	-	1	26	-	1	25	-
67	71.9	0	-	-	0	-	-	0	-	-	0	-	-
72	76.9	1	6	-	1	5	-	1	5	-	1	5	-

Table 13 R34 distance for Stage II - rapid intensification.

V_t		LF			RF			RR			LR		
min	max	n	μ	SD	n	μ	SD	n	μ	SD	n	μ	SD
17	21.9	0	-	-	0	-	-	0	-	-	0	-	-
22	26.9	1	36	-	2	100	87.0	2	75	50.2	1	41	-
27	31.9	3	89	47.7	3	143	67.6	3	155	58.5	3	82	17.2
32	36.9	5	86	25.7	5	156	57.1	7	118	32.8	7	69	12.8
37	41.9	1	128	-	0	-	-	0	-	-	2	52	55.9
42	46.9	3	135	48.9	2	223	48.1	3	155	49.1	3	99	21.9
47	51.9	3	104	40.2	3	209	51.8	3	179	34.2	3	73	28.2
52	56.9	4	131	100.6	4	243	73.3	4	183	13.6	5	80	31.5
57	61.9	0	-	-	0	-	-	0	-	-	0	-	-
62	66.9	1	197	-	1	200	-	1	223	-	1	226	-
67	71.9	0	-	-	0	-	-	0	-	-	0	-	-
72	76.9	1	178	-	1	213	-	1	208	-	1	108	-

Table 14 Rmax distance for Stage IIa - decay.

V_t		LF			RF			RR			LR		
min	max	n	μ	SD	n	μ	SD	n	μ	SD	n	μ	SD
17	21.9	0	-	-	0	-	-	1	21	-	1	19	-
22	26.9	6	78	11.2	7	83	29.0	6	84	19.7	2	69	4.2
27	31.9	12	66	31.2	14	66	38.0	13	66	33.5	10	68	32.7
32	36.9	5	52	25.4	5	59	25.6	5	57	31.2	5	57	30.4
37	41.9	5	58	35.2	5	57	29.5	5	51	26.1	3	64	17.8
42	46.9	7	52	30.7	7	52	29.0	7	50	27.0	7	51	29.2
47	51.9	6	30	14.0	6	29	16.4	7	34	21.8	7	35	22.1
52	56.9	10	41	17.2	12	38	20.9	12	37	20.7	12	33	20.1
57	61.9	11	26	13.5	13	25	12.6	13	25	13.6	15	23	11.8
62	66.9	7	25	14.3	6	28	17.3	6	28	17.6	7	25	15.7
67	71.9	2	19	-	2	18	1.4	2	17	0.7	2	3	-

Table 15 R34 distance for Stage IIa - decay.

V_t		LF			RF			RR			LR		
min	max	n	μ	SD	n	μ	SD	n	μ	SD	n	μ	SD
17	21.9	0	-	-	0	-	-	1	34	-	1	27	-
22	26.9	6	122	28.3	7	137	54.2	6	135	19.1	2	115	8.5
27	31.9	12	189	55.6	14	206	102.1	13	202	77.3	10	202	75.9
32	36.9	5	177	43.1	5	238	38.5	5	236	15.8	5	200	56.1
37	41.9	5	264	80.8	5	301	82.0	5	256	37.7	3	254	15.1
42	46.9	7	247	84.7	7	317	53.2	7	282	40.6	7	227	55.4
47	51.9	6	251	54.9	6	295	52.3	7	286	39.2	7	230	34.6
52	56.9	10	262	85.4	12	313	62.3	12	280	62.2	12	222	95.7
57	61.9	11	203	68.3	13	257	74.0	13	233	72.1	15	153	77.6
62	66.9	7	220	97.4	6	287	35.3	6	261	32.5	7	212	91.5
67	71.9	2	104	26.2	2	197	38.9	2	152	4.2	2	63	2.8

Table 16 Rmax distance for Stage IIa - non-rapid intensification.

V_t		LF			RF			RR			LR		
min	max	n	μ	SD	n	μ	SD	n	μ	SD	n	μ	SD
17	21.9	0	-	-	2	25	5.7	2	24	4.2	0	-	-
22	26.9	3	61	6.4	4	79	36.6	4	65	17.1	1	64	-
27	31.9	15	50	17.7	16	51	20.0	16	51	22.9	12	46	21.6
32	36.9	6	47	17.7	8	52	21.4	8	52	23.7	7	49	17.8
37	41.9	14	42	17.8	15	40	18.4	15	42	19.3	14	39	18.7
42	46.9	14	47	26.1	17	48	23.1	19	52	26.0	18	52	24.8
47	51.9	13	41	29.8	13	40	31.1	13	41	32.8	11	45	34.8
52	56.9	2	62	61.5	5	42	37.9	5	44	38.9	4	25	8.5
57	61.9	11	38	29.6	11	39	28.1	12	38	26.5	12	34	22.8
62	66.9	4	31	15.0	4	30	17.3	4	30	18.4	4	30	15.8
67	71.9	2	29	1.4	2	29	2.1	2	29	1.4	2	27	2.1

Table 17 R34 distance for Stage IIa - non-rapid intensification.

V_t		LF			RF			RR			LR		
min	max	n	μ	SD	n	μ	SD	n	μ	SD	n	μ	SD
17	21.9	0	-	-	2	31	13.4	2	37	9.2	0	-	-
22	26.9	3	94	20.8	4	137	28.8	4	100	23.2	1	77	-
27	31.9	15	122	32.9	16	173	45.9	16	165	58.8	12	100	53.3
32	36.9	6	128	36.8	8	209	39.3	8	202	55.7	7	131	45.9
37	41.9	14	171	89.3	15	233	66.9	15	220	75.1	14	171	89.7
42	46.9	14	230	87.4	17	304	66.6	19	289	56.8	18	249	74.1
47	51.9	13	222	109.6	13	298	83.7	13	274	83.1	11	218	106.0
52	56.9	2	166	95.5	5	335	71.1	5	315	88.5	4	244	118.5
57	61.9	11	223	64.3	11	294	51.4	12	269	63.2	12	209	72.9
62	66.9	4	274	37.4	4	323	25.4	4	310	41.8	4	245	65.9
67	71.9	2	330	12.0	2	334	1.4	2	343	9.2	2	298	31.8

Table 18 Rmax distance for Stage IIa - rapid intensification.

V_t		LF			RF			RR			LR		
min	max	n	μ	SD	n	μ	SD	n	μ	SD	n	μ	SD
17	21.9	0	-	-	0	-	-	0	-	-	0	-	-
22	26.9	0	-	-	0	-	-	0	-	-	0	-	-
27	31.9	0	-	-	0	-	-	0	-	-	0	-	-
32	36.9	1	89	-	1	91	-	1	76	-	1	67	-
37	41.9	7	41	12.3	6	47	16.1	8	39	14.5	8	38	15.3
42	46.9	9	31	14.6	9	32	17.2	8	34	18.5	7	32	16.5
47	51.9	4	24	10.2	4	25	11.7	6	22	11.1	6	23	12.9
52	56.9	1	16	-	2	22	5.0	3	36	33.0	3	32	22.3
57	61.9	6	29	18.9	6	30	15.8	7	28	15.5	7	27	14.8
62	66.9	4	30	6.0	4	33	6.1	6	25	11.5	6	21	15.3
67	71.9	10	23	11.4	10	23	10.4	10	23	11.0	10	20	12.5

Table 19 R34 distance for Stage IIa - rapid intensification.

V_t		LF			RF			RR			LR		
min	max	n	μ	SD	n	μ	SD	n	μ	SD	n	μ	SD
17	21.9	0	-	-	0	-	-	0	-	-	0	-	-
22	26.9	0	-	-	0	-	-	0	-	-	0	-	-
27	31.9	0	-	-	0	-	-	0	-	-	0	-	-
32	36.9	1	188	-	1	294	-	1	271	-	1	107	-
37	41.9	7	132	55.1	6	226	75.1	8	211	64.0	8	120	65.0
42	46.9	9	186	70.8	9	227	78.2	8	238	82.2	7	183	94.6
47	51.9	4	164	55.5	4	248	19.1	6	209	68.1	6	140	121.6
52	56.9	1	139	-	2	267	33.9	3	259	77.5	3	188	103.4
57	61.9	6	218	65.4	6	280	51.8	7	234	64.9	7	158	104.3
62	66.9	4	274	38.0	4	336	22.1	6	230	100.6	6	190	102.3
67	71.9	10	245	86.5	10	300	50.4	10	267	55.2	10	217	100.7

Table 20 Rmax distance for Stage III - decay.

V_t		LF			RF			RR			LR		
min	max	n	μ	SD	n	μ	SD	n	μ	SD	n	μ	SD
17	21.9	0	-	-	2	82	93.3	0	-	-	1	18	-
22	26.9	7	70	34.0	13	65	29.4	10	79	29.8	7	70	30.2
27	31.9	9	53	15.3	10	49	18.9	10	46	19.3	9	47	15.2
32	36.9	8	38	11.2	8	43	13.9	8	41	13.0	7	40	13.7
37	41.9	7	41	16.7	6	44	15.9	5	44	11.0	6	45	13.2
42	46.9	11	80	42.1	18	73	24.2	18	72	23.5	18	69	20.7
47	51.9	3	38	23.9	6	44	17.0	10	37	13.6	10	33	11.9
52	56.9	18	29	9.5	21	29	7.3	24	30	10.7	24	26	9.9
57	61.9	15	34	6.8	15	33	7.3	16	33	8.3	16	31	7.4
62	66.9	6	31	2.9	6	28	2.6	6	27	3.1	6	27	4.5
67	71.9	2	23	6.4	2	22	2.8	2	22	6.4	2	20	4.2

Table 21 R34 distance for Stage III - decay.

V_t		LF			RF			RR			LR		
min	max	n	μ	SD	n	μ	SD	n	μ	SD	n	μ	SD
17	21.9	0	-	-	2	123	150.6	0	-	-	1	18	-
22	26.9	7	105	36.5	13	136	54.7	10	132	57.6	7	84	38.1
27	31.9	9	127	49.0	10	146	61.5	10	111	48.3	9	94	32.9
32	36.9	8	129	57.5	8	170	62.1	8	134	39.2	7	81	26.5
37	41.9	7	116	65.6	6	187	60.1	5	167	17.5	6	94	44.4
42	46.9	11	299	106.6	18	339	71.1	18	330	79.2	18	285	78.1
47	51.9	3	265	35.5	6	268	68.1	10	270	30.6	10	234	43.8
52	56.9	18	289	55.5	21	308	33.3	24	297	51.5	24	254	63.0
57	61.9	15	306	50.5	15	336	45.5	16	301	45.6	16	254	50.6
62	66.9	6	309	26.3	6	329	38.0	6	353	19.9	6	323	20.7
67	71.9	2	264	16.3	2	322	4.2	2	276	6.4	2	205	10.6

THIS PAGE INTENTIONALLY LEFT BLANK

LIST OF REFERENCES

Alpert, P., S. O. Krichak, T. N. Krishnamurti, U. Stein, and M. Tsidulko, 1996: The relative roles of lateral boundaries, initial conditions, and topography in mesoscale simulations of lee cyclogenesis. *J. Appl. Meteor.*, **35**, 1091–1099.

Anthes, R. A., Y.-H. Kou, D. P. Baumhefner, R. M. Errico and T. W. Bettge, 1985: Predictability of mesoscale motions. *Advances in Geophysics*, Vol. 28, Academic Press, 159–202 pp.

Atlas, D., and C. W. Ulbrich, 1977: Path- and area-integrated rainfall measurement by microwave attenuation in the 1–3 cm band. *J. Appl. Meteor.*, **16**, 1322–1331.

Bao, J.-W., S. G. Gopalakrishnan, S. A . Michelson, F. D . Marks, and M. T. Montgomery, 2012: Impact of physics representations in the HWRFX on simulated hurricane structure and pressure-wind relationships. *Mon. Wea. Rev.*, **140**, 3278–3299.

Barrick, D. E., and C. T. Swift, 1980: The Seasat microwave instruments in historical perspective. *IEEE J. Oceanic Eng.*, **OE-5**, 74–79.

Baumhefner, D. P., and D. J. Perkey, 1982: Evaluation of lateral boundary errors in a limited-domain model. *Tellus*, **34**, 409–428.

Bender, M. A., 1997: The effect of relative flow on the asymmetric structure in the interior of hurricanes. *J. Atmos. Sci.*, **54**, 703–724.

Bister, M., 2001: Effect of peripheral convection on tropical cyclone formation. *J. Atmos. Sci.*, **58**, 3463–3476.

Black, P. G., and C. T. Swift, 1984: Airborne stepped frequency microwave radiometer measurements of rainfall rate and surface wind speed in hurricanes. Reprints, *Second Conf. on Radar Meteorology*, Zurich, Switzerland, Amer. Meteor. Soc., 433–438.

Carr, L. E., III, and R. T. Williams, 1989: Barotropic vortex stability to perturbations from axisymmetry. *J. Atmos. Sci.*, **46**, 3177–3191.

———, and R. L. Elsberry, 1997: Models of tropical cyclone wind distribution and beta-effect propagation for application to tropical cyclone track forecasting. *Mon. Wea. Rev.*, **125**, 3190–3209.

Charney, J. G., and A. Eliassen, 1964: On the growth of the hurricane depression. *J. Atmos. Sci.*, **21**, 68–75.

Chen, Y, and M. K. Yau, 2001: Spiral bands in a simulated hurricane. Part I: Vortex Rossby wave verification. *J. Atmos. Sci.*, **58**, 2128–2145.

DeMaria, M., 1996: The effect of vertical shear on tropical cyclone intensity change. *J. Atmos. Sci.*, **53**, 2076–2087.

———, S. D. Aberson, K. V. Ooyama, and S. J. Lord, 1992: A nested spectral model for hurricane track forecasting. *Mon. Wea. Rev.*, **120**, 1628–1643.

Demuth, J., M. DeMaria, and J. A. Knaff, 2006: Improvement of advanced microwave sounder unit tropical cyclone intensity and size estimation algorithms. *J. Appl. Meteor.*, **45**, 1573–1581.

Depperman, C. E., 1947: Notes on the origin and structure of Philippine typhoons. *Bull. Amer. Meteor. Soc.*, **28**, 399–404.

Diercks, J. W., and R. A. Anthes, 1976: Diagnostic studies of spiral rainbands in a nonlinear hurricane model. *J. Atmos. Sci.*, **33**, 959–975.

Dunion, J. P., C. W. Landsea, S. H. Houston, and M. D. Powell, 2003: A reanalysis of the surface winds for Hurricane Donna of 1960. *Mon. Wea. Rev.*, **131**, 1992–2011.

Elsberry, R. L., Ed., 1987: *A Global View of Tropical Cyclones.* Office of Naval Research, 185 pp.

———, 2002: Predicting hurricane landfall precipitation: Optimistic and pessimistic views from the Symposium on Precipitation Extremes. *Bull. Amer. Meteor. Soc.*, **83**, 1333–1340.

———, G. J. Holland, H. Gerrish, M. DeMaria, C. P. Guard, and K. Emanuel, 1992: Is there any hope for tropical cyclone intensity prediction - a panel discussion. *Bull. Amer. Meteor. Soc.*, **73**, 264–275.

———, T. D. B. Lambert, and M. A. Boothe, 2007: Accuracy of Atlantic and eastern North Pacific tropical cyclone intensity forecast guidance. *Wea. Forecasting*, **22**, 747–762.

———, and R. A. Stenger, 2008: Advances in understanding of tropical cyclone wind structure change. *Asian-Pacific J. Atmos. Sci.*, **44**, 11–24.

Emanuel, K. A., 1986: An air-sea interaction theory for tropical cyclones. Part I: Steady state maintenance. *J. Atmos. Sci.*, **43**, 585–604.

———, 1989: The finite-amplitude nature of tropical cyclogenesis. *J. Atmos. Sci.*, **46**, 3431–3456.

———, 1995a: The behavior of a simple hurricane model using a convective scheme based on subcloud-layer entropy equilibrium. *J. Atmos. Sci.*, **52**, 3960–3968.

———, 1995b: Sensitivity of tropical cyclones to surface exchange coefficients and a revised steady-state model incorporating eye dynamics. *J. Atmos. Sci.*, **52**, 3969–3976.

Errico, R., and D. Baumhefner, 1987: Predictability experiments using a high-resolution limited-area model. *Mon. Wea. Rev.*, **115**, 488–504.

———, T. Vukicevic, and K. Raeder, 1993: Comparison of initial and lateral boundary condition sensitivity for a limited-area model. *Tellus*, **45A**, 539–557.

Fiorino, M., and R. L. Elsberry, 1989: Some aspects of vortex structure related to tropical cyclone motion. *J. Atmos. Sci.*, **46**, 975–990.

Frank, W. M., and E. A. Ritchie, 1999: Effects of environmental flow upon tropical cyclone structure. *Mon. Wea. Rev.*, **127**, 2044–2061.

Franklin, J. L., S. J. Lord, S. E . Feuer, and F. D. Marks Jr., 1993: The kinematic structure of Hurricane Gloria (1985) determined from nested analyses of dropwindsonde and Doppler radar data. *Mon. Wea. Rev.*, **121**, 2433–2451.

———, M. L. Black, and K. Valda, 2003: GPS dropwindsonde wind profiles in hurricanes and their operational implications. *Wea. Forecasting*, **18**, 32–44.

Guinn, T., and W. H. Schubert, 1993: Hurricane spiral bands. *J. Atmos. Sci.*, **50**, 3380–3403.

Gray, M. W., 1968: Global view of the origin of tropical disturbances and storms. *Mon. Wea. Rev.*, **96**, 669–700.

———, and D. J. Shea, 1973: The hurricane's inner core region, II: Thermal stability and dynamic characteristics. *J. Atmos. Sci.*, **30**, 1565–1576.

Hanley, D. E., J. Molinari, and D. Keyser, 2001: A composite study of the interaction between tropical cyclones and upper-tropospheric troughs. *Mon. Wea. Rev.*, **129**, 2570–2584.

Hawkins, J. D., M. Helveston, T. F. Lee, F. J. Turk, K. Richardson, C. Sampson, J. Kent, and R. Wade, 2006: Tropical cyclone multiple eyewall configurations. Paper 6B.1, *27th Hurr. And Trop. Meteor. Conf.*, Monterey, CA, Amer. Meteor. Soc.

Hill, K. A., and G. M. Lackmann, 2009: Influence of environmental humidity on tropical cyclone size. *Mon. Wea. Rev.*, **137**, 3294–3315.

Holland, G. J., 1980: An analytic model of the wind and pressure profiles in hurricanes. *Mon. Wea. Rev.*, **108**, 1212–1218.

———, and R. T. Merrill, 1984: On the dynamics of tropical cyclone structure changes. *Quart. J. Roy. Meteor. Soc.*, **110**, 723–745.

Hsiao, L.-F., M. S. Peng, D.-S. Chen, K.-N. Huang, and T.-C. Yeh, 2009: Sensitivity of typhoon track predictions in a regional prediction system to initial and lateral boundary conditions. *J. Appl. Meteor. And Climo.*, **48**, 1913–1928.

Hughes, L., A., 1952: On the low level wind structure of tropical cyclones. *J. Meteor.*, **9**, 422–428.

Jorgensen, D. P., and P. L. Willis, 1982: A Z-R relationship for hurricanes. *J. Appl. Meteor.*, **21**, 356–366.

Kepert, J. D., 2001: The dynamics of boundary layer jets within the tropical cyclone core. Part I: Linear theory. *J. Atmos. Sci.*, **58**, 2469–2484.

———, and Y. Wang, 2001: The dynamics of boundary layer jets within the tropical cyclone core. Part II: Nonlinear enhancement. *J. Atmos. Sci.*, **58**, 2485–2501.

Kimball, S. K., and M. S. Mulekar, 2004: A 15-year climatology of North Atlantic tropical cyclones. Part I: Size parameters. *J. Climate*, **17**, 3555–3575.

Klein, L. A., and C. T. Swift, 1977: An improved model for the dielectric constant of sea water at microwave frequencies. *IEEE J. Oceanic Eng.*, **OE-2**, 104–111.

Knaff, J. A., J. P. Kossin, and M. DeMaria, 2003: Annular hurricanes. *Wea. Forecasting*, **18**, 204–223.

———, T. A. Cram, A. B. Schumacher, J. P. Kossin, and M. DeMaria, 2008: Objective identification of annular hurricanes. *Wea. Forecasting*, **23**, 17–28.

Kossin, J. P., and M. Sitkowski, 2009: An objective model for identifying secondary eyewall formation in hurricanes. *Mon. Wea. Rev.*, **137**, 876–892.

Kuo, H.-C., R. T. Williams, and J.-H. Chen, 1999: A possible mechanism for the eye rotation of typhoon Herb. *J. Atmos. Sci.*, **56**, 1659–1673.

———, C.-P. Chang, Y.-T. Yang, and H.-J. Jiang, 2009: A Western North Pacific typhoons with concentric eyewalls. *Mon. Wea. Rev.*, **137**, 3758–3770.

Kurihara, Y., 1976: On the development of spiral bands in a tropical cyclone. *J. Atmos. Sci.*, **33**, 940–958.

Langland, R. H., M. A. Shapiro, and R. Gelaro, 2002: Initial condition sensitivity and error growth in forecasts of the 25 January 2000 East Coast Snowstorm. *Mon. Wea. Rev.*, **130**, 957–974.

Lee, C. -S., K. K. W. Cheung, W. -T. Fang, and R. L. Elsberry, 2010: Initial maintenance of tropical cyclone size in the western North Pacific. *Mon. Wea. Rev.*, **138**, 3207–3223

Lewis, B. M., H. F. Hawkins, 1982: Polygonal eye walls and rainbands in hurricanes. *Bull. Amer. Meteor. Soc.*, **63**, 1294–1300.

Lord, S. J., and J. L. Franklin, 1987: The environment of Hurricane Debby (1982). Part I: Winds. *Mon. Wea. Rev.*, **115**, 2760–2780.

Lorenz, E. N., 1963: Deterministic nonperiodic flow. *J. Atmos. Sci.*, **20**, 130–141.

MacDonald, N. J., 1968: The evidence for the existence of Rossby-type waves in the hurricane vortex. *Tellus*, **20**, 138–150.

Merrill, R. T., 1984: A comparison of large and small tropical cyclones. *Mon. Wea. Rev.*, **112**, 1408–1418.

———, 1988: Environmental influences on hurricane intensification. *J. Atmos. Sci.*, **45**, 1678–1687.

Möller, J. D., and M. T. Montgomery, 1999: Vortex Rossby waves and hurricane intensification in a barotropic model. *J. Atmos. Sci.*, **56**, 1674–1687.

———, and M. T. Montgomery, 2000: Tropical cyclone evolution via potential vorticity anomalies in a three-dimensional balance model. *J. Atmos. Sci.*, **57**, 3366–3387.

Montgomery, M. T., and R. J. Kallenbach, 1997: A theory for vortex Rossby-waves and its application to spiral bands and intensity changes in hurricanes. *Quart. J. Roy. Meteor. Soc.*, **123**, 435–465.

———, and C. Lu, 1997: Free waves on barotropic vortices. Part I: Eigenmode structure. *J. Atmos. Sci.*, **123**, 435–465.

———, and R. K. Smith, 2013: Paradigms for tropical cyclone intensification. *Aust. Meteorol. And Oceanogr. J.*, in press.

Moyer, A. C., J. L. Evans, and M. Powell 2007: Comparison of observed gale radius statistics. *Meteorol. Atmos. Phys.*, **45**, 1678–1687.

Mullen, S. L., and D. P. Baumhefner, 1989: The impact of initial condition uncertainty on numerical simulations of large-scale explosive cyclogenesis. *Mon. Wea. Rev.*, **117**, 2800–2821.

National Oceanic and Atmospheric Administration, cited 2007: Background on the HRD surface wind analysis system. [Available from http://www.aoml.noaa.gov/hrd/.]

Naval Research Laboratory, cited 2007: Tropical cyclone satellite imagery archive. [Available from http://www.nrlmry.navy.mil/TC.html.]

Nguyen, V. S., R. K. Smith, and M. T. Montgomery, 2008: Tropical-cyclone intensification and predictability in three dimensions. *Quart. J. Roy. Meteor. Soc.*, **134**, 563–582.

Nolan, D. S., and M. T. Montgomery, 2002: Nonhydrostatic, three-dimensional perturbations to balanced, hurricane-like vortices. Part I: Linearized formulation, stability, and evolution. *J. Atmos. Sci.*, **59**, 2989–3020.

Olsen, R. L., D. V. Rogers, and D. B. Hodge, 1978: The aR^b relation in the calculation of rain attenuation. *IEEE Trans. Antennas Propagat.*, **AP-26**, 318–329.

Ooyama, K. V., 1969: Numerical simulation of the life cycle of tropical cyclones. *J. Atmos. Sci.*, **26**, 3–40.

———, 1984: A model for hurricane prediction. Postprints, *15th Conf. on Hurricane and Tropical Meteorology*, Miami, FL, Amer. Meteor. Soc., 344–349.

———, 1987: Scale-controlled objective analysis. *Mon. Wea. Rev.*, **115**, 2479–2506.

Pedersen, L. T., 1990: Microwave radiometers. *Microwave Remote Sensing for Oceanographic and Marine Weather-Forecast Models*, R. A. Vaughn, Ed., Kluwer Academic, 177–190.

Peng, M. S., B.-F. Jeng, and R. T. Williams, 1999: A numerical study on tropical cyclone intensification. Part I: Beta effect and mean flow effect. *J. Atmos. Sci.*, **56**, 1404–1423.

Pielke, R. A., and C. W. Landsea, 1998: Normalized hurricane damages in the United States: 1925–1995. *Wea. Forecasting*, **13**, 621–631.

Powell, M. D., 1980: Evaluations of diagnostic marine boundary layer models applied to hurricanes. *Mon. Wea. Rev.*, **108**, 757–766.

———, and S. H. Houston, 1996: Hurricane Andrew's landfall in south Florida. Part II: Surface wind fields and potential real-time applications. *Wea. Forecasting*, **11**, 329–349.

———, ———, and T. A. Reinhold, 1996: Hurricane Andrew's landfall in south Florida. Part I: Standardizing measurements for documentation of surface wind fields. *Wea. Forecasting*, **11**, 304–328.

———, ———, L. R. Amat, and N. Morisseau-Leroy, 1998: The HRD real-time hurricane wind analysis system. *J. Wind Eng. Ind. Aerodyn.*, **77–78**, 53–64.

———, and T. A. Reinhold, 2007: Tropical cyclone destructive potential by integrated kinetic energy. *Bull. Amer. Meteor. Soc.*, **88**, 513–526.

———, E. W. Uhlhorn, and T. A. Reinhold, 2009: Estimating maximum surface winds from hurricane reconnaissance measurements. *Wea. Forecasting*, **24**, 868–883.

Reasor, P. D., M. T. Montgomery, F. D. Marks Jr., and J. F. Gamache, 2000: Low-wavenumber structure and evolution of the hurricane inner core observed by airborne Dual-Doppler radar. *Mon. Wea. Rev.*, **128**, 1653–1680.

Riehl, H., 1954: *Tropical Meteorology.* McGraw-Hill, 392 pp.

———, 1963: Some relations between wind and thermal structure of steady-state hurricanes. *J. Atmos. Sci.*, **20**, 276–287.

Rozoff, C. M., W. H. Schubert, and J. P. Kossin, 2008: Some dynamical aspects of tropical cyclone concentric eyewalls. *Quart. J. Roy. Meteor. Soc.*, **134**, 583–593.

———, ———, and B. D. McNoldy, 2006: Rapid filamentation zones in intense tropical cyclones. *J. Atmos. Sci.*, **63**, 325–340.

Saffir, H., 1975: Low cost construction resistant to earthquakes and hurricanes. No. ST/ESA/23, United Nations, 216 pp.

Sawada, M., and T. Iwasaki, 2010a: Impacts of evaporation from raindrops on tropical cyclones. Part I: Evolution and axisymmetric structure. *J. Atmos. Sci.*, **67**, 71–83.

———, and ———, 2010b: Impacts of evaporation from raindrops on tropical cyclones. Part II: Features of rainbands and asymmetric structure. *J. Atmos. Sci.*, **67**, 84–96.

Schubert, W. H., M. T. Montgomery, R. K. Taft, T. A. Guinn, S. R. Fulton, J. P. Kossin, and J. P. Edwards, 1999: Polygonal eyewalls, asymmetric eye contraction, and potential vorticity mixing in hurricanes. *J. Atmos. Sci.*, **56**, 1197–1223.

Shapiro, L. J., 1983: The asymmetric boundary layer flow under a translating hurricane. *J. Atmos. Sci.*, **40**, 1984–1998.

———, and H. E. Willoughby 1982: The response of balanced hurricanes to local sources of heat and momentum. *J. Atmos. Sci.*, **39**, 378–394.

Shin, S., and R. K. Smith, 2008: Tropical-cyclone intensification and predictability in a minimal three-dimensional model. *Quart. J. Roy. Meteor. Soc.*, **134**, 1661–1671.

Simpson, R. H., 1974: The hurricane disaster potential scale. *Weatherwise*, **27**, 169–186.

Smith, R. K., C. W. Schmidt, and M. T. Montgomery, 2011: An investigation of rotational influences on tropical-cyclone size and intensity. *Quart. J. Roy. Meteor. Soc.*, **137**, 1841–1855.

Stenger, R. A., and R. L. Elsberry 2008: Examining tropical cyclone structure variability using H*Wind analyses. *28th Conf. on Hurricane and Tropical Meteorology*, Orlando, FL, Amer. Meteor. Soc., 13C.3. [Available from https://ams.confex.com/ams/pdfpapers/138285.pdf.]

Terwey, W. D., and M. T. Montgomery, 2008: Secondary eyewall formation in two idealized, full-physics modeled hurricanes. *J. Geophys. Res.*, **113**, D12112, doi:10.1029/2007/JD008897.

Thompson, P., 1957: Uncertainty of initial state as a factor in the predictability of large scale atmospheric flow patterns. *Tellus*, **9**, 275–295.

Uhlhorn, E. W., and P. G. Black, 2003: Verification of remotely sensed sea surface winds in hurricanes. *J. Atmos. Oceanic Technol.*, **20**, 99–116.

———, ———, J. L. Franklin, M. Goodberlet, J. Carswell, and A. S. Goldstein, 2007: Hurricane surface wind measurements from an operational stepped frequency microwave radiometer. *Mon. Wea. Rev.*, **135**, 3070–3085.

Vukicevic, T., and R. M. Errico, 1990: The influence of artificial and physical factors upon predictability estimates using a complex limited-area model. *Mon. Wea. Rev.*, **118**, 1460–1482.

Wang, Y., 2001: An explicit simulation of tropical cyclones with a triply nested movable mesh primitive equation model: TCM3. Part I: Model description and control experiment. *Mon. Wea. Rev.*, **129**, 1370–1394.

———, 2002a: Vortex Rossby waves in a numerically simulated tropical cyclone. Part I: Overall structure, potential vorticity, and kinetic energy budgets. *J. Atmos. Sci.*, **59**, 1213–1238.

———, 2002b: Vortex Rossby waves in a numerically simulated tropical cyclone. Part II: The role in tropical cyclone structure and intensity changes. *J. Atmos. Sci.*, **59**, 1239–1262.

———, 2002c: An explicit simulation of tropical cyclones with a triply nested movable mesh primitive equation model: TCM3. Part II: Model refinements and sensitivity to cloud microphysics parameterization. *Mon. Wea. Rev.*, **130**, 3022–3036.

———, 2008a: Rapid filamentation zone in a numerically simulated tropical cyclone. *J. Atmos. Sci.*, **65**, 1158–1181.

———, 2008b: Structure and formation of an annular hurricane simulated in a fully compressible, nonhydrostatic model-TCM4. *J. Atmos. Sci.*, **65**, 1505–1527.

———, 2009: How do outer spiral rainbands affect tropical cyclone structure and intensity?. *J. Atmos. Sci.*, **66**, 1250–1273.

———, and G. J. Holland, 1996a: Beta drift of baroclinic vortices. Part I: Adiabatic vortices. *J. Atmos. Sci.*, **53**, 411–427.

———, and ———, 1996b: Beta drift of baroclinic vortices. Part II: Diabatic vortices. *J. Atmos. Sci.*, **53**, 3737–3756.

———, and ———, 1996c: Tropical cyclone motion and evolution in vertical shear. *J. Atmos. Sci.*, **53**, 3313–3332.

———, and C.-C. Wu, 2004: Current understanding of tropical cyclone structure and intensity change - a review. *Meteorol. Atmos. Phys.*, **87**, 257–278.

Warner, T. T., L. E. Key, and A. M. Lario, 1989: Sensitivity of mesoscale-model forecast skill to some initial-data characteristics, data density, data position, analysis procedure and measurement error. *Mon. Wea. Rev.*, **117**, 1281–1310.

———, R. A. Peterson, and R. E. Treadon, 1997: A tutorial on lateral boundary conditions as a basic and potentially serious limitation to regional numerical weather prediction. *Bull. Amer. Meteor. Soc.*, **78**, 2599–2617.

Weatherford, C. L., and W. M. Gray, 1988a: Typhoon structure as revealed by aircraft reconnaissance. Part I: Data analysis and climatology. *Mon. Wea. Rev.*, **116**, 1032–1043.

———, and ———, 1988b: Typhoon structure as revealed by aircraft reconnaissance. Part II: Structure variability. *Mon. Wea. Rev.*, **116**, 1044–1056.

Webster, W. L. J., T. T. Wilheit, D. B. Ross, and P. Gloersen, 1976: Spectral characteristics of the microwave emission from a wind-driven foam-covered sea. *J. Geophys. Res.*, **81**, 3095–3099.

Willoughby, H. E., 1978: A possible mechanism for the formation of hurricane rainbands. *J. Atmos. Sci.*, **35**, 838–848.

———, J. A. Clos, and M. G. Shoreibah, 1982: Concentric eyewalls, secondary wind maxima, and the evolution of the hurricane vortex. *J. Atmos. Sci.*, **39**, 395–411.

———, H.-L. Jin, S. J. Lord, and J. M. Piotrowicz, 1984: Hurricane structure and evolution as simulated by an axisymmetric, nonhydrostatic numerical model. *J. Atmos. Sci.*, **41**, 1169–1186.

Wu, C.-C., and H.-J. Cheng, 1999: An observational study of environmental influences on the intensity changes of typhoon Flo (1990) and Gene (1990). *Mon. Wea. Rev.*, **127**, 3003–3031.

Xu, J., and Y. Wang, 2010: Sensitivity of tropical cyclone inner-core size and intensity to the radial distribution of surface entrophy flux. *J. Atmos. Sci.*, **67**, 1831–1852.

Yang, Y.-T., H.-C. Kuo, E. A. Hendricks, and M. S. Peng, 2013: Structural and intensity changes of cencentric eyewall typhoons in the western North Pacific basin. *Mon. Wea. Rev.*, **141**, 2632–2648.

Zhu, H., and A. Thorpe, 2006: Predictability of extratropical cyclones: The influence of initial condition and model uncertainties. *J. Atmos. Sci.*, **63**, 1483–1497.

INITIAL DISTRIBUTION LIST

1. Defense Technical Information Center
   Fort Belvoir, Virginia

2. Dudley Knox Library
   Naval Postgraduate School
   Monterey, California